

# MAGNETIC FIELD EVOLUTION IN ISOLATED AND INTERACTING SPIRAL GALAXIES

**Dissertation**  
**Ph.D. Thesis**

an der Fakultät für Physik  
at the Faculty of Physics

der Ludwig-Maximilians-Universität (LMU) München  
of the Ludwig-Maximilians-University (LMU) Munich

vorgelegt von  
submitted by

**Hanna Helena Kotarba**

aus Zabrze, Polen  
from Zabrze, Poland

München, 8. April 2011  
Munich, 8. April 2011

Erstgutachter: Prof. Dr. Harald Lesch  
First Evaluator University Observatory of the Ludwig Maximilians University, Munich

Zweitgutachter: Prof. Dr. Hartmut Zohm  
Second Evaluator Max Planck Institute for Plasmaphysics, Garching

Datum der mündlichen Prüfung: 15. Juni 2011  
Date of the oral exam: 15. June 2011

*The larger our ignorance, the stronger the magnetic field.*  
Lodewijk Woltjer, Dutch astronomer, 1965.



---

## Zusammenfassung

Die vorliegende Doktorarbeit behandelt die Frage nach der Entstehung und Entwicklung von Magnetfeldern in Galaxien. Mit Hilfe von modernen, hochauflösenden numerischen Simulationen wird die kinematische Entwicklung von Magnetfeldern in isolierten Galaxien als auch ihre selbst-konsistente Entwicklung in kollidierenden Galaxien studiert. Zudem wird die Bedeutung einer durch galaktische Kollisionen getriebenen Magnetfeldverstärkung während der Phase der hierarchischen Strukturentstehung im Universum diskutiert.

Die Einleitung motiviert die Untersuchungen dieser Arbeit im Rahmen der derzeitigen Kenntnisse und Theorien über galaktische und extra-galaktische Magnetfelder. Neben einem kurzen historischen Überblick über das Phänomen Magnetismus behandelt sie die Grundlagen der Beobachtungsmethoden extra-terrestrischer Magnetfelder, Beobachtungen von Magnetfeldern in verschiedenen Typen von Galaxien, in Galaxienhaufen und im frühen Universum, als auch die theoretischen Konzepte der Dynamo-Prozesse, mit denen die beobachteten Magnetfeldstärken und -strukturen im lokalen Universum heutzutage erklärt werden. Darauf aufbauend werden offene Fragen zur Entwicklung von Magnetfeldern im Universum diskutiert. Insbesondere werfen die beobachteten Magnetfelder in sehr jungen Galaxien, die nicht durch die relativ langsamen Dynamo-Prozesse erklärt werden können, die Frage nach anderen, effizienten Verstärkungsmechanismen auf. In dieser Arbeit wird gezeigt, dass die durch galaktische Kollisionen getriebene Magnetfeldverstärkung ein vielversprechender Kandidat für einen solchen Mechanismus ist.

In der ersten der drei vorgestellten Veröffentlichungen wird eine Reihe von  $N$ -Teilchen ( $N$ -body) Simulationen einer Spiralgalaxie präsentiert, wobei hydrodynamische Gleichungen und die magnetische Induktionsgleichung mit Hilfe der SPH (Smoothed Particle Hydrodynamics) Methode behandelt werden. Ziel dieser Simulationen war die Untersuchung der kinematischen Reaktion eines gegebenen Anfangsmagnetfeldes auf das großräumige Geschwindigkeitsfeld einer Scheibengalaxie, deren Spiralstruktur sich selbstkonsistent entwickelt. Diese Simulationen sind die ersten ihrer Art und, im Gegensatz zu den meisten analytischen Betrachtungen, beruhen nicht auf vereinfachenden Annahmen wie z.B. Axialsymmetrie. Die wesentlichen Ergebnisse sind das Aufzeigen der Bedeutung von Abweichungen von der Axialsymmetrie für die Entwicklung von Magnetfeldern in Spiralgalaxien; die Erkenntnis, dass das großräumige Geschwindigkeitsfeld allein nicht in der Lage ist, Magnetfelder effizient zu verstärken; und ein Schätzwert der maximalen numerischen Divergenz des Magnetfeldes, bis zu welchem die Simulationen verlässlich sind.

Vollständige magnetohydrodynamische (MHD)  $N$ -body/SPH Simulationen zweier kollidierender Galaxien, namentlich der Antennae Galaxien, werden in der zweiten Veröffentlichung vorgestellt. Diese Simulationen sind die ersten MHD Simulationen kollidierender Galaxien die jemals durchgeführt wurden. Als wesentliches Ergebnis wird gezeigt, dass Galaxienkollisionen, während derer in hohem Maße Turbulenz getrieben wird, zu einer effizienten Verstärkung eines gegebenen Anfangsmagnetfeldes führen. Unabhängig von dem Anfangsmagnetfeld, welches zwischen  $10^{-9}$  und  $10^{-4}$  G variiert wurde, ist diese Verstärkung bei einer Feldstärke von einigen  $\mu\text{G}$  (Mikro-Gauss) gesättigt. Es zeigt sich, dass dieser Sättigungspunkt dem Gleichgewicht zwischen magnetischer und turbulenter Energie entspricht, ein Ergebnis, das auch theoretisch erwartet wird. Die gesättigte Magnetfeldstärke stimmt sehr gut mit beobachteten Feldstärken überein, und synthetische Radiokarten der erwarteten Synchrotron-Emission des simulierten Systems sind mit der beobachteten Radioemission der Antennae Galaxien vergleichbar.

Weiterführende numerische Untersuchungen der Kollision von drei Scheibengalaxien werden in der dritten Veröffentlichung präsentiert, wobei zusätzlich ein die Galaxien umgebendes intergalaktisches Medium (IGM) betrachtet wird. Die Anfangsmagnetfelder liegen im Bereich zwischen  $10^{-9}$  und  $10^{-6}$

G bzw.  $10^{-12}$  und  $10^{-9}$  G in den Galaxien bzw. im IGM. Diese Simulationen bestätigen die effiziente Verstärkung der galaktischen Felder während der Kollisionen bis zu  $\mu\text{G}$  Feldstärken und ihre Sättigung im Gleichgewichtszustand. Zudem treiben die Kollisionen Gas aus den Galaxien und Stoßwellen in das IGM, wodurch auch das Magnetfeld im IGM verstärkt wird. Dieses sättigt bei  $\approx 10^{-8}$  G, was ebenfalls dem Gleichgewicht zwischen magnetischer und turbulenter Energie entspricht. Darüber hinaus wird gezeigt, dass die Stoßwellen durch den magnetischen Druck zusätzlich getrieben werden, und so bei höherem Anfangsmagnetfeld höhere Mach-Zahlen erreichen. Die Mach-Zahlen liegen bei  $\approx 1.5$  für eine Vergleichs-Simulation ohne Magnetfelder, und bei  $\approx 6$  für die Simulation mit der höchsten Anfangsmagnetisierung. Durch die stärkeren Stoßwellen werden höhere Temperaturen in den durch den Stoß geheizten Regionen des IGM erreicht. Die gesättigten Magnetfeldstärken in den Galaxien und im IGM stimmen wieder gut mit Beobachtungen überein, und synthetische Karten der Radioemission und der erwarteten Stärke der Faraday-Rotation zu verschiedenen Zeitpunkten der Kollision geben Hinweise auf den Ursprung stark polarisierter Emission in kollidierenden galaktischen Systemen. Dabei kann ein hohes Maß an polarisierter Strahlung immer dann erwartet werden, wenn Stoßwellen und galaktisches Gas in das IGM getrieben werden.

Die in dieser Arbeit vorgestellten Untersuchungen sind auch für das Verständnis der Magnetfeldentwicklung im frühen Universum von Bedeutung. Es kann erwartet werden, dass die häufigen galaktischen Kollisionen während der Phase der Strukturentstehung von einer signifikanten Verstärkung der Magnetfelder in den jungen Galaxien und dem IGM begleitet wurden. Somit bieten galaktische Kollisionen eine mögliche Erklärung der beobachteten Magnetfelder im jungen Universum.

---

## Summary

This doctoral thesis covers the question about the existence and evolution of magnetic fields in galaxies. The kinematic evolution of magnetic fields in isolated spiral galaxies as well as their self-consistent evolution in interacting spirals is studied with the help of high-resolution state-of-the-art numerical simulations. Also, implications of an interaction-driven amplification for the magnetic field evolution during the phase of hierarchical structure formation in the Universe are discussed.

The introduction is meant to place the investigations of this thesis into the perspective of current knowledge and theory about galactic and extragalactic magnetic fields. Besides a short historical overview of the phenomenon magnetism, it comprises the basics of observational methods for extraterrestrial magnetic fields, observational knowledge about magnetic fields in different type of galaxies, galaxy clusters and in the early Universe, as well as the theoretical concepts of dynamo processes believed to be responsible for the observed magnetic field strengths and structures in the local Universe. Furthermore, open questions concerning the evolution of magnetic fields in the Universe are discussed. Particularly, the observed magnetic fields in very young galactic objects, which may not be explained by the comparatively slow classical galactic dynamo process, raise the question about other mechanisms able to amplify magnetic fields efficiently. Within this thesis, it is shown that galactic interactions are a viable candidate for such a mechanism.

In the first of the presented published articles, a set of three-dimensional  $N$ -body simulations of a spiral galaxy including hydrodynamics as well as the induction equation via the smoothed particle hydrodynamics (SPH) method is presented. These investigations were performed in order to assess the kinematic reaction of an initial magnetic field on the large-scale velocity field of a disc galaxy with self-consistently forming spiral structure. These simulations are the first of their kind and, contrary to most analytical calculations, do not require simplifying assumptions like axial symmetry. The main results are the demonstration of the importance of non-axisymmetry for the evolution of the magnetic field in spiral galaxies, the finding that a large-scale galactic velocity field alone is not able to amplify magnetic fields efficiently, and an estimate of the maximal numerical divergence error of the magnetic field up to which the numerical calculations are reliable.

Full MHD  $N$ -body/SPH simulations of two colliding galaxies, particularly the Antennae galaxies, are presented in the second article. These simulations are the first MHD simulations of interacting galaxies ever attempted. The main finding is that galactic interactions, which drive enhanced turbulence within the galaxies, result in an efficient amplification of an initial magnetic field. The magnetic field strength thereby saturates at a value of several  $\mu\text{G}$  (micro Gauss), independent of the initial magnetization which is varied between  $10^{-9}$  and  $10^{-4}$  G. It is shown that this saturation value corresponds to equipartition of the magnetic field energy with the turbulent energy, a result which is expected theoretically. The final magnetic field strength is in excellent agreement with observations, and synthetic maps of the expected radio synchrotron emission of the simulated system compare very well with the observed radio emission of the Antennae system.

Follow-up numerical investigations of a more general interaction of three disc galaxies with the additional inclusion of an ambient intergalactic medium (IGM) are presented in the third article. The initial magnetic field strengths lie in the range of  $10^{-9}$  to  $10^{-6}$  G in the galaxies and  $10^{-12}$  to  $10^{-9}$  G in the IGM, respectively. The efficient interaction-driven amplification of the initial magnetic field up to  $\mu\text{G}$  values in the galaxies and its saturation at the level of equipartition are confirmed. Furthermore, also the IGM magnetic field is amplified by interaction-driven shocks and galactic outflows. It saturates at  $\approx 10^{-8}$  G, again corresponding to equipartition between magnetic and turbulent energy. Moreover, the interaction-driven shocks are shown to be supported by the magnetic pressure, gaining higher Mach numbers in the presence of stronger magnetic fields. The Mach numbers range from  $\approx 1.5$  in a

non-magnetized reference simulation up to  $\approx 6$  for the highest initial magnetization, resulting in higher temperatures of the shock-heated intergalactic medium. The final galactic and IGM magnetic field strengths are again in good agreement with observational estimates, and synthetic radio and Faraday rotation measure maps for different phases of the evolution give clues on the origin of polarized emission in interacting galactic systems. Thereby, a high amount of polarized emission can be expected at times when shocks and galactic outflows are driven into the IGM.

The investigations covered by these articles have important implications for the current view of magnetic field evolution in the early Universe. Frequent galactic interactions during the phase of structure formation are expected to have been accompanied by a significant amplification of the magnetic field within young galactic objects and the intergalactic medium. Thus, galactic interactions provide a possible explanation for the observed magnetic fields in the early Universe.

# Contents

<b>Zusammenfassung</b>	<b>v</b>
<b>Summary</b>	<b>vii</b>
<b>1 Introduction</b>	<b>1</b>
1.1 Background . . . . .	1
1.1.1 History of magnetism . . . . .	1
1.1.2 The magnetic field of the Earth . . . . .	2
1.1.3 Extraterrestrial magnetic fields . . . . .	4
1.2 Observational methods of extraterrestrial magnetic fields . . . . .	6
1.2.1 Zeeman effect . . . . .	6
1.2.2 Synchrotron radiation . . . . .	7
1.2.2.1 Total synchrotron radiation . . . . .	7
1.2.2.2 Polarized synchrotron radiation . . . . .	11
1.2.3 Faraday rotation . . . . .	12
1.2.4 Polarization of optical starlight . . . . .	12
1.3 Observations of magnetic fields . . . . .	13
1.3.1 Magnetic fields in disk galaxies . . . . .	13
1.3.2 Magnetic fields in elliptical galaxies and galaxy clusters . . . . .	15
1.3.3 Magnetic fields in distant, young galaxies . . . . .	17
1.4 The dynamo theory . . . . .	18
1.4.1 Physics of the interstellar medium . . . . .	18
1.4.2 The kinematic dynamo . . . . .	21
1.4.3 The mean-field dynamo . . . . .	22
1.4.4 The cosmic ray driven dynamo . . . . .	25
1.4.5 The fluctuating dynamo . . . . .	28
1.5 Open Questions . . . . .	29
1.5.1 Seed fields . . . . .	29
1.5.2 Magnetic fields in different galactic objects and the intergalactic medium . . . . .	31
1.5.3 Magnetic fields in the early Universe . . . . .	32
1.6 Aim of this thesis . . . . .	33
<b>2 Paper I: Magnetic fields in spiral galaxies</b>	<b>37</b>
H. Kotarba, H. Lesch, K. Dolag, T. Naab, P. H. Johansson & F. A. Stasyszyn, 2009, <i>Monthly Notices of the Royal Astronomical Society</i> , 397, 733-747	
2.1 Introduction . . . . .	38

2.2	Theoretical Expectations . . . . .	41
2.3	Numerical methods . . . . .	42
2.3.1	VINE . . . . .	42
2.3.1.1	SPH basics . . . . .	42
2.3.1.2	Continuity equation . . . . .	42
2.3.1.3	Momentum and Energy equation . . . . .	43
2.3.1.4	Artificial viscosity . . . . .	43
2.3.1.5	Induction equation . . . . .	44
2.3.1.6	Euler potentials . . . . .	44
2.3.1.7	Timestepping . . . . .	45
2.3.2	GADGET . . . . .	46
2.4	Simulations . . . . .	47
2.4.1	Setup . . . . .	47
2.4.2	Direct magnetic field simulations . . . . .	49
2.4.3	SPH with Euler Potentials . . . . .	52
2.5	Evaluation . . . . .	52
2.5.1	Magnetic field growth . . . . .	52
2.5.2	Numerical resolution . . . . .	58
2.5.3	Inspection of the induction equation . . . . .	59
2.6	Conclusion and Outlook . . . . .	62
<b>3</b>	<b>Paper II: Magnetic fields in the Antennae</b>	<b>65</b>
	H. Kotarba, S. J. Karl, T. Naab, P. H. Johansson, K. Dolag, H. Lesch & F. A. Stasyszyn, 2010, <i>The Astrophysical Journal</i> , 716, 1438-145	
3.1	Introduction . . . . .	66
3.2	Properties of the Antennae systems . . . . .	68
3.3	Simulations . . . . .	69
3.3.1	Numerical methods . . . . .	69
3.3.2	Setup . . . . .	70
3.3.2.1	Isolated disks . . . . .	70
3.3.2.2	The match to the Antennae system . . . . .	75
3.3.3	Evolution of the Antennae system . . . . .	75
3.3.3.1	Magnetic field evolution . . . . .	75
3.3.3.2	Numerical stability . . . . .	77
3.3.3.3	Self-regulation of the amplification . . . . .	81
3.4	Simulated radio emission and polarization maps . . . . .	86
3.4.1	Computation method . . . . .	86
3.4.2	Applications . . . . .	87
3.5	Conclusion and Discussion . . . . .	90
<b>4</b>	<b>Paper III: Magnetic fields in colliding galaxies</b>	<b>93</b>
	H. Kotarba, H. Lesch, K. Dolag, T. Naab, P. H. Johansson, J. Donnert & F. A. Stasyszyn, 2011, accepted for publication by the <i>Monthly Notices of the Royal Astronomical Society</i> , <i>ArXiv e-prints</i> : 1011.5735	
4.1	Introduction . . . . .	94
4.2	Numerical Method . . . . .	95
4.3	Setup . . . . .	96
4.3.1	Galaxies . . . . .	96

---

4.3.2	Orbits . . . . .	97
4.3.3	IGM . . . . .	97
4.3.4	Magnetic fields . . . . .	98
4.4	Simulations . . . . .	99
4.4.1	Morphological evolution . . . . .	99
4.4.2	Differences between the scenarios . . . . .	103
4.4.2.1	Differences in the shock propagation . . . . .	103
4.4.2.2	Differences in the magnetic field evolution . . . . .	105
4.4.2.3	Differences in the temperature evolution . . . . .	108
4.4.3	Global evolution . . . . .	109
4.4.3.1	Magnetic fields . . . . .	109
4.4.3.2	Numerical divergence . . . . .	112
4.4.3.3	Pressures . . . . .	113
4.5	Synthetic radio emission, polarization and <i>RM</i> maps . . . . .	116
4.6	Conclusions and Outlook . . . . .	121
4.A	Appendix . . . . .	123
4.A.1	Magnetic fields . . . . .	123
4.A.2	Temperatures . . . . .	123
4.A.3	RMS velocities . . . . .	123
<b>5</b>	<b>Discussion and Outlook</b>	<b>133</b>
	<b>Bibliography</b>	<b>139</b>
	<b>Curriculum Vitae</b>	<b>157</b>
	<b>List of scientific publications</b>	<b>159</b>
	<b>Danksagung</b>	<b>161</b>



# Chapter 1

## Introduction

### 1.1 Background

#### 1.1.1 History of magnetism

Magnetism is a phenomenon which leads to a number of effects, among which magnetic attraction is the most familiar to most people. This effect has been mentioned already circa 600-500 B.C. by Thales of Miletus, who described the mutual attraction of pieces of lodestone or magnetite (the iron oxide  $\text{Fe}_3\text{O}_4$ , mentioned in the Aristotele's book *De Anima*). Plato (circa 400 B.C.) described the attraction of iron to the lodestone (e.g. Chapman and Bartels, 1940). One site where such stones were found was near the city of Magnesia in Asia Minor (Anatolia), which probably gave name to the phenomenon *magnetism*. Around roughly the same time, the Indian surgeon Sushruta was the first to make use of the magnet for removing loose iron arrows from a wound (described in *Sushruta Samhita*, Sushruta, 1907).

Interestingly, archeological findings show that magnetic materials have been used even at earlier times. For example, a bar-shaped iron ore artifact discovered at the site of San Lorenzo (present-day Mexico) and dated 1400-1000 B.C. exhibits a strong remnant magnetization parallel to its long axis. This magnetized bar suggests the existence of a device similar to a compass that predates the Chinese discovery (see below) by 2000 years (Evans, 1977). Malmstrom (1976) discovered a magnetized, iron-rich basaltic sculpture of the head of a turtle (circa 600 B.C. - 100 A.D.) at Izapa in the Pacific coastal plain of south-eastern Chiapas state. The magnetic lines of force are thereby pointing towards the snout of the turtle, indicating that the Izapans knew about magnetism and have shaped the turtle head according to the magnetization of the basaltic boulder. Guimarães (2004) also mentions a statue of a jaguar with magnetic poles in each raised paw, and a further statue of two seated men with magnetic poles on either side of the navel found in the coastal plain of Guatemala. The latter statue is dated 2000-1500 B.C. The significance of the location of the magnetic poles in these objects indicates an intention of the artisans. These findings clearly show that our ancestors knew about and were fascinated by the phenomenon magnetism.

However, the Chinese appear to be the first to use the lodestone as a device for navigation, i.e. as a compass (circa 1100 A.D., e.g. Chapman and Bartels, 1940; Parker, 1979). They found that a freely floating piece of lodestone aligns itself north or south, independent of time, weather or other external conditions. Thus, they are to be credited with discovering and using for the first time the general magnetic field of the Earth. However, there is no indication that they realized the alignment to be caused by a property of the Earth itself. The compass was quickly adopted by Arabs and Europeans and was used by Christopher Columbus (1451-1506), Vasco Da Gama (1460-1524) and Ferdinand Magellan (1480-1521) during their great sea voyages (Mitchell, 1932, 1937). It remained to William

Gilbert (1544-1603), personal physician of Queen Elizabeth I, to finally give a convincing explanation of the action of the compass. In his book *De Magnete*, which appeared in 1600 (Gilbert, 1958), he points out that Earth itself behaves like a large lodestone. He reached his conclusion with the help of a spherical magnet, a model of the Earth which he named *terrella* (little Earth). Sliding a compass over the surface of the *terrella*, he observed that its needle pointed toward the magnetic poles. In *De Magnete* Gilbert collected all that was known by his time about magnetism and electricity. This book was one of the most important scientific books of the era of Galileo and among other things contained the first use of the term *electric force* which led to the later term *electricity*.

Important advances in the field of electromagnetism followed in the next two centuries (Chapman and Bartels, 1940). 1820, Hans Christian Oersted (1777-1851), who was interested in electricity, chemistry and on what then was still a novelty, the electric battery, gave a lecture on electricity and magnetism. One of his demonstrations involved heating a thin metal wire by an electric current from a battery, whereby the wire passed near a compass. Whenever the wire was connected to the battery and a current flowed, the magnetic needle moved, and whenever the current ceased, it returned to its old position. Thereby, the needle tried to turn at right angles to the electric current. This was the first evidence connecting electricity and magnetism, and in the same year Oersted announced it to the world in a 4-page report (Shamos, 1959, see also Stern, 2002). The experiment was easy to repeat, and the best scientists in Europe, among them, André-Marie Ampère (1777-1836), turned to explore this new *electromagnetism*.

In a series of experiments, Ampère confirmed a completely new view of magnetism (Williams, 1989; Sergé, 1984). According to his work, the basic ingredient of magnetism was the force between electric currents. He showed that an electric current circulating around a wire loop acted like a short magnet. This implied that magnetism would have existed even if there were no permanent magnets.

Thus, Oersted and Ampère had shown that electric currents were the primary source of magnetism. However – reversing the process – a permanent magnet does not produce any electric current. Instead, Michael Faraday (1791-1867) discovered that electric currents were generated only if a changing magnetic field was present (electromagnetic induction). The change could come from variations in the strength of the magnetic field, or it could arise from relative motion between the field and the conductor. These findings led to machines called *dynamos* (today more commonly *generators*) in which conductors are whirled around within the fields of magnets, producing electric currents. However, not every motion qualifies, because there is also the matter of energy. As Ampère had shown, a wire moved through a magnetic field encounters a force. Only when the force opposes the motion, so that one has to invest energy to overcome it, does a current flow, whereby the energy invested exactly equals the energy needed to drive the current. Faraday also introduced the terms *electric field* and *magnetic field*.

The idea of electromagnetic fields was the basis for James Clerk Maxwell's (1831 - 1879) theory of electromagnetism culminating in the famous Maxwell's equations (see section 1.4), which describe the relationship between electric and magnetic fields. These equations predicted the existence of electromagnetic radiation, which was finally proved by Heinrich Hertz (1857 - 1894).

Modern life is unthinkable without electromagnetism. Electromagnetic induction is the basis of operation for electrical generators, induction motors, and transformers. Electronic engineering including PC processors and chips is based on the theory of electromagnetism. Electromagnetic radiation is used in medical diagnostics, telecommunications, for the remote control of satellites, space shuttles and robots. In short, this theory completely changed our way of living.

### 1.1.2 The magnetic field of the Earth

The work of Oersted and Ampère led to the studies of Carl Friedrich Gauss (1777-1855). Gauss used a precise mathematical method to represent the global magnetic field of the Earth (e.g. Stern, 2002). He used spherical harmonic analysis, which was introduced to geomagnetism by the French

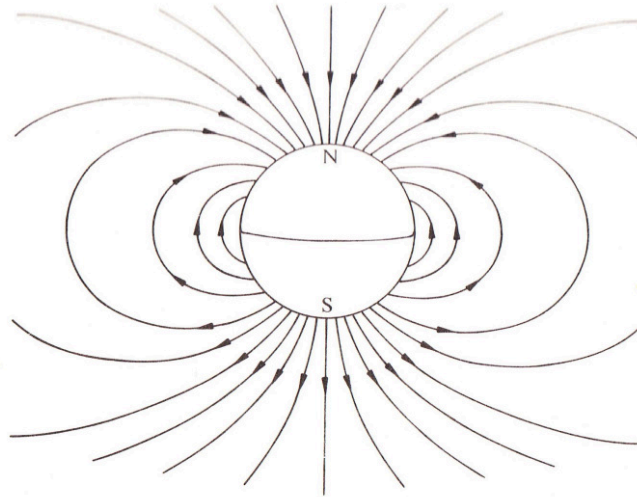


Figure 1.1: Map of the line of force (the field lines) of a dipole field such as the external magnetic field of the earth. Geographic north and south are indicated at the top and bottom of the circle representing the Earth. From Parker (1979).

mathematician Simeon Denis Poisson (1781-1840) (Chapman, 1964). This new tool provided the first quantitative description of the Earth's magnetic field, both its direction and strength, and showed that the main component of the Earth magnetic field is a dipole field (a combination of an attracting and an repelling monopole with a non-vanishing distance). In other words, Gilberts 2-pole terrella has always been a good approximation to the actual magnetic field of the earth.

A simple way of visualizing the magnetic field developed by Faraday (Williams, 1965; Sergé, 1984) is based on connecting the directions of magnetic force at every point in space with continuous lines. For the Earth, these *field lines* spread out from the magnetic north pole (which lies close to the geographic south pole), arch around the Earth and converge again near the magnetic south pole (Fig. 1.1). These magnetic field lines also tell about the strength of that force: where the lines are close together, the force is strong, where they are spaced widely apart, it is weak. The mean magnetic field strength of the Earth is approximately 0.5 G (Gauss).

The method used by Gauss also showed that at least 99% of the field originated inside the Earth, however, Gauss avoided speculating on the source of the Earth's magnetism. Nowadays we know that the magnetic field of the earth is maintained by the *geodynamo*, a process based on the amplification of magnetic fields by the motion of the electrically conducting liquid outer metal core of the Earth (e.g. Parker, 1979, see also section 1.4). The motion of this fluid is thereby a combination of non-uniform rotation and cyclonic turbulence due to convective motions. Although the details of the geodynamo are still under debate (Glatzmaier et al., 1999; Sakuraba and Roberts, 2009), the theory of dynamos in rotating, convecting bodies is well established.

The presence of the magnetic field of the Earth has many fascinating implications. For example, it is responsible for the beautiful *polar aurora* or northern/southern lights: Auroral emissions are produced by particles, originating from the sun and the Earth's atmosphere, that collide with the Earth's atmosphere along streamlines modulated by electric and magnetic fields in the Earth's *magnetosphere* and ionosphere. Due to these collisions, atmospheric atoms get ionized and subsequently emit light (fluorescence) when recombining. This light is then visible as aurora (e.g. Kivelson and Russell, 1995). Also, there is evidence that animals can sense magnetic fields. Migratory birds use the Earth's mag-

netic field for navigation, whereby they sense the field most probably with photoreceptor molecules in the retina of their eyes (Mourtisen et al., 2004; Ritz et al., 2004). More astonishing, cows and deer align their bodies with the magnetic field when grazing or resting (Begall et al., 2008). All these issues add up to the fascination of magnetism.

### 1.1.3 Extraterrestrial magnetic fields

The story of the Earth's magnetism is strongly tied to that of solar research. Large magnetic storms and observations of aurora far south from their usual locations were found to be associated with solar phenomena. In 1859 Richard Carrington (1826-1875) observed a bright outburst of light in a group of large sunspots (dark spots on the sun's surface), lasting about five minutes and followed 17 hours later by a very powerful magnetic storm, strongly suggesting a connection (see e.g. Meadows, 1970; Stern, 2002). Using the Zeeman effect (see section 1.2.1), George Ellery Hale (1868-1938) showed that sunspots were in fact strongly magnetic, with a typical field intensity of 1500 G (Hale, 1908). The spots generally appeared in pairs of opposite polarity, suggesting that field lines emerged from the sun at one of the pair and re-entered at the other. Long-term observations of the polarity and movement of the sunspots on the surface of the sun subsequently revealed that there is a cycle of solar activity with an average period of 22 years, and that this cycle has to be a magnetic phenomenon. The Sun is a giant ball of gas, hot enough to conduct electricity (i.e. a plasma), much hotter than anything that exhibits permanent magnetism. Sunspot magnetism therefore had to come from electromagnetic activity, and in 1919 Sir Joseph Larmor (1857-1942) proposed a self-sustaining fluid dynamo (Larmor, 1919a,b), a mechanism which is essentially based on the effect of a conducting fluid circulating in the core of the astronomical body (see also section 1.4). However, it took more than 40 years until Eugene N. Parker could show that the dynamo can actually work in rotating bodies like the sun (Parker, 1963). Such a dynamo is active in the Earth as well as in the sun.

Most of the material in the Universe is in the conducting plasma state, i.e. composed of ionized or partially ionized gas. Stars, galaxies, the interstellar medium (ISM) and the intergalactic medium (IGM) consist of plasma. Temperatures are high, and thermal energies are larger than the magnetic energies (with some exceptions, e.g. pulsars). Therefore only conductivity and collective plasma motions play a role. Hence, in principle, it is straight-forward to apply the fluid dynamo to these objects. However, until the mid of the 20th century, cosmic magnetic fields were known to exist only in our solar system. Magnetic fields of other stars were detected as recently as 1958 in by Horace Babcock (1912-2003) (Babcock, 1958). Also, magnetic fields of the ISM of our Galaxy became a subject for discussion only after the Second World War, due to a growing interest in cosmic rays (high energy particles observed on Earth originating in the outer space, see section 1.4.4) and non-thermal radio emission (section 1.2.2). The presence of a uniform magnetic ISM field had been inferred in the 50s and 60s of the last century from the observation of optical polarization (e.g. Hiltner, 1951) as well as from the detection of linearly polarized radio emission (Razin, 1958; Westerhout et al., 1962; Wielebinski and Shakeshaft, 1962, see also section 1.2 on observational methods).

In fact, magnetic fields are detected in all kinds of planetary and stellar objects, proto-stellar disks, molecular clouds, in galaxies of all type and galaxy clusters whenever appropriate measurements are made (e.g. Vallee, 1998; Widrow, 2002, see also 1.3). Table 1.1 lists different astrophysical objects known to host magnetic fields together with their approximate size and magnetic field strength (numbers taken from Zeldovich et al., 1983; Vallee, 1997, 1998; Widrow, 2002; de Gouveia Dal Pino, 2010).

Assuming perfect conductivity of the plasma, the behavior of the magnetic field  $\mathbf{B}$  pervading it is controlled completely by the motion of the plasma. In this case the magnetic field is said to be *frozen-in* the plasma (Alfvén, 1950). This means that a pair of particles on the same field line will always remain on this line, and a pair of particles which are not on the same line will never share the same line. This implies that whenever a plasma gets compressed, the magnetic field lines have

Object	Size [pc]	Size [km]	Magnetic field [G]
Neutron stars & Pulsars	$10^{-13}$	10	$> 10^{12}$
White dwarfs	$5 \cdot 10^{-11}$	$2 \cdot 10^3$	$10^6 - 10^8$
The Earth	$5 \cdot 10^{-10}$	$10^4$	$5 \cdot 10^{-1}$
Other planets	$10^{-9}$	$10^4 - 10^5$	$6 \cdot 10^{-4} - 4$
Sun	$10^{-7}$	$10^6$	10
Other stars	$10^{-7}$	$10^6 - 10^7$	$10 - 10^4$
Molecular clouds & proto-stellar disks	$2 \cdot 10^{-1}$	$6 \cdot 10^{12}$	$10^{-5} - 10^{-3}$
The Galaxy	$3 \cdot 10^4$	$10^{18}$	$6 \cdot 10^{-6}$
Other spiral galaxies	$10^3 - 10^5$	$3 \cdot 10^{16} - 3 \cdot 10^{18}$	$5 \cdot 10^{-6} - 5 \cdot 10^{-5}$
Elliptical galaxies	$10^2 - 10^5$	$3 \cdot 10^{15} - 3 \cdot 10^{18}$	$1 \cdot 10^{-5}$
Galaxy clusters	$2 \cdot 10^6 - 10^7$	$6 \cdot 10^{19} - 3 \cdot 10^{20}$	$10^{-6}$

Table 1.1: Astrophysical objects and their approximate sizes and magnetic fields.

to come closer together (i.e., the magnetic flux has to be conserved). A higher density of magnetic field lines, however, implies a stronger magnetic field. Thus, the magnetic field gets strengthened in direct proportion to the gas number density  $n$ . In case of isotropic compression, the magnetic field is thereby proportional to the density to the power of 2/3 or  $\approx 0.6$  (e.g. Zeldovich et al., 1983). In fact, such a correlation has been found for the magnetic field and the density of the (almost) neutral gas in spiral galaxies (Niklas and Beck, 1997), and for the magnetic field and the density of compressed interstellar gas (e.g. clouds and interclumps with number density  $> 100 \text{ cm}^{-3}$ ) in our Galaxy (Vallée, 1995, Fig. 1.2). Thereby,  $B \sim n^{0.5}$ . However, due to turbulence and radiation effects, the physics of interstellar clumps are too complicated to assume simple compression, which is why other theories try to explain the 0.5-slope of the observations in our Galaxy (Vallée, 1995).

The conservation of the magnetic flux due to the frozen-in condition is a viable explanation of the high magnetic fields of white dwarfs and neutron stars (NS). White dwarfs and NS are final products of stellar evolution. Very simply said, as soon as the nuclear reactions within a star cease and the star is no longer supported by radiation pressure, it collapses due to its own gravity to a much smaller and denser object. Dependant on the mass of the star, this object may be e.g. a NS. A typical star has a radius of  $r_{\text{star}} \approx 10^6 \text{ km}$  and a magnetic field strength of  $B_{\text{star}} \approx 10^2 \text{ G}$ . Flux conservation during the collapse leads the relation  $B_{\text{NS}} = B_{\text{star}} \cdot (r_{\text{star}}/r_{\text{NS}})^2$ . Thus, given that  $r_{\text{NS}} = 10 \text{ km}$ , the expected magnetic field for the NS is  $10^{12} \text{ G}$ , consistent with other estimates based on observations (e.g. Zeldovich et al., 1983).

Magnetic flux conservation was also the basis for an explanation of the origin of observed magnetic fields of larger cosmic structures, e.g. galaxies. According to this explanation, the observed magnetic fields are a direct result of the compression of an ancient “relict” field, which had to have been generated at an early epoch of the Universe (e.g. Piddington, 1972, see also section 1.5.1). However, observational data obtained from the polarization of the emission of remote radio sources does not reveal the existence of any noticeable relict field. Moreover, without a process maintaining an established magnetic field, turbulent diffusion would lead to a decay of the large-scale field of a galaxy within approximately  $10^8 - 10^9$  years (Parker, 1973), which is less than or comparable with the age of the Galaxy. Therefore, another process for the generation and maintenance of magnetic fields in astrophysical objects like galaxies and galaxy clusters has to be requested for. The dynamo process is thereby a perfect candidate (see section 1.4).

Today, there are no doubts that magnetic fields play a crucial role in many astrophysical processes. They influence the star formation process, are responsible for solar and stellar activity, they bunch

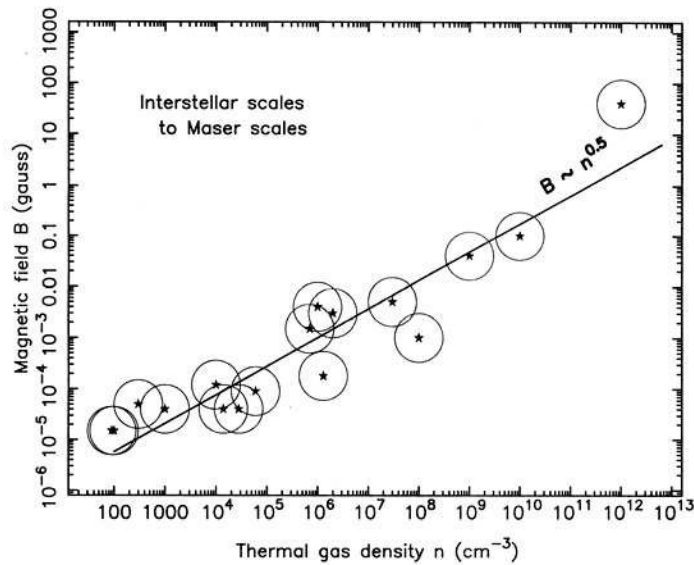


Figure 1.2: Observed behavior of the magnetic field  $B$  as a function of the total gas density  $n$ , for  $n > 100 \text{ cm}^{-3}$ . The statistical results gave  $B \sim n^{0.5}$ . From Vallee (1997).

the radiation from pulsars, help to transport angular momentum in accretion disks around stars and black holes, they are crucial for the formation and stability of jets driven out from stellar objects and active galactic nuclei, determine the formation and propagation of cosmic rays, contribute to the total pressure which balances the gas disks of galaxies against gravitation, and many more. However, despite their importance, the origin and evolution of magnetic fields as well as their influence on galaxy evolution and structure formation in the early Universe are still not well understood (see e.g. de Gouveia Dal Pino, 2010 and references therein). This deficit is the fundamental motivation for the research studies presented below.

## 1.2 Observational methods of extraterrestrial magnetic fields

Magnetic fields can not be observed directly. Instead, one has to consider their impact on different radiation processes in order to estimate their strength and structure. Moreover, unlike the fields in laboratories, cosmic magnetic fields are very remote, which makes their measurement nontrivial. When comparing theoretical results to measurements, however, it is necessary to understand what kind of information is contained in the measured data. Therefore, this section summarizes the principles of the measurement of extraterrestrial magnetic fields (More detailed descriptions of the methods can be found in e.g. Longair, 1981; Zeldovich et al., 1983; Rybicki and Lightman, 1986 and Widrow, 2002).

### 1.2.1 Zeeman effect

In 1896 Pieter Zeeman (1865-1943) discovered the *Zeeman effect*. This quantum-mechanical effect is based on the splitting of atomic energy levels in the presence of a magnetic field. In the absence of a field, atomic energy levels do not depend on the direction of the total angular momentum, they are degenerate. A magnetic field breaks up this degeneracy by picking out a particular direction in space. If the total angular momentum of an atom is  $\mathbf{J}$  (= spin angular momentum  $\mathbf{S}$  plus orbital

angular momentum  $\mathbf{L}$ ) there will be  $2j + 1$  levels where  $j$  is the quantum number associated with  $\mathbf{J}$ . In the simplest case ( $j = 1$ ), a single energy level will split into a triplet of levels. The shift between the “new” neighboring levels is thereby  $\Delta E = g\mu B$  where  $g$  is the Lande factor which relates the angular momentum of an atom to its magnetic moment and  $\mu = e\hbar/2m_e c = 9.3 \cdot 10^{-21}$  erg G $^{-1}$  is the Bohr magneton (with  $e$  the electron charge,  $m_e$  the electron mass,  $c$  the speed of light and  $\hbar$  the reduced Planck constant). The splitting of the energy levels leads to a corresponding splitting of the spectral lines emitted or absorbed by the atom. Thereby, the middle of the three lines (which is unshifted with respect to the degenerate line) is linearly polarized. The two shifted lines have right-handed and left-handed circular polarization, respectively. These different polarizations are the reason why observers usually see only two of the lines: If the magnetic field responsible for the splitting is directed towards the observer, only the circularly polarized components can be seen. If the field is perpendicular to the line-of-sight, all three components are visible. Furthermore, the intensities and the observed polarizations of the components depend on the orientation of the field. As a consequence, when observing e.g. a sunspot, from which the magnetic field lines spread out towards the observer, typically only two of the three lines are visible. Altogether, the total magnetic field strength can be found by measuring the separation of the Zeeman components, and the knowledge about the intensities and polarizations of the components yields information about the orientation of the field.

Unfortunately, as astrophysical magnetic fields are usually weak, the Zeeman shifts are small. Usually, they are smaller than the Doppler broadening of lines caused by the thermal motion of the atoms. Hence, positive detections have been restricted to regions of low temperature and high magnetic field. In the optical range, direct measurements are possible for magnetic fields  $\geq 10^3$  G, i.e. for stars and sunspots. In the radio frequency range, the Zeeman splitting of the 21cm hydrogen line can be detected for magnetic fields  $> 10^{-5}$  G, which are typical for gas clouds in the interstellar medium. However, the typical magnetic fields of galaxies are usually too small to allow for measurements of the Zeeman effect.

## 1.2.2 Synchrotron radiation

### 1.2.2.1 Total synchrotron radiation

Relativistic electrons gyrating along magnetic field lines (which they do because of the Lorentz-force) are known to emit Bremsstrahlung, which in this case is also called Synchrotron radiation. The emission is thereby concentrated in a cone of maximal radiation, which central axis lies along the magnetic field and opening angle corresponds to the pitch angle, the angle between the magnetic field and the velocity vector of the electron (Fig. 1.3, see Ginzburg and Syrovatskii, 1965 for a detailed description of this process). Synchrotron radiation is a non-thermal radiation, wherefore it can be distinguished from all thermal radiation processes. Whenever synchrotron radiation is detected, magnetic fields have to be present. Synchrotron emission is most important for observations of galactic magnetic fields.

The energy lost due to synchrotron radiation by a relativistic electron with energy  $E$  gyrating in a magnetic field of the strength  $B$ , averaged over all pitch angles, is proportional to the strength of the magnetic field:

$$-\left(\frac{dE}{dt}\right) = \frac{4}{3}\sigma_T c \gamma^2 \frac{B^2}{8\pi} = \frac{4}{3}\sigma_T c \left(\frac{E}{m_e c^2}\right)^2 \frac{B^2}{8\pi} \sim E^2 B^2, \quad (1.1)$$

whereby  $\sigma_T$  is the Thomson cross section and  $\gamma = (E/m_e c^2)$  the Lorentz factor of the electron. The frequency  $\nu$  of this synchrotron radiation can be shown to be approximately

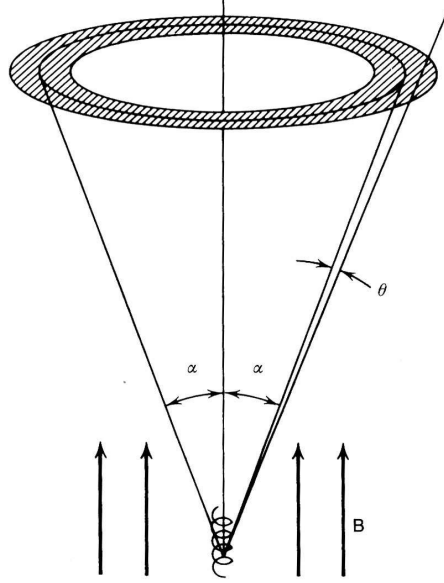


Figure 1.3: Synchrotron emission from a charged particle with a pitch angle  $\alpha$ . The radiation is confined to the shaded solid angle. From Rybicki and Lightman, 1986.

$$\nu \approx \gamma^2 \nu_g = \left( \frac{E}{m_e c^2} \right)^2 \frac{eB}{2\pi m_e}, \quad (1.2)$$

with  $\nu_g = eB/2\pi m_e$  the gyroradius (or Larmor radius) of the electron. Eq. 1.2 yields the relations

$$E \sim \frac{\nu^{1/2}}{B^{1/2}}, \quad (1.3)$$

$$\Rightarrow \frac{dE}{d\nu} \sim \frac{1}{\nu^{1/2} B^{1/2}}. \quad (1.4)$$

For a given synchrotron source (e.g. a galaxy), the total synchrotron emission will depend on the energy distribution of electrons within this source,  $N(E)$ . A commonly used class of models is based on a power-law distribution

$$N(E) = \kappa E^{-p}, \quad (1.5)$$

whereby the exponent  $p$  is called the spectral index, while the constant  $\kappa$  sets the normalization of the distribution. The synchrotron emission  $j$  emitted within a frequency interval  $\nu + d\nu$  from electrons in an energy range  $E + dE$  can be expressed as

$$j(\nu)d\nu = - \left( \frac{dE}{dt} \right) N(E)dE, \quad (1.6)$$

and inserting the relations 1.3, 1.4 and 1.5 yields an expression for the synchrotron emission at frequency  $\nu$  for a source with a power-law distribution of electrons in dependence of the magnetic field:

$$j(\nu) \sim \kappa \nu^{(1-p)/2} B^{(1+p)/2} \quad (1.7)$$

In case of galaxies, with typical magnetic field strength in the order of  $1 - 10 \mu\text{G}$ , the synchrotron radiation is usually observed in the radio frequency range (30 kHz to 300 GHz).

However, given the observed synchrotron emission at a particular frequency and not knowing the spectral index of the energy distribution of relativistic electrons within the observed source, it is still not possible to derive  $B$  from Eq. 1.7. The observed radio power can be the result of a large number of relativistic electrons in a weak magnetic field or of few electrons in a strong field. Thus, a further assumption is needed, which is usually based on considerations of the energy budget of the synchrotron source. The energy density of relativistic electrons  $e_e$  is

$$e_e = \int_{E_{\min}}^{E_{\max}} N(E) E dE, \quad (1.8)$$

whereby  $E_{\min, \max} \sim (\nu_{\min, \max}/B)^{1/2}$ . Integration and transformation utilizing the above formulae yields

$$e_e \sim j(\nu) B^{-3/2}. \quad (1.9)$$

The relativistic electrons responsible for the synchrotron radiation are part of the galactic cosmic ray population. Cosmic rays are energetic particles which population is composed of mainly protons and electrons (by number, see also section 1.4.4). Thus, the total energy of the synchrotron source is the kinetic energy of the protons and electrons plus the magnetic energy. To take account of the protons, it is customary to assume that they have an energy  $k$  times that of the electrons, i.e.  $e_{\text{kin}} = e_{\text{protons}} + e_e = (1+k)e_e$  (Longair, 1994). The total energy is therefore  $e_{\text{tot}} = (1+k)e_e + e_{\text{mag}}$ , with  $e_{\text{mag}} = B^2/8\pi$ .  $e_{\text{tot}}$  is thus a function of  $B$  only, and one can estimate the magnetic field strength either by assuming equipartition ( $(1+k)e_e = e_{\text{mag}}$ ) or by minimizing  $e_{\text{tot}}$  with respect to  $B$ . In fact, both approaches lead to a similar result, as can be seen in Fig. 1.4.

Assuming either equipartition or minimum energy yields the relation  $B_{\text{eq}} \sim j(\nu)^{2/7}$ , or, more precisely (cf. Longair, 1994),

$$B_{\text{eq}} = [6\pi C(1+k)j(\nu)]^{2/7}, \quad (1.10)$$

where  $C$  is a constant which depends only weakly on  $p$ ,  $\nu_{\max}$  and  $\nu_{\min}$  if  $p \approx 2.5$ . Eq. 1.10 finally allows for estimations of the magnetic field strength from the observed synchrotron emission. Note, however, that by averaging over all pitch angles in Eq. 1.1, we have implicitly assumed that the magnetic field is isotropic. Synchrotron radiation from relativistic particles is collimated in a cone of maximal radiation (Fig. 1.3), and one can only observe the part of the radiation which is ‘‘by chance’’ hitting the observer. Whether this is the case for a given pitch angle is determined by the direction of the magnetic field. Particularly, it is only the case if the magnetic field has a component perpendicular to the line of sight, i.e.  $B_{\perp}$ , which means that observations of synchrotron radiation are only sensitive to this part of the magnetic field.

The validity of the assumption of equipartition can be tested directly in the local Galaxy. There, direct measurements of the local cosmic electron energy density and independent estimates of the local

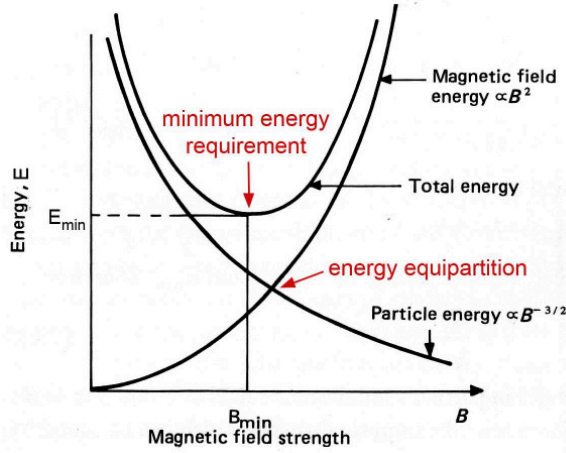


Figure 1.4: Energies as a function of magnetic field strength for a synchrotron source. The three lines correspond to the kinetic particle energy  $E_{\text{kin}} \sim B^{-3/2}$ , the magnetic energy  $E_{\text{mag}} \sim B^2$  and the total energy. The magnetic field derived from the minimum energy requirement  $B_{\text{min}}$  is comparable to the magnetic field at energy equipartition. Adopted from Longair, 1994.

cosmic ray proton density from diffuse continuum  $\gamma$ -emission<sup>1</sup> are available. A combination of radio synchrotron emission measurements with these results yields a field strength in excellent agreement with the results using the assumption of equipartition (Beck, 2002).

Furthermore, Vallee (1995) statistically confirmed the validity of the equipartition method for a sample of seven nearby galaxies (including the Milky Way) by showing that the equipartition values of the magnetic field converge towards similar values obtained independently from the Faraday method (section 1.2.3).

Moreover, Hummel (1986) found strong indications for the validity of the equipartition assumption by comparing the cumulative frequency distribution<sup>2</sup> of the ratio  $R$  of radio power  $P_{\text{radio}}$  to far infrared (FIR) power  $P_{\text{FIR}}$  with the cumulative frequency distribution of  $B_{\text{eq}}^{(1+p)/2}$  for a sample of 65 spiral galaxies. It is well known that  $P_{\text{radio}}$  and  $P_{\text{FIR}}$  follow a very tight correlation, the Radio-FIR correlation (see e.g. Condon, 1992 and references therein). Thus, the cumulative frequency distribution of  $R$  in fact reproduces the small dispersion of the Radio-FIR correlation. In a rough approximation,  $P_{\text{radio}}$  is proportional to the number density of relativistic electrons  $n_e$  times  $B^{(1+p)/2}$ . As FIR radiation is emitted by interstellar dust particles heated by stellar radiation (Jones et al., 2002),  $P_{\text{FIR}}$  is roughly proportional to the number density of stars,  $n_*$ . Thus,  $R \sim B^{(1+p)/2} \cdot n_e/n_*$ . Furthermore,  $n_e$  and  $n_*$  are both determined by the star formation rate (cf. also section 1.4.4). Thus,  $n_e/n_*$  is approximately constant and hence the cumulative frequency distribution of  $R$  is in fact the frequency distribution of  $B^{(1+p)/2}$ . Hummel (1986) found that applying  $p \approx 2.8$  (a value close to other estimates of  $p$  in spiral galaxies), the distribution of  $B_{\text{eq}}^{(1+p)/2}$  follows closely the distribution of the observed ratio  $R$ . This coincidence strongly indicates that the equipartition assumption is valid.

Hence, the validity of equipartition between cosmic ray energies and magnetic energies and thus the derivation of  $B_{\text{eq}}$  from the total synchrotron radiation of a radio source is observationally well established.

<sup>1</sup>The Galactic  $\gamma$ -emission is dominated by decays of neutral pions produced in interactions of cosmic ray protons with interstellar matter (Ferrière, 2001).

<sup>2</sup>Cumulative frequency analysis is the analysis of the frequency of occurrence of values of a phenomenon less than a reference value.

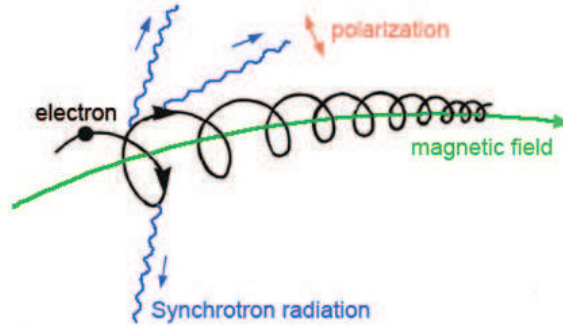


Figure 1.5: An electron gyrating along a magnetic field line. The red arrow indicates the direction of the electric vector of the radiated synchrotron waves (blue), i.e. the direction of polarization.

### 1.2.2.2 Polarized synchrotron radiation

One of the characteristic features of synchrotron radiation is its polarization. In the coordinate system of the electron the principal direction of the electric vector of the radiated wave lies in the same plane as the direction of acceleration (Fig. 1.5). Thus, The polarization is circular when observed approximately along the direction of the magnetic field, and linearly polarized when observed perpendicular to the magnetic field (if motion along the field is neglected). Obviously, in the latter case, the polarization direction is perpendicular to the magnetic field component projected onto the plane of sky  $B_{\perp}$ . In general, for arbitrary angles between the line-of-sight and the magnetic field, the synchrotron radiation of an electron will be elliptically polarized. The sense of the polarization (right- or left handed) is thereby determined by whether the line-of-sight lies just inside or just outside the cone of maximal radiation. However, for any reasonable distribution of electrons that varies smoothly with pitch angle, the elliptical component will cancel, as emission cones will contribute equally from both sides of the line-of-sight. Thus, the radiation will be partially linearly polarized, with the electric vector of the polarized emission lying perpendicular to the direction of  $B_{\perp}$ .

It can be shown that the degree of polarization  $\Pi$  (the ratio of polarized to total emission) of the radiation in a homogeneous magnetic field depends only on the spectral index  $p$  of the energy spectrum of the electrons:

$$\Pi = \frac{p + 1}{p + \frac{7}{3}} \quad (1.11)$$

For values of  $p$  appropriate to spiral galaxies ( $p \approx 2.6$ ), this implies a degree of polarization of  $\approx 0.73\%$ . The observed values –  $\Pi = 10\%–20\%$  for a typical spiral galaxy – are much smaller. There are various effects which can lead to the depolarization of the synchrotron emission observed in spiral galaxies. These effects include the presence of a fluctuating component of the magnetic field, inhomogeneities in the plasma medium and relativistic electron density, Faraday depolarization (see below) and beam-smearing.

In summary, the intensity of the observed synchrotron emission is a measure of the strength of the total magnetic field component in the plane of the sky,  $B_{\perp}$ , whereby polarized emission emerges from ordered fields. However, as polarization “vectors” are ambiguous by  $180^{\circ}$ , they cannot distinguish *regular fields* with a constant direction from *anisotropic fields* which reverse their direction on small scales. Unpolarized synchrotron emission indicates *turbulent fields* with random directions.

### 1.2.3 Faraday rotation

Electromagnetic waves, propagating through a region of both magnetic field and free electrons, experience Faraday rotation, whereby the direction of polarization is rotated. This effect arises because – in the limit of  $\nu_p/\nu \ll 1$  and  $\nu_g/\nu \ll 1$ , with  $\nu$  the frequency of the radiation passing the medium and, respectively,  $\nu_p = \sqrt{4\pi n_e e^2/m_e}$  the plasma frequency and  $\nu_g$  the gyrofrequency of the electrons in the medium – left and right-circular polarization states travel with different phase velocities. For linearly polarized radiation with a wavelength  $\lambda$ , this results in a rotation with time (or equivalently path length  $l$ ) of the electric field vector by an angle  $\phi = RM \cdot \lambda^2$ , with the rotation measure

$$RM \sim \int_0^l n_e(l) B_{\parallel} dl, \quad (1.12)$$

whereby  $B_{\parallel}$  is the magnetic field component parallel to the line-of-sight. Here,  $n_e$  is the density of thermal electrons along the line of sight.

In general, the polarization angle must be measured at three or more wavelengths in order to determine  $RM$  accurately and remove the  $\phi = \phi \pm n\pi$  degeneracy. Once  $RM$  is measured and  $n_e$  is known (or estimated), relation 1.12 can be used to determine  $B_{\parallel}$ .  $RM$  is positive (negative) for a magnetic field directed toward (away from) the observer. Hence, only regular fields can give rise to Faraday rotation, while anisotropic and random fields do not. The Faraday rotation angle includes contributions from magnetized regions along the line of sight to the source. Observing a distant object, these regions are generally the source itself, the intergalactic medium between the source and our Galaxy, and the interstellar gas of the Galaxy. For the relatively weak fields typical for intergalactic and interstellar space, the rotation measure is generally smaller than a few hundred radians per square meter. Thus, to guarantee  $\phi \approx 1$  to  $2\pi$ , measurements of Faraday rotation are usually carried out at radio frequencies. For longer wavelengths,  $\phi$  may rotate through many radians resulting in depolarization of the radiation, and for shorter wavelengths (e.g. the optical range), the Faraday rotation may be too small for measurements. Measurements of Faraday rotation allow to determine the strength and direction of the regular field along the line-of-sight. In combination with the total and the polarized synchrotron intensity this can yield a three-dimensional picture of the magnetic field.

Faraday rotation measurements of the polarized light of distant radio sources (e.g. radiation from jets of active galactic nuclei (quasars), pulsars or radio galaxies) have been used to determine the magnetic field strength of the ISM (e.g. Uyaniker and Landecker, 2002) and of the intergalactic gas in clusters of galaxies (e.g. Govoni and Feretti, 2004). In external galaxies, recognition of magnetic structures is possible from Faraday rotation measurements towards background sources or from a continuous rotation measure map obtained from the diffuse polarized emission from the galaxy itself.

Faraday rotation from an extended source leads to a decrease in the polarization: The combined signal from waves originating in different regions of the source will experience different amounts of Faraday rotation, thus leading to a spread in polarization directions. However, *Faraday depolarization* can in fact be a useful measure of magnetic fields in the foreground of a source of polarized synchrotron emission.

### 1.2.4 Polarization of optical starlight

Polarized light from stars can reveal the presence of large-scale magnetic fields in our Galaxy and those nearby. Davis and Greenstein (1951) suggested the basic idea in order to explain the surprisingly high polarization levels (up to 10% instead of the expected 1-2%) of starlight that were observed by Hiltner (1949a,b) and Hall (1949). According to this idea, elongated dust grains in the interstellar medium of the Galaxy have a preferred orientation due to the magnetic field: for prolate grains, one

of the short axes coincides with the direction of the magnetic field. The grains, in turn, preferentially absorb light polarized along the long axis of the grain, i.e., perpendicular to the field. The net result is that the transmitted radiation has a polarization direction parallel to the magnetic field. This effect is referred to as the *Davis-Greenstein effect*.

However, polarization of optical starlight has limited value as a probe of extragalactic magnetic fields. One reason is that anisotropic scattering in the ISM can also lead to polarization of starlight, thus distorting the data. Furthermore, the starlight polarization effect is self-obscuring since it depends on extinction. Moreover, the precise mechanism by which dust grains are oriented in a magnetic field is not well understood (e.g. Lazarian et al., 1997). Nevertheless, polarization of starlight can provide information that is complementary to what can be obtained from radio observations (see Beck, 2008 and references therein).

### 1.3 Observations of magnetic fields

Owing to the development of the observational methods described in the previous section, particularly in the field of radio astronomy, it is possible to observe magnetic fields in local galaxies (within a distance of less than approximately 50 Mpc) with a spatial resolution up to a few 100 pc. Observations are carried out with instruments like the 100m radio telescope Effelsberg in Bonn, Germany, or with aperture synthesis interferometry at e.g. the Very Large Array (VLA, USA). The most promising instrument to come is the the Square Kilometre Array (SKA), which is going to be commissioned in 2016-2020 (Gaensler et al., 2004). The high resolution of the observations results in a detailed knowledge of the strength and structure of magnetic fields in these objects. Furthermore, sometimes it is even possible to observe the magnetic fields of very distant objects at cosmological redshifts, providing hints on the evolution of magnetic fields during the phase of structure formation in the early Universe. This section summarizes our current knowledge about the magnetic fields in different kinds of local as well as very distant galaxies.

#### 1.3.1 Magnetic fields in disk galaxies

Spiral galaxies, like the Milky Way, are a class of disk galaxies – with the height  $H$  of the disk usually much smaller than its radius ( $\approx 1 - 50$  kpc) – which exhibit a spiral structure with two or more arms that extend from the center into the disk. Disk galaxies are flat, because the stars and gas in the disk rapidly rotate. The visual image of a galaxy is dominated by the optical light of stars which contribute most to the visible galactic mass ( $2 \cdot 10^{11}$  solar masses for the Milky Way). A few percent of the galactic mass is due to the interstellar gas. The formation of the spiral structure is commonly explained by spiral density waves (first proposed by Lin and Shu, 1964), which arise from perturbations of the disk enhanced by Lindblad resonances (see Binney and Tremaine, 1987 for details). Gas compression within the density waves results in an enhanced star formation, and thus the spiral pattern is visible in the optical and the infrared. Disk galaxies have a flat rotation curve, i.e. they are rotating differentially (except for the inner  $1 - 2$  kpc, where the rotation curve drops almost to zero at the galaxy's center), with typical rotation velocities around  $200 \text{ km s}^{-1}$  (Sofue and Rubin, 2001). The flatness of the rotation curve is explained by the presence of a dark matter halo within which the stellar and gaseous disk is residing.

The typical equipartition strength of the total magnetic field in spiral galaxies, determined from their total synchrotron emission, is about  $10 \mu\text{G}$ . Radio-faint galaxies like M 31 (the Andromeda galaxy) and M 33 have weaker total magnetic fields of about  $5 \mu\text{G}$ . Gas-rich galaxies with high star formation rates, e.g. M 51 (the Whirlpool galaxy, Fig. 2.1), M 93 (the Southern Pinwheel galaxy) or NGC 6946 (the Fireworks galaxy), have higher average field strengths of  $15 \mu\text{G}$  (Beck, 2008). The strongest fields ( $50\text{-}100 \mu\text{G}$ ) are measured in starburst galaxies, e.g. M 82 (the Cigar galaxy,

Klein et al., 1988) or NGC 4038/39 (the Antennae galaxies, Chyży and Beck, 2004), which is in fact a system of two spiral galaxies in the process of merging (see also chapter 3 and Fig. 3.1).

The total radio emission usually exhibits a spiral pattern which is similar to the spiral pattern observed in the far-infrared, indicating that the magnetic field is stronger in star forming regions. In massive spiral arms (e.g. in M 51, Fig. 2.1) the total equipartition field strength can be up to  $30 \mu\text{G}$  (e.g. Beck, 2008). However, the degree of radio polarization within the arms is often only a few %, indicating the the magnetic field in these regions is highly irregular, probably tangled by increased turbulent motions of gas clouds or by supernova shock fronts. The strength of resolved ordered fields in spiral galaxies traced by the polarized emission is typically  $1 - 5 \mu\text{G}$ , whereby exceptionally strong ordered magnetic fields (with polarization degrees up to 50%) are detected between the optical spiral arms (e.g.  $\approx 13 \mu\text{G}$  in NGC 6946 and  $\approx 15 \mu\text{G}$  in M 51). Thereby, the magnetic field is oriented parallel to the adjacent optical arms (Fig. 1.6, Beck and Hoernes, 1996). The large scale magnetic field is ordered on kpc scales and beyond.

Some spiral galaxies have bars – central elongated structures composed of stars. Numerical simulations have shown that differentially rotating disks are wildly unstable and will spontaneously form bars (on the other hand, there are partly stabilized by the presence of a dark matter halo, e.g. Ostriker and Peebles, 1973). Hence, approximately 30% of spiral galaxies are barred. The gravitational perturbation from the bar causes the material in the disk to form a pair of spiral arms that extend from the ends of the bar. The magnetic field lines in those barred galaxies, e.g. NGC 1097, seem to follow the gas flow (Fig. 1.7). The total magnetic field strength can be as high as  $60 \mu\text{G}$  in some regions of barred galaxies (Beck et al., 2005).

The ordered magnetic field forms spiral patterns in almost every galaxy seen face-on, even in ringed galaxies like NGC 4736 (Fig. 1.8, Chyży and Buta, 2008) or flocculent galaxies which do not show an optical spiral structure like NGC 4414 (Fig. 1.9, Soida et al., 2002). NGC 4736 and NGC 4414 have mean total magnetic field strengths of  $\approx 17 \mu\text{G}$  and  $\approx 15 \mu\text{G}$ , respectively. The mean degree of polarization in flocculent galaxies is similar to that in grand-design spiral galaxies (Knapik et al., 2000). The observed magnetic spiral patterns in all of these objects have large opening angles of the spiral arms (pitch angles) of about  $20^\circ - 40^\circ$ . The similarity of the magnetic spiral patterns in regular as well as irregular disk galaxies is a strong indication for a common process of the generation of the pattern.

In the outer parts of spiral galaxies ( $r > 15 \text{ kpc}$ ), there are not enough relativistic particles to illuminate the magnetic field. Hence, the assumption of equipartition between the magnetic field and the energy density of relativistic particles may lead to an underestimation of the field. However, field strengths in the outer parts of galaxies can be measured by Faraday rotation of polarized background sources. For example, those measurements have shown that the regular field in M 31 (the Andromeda galaxy) extends out to 25 kpc with a similar strength as in the inner region (Han et al., 1998). In the outermost regions of spiral galaxies the magnetic field energy density may even reach the level of the global rotational energy and thus affect the rotation curve (Battaner and Florido, 2000).

Nearby disk galaxies seen edge-on generally show a disk-parallel field near the plane of the disk. However, observations of NGC 253 (the Sculptor galaxy, Heesen et al., 2009), NGC 891, NGC 4631 (the Whale galaxy, Krause, 2009) and other galaxies revealed a “X-shaped” field in the halo of the galaxies (Fig. 1.10). This field pattern arises probably due to an outflow emerging from the disk, i.e. a galactic wind.

In interacting galaxies, magnetic fields trace regions of gas compression, strong shear and enhanced turbulence. For example, in the Antennae galaxies, bright, extended radio emission is observed in the two interacting galactic disks and the bases of the tidal tails (section 3, Fig. 3.1). Particularly strong emission comes from regions with strong star formation driven by the interaction. There, the highly tangled field reaches strengths of  $\approx 30 \mu\text{G}$ . Away from star forming regions, the magnetic field shows a coherent polarized structure, probably the result of gas shearing motions along the tidal tail (Chyży and Beck, 2004). Also, observations of the compact group of galaxies Stephan’s Quintet,

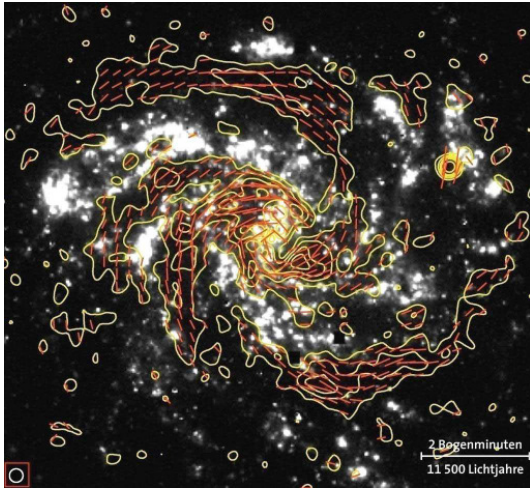


Figure 1.6: Polarized radio emission (contours) and magnetic field vectors derived from the polarized emission of NGC 6946, combined from observations at 6 cm wavelength with the VLA and Effelsberg 100m telescopes (from Beck and Hoernes, 1996). The background image shows the  $H\alpha$  emission tracing HII regions which are sites of star formation (from Ferguson et al., 1998). The ordered magnetic field lines are seen between the optical arms. Copyright: MPIfR Bonn. Graphics: ‘Sterne und Weltraum’.

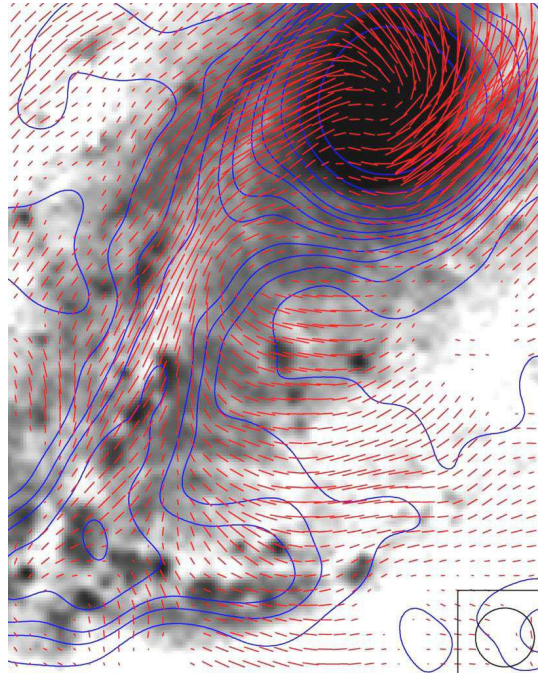


Figure 1.7: Total radio intensity contours and magnetic field vectors derived from the polarized emission of the central and southern parts of NGC 1097 at  $\lambda = 6.2$  cm observed with the VLA (Beck et al., 2002, image taken from Beck et al., 2005), overlaid on an optical image from the Cerro Tololo Observatory. The magnetic field lines seem to follow the gas flow.

which consists of four interacting spiral galaxies, show a prominent ridge of radio emission crossing through the system in between the galaxies (Fig. 1.11, Xu et al., 2003). This ridge of radio emission is believed to result from a shock front driven by a former interaction between two galaxies of the group. Due to the shock compression, the magnetic field of the ambient gas might have been amplified.

### 1.3.2 Magnetic fields in elliptical galaxies and galaxy clusters

Elliptical galaxies have a smooth brightness profile and – as the name implies – an approximately ellipsoidal shape. They cover a wide range in size ( $0.1 - 100$  kpc) and mass ( $10^7 - 10^{13}$  solar masses), and they do not significantly rotate (i.e. the rotation velocity is less than or similar to the overall velocity dispersion). Elliptical galaxies are believed to be the final result of the merging of two or more disk galaxies, whereby the galactic interaction has driven enhanced star formation and depleted most of the gas from the progenitor galaxies. The most massive of them have probably formed rapidly during the phase of structure formation through multiple mergers (see e.g. Naab and Ostriker, 2009 and references therein). Thus, elliptical galaxies are gas poor and consist of predominantly old, red stars. The residual gas is hot ( $\approx 10^7$  K), heated by supernovae, stellar winds and random motions of stars, and gives rise to X-ray emission (Fabbiano, 1989). As the interstellar gas is dilute, both relativistic and thermal electrons have low density, and any synchrotron emission and Faraday rotation can only

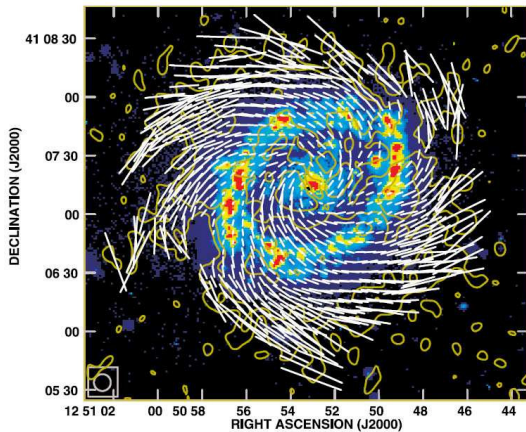


Figure 1.8: Polarized intensity (contours) and magnetic field vectors derived from polarized emission of NGC 4736 observed at 8.46 GHz with the VLA (from Chyży and Buta, 2008), overlaid on a  $H\alpha$  image (from Knapen et al., 2003). The spiral structure of the ordered magnetic field does not follow the ring structure of the galaxy.

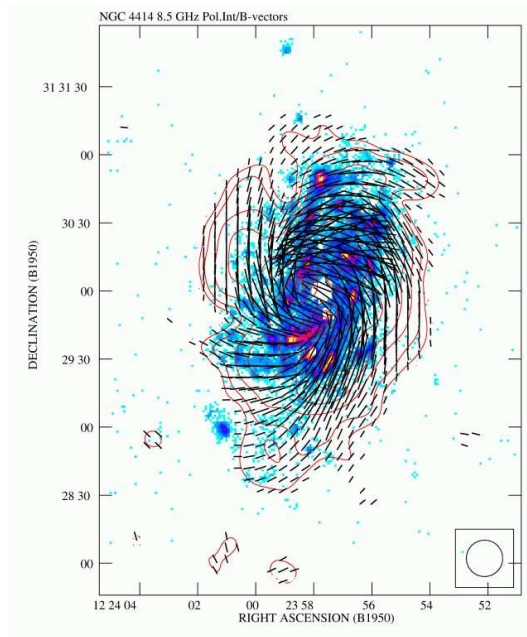


Figure 1.9: Polarized intensity (contours) and magnetic field vectors derived from polarized emission of NGC 4414, observed at 8.46 GHz (from Soida et al., 2002), overlaid on a  $H\alpha$  image (from Pogge, 1989). There exists a spiral pattern of the ordered magnetic field although the galaxy has no optical spiral structure.

be weak. Nevertheless, there is evidence that ellipticals are pervaded by significant magnetic fields. Diffuse, extended nonthermal radio emission is observed wherever more or less intense star formation is present (Wrobel and Heeschen, 1988, 1991). Stronger evidence is provided via Faraday rotation when a source of polarized radio emission is seen through the interstellar gas of a parent elliptical galaxy, which is then usually classified as a radio galaxy. Examples of this kind include NGC 4374 (Laing and Bridle, 1987), 3C 218 (Hydra A, Taylor et al., 1990) and NGC 5128 (Centaurus A, Clarke et al., 1992). Depolarization studies of extended radio sources (Strom and Jaegers, 1988) provide further evidence. In no known case polarized synchrotron emission has been observed, thus, either the emission is completely depolarized, or the magnetic field is completely random, or both. As the interstellar gas in elliptical is expected to be turbulent, these observations led to the idea of a fluctuating dynamo (section 1.4.5) working in these objects, whereby turbulence can generate random magnetic fields of  $0.3 \mu\text{G}$  at the turbulent scale ( $\approx 400 \text{ pc}$ ), resulting in the observed Faraday rotation (Shukurov, 2002). Similar considerations have shown that turbulent motions in the ISM of ellipticals may amplify the magnetic field to approximately  $1\text{--}10 \mu\text{G}$  (Moss and Shukurov, 1996; Mathews and Brighenti, 1997; Lesch and Bender, 1990). Complementary, the magnetic fields observed in elliptical galaxies could also be a consequence of the magnetization of the progenitor galaxies, whereby the ordered magnetic fields of the progenitors (assumed to be disk galaxies) got tangled during the interaction. In summary, the hot gas in elliptical galaxies contains magnetic fields with strengths comparable to those in spiral galaxies, but with the significant component being spatially disordered.

Clusters of galaxies are large ( $2\text{--}10 \text{ Mpc}$  in diameter) assemblages of galaxies bound by gravitation. They contain 50 to 1000 galaxies and have total masses of  $10^{14} - 10^{15}$  solar masses. Like elliptical

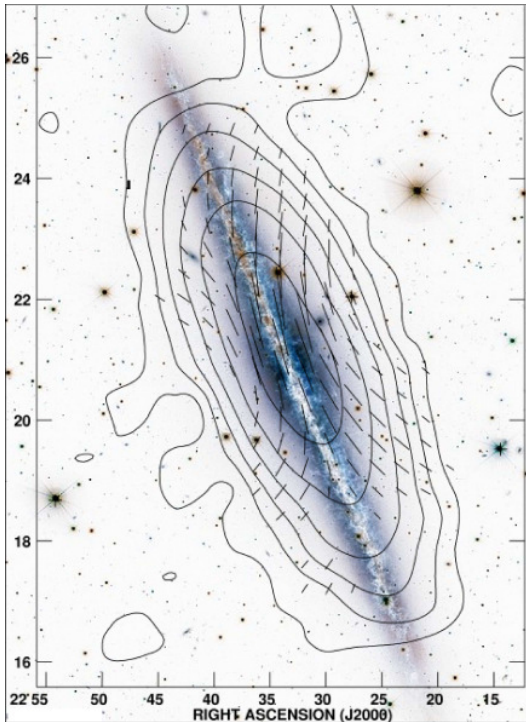


Figure 1.10: Total radio emission (contours) and magnetic field vectors derived from polarized emission of the edge-on galaxy NGC 891, a galaxy similar to the Milky Way, observed at 8.4 MHz with the Effelsberg telescope. The background optical image is from the Canada-France-Hawaii Telescope (CFHT). The magnetic field lines in the halo show a X-shaped structure. Copyright: MPIfR Bonn and CFHT/Coelum (from Krause, 2009).

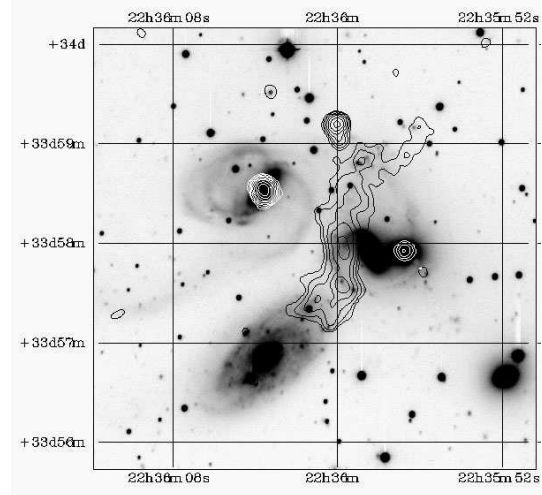


Figure 1.11: Total radio emission (contours) of the compact galaxy group Stephan's Quintet observed at 1.40 GHz with the VLA, overlaid on an R-band CCD image (from Xu et al., 2003). A prominent ridge of radio emission is crossing the system.

galaxies, they are filled with hot, X-ray emitting gas and contain large amounts of dark matter. Notable galaxy clusters in the relatively nearby universe include the Virgo cluster, Fornax Cluster, Hercules Cluster, and the Coma Cluster. Magnetic fields in galaxy clusters have been detected by radio observations, via the Faraday rotation signal of the magnetized intracluster medium (ICM) towards polarized radio sources in or behind clusters and from diffuse synchrotron emission of the ICM. Typical field strengths are of order  $1 \mu\text{G}$  with high areal filling factors out to Mpc radii. In some locations, such as the cores of some clusters, the magnetic fields can even have strengths of  $10 - 40 \mu\text{G}$  (see e.g. Carilli and Taylor, 2002 and Ferrari et al., 2008 for reviews).

Summing up, any structure in the local Universe seems to be pervaded by magnetic fields, whereby the typical magnetic field strengths in galaxies and galaxy clusters are of the order of  $1 - 10 \mu\text{G}$ .

### 1.3.3 Magnetic fields in distant, young galaxies

There is mounting evidence that strong magnetic fields exist also in galaxies at high redshift, i.e. in the early Universe. Faraday rotation measurements of distant quasars with redshifts up to  $z \approx 3$  suggest that the magnetic fields revealed by these measurements are comparable to those seen today (e.g. Athreya et al., 1998; Kronberg et al., 2008). Investigations combined with the incidence of

foreground metal line absorption have shown that the observed rotation measures are caused by ordered magnetic fields of surprisingly high strength within normal galaxies (Bernet et al., 2008) or damped Ly- $\alpha$  systems (DLAS, Wolfe et al., 1992) with redshifts  $z > 1$  along the line-of-sight to the quasars. Wolfe et al. (1992) estimated the magnetic fields in two DLAS with redshifts  $z \approx 2$ , i.e. when the Universe was less than one-third of its present age, to have strengths of a few  $\mu\text{G}$ .

DLAS, which are a class of quasar light absorbers with column densities of neutral gas  $> 2 \cdot 10^{20} \text{ cm}^{-2}$ , have often been interpreted as large progenitors of present-day galaxies (see Wolfe et al., 2005 for a review). They are dense, gravitationally bound concentrations of gas, exhibit a low velocity dispersion ( $< 10 \text{ km s}^{-1}$ ) and are comparatively cold ( $T < 1000 \text{ K}$ ). The minimum mass of their dark matter haloes is estimated to  $10^8 - 10^9$  solar masses with virial radii of  $5 - 50 \text{ kpc}$ . DLAS are believed to dominate the neutral gas content of the Universe and thus to serve as neutral gas reservoirs for star formation at high redshifts. In this context, the observed strong magnetic fields in these objects are of particular interest for the evolution of cosmic magnetism.

## 1.4 The dynamo theory

By 1971, the dynamo theory of magnetic field amplification originally suggested by Larmor (1919a,b) and Parker (1963) had been modified to explain the observed galactic magnetic fields (Parker, 1971; Vainshtein and Ruzmaikin, 1971; Stix, 1975 and White, 1978). This section reviews the basic ideas of the theory of galactic dynamos, starting with the physical conditions of the ISM and the derivation of the MHD induction equation from Maxwell's equations (see eg. Reitz et al. (1992) for a detailed treatment of the electromagnetic theory).

### 1.4.1 Physics of the interstellar medium

The evolution of the magnetic field is tightly coupled to the physics of the plasma. The ISM in disk galaxies like our Milky Way consists of about 99% gas and 1% dust by mass. As a result of primordial nucleosynthesis, the gas in the ISM contains roughly 75% hydrogen, 25% helium and small amounts of heavier elements (by mass). The interstellar gas consists partly of neutral atoms and molecules, as well as ions and electrons. This gas is dilute, with a mean number density of  $\approx 1 \text{ cm}^{-3}$  ( $10^{-24} \text{ g cm}^{-3}$ ) and a mean temperature of  $\approx 10^4 \text{ K}$ . It is ionized by the stellar UV radiation, the X-ray radiation from e.g. supernova (SN) remnants and by cosmic rays (cf. section 1.4.4). The degree of ionization ranges from 30% to 100% in various phases.

Thus, the ISM is an electrically conducting medium, i.e. an electric potential difference  $\nabla\phi$  is able to drive currents within the plasma. The currents are thereby determined by the drift velocity  $\mathbf{v}_D$  of the electrons relative to the massive ions ( $\mathbf{j} = -en_e\mathbf{v}_D$ ), which, in turn, is determined by the characteristic time  $\tau$  of momentum losses due to Coulomb collisions between the particles, and the force due to the electric potential  $\mathbf{F} = e\mathbf{E} = -e\nabla\phi$  (where  $\mathbf{E}$  is the electric field) via

$$\mathbf{F} = m_e \frac{\mathbf{v}_D}{\tau} = e\mathbf{E}, \quad (1.13)$$

$$\Rightarrow \mathbf{j} = \underbrace{\frac{e^2 n_e}{m_e}}_{=: \sigma} \tau \mathbf{E}. \quad (1.14)$$

Eq. 1.14 represents Ohm's law, with  $\sigma$  defined as the electric conductivity. In a plasma with temperature  $T$  and electron density  $n_e$ , and assuming that the drift velocity  $\mathbf{v}_D$  is much smaller than the thermal velocity  $\mathbf{v}_{\text{th}}$ ,  $\tau$  is given by  $\tau \sim T^{3/2}/n_e$  ( $\sim \mathbf{v}_{\text{th}}^3$ ), and thus  $\sigma \sim T^{3/2}$ , or, more precisely,

$$\sigma[\text{s}^{-1}] = 6.5 \cdot 10^6 (T[\text{K}])^{3/2}. \quad (1.15)$$

This is the so called Spitzer conductivity (see Cowling, 1945; Spitzer and Härm, 1953). Thus, the high temperatures of astrophysical plasmas imply a high electric conductivity. As a consequence, any electric field within the plasma will be canceled on a short timescale.

To a good approximation, the interstellar plasma consists of protons and electrons only, is quasi-neutral, and can be described as a fluid (the effective mean free path is small compared to the typical length scale of the system ( $\approx 1$  kpc) and the collision and gyration timescales are short compared to the system's time scale). As the electron mass  $m_e$  is much smaller than the proton mass  $m_p$ , the fluid properties can be described as follows:

$$\text{mass density: } \rho \approx m_p n, \quad (1.16)$$

$$\text{velocity: } \mathbf{v} \approx \mathbf{v}_p, \quad (1.17)$$

$$\text{current density: } \mathbf{j} = en(\mathbf{v}_p - \mathbf{v}_e), \quad (1.18)$$

$$\text{charge density: } \epsilon \approx 0, \quad (1.19)$$

with  $\mathbf{v}_p$  and  $\mathbf{v}_e$  the proton and electron velocities, respectively, and  $n$  the number density of protons (which is equal to the number density of electrons). Thus, one can use the standard equations of magnetohydrodynamics (MHD) to describe the behavior of the interstellar plasma:

$$\text{mass continuity equation: } \frac{\partial \rho}{\partial t} + \nabla \cdot (\rho \mathbf{v}) = 0 \quad (1.20)$$

$$\text{momentum equation: } \frac{\partial \mathbf{v}}{\partial t} + (\mathbf{v} \cdot \nabla) \mathbf{v} = \frac{1}{\rho} (-\nabla p + \mathbf{j} \times \mathbf{B}) \quad (1.21)$$

$$\text{Ohm's law: } \mathbf{E} + \frac{1}{c} \mathbf{v} \times \mathbf{B} = \frac{1}{\sigma} \mathbf{j} \quad (1.22)$$

$$\text{Maxwell's equations: } \nabla \cdot \mathbf{B} = 0 \quad (1.23)$$

$$\nabla \cdot \mathbf{E} = 4\pi\epsilon \quad (1.24)$$

$$\nabla \times \mathbf{B} = \frac{4\pi}{c} \mathbf{j} + \frac{1}{c} \frac{\partial \mathbf{E}}{\partial t} \quad (1.25)$$

$$\nabla \times \mathbf{E} = -\frac{1}{c} \frac{\partial \mathbf{B}}{\partial t} \quad (1.26)$$

The contributions to the force acting on the plasma (Eq. 1.21) are thereby the force due to pressure gradients  $-\nabla p$  and the force which is experienced by the plasma when moving perpendicular to the magnetic field  $\mathbf{j} \times \mathbf{B}$ , which is the magnetic pressure and the magnetic field line tension (viscous forces and external forces like gravity are thereby neglected). Eq. 1.22 is the Ohm's law (Eq. 1.14 is referring to the rest-frame of the fluid). Eq. 1.23 represents the fact that single magnetic monopoles have never been observed, i.e. the fact that magnetic field lines have always to be closed, and Eq. 1.24 accounts for electric charges being the source of electric fields. Eq. 1.25 is Ampère's law of electric currents being sources of magnetic fields, whereby the displacement current  $c^{-1} \partial \mathbf{E} / \partial t$  was introduced by James Clerk Maxwell (1831-1879), originally to overcome some inconsistencies arising from Ampère's original law (actually, it is this term which is responsible for the existence of electromagnetic waves). However, given a high conductivity as in case of the ISM, electric fields are weak, and thus the displacement current can be neglected. Finally, Eq. 1.26 is the mathematical form of Faraday's law of electromagnetic induction.

Ohm's law (Eq. 1.22) can be used to prove the frozen-in condition of ideal MHD ( $\sigma \rightarrow \infty$ ). This condition, which states that the magnetic flux within a plasma has to be conserved, has a further important implication: The topology of magnetic field lines can never be changed in ideal MHD, which means that magnetic flux tubes can be indeed twisted, but never torn apart. The magnetic field loops erupting from the sun's surface are an example for such magnetic flux tubes.

Taking the curl of Eq. 1.22 and inserting Eq. 1.25 (neglecting the displacement current) and Eq. 1.26 yields an equation for the evolution of the magnetic field with time, the induction equation:

$$\frac{\partial \mathbf{B}}{\partial t} = \nabla \times ((\mathbf{v} \times \mathbf{B}) - \eta(\nabla \times \mathbf{B})) \quad (1.27)$$

Thereby,  $\eta = \frac{c^2}{4\pi\sigma}$  is the resistive magnetic diffusivity. Obviously, magnetic field can only be generated by the first right-hand-side convective term  $\nabla \times (\mathbf{v} \times \mathbf{B})$ , and to a first order approximation, the diffusive term  $-\nabla \times (\eta(\nabla \times \mathbf{B}))$  can be neglected ( $\sigma \rightarrow \infty \Rightarrow \eta \rightarrow 0$ ). In this limit, the magnetic field may be distorted and amplified, but no net flux is created. This means that if at any time  $\mathbf{B}$  is zero everywhere, it must be zero at all times. This follows directly from the assumption of quasineutrality. When this assumption breaks down, currents driven by non-electromagnetic forces can create magnetic fields even if  $\mathbf{B}$  is initially zero.

Given a finite conductivity, the corresponding characteristic diffusion timescale over a scale  $L$  is  $\tau = L^2/\eta$ . In astrophysical plasmas with high conductivity, these timescales are huge. In the solar convective zone and in the ISM the temperature is  $T \approx 10^4$  K, resulting in a conductivity of  $\approx 10^{13} \text{ s}^{-1}$  (Eq. 1.15) and thus a diffusivity of  $\eta \approx 10^7 \text{ cm}^2 \text{ s}^{-1}$ . Hence, for the sun, with  $L \approx 10^4$  km,  $\tau \approx 10^{11} \text{ s} \approx 3 \cdot 10^3 \text{ yr}$ . In the Galaxy ( $L \approx 100 \text{ pc}$ ),  $\tau \approx 9 \cdot 10^{33} \text{ s} \approx 3 \cdot 10^{26} \text{ yr}$ , which is by 16 orders of magnitude larger than the age of the Universe. This slow resistive diffusion of magnetic fields in astrophysical objects supports the relic field hypothesis, as even weak primordial fields – once enhanced by compression during the gravitational collapse of galaxies – may have persisted until today. However, there are two main problems with these diffusion timescales: First, the solar cycle requires that the structure of the solar magnetic field gets completely destroyed and reestablished again within 22 years, which is much shorter than the timescale given by the resistive diffusion. Second, the resistive diffusivity in Galaxies suggests an almost frozen-in magnetic field. In this case, differential rotation of disk galaxies would lead to tightly wound magnetic field lines: Within the lifetime of  $\approx 10^9 \text{ yr}$ , a typical galaxy rotates  $\approx 35$  times at a radius of 1 kpc, but only few times at a radius of 10 kpc. Such a tightly wound magnetic field pattern is in contradiction to observations. Thus, the diffusion time scale in cosmic plasmas apparently has to be much shorter. This can be achieved by considering turbulent diffusion (Parker, 1973).

The structure of the ISM is controlled by stellar winds and SN explosions. These explosions release large amounts of energy ( $E_{\text{SN}} \approx 10^{51} \text{ erg}$ ), and the supersonic blast waves driven by the (randomly distributed) SN explosions carry the energy into the ISM. As a consequence, the ISM becomes turbulent (e.g. Lozinskaya, 1992). The ability of the ISM to become turbulent can also be understood in terms of the Reynolds number  $Re$ , which is the ratio between inertial forces  $\rho(\mathbf{v} \cdot \nabla)\mathbf{v}$  and viscous forces  $\rho\nu_{\text{visc}}\Delta\mathbf{v}$  (with  $\nu_{\text{visc}}$  the kinematic viscosity) acting on the fluid (the plasma). With  $V$  the typical velocity of the fluid and  $L$  the typical spatial dimension, it follows (e.g. Tritton, 1988):

$$Re = \frac{\rho V^2/L}{\rho\nu_{\text{visc}}V/L^2} = \frac{VL}{\nu_{\text{visc}}}. \quad (1.28)$$

In general, the flow will be laminar for small  $Re$ , and become turbulent above a critical Reynolds number  $Re_{\text{crit}} \approx 10^3$  (e.g. Longair, 1994). The viscosity of a plasma due to Coulomb collisions can be approximated by

$$\nu_{\text{visc}} \approx \frac{\lambda_{\text{free}}^2}{\tau} = \frac{(v_{\text{th}} \cdot \tau)^2}{\tau} = v_{\text{th}}^2 \cdot \tau, \quad (1.29)$$

where  $\lambda_{\text{free}}$  is the mean free path of the particles. As  $v_{\text{th}} \sim T^{1/2}$  and  $\tau \sim T^{3/2}/n_e$ ,  $\nu_{\text{visc}}$  is proportional to  $T^{5/2}/n_e$  (this is also called the Spitzer viscosity, Spitzer, 1962). More precisely,

$$\nu_{\text{visc}}[\text{cm}^2 \text{ s}^{-1}] \approx 10^{10} \frac{(T[\text{K}])^{5/2}}{n_e[\text{cm}^{-3}]}. \quad (1.30)$$

Given  $T \approx 10^4$  K and  $n_e \approx 1 \text{ cm}^{-3}$ , a typical viscosity of the ISM is  $\nu_{\text{visc}} \approx 10^{20} \text{ cm}^2 \text{ s}^{-1}$ . For a typical velocity – the sound speed –  $V = c_s \approx 10 \text{ km s}^{-1} = 10^6 \text{ cm s}^{-1}$  and a typical length scale  $L \approx 1 \text{ kpc} \approx 3 \cdot 10^{21} \text{ cm}$ , the Reynolds number is  $Re \approx 3 \cdot 10^7$ . Hence, mainly due to the large spatial scales, the Reynolds numbers in astrophysical systems are usually very large, wherefore astrophysical plasmas are expected to get turbulent (see e.g. Brandenburg and Nordlund, 2009).

The turbulence reveals itself observationally due to the reduced degree of polarization of synchrotron emission and by Doppler shift broadening of spectral lines beyond their width expected from thermal motions alone. The turbulent length and velocity scales are

$$l_T \approx 0.05 - 0.1 \text{ kpc}, \quad (1.31)$$

$$v_T \approx 10 - 30 \text{ km s}^{-1}, \quad (1.32)$$

whereby  $v_T$  is of the same order of magnitude as the sound speed of the ISM. The corresponding turbulent diffusivity follows as (Parker, 1973, see also section 1.4.3)

$$\eta_T \approx 0.1 l_T v_T \approx (0.5 - 3) \cdot 10^{26} \text{ cm}^2 \text{ s}^{-1}. \quad (1.33)$$

This increase of the diffusion coefficient compared to resistive diffusion leads to a decrease of the magnetic diffusion timescale needed to explain observational facts like the large pitch angles of the magnetic spiral arms. In spiral galaxies, this timescale is less than their age, implying that any primordial magnetic field should be decayed until today. Thus, as we still observe strong magnetic fields in the local universe, there has to be a process which is continuously amplifying magnetic fields.

### 1.4.2 The kinematic dynamo

The simplest approach to magnetic field amplification is the investigation of the induction equation (Eq. 1.27) assuming  $\eta \rightarrow 0$ . Furthermore, in many situations, the fields are weak and the Lorentz term  $(\mathbf{j} \times \mathbf{B})/\rho$  in Eq. 1.21 can be neglected (kinematic approximation). In the context of spiral galaxies, it is appropriate to use cylindrical coordinates and some simplifying assumptions can be made: First, the system is nearly axially symmetric. Second,  $\partial v_\varphi / \partial r \approx 0$  within the disk (differential rotation). Third, the height of the disk is much smaller than its radius (thin disk approximation), implying small  $z$ -velocities. Finally, the initial magnetic field is assumed to have no  $z$ -component. Using these assumptions, Eq. 1.27 reduces to

$$\frac{\partial B_r}{\partial t} = -B_r \frac{v_r}{r}, \quad (1.34)$$

$$\frac{\partial B_\varphi}{\partial t} = -B_\varphi \frac{\partial v_r}{\partial r} + B_r r \frac{\partial \Omega}{\partial r}, \quad (1.35)$$

$$\frac{\partial B_z}{\partial t} = B_r \frac{\partial v_z}{\partial r}, \quad (1.36)$$

with  $\Omega(r) = v_\varphi/r$  the angular velocity of rotation.

In fact, due to differential rotation (last term in Eq. 1.35), the azimuthal component  $B_\varphi$  of an initially uniform field lying in the plane of the disk will grow linearly with time, whereby the magnetic field will be wound up and stretched. This process is known as the “ $\Omega$ -effect” and is dominant because  $v_\varphi \gg (v_r, v_z)$ . However, this amplification can not proceed infinitely, as the subsequent winding will result in a tightly wound field pattern which – given a large but not infinite conductivity – will finally be completely toroidal. Without a radial component  $B_r$  to be further amplified, the magnetic field will be subject to magnetic diffusion, thus, on the long run, it will vanish. This fact has been already noticed by Cowling (1953), who laid down the theorem that an axisymmetric magnetic field cannot be maintained via dynamo action. The only possibility for a steady growth of the magnetic field is therefore a constant supply of  $B_r$ . According to Eq. 1.34, the radial magnetic field component can be amplified in the presence of a radial velocity component directed to the center of the disk,  $-v_r$ . Such radial gas flows occur when angular momentum is transported outwards in radial direction, which is particularly the case in the presence of a spiral or barred disk structure (e.g. Lynden-Bell and Kalnajs, 1972). Furthermore,  $B_\varphi$  can be additionally amplified if the radial velocity decreases with increasing radius. The fundamental question is thereby whether the radial flows are strong enough to lead an efficient constant amplification, and whether the non-axisymmetry of the galactic spiral pattern (which is neglected in most theoretical considerations) has an additional influence on the magnetic field evolution. This idea was the basis of the numerical studies presented in Kotarba et al. (2009) (chapter 2), where I have investigated the magnetic field structure due to the global velocity field in spiral galaxies. I did not find an amplification of the magnetic field beyond the winding-effect, however, I could show the importance of non-axisymmetry for the evolution of the magnetic field.

### 1.4.3 The mean-field dynamo

The difficulty of explaining the maintenance of the observed magnetic fields of the Earth, the sun and in disk galaxies against magnetic diffusion led, in particular, to the development of the concept of a mean-field dynamo, which is now the standard theory of magnetic field evolution in disk galaxies (see Steenbeck et al., 1966; Moffatt, 1978; Parker, 1979; Krause and Raedler, 1980; Zeldovich et al., 1983; Krause and Wielebinski, 1991; Beck et al., 1996; Kulsrud, 1999; Widrow, 2002 for detailed treatments of this theory). This concept makes use of a statistical mean-field approximation to describe the effect of turbulence on the evolution of the magnetic field. Thereby it is assumed that the velocity (magnetic) field may be expressed in terms of an ensemble averaged mean field  $\bar{\mathbf{v}}$  ( $\bar{\mathbf{B}}$ ) plus a fluctuating (turbulent) component  $\tilde{\mathbf{v}}$  ( $\tilde{\mathbf{B}}$ , with  $\bar{\tilde{\mathbf{v}}} = \bar{\tilde{\mathbf{B}}} = 0$ ):

$$\mathbf{B} = \bar{\mathbf{B}} + \tilde{\mathbf{B}} \quad \mathbf{v} = \bar{\mathbf{v}} + \tilde{\mathbf{v}} \quad (1.37)$$

This splitting is of course also valid for the electric field  $\mathbf{E}$  and the current  $\mathbf{j}$ . Because of their linearity, the Maxwell’s equations remain valid for the ensemble averaged quantities, however, a new term arises in the Ohm’s law:

$$\frac{1}{\sigma} \bar{\mathbf{j}} = \bar{\mathbf{E}} + \frac{1}{c} (\bar{\mathbf{v}} \times \bar{\mathbf{B}} + \mathcal{E}), \quad (1.38)$$

with  $\mathcal{E} = \overline{\tilde{\mathbf{v}} \times \tilde{\mathbf{B}}}$  the mean electromotive force due to fluctuations of the magnetic field as it is carried around by the plasma. This term does not vanish as  $\tilde{\mathbf{v}}$  and  $\tilde{\mathbf{B}}$  are not independent because of the high conductivity of the plasma. Rather, the fluctuations of the magnetic field  $\tilde{\mathbf{B}}$  are caused by the fluctuating motions of the plasma, i.e.  $\tilde{\mathbf{v}}$ . In case of homogeneous isotropic turbulence,  $\mathcal{E}$  can be expressed in terms of two scalar coefficients  $\alpha$  and  $\beta$  (Krause and Rädler, 1971),

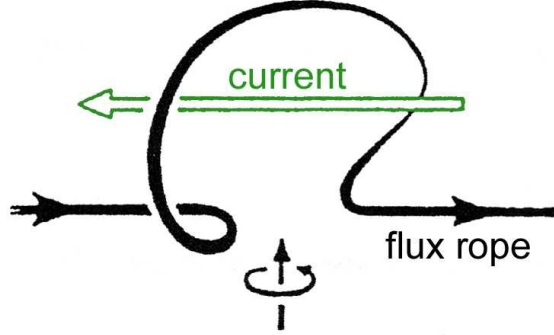


Figure 1.12: A magnetic flux rope undergoing the influence of a helical motion is shaped into a loop and gives rise to a current with a component parallel to the mean magnetic field. Adopted from Krause and Wielebinski (1991).

$$\mathcal{E} = \overline{\tilde{\mathbf{v}} \times \tilde{\mathbf{B}}} = \alpha \overline{\mathbf{B}} - \beta \nabla \times \overline{\mathbf{B}}, \quad (1.39)$$

whereby  $\alpha$  and  $\beta$  depend only on  $\tilde{\mathbf{v}}$ , not on  $\tilde{\mathbf{B}}$ . It can be shown that  $\alpha$  does not vanish only in case of helical turbulence with a favored sense of rotation (Parker, 1971). Typical motions of this type are rising plasma bubbles with a preferred sense of rotation around the direction of their motion. As the magnetic field lines assumed to be frozen into the plasma are carried along with the plasma, they will be twisted by the rising and rotating bubble and form a loop as shown in Fig. 1.12. According to Maxwell's equation 1.25 (neglecting the displacement current), the magnetic loop is connected with a current, and because of the twist this current has a component parallel to the mean magnetic field. This is the effect described by the term  $\alpha \overline{\mathbf{B}}$  in Eq. 1.39, and is called the “ $\alpha$ -effect”.

The  $\alpha$ -effect is particularly relevant because it occurs naturally in rotating turbulent systems like stars and galaxies. In a rotating galactic disk, SN explosions are sources of turbulence which can drive the plasma of the ISM out of the galactic plane. Those rising plasma bubbles will expand outside the disk because of the lower gas pressure, which decreases with increasing height above the disk. The expansion of the bubble corresponds to a sidewise velocity component  $v_r$  of the plasma. Thus, as the disk is rotating, the bubble will be subject to the Coriolis force  $\sim \Omega v_r$ . It will start to rotate around an axis perpendicular to the plane of the disk, which is exactly the motion needed for the  $\alpha$ -effect. Thereby, the vorticity  $\nabla \times \mathbf{v}$  of descending and thus contracting bubbles will be the same but negative as the vorticity of rising bubbles. Hence, the helicity  $\mathbf{v} \cdot (\nabla \times \mathbf{v})$  (a pseudoscalar) will be the same for rising and descending bubbles above the disk, and the same but negative below the disk. On the basis of this relation,  $\alpha$  can be expressed in terms of the helicity of the turbulence and the turbulent correlation time scale  $\tau_{\text{cor}} = l_T/v_T$  (Steenbeck and Krause, 1969):

$$\alpha = -\frac{\tau_{\text{cor}}}{3} \langle \tilde{\mathbf{v}} \cdot \nabla \times \tilde{\mathbf{v}} \rangle \quad (1.40)$$

Deriving the induction equation (Eq. 1.27) in due consideration of Eq. 1.38 and 1.39 results in an extended expression for the evolution of the magnetic field:

$$\frac{\partial \overline{\mathbf{B}}}{\partial t} = \nabla \times (\overline{\mathbf{v}} \times \overline{\mathbf{B}}) + \nabla \times \alpha \overline{\mathbf{B}} - \nabla \times \eta_T (\nabla \times \overline{\mathbf{B}}), \quad (1.41)$$

where  $\eta_T = \eta + \beta$  is the turbulent diffusivity.  $\beta$  can be shown to be always positive (Krause and Rädler, 1971), thus, the turbulent diffusivity  $\eta_T$  is always larger than the resistive diffusivity  $\eta$ .  $\eta_T$  is related to the intensity of turbulence, and, in case of high conductivity, it can be expressed as

$$\eta_T \approx \beta = \frac{\tau_{\text{cor}}}{3} \langle \tilde{\mathbf{v}}^2 \rangle. \quad (1.42)$$

Eq. 1.41 further demonstrates the importance of the  $\alpha$ -effect for the evolution of magnetic fields in disk galaxies: Given a completely toroidal mean magnetic field  $\overline{\mathbf{B}}$ , the  $\alpha$ -term will result in a new poloidal magnetic field component. This can be understood in terms of the twisting of magnetic field ropes by turbulent helical motions, whereby magnetic diffusion is needed for poloidal loops above and below the disk to combine and form large-scale poloidal components. The new poloidal component can in turn be sheared and wound up by differential rotation, resulting in an enhanced toroidal magnetic field component. This combination of the  $\alpha$ -effect and the  $\Omega$ -effect leads to an exponential growth of the toroidal (“regular”) magnetic field and is thus called the  $\alpha\Omega$ -Dynamo, or, in case of disk galaxies, the galactic dynamo. It allows for the maintenance of axisymmetric magnetic fields against magnetic diffusion, thus nullifying Cowling’s theorem. Furthermore, due to the stretching of the turbulent magnetic field by differential rotation, the galactic dynamo is able to produce ordered magnetic fields with coherence lengths far above the turbulent length scale  $l_T$ . Thereby, axisymmetric solutions of Eq. 1.41 are preferred, but non-axisymmetric solutions also exist (Ruzmaikin et al., 1988). Thus, the galactic dynamo can successfully reproduce the structure of the observed magnetic patterns in disk galaxies (section 1.3.1).

The dynamo equation 1.41 is solved using the ansatz  $B(x, t) \sim e^{\Gamma t}$  and, in case of disk galaxies, taking into account the thin disk approximation and the flatness of the rotation curve. Then, the intensity of the  $\Omega$ - and the  $\alpha$ -effect with respect to turbulent diffusion can be characterized by two dimensionless numbers,  $R_\Omega$  and  $R_\alpha$  (Ruzmaikin et al., 1988):

$$R_\Omega = \frac{h^2}{\eta_T} \cdot \frac{rd\Omega}{dr}, \quad (1.43)$$

$$R_\alpha = \frac{\alpha h}{\eta_T}, \quad (1.44)$$

with  $h$  the half-thickness of the galactic disk ( $\approx 400$  pc), and  $rd\Omega/dr \approx -\Omega \approx 10^{-15} \text{ s}^{-1}$  within the disk. According to simple mixing length theory and assuming  $l_T = 100$  pc and  $v_T = 10 \text{ km s}^{-1}$ , the turbulent diffusivity is estimated to  $\eta_T = l_T v_T / 3 = 10^{26} \text{ cm}^2 \text{ s}^{-1}$  (cf. Eq. 1.33 and 1.42). A typical value of  $\alpha$ , which depends on the strength of the Coriolis force, the size of the turbulent eddies and the density gradient, is  $\alpha_0 \approx l_T^2 \Omega / h$  (e.g. Zeldovich et al., 1983). Generally,  $\alpha$  will depend on the height above the disk, i.e.  $\alpha(z) = \alpha_0 \cdot f(z)$ . Inserting the typical values,  $R_\Omega \approx -10$  and  $R_\alpha \approx 1$ . Hence, in disk galaxies,  $|R_\Omega|$  is usually much larger than  $|R_\alpha|$ . The joint action of both generators can be described by the dynamo number

$$D = R_\Omega R_\alpha. \quad (1.45)$$

The galactic dynamo is a threshold phenomenon. For the dynamo effect to overcome turbulent diffusion, i.e. for an exponential growth of the field,  $|D|$  has to be larger than some critical dynamo number  $D_{\text{cr}}$ . Analytical estimates give  $D_{\text{cr}} \approx 6 - 10$ , depending on the exact profile adopted for  $\alpha(z)$ . From numerical simulations of galactic dynamo models, Ruzmaikin et al. (1988) have derived  $D_{\text{cr}} \approx 7$ . The dynamo growth rate  $\Gamma$  is given by the relation

$$\Gamma = |D|^{1/2} \frac{\eta_T}{h^2}, \quad (1.46)$$

whereby  $\tau = h^2/\eta_T$  is the time of turbulent diffusion over the half-thickness of the disk. Thus, the timescale of exponential growth of the magnetic field due to the mean-field dynamo is

$$t_{\text{exp}} = \frac{1}{\Gamma} \approx 1.5 \cdot 10^8 \text{ yr.} \quad (1.47)$$

The persuasive power of the concept of a mean-field galactic dynamo is the agreement of its predictions with observations, particularly the large scale structure of the observed magnetic fields. However, for the above discussion it was assumed that the back-reaction of the magnetic field on the plasma is unimportant, an assumption which of course can and has been challenged on the following ground: In a highly conducting turbulent plasma, the magnetic field on small scales builds up rapidly via the fluctuating dynamo (section 1.4.5). Thus, the Lorentz force on small scales can react back on the plasma suppressing the turbulent motions responsible for field amplification. If turbulent motions are suppressed, however, then the  $\alpha$ -effect and the turbulent diffusion (the cascade of magnetic energy to smaller diffusive scales) are also reduced, resulting in an effective shut off of the mean-field dynamo (Cattaneo and Vainshtein, 1991; Kulsrud and Anderson, 1992; Vainshtein and Cattaneo, 1992). The suppression of the  $\alpha$ -effect is known as “ $\alpha$ -quenching”, and is the main reason for criticism of the mean-field dynamo theory. Yet, the fluctuating dynamo and thus the  $\alpha$ -quenching is more efficient the smaller the turbulent scale. Thus, a possible solution to the problem of  $\alpha$ -quenching is to suppose that the “turbulence” responsible for the  $\alpha$ -effect and for the  $\beta$  term in the mean-field theory acts on much larger scales than the scale of turbulence where  $\alpha$ -quenching is efficient. This solution was proposed by Parker (1992) and is discussed in the next section.

However, even if the problem of  $\alpha$ -quenching on small scales can be resolved, the back-reaction of the magnetic field on the plasma certainly becomes important once the energy density of the *total* magnetic field  $e_{\text{mag}}$  becomes comparable to the kinetic energy density of the turbulence  $e_{\text{turb}} = 0.5 \cdot \rho v_T^2$  responsible for the field amplification. If the magnetic energy reaches the level of the turbulent kinetic energy, i.e.

$$\frac{B^2}{8\pi} = \frac{1}{2} \rho v_T^2, \quad (1.48)$$

a quasisteady state of “equipartition” should emerge. In typical local disk galaxies with  $B \approx 1 \mu\text{G}$  and  $\rho \approx 10^{-24} \text{ g cm}^{-3}$ , both the magnetic and turbulent energy densities are comparable ( $\approx 5 \cdot 10^{-14} \text{ erg cm}^{-3}$ ). Thus, these evolved galaxies seem to have already reached the equipartition state. Quenching of the galactic dynamo at equipartition field strength can be achieved by the phenomenological formulae

$$\alpha_Q = \alpha \left( 1 + \frac{B^2}{B_{\text{eq}}^2} \right)^{-1}, \quad (1.49)$$

where  $B_{\text{eq}}$  is the equipartition field strength (e.g. Krause and Raedler, 1980).

#### 1.4.4 The cosmic ray driven dynamo

The Earth is continually bombarded by highly energetic, electrically charged particles from space. Their extraterrestrial origin was established by the balloon experiment conducted by F. Hess (1912),

wherefore they have been referred to as cosmic rays (CRs). Later, it was realized that they are in fact material particles rather than photons (Bothe and Kolhörster, 1929). However, their widespread distribution throughout the Milky Way were not recognized until the observed Galactic radio emission was correctly identified as synchrotron radiation from CR electrons (Ginzburg and Syrovatskii, 1965). Measurements from instrumented balloons and satellites have shown that CRs comprise protons,  $\approx 10\%$  of helium nuclei (by mass),  $\approx 1\%$  of heavier nuclei,  $\approx 2\%$  of electrons, and smaller amounts of positrons and antiprotons (Bloemen, 1987; Blandford and Eichler, 1987). They have typical velocities close to the speed of light and span a whole range of kinetic energies  $E$ . The majority of CRs with  $E < 0.1 \cdot 10^9$  eV/nucleon originate in the Sun. More energetic CRs are of galactic or extragalactic origin and follow a steep spectrum from  $10^9$  to  $10^{20}$  eV/nucleon which can be described by a power law  $N(E) \sim E^{-p}$  with a typical spectral index  $p = 2.6$  (cf. section 1.2.2). Thus, CRs are non-thermal. SN remnants are the most likely source for CRs with  $E < 10^{18}$  eV/nucleon, whereby the CRs are accelerated by repeated scattering across the SN shock-wave. CRs with higher energies are believed to originate in Jets of black holes or pulsars, and are probably of extragalactic origin (The Pierre AUGER Collaboration et al., 2008). As CRs are charged and thus subject to Lorentz forces, they are coupled to the magnetic field. They propagate through the ISM by diffusing on the irregularities of the Galactic magnetic field and, additionally, by advection. Thereby, they loose energy due to ionization losses, bremsstrahlung (synchrotron radiation) and inverse Compton (IC) scattering. Thus, they provide an important source of heating and ionization of the ISM. The bulk of the CR energy density  $e_{\text{CR}} \approx 1 \text{ eV cm}^{-3} \approx 1.6 \cdot 10^{-12} \text{ erg cm}^{-3}$  is due to mildly relativistic protons with kinetic energies of a few GeV (Boulares and Cox, 1990, see also Ferrière, 2001). In our Galaxy, the number density of CRs is  $\approx 10^{-10} \text{ cm}^{-3}$ , whereas the density of thermal gas is  $\approx 1 \text{ cm}^{-3}$ . Thus, CRs are a weightless pressure component of the ISM.

CRs are an essential dynamical ingredient of the ISM of galaxies. The energy density of CRs is comparable to that of magnetic fields and turbulent gas motions, suggesting a significant coupling between these components<sup>3</sup>. CRs are bound to and confined by the magnetic field due to their charge. The magnetic field in turn is affected by the thermal plasma (which is turbulent due to stellar activity) because of the high conductivity. Due to this linkage and because of their non-thermal pressure, CRs are also coupled to the thermal gas. This coupling may play a significant role in the regulation of star formation and evolution of galaxies (Fatuzzo et al., 2006; Socrates et al., 2008; Sironi and Socrates, 2010). Furthermore, as SN explosions are the most likely source of galactic CRs, the star formation rate of a galaxy should be a measure of the cosmic ray flux. This cross-correlation of the thermal plasma and the star formation rate with the non-thermal CRs and magnetic fields suggests a self-regulated state and equipartition between all corresponding pressure components. This scenario is supported by the observed tight correlation between the non-thermal radio flux and the thermal FIR flux, i.e. the radio-FIR correlation (Condon, 1992).

This relationship between the components of the ISM – ionized gas, magnetic fields and cosmic rays – is the basis of the concept of a cosmic ray driven galactic dynamo. This concept was originally developed by Parker (1992) in view of the problems concerning the galactic dynamo described above. The idea is as follows: The two weightless components of the ISM – CRs and magnetic fields – support the heavy thermal gas against vertical gravitational forces due to the stellar disk. Such a configuration is intrinsically unstable against vertical perturbations of initially azimuthal magnetic field lines (Fig. 1.13). If the magnetic field lines are slightly bent out from the disk by a vertical perturbation, the ionized gas slips down along the field lines and forms gas condensations in the valleys, whereas the weightless CR gas tends to escape from the disk together with an amount of the magnetic field to which it is confined. Thus, the initial perturbation is enhanced. This process is called the Parker buoyancy instability (Parker, 1966, 1967a,b). Buoyancy due to both the magnetic

---

<sup>3</sup>Note that we have assumed a rather weak magnetic field of  $1 \mu\text{G}$  in calculating the energy density of the magnetic field  $e_{\text{mag}} \approx 5 \cdot 10^{-14}$  in the previous section. Assuming  $B \approx 10 \mu\text{G}$ ,  $e_{\text{mag}} \approx 5 \cdot 10^{-12} \text{ erg cm}^{-3} \approx e_{\text{CR}}$ .

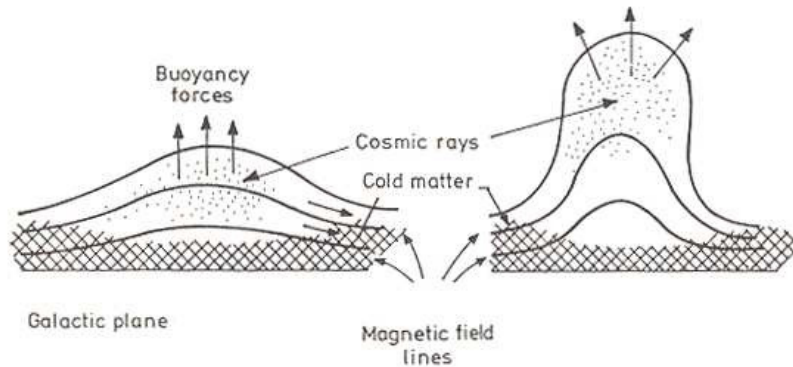


Figure 1.13: The Parker instability. Buoyancy forces of cosmic rays result in magnetic lobes escaping from the galactic disk. From Longair (1994).

field and the CRs inflates the raised region and thus magnetic lobes are formed, which are exactly the kind of lobes that are needed to drive dynamo action. Thereby, the CR pressure inside a lobe will make it buoyant even if the magnetic field is weak (Hanasz and Lesch, 1993, 1997, 1998). In fact, with a weak field, magnetic tension, which tends to limit the Parker instability, will be unimportant. Here, the “turbulence” needed to drive the  $\alpha\Omega$ -dynamo corresponds to the waviness of the ISM caused by the Parker instability. The typical length-scale of this waviness is of order of 1 kpc, i.e. much larger than the 100 pc assumed in classical mean-field dynamo investigations, thus avoiding the problem of  $\alpha$ -quenching.

In case of the CR driven dynamo, magnetic dissipation in the limit of high conductivity is established through fast magnetic reconnection. On the boundary of the inflated and thus closely packed magnetic loops magnetic field lines of opposite direction come close together. There, fast magnetic reconnection starts to rearrange the magnetic field configuration, whereby the loops sever from the disk field. These loops are free to rotate under the influence of the Coriolis force. Further reconnection restructures the loops into a large-scale poloidal field which can be converted to an azimuthal field by differential rotation. While the underlying physics of Parker’s model is quite different from that of classical mean-field dynamo, the generation of poloidal field from toroidal field as well as the elimination of spurious magnetic flux can be described by  $\alpha$  and  $\beta$ -like terms in an equation for the large-scale field.

Furthermore, Hanasz and Lesch (2000) showed that a Parker instability triggered by the injection of CRs in SN remnants is faster than the Parker instability excited by a small vertical perturbation, resulting in a strong dynamo effect. As described above, the assumption of a supply of CRs by SN remnants is realistic. Moreover, the seed field needed before the onset of dynamo action may also be supplied by SN remnants, which release small scale, dipolar magnetic fields into the ISM (see section 1.5.1). Such a scenario of a CR driven dynamo has been recently successfully simulated by means of grid-based numerical simulations for a Milky-Way like galaxy by Hanasz et al. (2009c). They found an exponential growth of the magnetic field with an  $e$ -folding time of  $2.7 \cdot 10^8$  yr, comparable to the  $e$ -folding time of the classical mean-field dynamo. Thereby, the amplification ceases as soon as the energy density of the magnetic field reaches equipartition with the energy density of the cosmic rays, a result which is expected from theory and supported by observations (cf. section 1.2.2). Also, the initially randomly distributed small scale dipolar fields develop into a magnetic spiral structure in the face-on view, with coherence lengths of several kpc. In the edge-on view, the magnetic field distribution reveals a X-shaped structure similar to the observed one (section 1.3.1).

The CR driven dynamo is thus able to avoid the problems of classical mean-field investigations

and to reproduce the observed field strengths and structures of present-day galaxies. Hence, it is the today most promising concept of galactic magnetism in the local universe. Furthermore, as star formation rates were higher in the early universe, the CR driven dynamo may have been more efficient at higher redshifts, thus providing one possible explanation of the observed high redshift magnetic fields (Lesch and Hanasz, 2003, see also section 1.5.3).

### 1.4.5 The fluctuating dynamo

In the mean-field and CR driven dynamo models devised to explain magnetic fields in disk galaxies (as well as in stars and planets), global rotation plays a central role. It provides a reservoir of energy for field amplification through both the  $\Omega$ - and the  $\alpha$ -effect. On the one hand, differential rotation is responsible for the shear of turbulent magnetic fields which is needed to explain the large coherence lengths of the observed magnetic fields in disk galaxies. On the other hand, the  $\alpha$ -effect requires net helicity, which occurs because of the Coriolis effect in rapidly rotating systems. However,  $\mu\text{G}$  magnetic fields are observed also in non- (or only slowly) rotating galactic objects like elliptical galaxies and galaxy clusters.

Yet, it is well known that chaotic motions of a conducting plasma can amplify seed fields resulting in chaotic magnetic fields under the restriction that the magnetic Reynolds number  $R_m = v_T l_T / \eta$  (where  $\eta$  is the resistive diffusivity of magnetic fields) exceeds a threshold value of about 100, i.e. that magnetic advection dominates over magnetic diffusion (e.g. Zeldovich et al., 1990; Brandenburg and Subramanian, 2005). Given the high conductivity of astrophysical plasmas, this constraint is usually fulfilled. The amplification of the magnetic field is a result of a random stretching of magnetic fields by the local velocity shear. This process is known as the fluctuating or turbulent dynamo<sup>4</sup>. The fluctuating dynamo can amplify magnetic fields exponentially, whereby the  $e$ -folding timescale of amplification is given by the turbulent correlation time scale  $\tau_{\text{cor}} = l_T / v_T \approx 10^7$  yr (e.g. Batchelor, 1950; Kazantsev, 1968). For Kolmogorov type turbulence, where  $v_T \sim l_T^{1/3}$ ,  $\tau_{\text{cor}} \sim l_T^{2/3}$ , and thus the  $e$ -folding time is shorter on small scales. Hence, smaller turbulent eddies amplify the magnetic field faster. Similarly to the mean-field dynamo, the amplification is limited to equipartition between the magnetic energy density  $e_{\text{mag}}$  and the energy density of the relevant turbulent motions  $e_{\text{turb}}$ . However, contrary to the mean-field dynamo, the coherence length of the fields generated by the fluctuating dynamo is limited by the characteristic scale of the turbulence.

The fluctuating small-scale dynamo is believed to operate in elliptical galaxies (section 1.3.2) and in the optical arms of spiral galaxies, where enhanced star formation drives turbulent motions. Within the latter, the fluctuating dynamo results in the strong but unordered magnetic fields giving rise high but unpolarized synchrotron emission (section 1.3.1). On the contrary, the ordered magnetic fields giving rise to the polarized radio emission in spiral as well as barred or irregular galaxies are believed to be the result of large-scale (mean-field or CR driven) dynamo action.

Summing up, the  $e$ -folding timescales of the different dynamo processes are as follows:

$$t_{\text{exp}}(\text{mean - field dynamo}) \approx 1.5 \cdot 10^8 \text{ yr}, \quad (1.50)$$

$$t_{\text{exp}}(\text{CR driven dynamo}) \approx 2.5 \cdot 10^8 \text{ yr}, \quad (1.51)$$

$$t_{\text{exp}}(\text{fluctuating dynamo}) \approx 10^7 \text{ yr}. \quad (1.52)$$

The time  $t$  needed to enhance a given seed magnetic field  $B_0$  to a final value  $B$  by a dynamo process is given by the relation

---

<sup>4</sup>There is sometimes confusion about the denotation of the different dynamo processes, as the mean-field as well as the fluctuating dynamo are both based on turbulent motions. Therefore, both processes are often referred to as “turbulent dynamo”. However, they are easily distinguished by the presence or absence of global rotation.

$$t = t_{\text{exp}} \ln(B/B_0), \quad (1.53)$$

thus, assuming an initial seed field of  $B_0 = 10^{-9}$  G (which is optimistic, see section 1.5.1), it takes  $\approx 1 - 2 \cdot 10^9$  yr for the mean-field and the CR driven dynamos (hereafter referred to as galactic dynamos) to reach a final field of  $B = 10^{-6}$  G, and  $\approx 7 \cdot 10^7$  yr for the fluctuating dynamo. Disk galaxies have formed at a redshift of  $\approx 2$ , i.e. about  $10^{10}$  yr ago. Thus, all dynamo processes would have had enough time to amplify the initial field to the value of several  $\mu\text{G}$  observed today, whereby the galactic dynamo has to be preferred because of its ability to generate magnetic fields with coherence scales of kpc and above. Hence, concerning present-day galaxies, the scenario seems satisfactory.

## 1.5 Open Questions

Although the concepts of galactic dynamos seem to be able to explain the strengths and structures of magnetic fields in present-day galaxies assuming a seed field of  $10^{-9}$  G or slightly less at a redshift of  $\approx 2$ , there are still many open questions challenging this scenario. First, where did the seed fields itself come from and how could they reach the strengths needed to explain present-day magnetic fields? Second, the evolution of galaxies is much more complex than the simple assumption of steadily rotating disk galaxies. Within the standard cold dark matter (CDM) structure formation models, galaxies evolve through a continuous merging and accretion of galactic subunits in the early universe ( $z \leq 2$ ), and experience subsequent major and minor mergers during their lifetimes. These processes drive enhanced star formation which in turn may drive galactic winds. Mergers can also disrupt the flat, rotating, galactic disks needed for dynamo action, and may result in a transformation of the progenitor galaxies to other galactic types, e.g. elliptical galaxies. Hence, what is the impact of galactic interactions and mergers on the evolution of the magnetic field? Finally, observations of  $\mu\text{G}$  magnetic fields at high redshifts suggest that there have to be other mechanisms apart from the galactic dynamo in order to explain these observations. This section summarizes the current efforts to meet these questions.

### 1.5.1 Seed fields

The induction equation 1.27 and the dynamo equation 1.41 give a finite magnetic field only if  $B(t = 0) \neq 0$ , that is, the dynamo processes presented in section 1.4 rely on the presence of a seed magnetic field before the onset of dynamo action. But how are these fields generated?

The most popular hypothesis of seed field generation is that magnetic fields are created by physical processes which exploit the different mobility of electrons and ions. This difference can lead to charge separation effects and a breakdown of the MHD approximation. In an ionized gas, electrons tend to be accelerated much more than the ions by a given pressure gradient. This leads in general to an electric field, which couples back positive and negative charges. If such a (thermally) generated electric field has a curl, then from Faraday's law of induction (Eq. 1.26), a magnetic field can grow. The resulting battery effect, known as the "Biermann battery", was first proposed as a mechanism for the thermal generation of stellar magnetic seed fields (Biermann, 1950).

A thermally generated electric field is given by  $E_{\text{Bier}} = -\nabla p_e / en_e$ , whereby it is assumed that the force on the electrons due to pressure gradients  $\nabla p_e$  is balanced by the electric field. The curl of this electric field yields an additional term in the induction equation (Eq. 1.27):

$$\frac{\partial \mathbf{B}}{\partial t} = \nabla \times ((\mathbf{v} \times \mathbf{B}) - \eta(\nabla \times \mathbf{B})) - \frac{c}{e} \nabla n_e \times \nabla p_e. \quad (1.54)$$

Thus, additionally to the convective and diffusion terms there is now a source term which is nonzero if the density and pressure gradients (or – in case of an ideal gas – equivalently the temperature gradient) are not parallel to each other. Interestingly, a very similar term is also the source of vorticity, meaning that battery effects are generally accompanied by rotational density perturbations and vice versa (see the reviews by Widrow, 2002; Kulsrud and Zweibel, 2008; Subramanian, 2008 and references therein for details). In the cosmological context, non-collinear density and pressure gradients can arise in a number of ways, particularly in gravitationally stratified and differentially rotating systems like stars and proto-galactic objects. However, the strength of the resulting magnetic fields in proto-galaxies is usually tiny, generally being less than  $10^{-21}$  G. The Biermann battery may also work in case of cosmic ionization fronts produced when the first UV sources (e.g. quasars) turn to ionize the IGM during the phase of reionization ( $6 < z < 20$ ). The temperature gradient produced by these ionization fronts is normal to the front, and non-collinear density gradients can arise if the front is sweeping across arbitrarily laid down density fluctuations, which will later collapse to form galaxies and clusters. Gnedin et al. (2000) showed that the magnetic fields created in this way may be somewhat larger ( $10^{-17} - 10^{-18}$  G). The Biermann battery has also been shown to generate both vorticity and magnetic fields in oblique cosmological shocks which arise during cosmological structure formation, resulting in  $10^{-21}$  G fields by  $z \approx 3$  (Kulsrud et al., 1997).

An alternative possibility for seed field generation was proposed by Harrison (1970), who suggested a pre-galactic battery mechanism operating before the recombination epoch ( $\approx 380\,000$  yr after the Big Bang,  $z \approx 1000$ ). At this time, photons of the background thermal radiation are strongly coupled to the electrons via Thomson scattering<sup>5</sup>, but weakly coupled to the ions. The electrons therefore tend to be dragged along by the photons. In a rotating, expanding plasma eddy, this will result in a difference of the angular velocities of the electron and ion gases, respectively. The different angular velocities in turn result in an electric current and thus a magnetic field. Harrison's mechanism, which would require non-zero vorticity in the primordial perturbation, could provide for a seed magnetic field of  $10^{-20}$  G. The most severe criticism of the model is that, prior to structure formation, vorticity would decay rapidly during the cosmic expansion (Rees, 1987). The implication is that vorticity in disk galaxies is not primordial but rather generated during structure formation.

A battery mechanism which is analogous to Harrison's scheme could have generated seed magnetic fields in the proto-galactic phase. After proto-galaxies have formed and matter has been re-ionized, a current could build up because Compton drag on the microwave background applies a torque tending to slow down the rotation of the electron gas, without there being a corresponding drag on the ions. For a proto-galaxy at redshift  $z \approx 5$ , this process may generate a field of order  $10^{-21}$  G (Rees, 2006). After the collapse of proto-galaxies, dynamo processes, which amplify magnetic fields exponentially, lead to a much more efficient magnetic field growth than any of the battery processes mentioned above. This is why battery processes can be neglected in discussions of the evolution of magnetic fields after the formation of the first galaxies.

Another mechanism by which the seed magnetization of proto-galaxies could be provided was proposed by Wiechen et al. (1998, 1999, 2000) and extended by Birk et al. (2002). According to their work, relative shear flows and collisional friction of the ionized and neutral fluid components in partially ionized self-gravitating and rotating proto-galactic clouds result in a self-magnetization of the clouds. Thereby, the gravitational potential of the collapsing cloud is the ultimate source of energy that is partly converted to magnetic fields and the associated electric currents by collisional momentum transfer in the partially ionized system. Their numerical investigations show that magnetic fields of the order of some  $10^{-14}$  G can be generated by this process in about  $7 \cdot 10^6$  yr.

Furthermore, interest in the exotic environment of the very early Universe, i.e. the inflation phase ( $< 10^{-30}$  s after the Big Bang), the electro-weak phase transition ( $10^{-12}$  s) and the QCD phase

---

<sup>5</sup>Elastic scattering of radiation by a free charged particle. Thomson scattering is the low-energy limit of Compton scattering and is valid as long as the photon energy (in the rest frame of the particle) is much less than the mass energy of the particle.

transition ( $10^{-5}$  s), has spawned numerous ideas for the creation of primordial magnetic fields during this epoch (see Widrow, 2002 and references therein). However, the exotic physics of the very early Universe make these ideas highly speculative. Also, the influence of the dense photon field before the recombination epoch leads to an efficient radiation dominated electric conductivity which is too fast to allow for any significant macroscopic magnetic field generated before this epoch (Lesch and Birk, 1998).

Another promising origin of magnetic seed fields are the very first stars which expel their field during SN explosions (Rees, 1987, 1994, 2006). The magnetic field of e.g. the Crab Nebula (a SN remnant and pulsar wind nebula) has a strength of  $10^{-4}$  G, pervading a volume of several cubic parsecs. It could have been built up during the lifetime of the precursor star (through e.g. Biermann and dynamo processes acting on the short dynamical timescales of stellar rotation) and then expelled via a wind spun off the remnant pulsar. Given that we expect a huge number ( $\approx 10^6$ ) of stars forming in a proto-galaxy, the mean field strength permeating the galaxy could be by orders of magnitude higher than that generated by the processes mentioned before. Rees (2006) estimates a strength of  $3 \cdot 10^{-8} - 3 \cdot 10^{-9}$  G for the large-scale component of the field in a proto-galactic disk of 10 kpc radius. However, as the magnetic fields expelled by the SN remnants should be randomly distributed, one might worry about cancelation effects of oppositely directed magnetic field lines (e.g. Kulsrud and Zweibel, 2008).

A further scenario is the production of galactic and extragalactic magnetic fields in active galactic nuclei (AGN, see Widrow, 2002 and references therein). AGN are powered by the release of gravitational potential energy as material accretes onto a central compact object, e.g. a supermassive black hole. There, battery and dynamo processes can generate and amplify magnetic seed fields on very short timescales (the dynamical timescale in the nucleus itself may be as short as a few hours). Finally, collimated jets can transport these magnetic fields into the proto-galactic or intergalactic medium. Some of the highest-redshift ( $z \approx 5$ ) radio galaxies have radio lobes up to 50 kpc in size, containing ordered fields of  $10^{-5}$  G. A galactic disk forming out of the medium contaminated with magnetic fields by a radio source lobe may thus acquire a large-scale seed magnetic field of  $\approx 10^{-9}$  G (Rees, 2006). However, radio galaxies are relatively thinly spread through the Universe, being far less common than disk galaxies.

In view of this multitude of different mechanisms proposed to explain the birth of cosmic magnetic fields it becomes apparent that we still do not know the true story. Yet, in any case, there seems to be little difficulty with producing an initial field of order  $10^{-20}$  G which can serve as a seed field for dynamo amplification. Such small seed fields, however, need to be amplified by more than 14 orders of magnitude to reach the observed present-day values. This challenging requirement suggests that we should explore all possibilities of magnetic field amplification during and after the phase of large-scale structure formation in the Universe.

### 1.5.2 Magnetic fields in different galactic objects and the intergalactic medium

The galactic dynamo process relies on the combination of differential rotation and helical motions in a stratified medium. It has also been shown numerically that the dynamo is much less efficient in dwarf and irregular galaxies which differential rotation is not strong enough to support dynamo action (Gressel et al., 2008). Hence, given seed magnetic fields as small as  $10^{-20}$  G, how did non (or only slowly) rotating objects like irregular and elliptical galaxies gain their  $\mu$ G magnetic fields (sections 1.3.1 and 1.3.2)?

Due to the high irregularity of the observed magnetic fields in elliptical galaxies, the fluctuating dynamo (section 1.4.5) seems to be a good candidate for the amplification of magnetic fields in these objects (section 1.3.2). However, it is commonly believed that elliptical galaxies form through the merging of smaller progenitor galaxies (e.g. Naab and Ostriker, 2009), presumably disk galaxies.

Thus, their magnetization may also be the result of the magnetization of the progenitor galaxies. Alternatively, the foregone interaction of the progenitor galaxies, or interactions between galaxy clusters themselves, might have driven the turbulence needed for the fluctuating dynamo to work efficiently. The latter idea is supported by the fact that diffuse radio emission is observed only in clusters which seem to have recently experienced significant merger activity enhancing the turbulence in these clusters (Venturi et al., 2008). Yet, these possibilities are only now beginning to be studied seriously with means of numerical investigations (Donnert et al., in preparation).

An even more difficult problem is the origin of magnetic fields observed in the intergalactic (IGM) and intracluster (ICM) medium, respectively. ICM fields are coherent on scales of several kpc and appear to be several  $\mu\text{G}$  in strength (section 1.3.2). But how did they get there? One idea is that magnetized gas stripped from the cluster galaxies has enriched the ICM with magnetic fields. However, the gas density of the ICM is 2-3 orders of magnitude lower than the mean density in galaxies. Hence, also the magnetic field should be lower unless it is further amplified by a dynamo process. The large spatial scale of a cluster and the lack of global rotation make the operation of an  $\alpha\Omega$ -type dynamo problematic. However, a turbulent dynamo could account for the amplification of the magnetic field. Donnert et al. (2009) has presented cosmological MHD simulations which suggest that turbulent amplification of magnetic seed fields during the build-up of the cluster - i.e. during the phase of structure formation - could in fact account for the observed magnetic fields today. The seed fields thereby originate from star-burst driven, galactic outflows. A further possible explanation of the ICM fields might be the contamination of intergalactic space with magnetic fields by radio lobes from AGN (e.g. Kronberg et al., 2001).

A similar situation arises for the wider IGM which is not part of a galaxy cluster. Extracuster fields have been detected by Kim et al. (1989) in the region between the Coma cluster and the cluster Abell 1367. They found a “bridge” in radio emission between the two clusters, and estimated the strength of the corresponding equipartition magnetic field to  $0.2 - 0.6 \mu\text{G}$ . Similar to the ICM, the extracuster IGM might have been magnetized by AGN activity, or, elsewise, by turbulent amplification during structure formation. Also, using numerical simulations, Dubois and Teyssier (2010) have shown that winds from dwarf galaxies may explain the enrichment of the IGM. After a galactic dynamo has amplified the magnetic field within young dwarf galaxies, SN feedback may launch strong winds, thus expelling magnetic fields into the IGM. Given the large number of dwarf galaxies in the early Universe, the overall magnetization of the IGM due to dwarf galaxies might be significant (Kronberg et al., 1999).

Although all of the proposed explanations may qualify, to me, the most persuasive of them is a magnetic field amplification accompanying the structure formation in the Universe. During the collapse of large as well as smaller structures, and during mutual interactions and merger events of these structures, large amounts of gravitational energy are released. Thus, it is natural to assume that at least parts of these energy are converted into magnetic energy, either directly by the compression of a given seed field, or, indirectly, by inducing turbulence and thus turbulent magnetic field amplification, or both (e.g. Ryu et al., 2008).

### 1.5.3 Magnetic fields in the early Universe

The idea of magnetic field amplification during the phase of structure formation ( $z > 20$ ) is supported by the observations of significant magnetic fields at high redshifts (section 1.3.3). It takes  $\approx 6 \cdot 10^9$  yr for an efficient galactic dynamo to amplify a seed field of  $10^{-20}$  G to the observed  $\mu\text{G}$  level. Hence, such a seed field is enough to explain  $\mu\text{G}$  magnetic fields up to a redshift of  $\approx 1$ . Yet,  $\mu\text{G}$  and even stronger fields have been observed in high redshift objects up to a redshift of 2, when the Universe was only few  $10^9$  yr old. Thus, even if these objects were disk galaxies allowing for efficient dynamo action (which are believed to have formed only at  $z \approx 2$ ), the magnetic fields would not have had enough time to grow to the observed level. Then, what made the magnetic fields in the early Universe grow so fast?

Lesch and Chiba (1995) put the battery mechanisms (section 1.5.1) into a proto-galactic scenario. They showed analytically that very weak magnetic fields of  $10^{-19} - 10^{-23}$  G created in an expanding overdense region can be enhanced by a factor of  $\approx 10^4$  as the proto-galaxy collapses. The field strengths in the fully formed disk galaxies can thus reach values of  $\approx 10^{-17}$  G, and subsequent amplification by strong non-axisymmetric flows may yield a field of  $\mu\text{G}$  strength at a redshift of  $\approx 2$ . This calculation already showed the importance of structure formation for the evolution of the magnetic field (see also Lesch and Chiba, 1997).

Within the framework of standard CDM hierarchical clustering models, structures grow hierarchically through gravitational instabilities (Blumenthal et al., 1984; White and Rees, 1978; White and Frenk, 1991; Padmanabhan, 1993; Benson, 2010). Thus, the formation of galaxies is characterized by more or less intense merging of smaller galactic subunits. This scenario has been confirmed by dark matter (DM) only numerical simulations (Davis et al., 1985; Springel et al., 2005c), which results compare excellently with measurements delivered by galaxy surveys, e.g. the Sloan Digital Sky Survey (SDSS). Particularly, DLAS, the probable progenitors of present-day galaxies (section 1.3.3), may be formed through the assembling of numerous self-gravitating rotating gas clumps or galactic subunits (Rauch et al., 1997; Haehnelt et al., 1998).

The gravitational energy released during the collapse and interactions of the forming substructures is converted into thermal energy of hot gas (e.g. Nath and Silk, 2001), kinetic energy of high energy particles (Loeb and Waxman, 2000) and/or turbulent energy. However, some of this energy is expected to be converted into magnetic field energy by field line compression and turbulent magnetic field amplification (Ryu et al., 2008). Even if the fraction of the released gravitational energy converted into magnetic energy may be small, the resulting magnetic field could be significant. In a first simple approach, one could imagine a scenario where small magnetic seed fields are efficiently amplified by the fluctuating dynamo within the highly turbulent proto-galactic clouds, whereby they may reach  $\mu\text{G}$  levels already at redshifts  $> 2$ . Then, the galactic dynamo may restructure, maintain or further amplify galactic magnetic fields until the present day. Such a scenario was first proposed by Beck et al. (1994) and recently revised by Arshakian et al. (2009). However, their scenario is based on only rough theoretical estimates of the involved amplification timescales and, particularly, the influence of mergers and interactions during the phase of structure formation is only included as an estimate of the thereby induced turbulence.

In summary, today there is no doubt that the standard mean-field dynamo is not sufficient to explain the observed magnetization of the Universe, although its importance for the evolution of the ordered magnetic fields in spiral galaxies remains valid. Therefore, alternative scenarios for the magnetization of the different structures in the local and distant Universe are being suggested (Rees, 2006; Kulsrud and Zweibel, 2008; Arshakian et al., 2009). Yet, it is not only for the sake of the magnetic field evolution itself why studies of the magnetization of the early Universe are interesting. Magnetic fields are crucial for the physics of cosmic ray production and propagation (section 1.4.4). The associated magnetic and CR pressures might help in driving galactic winds necessary to explain the observed relations between the central spheroids (bulges) and the disks of galaxies (Breitschwerdt et al., 1991, 1993). Also, star formation will proceed differently in the presence of magnetic fields (e.g. Price and Bate, 2007). A large scale magnetic field might even have an impact on the dynamics of cosmic baryon flows, the thermal and ionization history of the Universe, and the onset of structure formation (Sethi et al., 2008; Doumler and Knebe, 2010). For these reasons, it is definitely important to assess the history of magnetic fields in the Universe.

## 1.6 Aim of this thesis

The hierarchical build-up of structure in the Universe including the collapse of proto-galaxies and their mutual interaction is a highly nonlinear process. Therefore, it is accessible only through direct

numerical simulations (e.g. Springel et al., 2005a). This is even more true if hydrodynamics and particularly magnetohydrodynamics are included in the investigations. In order to capture the associated physics, much time has to be invested into the development of a numerical tool. Furthermore, the large dynamical range of the processes involved in structure formation requires a high resolution of those simulations, generally resulting in enormous computing times. Therefore, practically all of the codes have to be parallelized and optimized to reduce the CPU costs. Yet, thanks to some dedicative code developers and the growing computational power in the recent decades, particle-based ( $N$ -body) and grid-based hydrodynamic and even full MDH codes capable of simulating self-gravitating structures are now upcoming. The most noticeable among them are the particle-based codes GADGET (Springel, 2005; Dolag and Stasyszyn, 2009), VINE (Wetzstein et al., 2009; Nelson et al., 2009), PHANTOM (e.g. Price and Federrath, 2010) and GASOLINE (Wadsley et al., 2004), and the grid-based codes ATHENA (Stone et al., 2008), RAMSES (Teyssier, 2002; Teyssier et al., 2006), FLASH (Fryxell et al., 2000; Dubey et al., 2008) and PIERNIK (Hanasz et al., 2010a,b). However, their opportunities have not yet been fully taken advantage of.

Therefore, as a further step towards a more complete understanding of the magnetic field evolution in the Universe, the aim of this thesis was to perform and analyze for the first time fully self-consistent high-resolution 3D numerical simulations of the evolution of magnetic fields in isolated and particularly interacting galaxies. Such simulations require a high numerical resolution in order to capture the physics within the dense galactic centers and merger remnants. However, a high resolution in the dilute outer regions of the galaxies and the IGM would unnecessarily increase the CPU costs. Therefore, a method which is able of adapting the resolution according to the density should be preferred. This is provided by the  $N$ -body method combined with smoothed particle hydrodynamics (SPH, Monaghan, 1992; Price and Monaghan, 2004a,b,c, 2005; Monaghan, 2005) to treat MHD. Within the  $N$ -body/SPH method the (hydrodynamical) resolution is given by the so called smoothing length, which is given by the radius of a sphere defined to contain a certain number (or total mass) of particles. Hence, the denser the medium, i.e. the higher the number density of the simulated particles, the smaller the smoothing length and thus the higher the resolution. Therefore, all calculations presented in this thesis have been performed with the  $N$ -body/SPH method using the codes GADGET and VINE. These codes have been developed only few years ago at the Max Planck Institute for Astrophysics and the University Observatory in Munich, respectively, and are still continuously advanced. Thus, the simulations presented in this thesis are performed with two of the best state-of-the-art numerical tools.

Numerical simulations are able to follow the interplay between the magnetic field and the complex gas velocities arising during the galactic evolution in full 3D, without restrictions on the gas flow up to the resolution limit. This is a clear advantage over analytical calculations, which often rely on simplifying assumptions, e.g. an axial symmetry of the galactic disks. Using numerical tools, it is possible to study complex, non-axisymmetric and highly variable situations, which are crucial for the magnetic field evolution in the early and local Universe. The numerical investigations presented in this thesis cover the first detailed, self-consistent, galactic-scale simulations including magnetic fields ever attempted. They were published in three successive peer-reviewed articles.

The first article (Kotarba et al., 2009, section 2), was dedicated to the analysis of the simulated evolution of magnetic fields within an evolving Milky-Way like spiral galaxy using the codes VINE and GADGET. Thereby, particular emphasis was placed on the numerical stability of the implementations. The main drawback of the SPMHD (SPH including MHD) method is that the  $\nabla \cdot \mathbf{B} = 0$  constraint is numerically not fulfilled. The numerical divergence may lead to defective calculations of the evolution of the magnetic field, particularly to spurious magnetic field growth. Therefore, the standard SPH implementation of the induction equation was compared with an implementation using Euler potentials (Stern, 1970, 1976). Within the Euler potential description, the (physical) divergence is zero by definition, however, a numerical divergence arising from the SPH approximation still develops. The comparison of the standard and Euler implementations within the VINE code with equivalent imple-

mentations within the GADGET code revealed an upper limit of the numerical divergence up to which the simulations may be trusted. Furthermore, detailed investigations of these simulations allowed for conclusions about the evolution of magnetic fields due to the 3D, non-axisymmetric velocity field of an isolated galaxy with self-consistent spiral arm formation, i.e. the kinematic dynamo (section 1.4.2).

The subsequent articles (Kotarba et al., 2010a,b, sections 3 and 4, respectively), cover the first numerical studies of the evolution of magnetic fields within interacting spiral galaxies in the local Universe using the code GADGET. The main goal of these investigations was to assess the theoretically expected interaction-driven amplification of an initially small magnetic field and the impact of the violently disturbed velocity fields on the structure of the magnetic field. One of the best observed local pair of interacting galaxies are the Antennae galaxies, particularly, there exist detailed observations of the magnetic field within this system (Chyży and Beck, 2004). Therefore, in Kotarba et al., 2010a, simulations of the Antennae system together with synthetic radio maps are presented. The synthetic radio maps, calculated on basis of the simulated data, are compared with the observations. The key issue of these investigations is the analysis of the interdependent evolution of the magnetic field and the turbulence within the simulated system.

In Kotarba et al., 2010b, these investigations are continued on a more general setup of three colliding galaxies, extended by the inclusion of an ambient IGM. The main goal was a further analysis of the interaction-driven turbulence and magnetic field amplification. Furthermore, the inclusion of the IGM allows for the first numerical studies of its magnetization during a galactic interaction. Simultaneously, the influence of the initial magnetic field strength within the IGM and the progenitor galaxies on the propagation of interaction-driven shocks within the IGM is analyzed. Moreover, synthetic radio and RM maps reveal how the simulated system might have looked like when observed at different evolutionary stages, an insight not available observationally.

In the context of the questions raised by the observations of significant magnetic fields in different extragalactic objects and in the early Universe (sections 1.5.2 and 1.5.3), the investigations covered by this thesis gain particular importance. The studies of the interaction-driven magnetic field amplification within the galaxies and the IGM are a first step towards a deeper understanding of the evolution of magnetic fields in the course of structure formation in the Universe.



## Chapter 2

### Paper I: Magnetic field structure due to the global velocity field in spiral galaxies

H. Kotarba, H. Lesch, K. Dolag, T. Naab, P. H. Johansson & F. A. Stasyszyn, 2009, *Monthly Notices of the Royal Astronomical Society*, 397, 733-747

#### ABSTRACT

We present a set of global, self-consistent  $N$ -body/SPH simulations of the dynamic evolution of galactic discs with gas and including magnetic fields. We have implemented a description to follow the evolution of magnetic fields with the ideal induction equation in the SPH part of the VINE code. Results from a direct implementation of the field equations are compared to a representation by Euler potentials, which pose a  $\nabla \cdot \mathbf{B}$ -free description, a constraint not fulfilled for the direct implementation. All simulations are compared to an implementation of magnetic fields in the GADGET code which includes also cleaning methods for  $\nabla \cdot \mathbf{B}$ .

Starting with a homogeneous seed field we find that by differential rotation and spiral structure formation of the disc the field is amplified by one order of magnitude within five rotation periods of the disc. The amplification is stronger for higher numerical resolution. Moreover, we find a tight connection of the magnetic field structure to the density pattern of the galaxy in our simulations, with the magnetic field lines being aligned with the developing spiral pattern of the gas.

Our simulations clearly show the importance of non-axisymmetry for the evolution of the magnetic field.

**Key words:** methods:  $N$ -body simulations – galaxies: spiral – galaxies: evolution – galaxies: magnetic fields – galaxies: kinematics and dynamics

## 2.1 Introduction

Radio observations have revealed that disc galaxies are permeated by large scale magnetic fields ordered on kpc scales and beyond (Beck and Hoernes, 1996, Hummel and Beck, 1995, Beck et al., 1985). The typical field strength, determined from polarization, Faraday rotation and energy equipartition is of the order of  $10 \mu\text{G}$  (e.g. Beck, 2004). The spatial structure of the  $\mathbf{B}$ -field reflects the spiral and/or barred structure of the gas distribution within the galactic discs (Beck, 2009a). For example, Fig. 2.1 shows optical observations of the spiral galaxy M51 overlaid with contours of total synchrotron intensity (tracing the total magnetic field) and magnetic field vectors. It reveals the tight connection of magnetic field with the gas distribution in the galactic disc.

The motion of the gas within the gravitational potential of a galaxy strongly influences the strength and direction of the magnetic field in the interstellar medium. This can be seen by inspecting the well known induction equation of magnetohydrodynamics (MHD), i.e. the temporal evolution equation for the magnetic field,

$$\frac{\partial \mathbf{B}}{\partial t} = \nabla \times (\mathbf{v} \times \mathbf{B}) - (\nabla \times \eta (\nabla \times \mathbf{B})), \quad (2.1)$$

where  $\mathbf{v}$  denotes the gas velocity and  $\eta$  represents the magnetic diffusivity which is inversely proportional to the electrical conductivity.

Apparently, within the frame of MHD, the role of the galaxy as a whole is simply to provide for the gas velocity field. Since the conductivity of the interstellar medium is very high, the magnetic field is closely coupled to the gas motion. It is this ‘frozen-in’-property of both, the magnetic field and the gas, which determines the spatial structure of the magnetic field. In other words, a detailed investigation of the velocity field of the interstellar gas in disc galaxies is necessary for a deeper physical understanding of the evolution of galactic magnetic fields.

The gas in the disc rotates differentially within the global gravitational potential. Angular momentum transport via spiral arms, bars and gravitational interaction forces the gas to move towards the central regions, and eventually, star formation activity in the disc (superbubbles, winds etc.) drives gas perpendicular to the plane of the disc towards the galactic halo. In general, the axisymmetric rotation velocity is the dominant component, followed by non-axisymmetric and radial components. The velocity components perpendicular to the disc are typically the smallest. Altogether,  $\mathbf{v}$  in Eq. 2.1 represents a complex three-dimensional non-axisymmetric velocity field strongly coupled to the global properties of the galaxy, including the dark matter halo, stellar component and internal disc activity.

Beside the large scale components of the gas velocity field there are also small scale velocity fluctuations of interstellar gas driven by all kinds of local disc activity, i.e. stellar winds, supernova explosions, cloud-cloud collisions, galactic winds, etc (see e.g. Ferriere, 1992a, Efstathiou, 2000, Johansson and Efstathiou, 2006, Kulsrud and Zweibel, 2008, Gressel et al., 2008). These unordered velocity components generate two effects which are known as helicity (in terms of a convective turbulent motion perpendicular to the disc) and turbulent diffusion (magnetic field lines with antiparallel direction reconnect and annihilate partially). Helicity supports the amplification of the magnetic field, whereas turbulent diffusion reduces the field strength (see, e.g. Brandenburg and Subramanian, 2005 for a review of nonlinear dynamo theory). Therefore, an incorporation of these small scale velocity components into the analysis requires some manipulation of the induction equation (Eq. 2.1) in terms of a mean-field theory (Steenbeck and Krause, 1969, Wielebinski and Krause, 1993, Sur et al., 2007). Within the frame of the mean-field description the velocity and magnetic fields are considered as superpositions of the mean and fluctuating parts ( $\mathbf{v} = \langle \mathbf{v} \rangle + \mathbf{v}'$  and  $\mathbf{B} = \langle \mathbf{B} \rangle + \mathbf{B}'$ ). The fluctuating velocity components are coupled to small-scale fluctuations of the magnetic field. The coupling terms are then given by  $\nabla \times \alpha \langle \mathbf{B} \rangle$ , where  $\alpha = \frac{1}{3} \tau \langle \mathbf{v}' \cdot (\nabla \times \mathbf{v}') \rangle$  (Zeldovich et al., 1983), and by  $\eta_T \Delta \langle \mathbf{B} \rangle$ ,

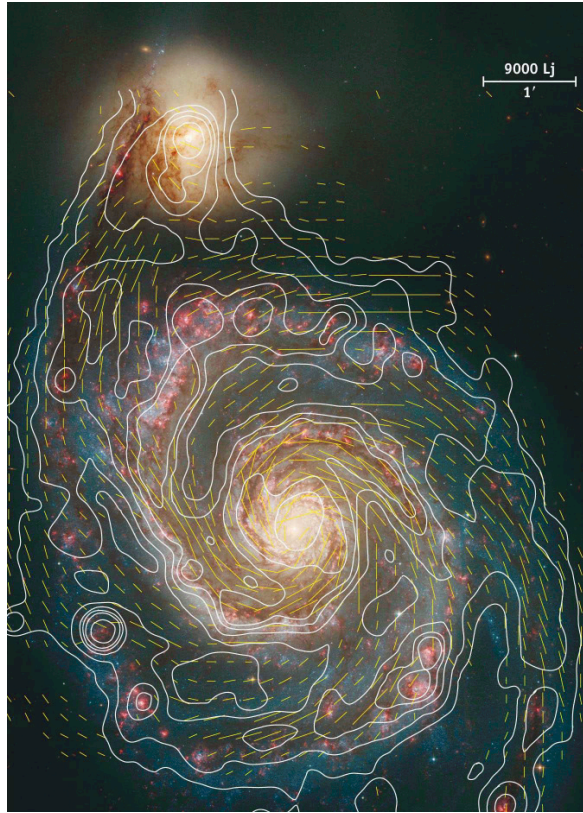


Figure 2.1: Optical image of M51 (Hubble) overlaid with contours of total synchrotron intensity as measure for the total magnetic field (combined observations at Effelsberg and VLA at 6 cm) and vectors of magnetic field. From A. Fletcher & R. Beck (MPIfR) and Hubble Heritage Team (STScI), published by 'Sterne und Weltraum', September 2006.

where  $\eta_T$  now describes the turbulent diffusion coefficient  $\eta_T \propto v_{\text{turb}} \cdot l_{\text{turb}}$ , where  $v_{\text{turb}}$  and  $l_{\text{turb}}$  are the typical velocity and length scale of the turbulent motion, respectively.

This leads to the dynamo equation

$$\frac{\partial \mathbf{B}}{\partial t} = \nabla \times (\mathbf{v} \times \mathbf{B}) + \nabla \times \alpha \mathbf{B}, \quad (2.2)$$

where we have neglected the diffusivity and dropped the mean-brackets for convenience (here, and in the following,  $\mathbf{B}$  and  $\mathbf{v}$  refer to their mean values).

Eq. 2.2 is the central equation of cosmic mean field dynamos. It describes the circle of amplification of the different components. The classical dynamo model describes the amplification of the magnetic field through the following chain of  $\alpha$  (convective turbulence) and  $\Omega$  (differential rotation) actions: The radial component  $B_r$  is amplified through  $\alpha$ -action from turbulence; then  $B_\varphi$  is generated from  $B_r$  through  $\Omega$ -action from the shear of the galactic differential rotation. Such an  $\alpha\Omega$  mean field dynamo amplifies the magnetic field by repeating the chain of  $\alpha$  and  $\Omega$  actions (see Widrow, 2002 and Stefani et al., 2008 for a review of dynamo theory). However, the origin of the  $\alpha$ -effect is still under discussion (Cattaneo and Vainshtein, 1991, Vainshtein and Cattaneo, 1992, Kulsrud and Anderson, 1992).

We emphasize that the described classical dynamo models use only one velocity component, the differential rotation. To be more precise the role of any deviation from axisymmetry is considered to

be unimportant for the evolution of the large-scale magnetic field, which is not necessarily true in real galaxies.

On this account, there have been three-dimensional numerical simulations using an analytical turbulent velocity field, where deviations from axisymmetry were incorporated in the gas- and turbulence-profiles (Rohde et al., 1997, Rohde and Elstner, 1998). These studies showed, that even accounting for the  $\alpha$ -effect calculated out of the analytical velocity field an initial magnetic field cannot survive for more than 500 Myr.

Moreover, Elstner et al., 2000 performed  $N$ -body simulations of two component (collisionless stars and gaseous clouds moving in the gravitational potential of the stellar population), self-gravitating discs embedded in an analytical bulge- and halo-potential. These simulated clouds provided an already very good approximation of the gas velocity field. However, full hydrodynamics was not incorporated. The obtained velocity field was used in an  $\alpha\Omega$ -dynamo description. Without including the  $\alpha$ -effect, the non-azimuthal 3D gas flow alone did not provide an amplification of the magnetic field. The field got amplified by several orders of magnitude within 0.7 Myr only when the  $\alpha$ -effect was included. In addition, they found an alignment of the magnetic field with the developed spiral pattern of the disc.

Recently, Dobbs and Price (2008) performed three dimensional, full MHD, single and two-component (cold and hot gas) simulations using smooth particle hydrodynamic (SPH) methods to treat MHD. They applied a spiral potential to the gas, thus, the self-induced formation of spiral structure was not included. Their work concentrated on structure formation in the disc, like molecular clouds and inter-arm spurs. They found that the main effect of adding a magnetic field to these calculations was to inhibit the formation of structure in the disc. They did not consider global enhancement and structure formation of the magnetic field, but nevertheless, they found that the global magnetic field was following the large scale velocity field.

It is the aim of this paper to present further steps towards a more complete dynamo model. We perform for the first time a set of self-consistent  $N$ -body calculations of a spiral galaxy including hydrodynamics as well as the induction equation via the SPH method to obtain the complex three dimensional velocity field. Compared to all previous work, we use no analytical potential for any component of the galaxy. All components (disc, gas, bulge and halo) are represented by particles which are treated as self-gravitating  $N$ -body-particles, while hydrodynamics is applied to the gas component only. We use more than one order of magnitude more particles than Elstner et al. (2000). We follow the evolution of the magnetic field according to the induction equation (eq. 2.1). Thus, we have implemented the SPH variant of the induction equation as well as the representation of the magnetic fields by Euler potentials in the SPH code VINE and compare the results with simulations performed using the SPH code GADGET.  $N$ -body/SPH methods are well adapted for simulating whole galactic discs as the simulated discs stay stable for at least 15 dynamical times (where we define the dynamical time for a disc galaxy as its half mass rotation period). As we will show in section 2.4, our discs are forming spiral structure without applying a spiral potential or any other mechanism to provide extraordinary flows.

In summary, we investigate here the kinematic reaction of a large-scale magnetic field on the complete three-dimensional, large-scale velocity field of a disc galaxy obtained from the  $N$ -body SPH simulations, using two different numerical codes.

The paper is organized as follows: Section 2.2 gives shortly the theory of magnetic field evolution in differentially rotating systems. A summary of the SPH method and the treatment of magnetic fields including the method based on Euler potentials is given in section 2.3. The simulations together with a comparison of the performance of the VINE and GADGET codes are presented in section 2.4. The results are discussed in section 2.5, where we also analyse the terms of the induction equation in detail. Finally, we summarise and conclude in section 2.6.

## 2.2 Theoretical Expectations

When only studying the effect of the gas velocity on the evolution of the magnetic field, we can neglect the diffusive term in eq. 2.1. Keeping this term, one would physically expect the magnetic field to dissipate depending on the value of  $\eta$  and reconnect when converse magnetic field lines come together. Technically,  $\eta$  is not always assumed to be spatially dependent, so that the diffusive term reads  $-\eta\nabla^2\mathbf{B}$ . However, this formulation leads only to an effective smoothing, and not a real diffusion of the magnetic field. Neglecting the diffusive term thus corresponds to considering an upper limit of field amplification. Additionally,  $\eta$  is assumed to be small except within strong shocks.

The induction equation 2.1 then yields

$$\frac{\partial\mathbf{B}}{\partial t} = (\mathbf{B}\cdot\nabla)\mathbf{v} + \underbrace{\mathbf{v}(\nabla\cdot\mathbf{B})}_{=0} - \mathbf{B}(\nabla\cdot\mathbf{v}) - (\mathbf{v}\cdot\nabla)\mathbf{B}, \quad (2.3)$$

and applying cylindrical coordinates eq. 2.3 reads:

$$\begin{aligned} \frac{\partial B_r}{\partial t} = & -B_r\frac{v_r}{r} - \frac{1}{r}B_r\frac{\partial v_\varphi}{\partial\varphi} - B_r\frac{\partial v_z}{\partial z} + \frac{1}{r}B_\varphi\frac{\partial v_r}{\partial\varphi} \\ & + B_z\frac{\partial v_r}{\partial z} - v_r\frac{\partial B_r}{\partial r} - \frac{v_\varphi}{r}\frac{\partial B_r}{\partial\varphi} - v_z\frac{\partial B_r}{\partial z}, \end{aligned} \quad (2.4)$$

$$\begin{aligned} \frac{\partial B_\varphi}{\partial t} = & -B_\varphi\frac{\partial v_r}{\partial r} - B_\varphi\frac{\partial v_z}{\partial z} + B_r\frac{\partial v_\varphi}{\partial r} + B_z\frac{\partial v_\varphi}{\partial z} \\ & - v_r\frac{\partial B_\varphi}{\partial r} - \frac{v_\varphi}{r}\frac{\partial B_\varphi}{\partial\varphi} - v_z\frac{\partial B_\varphi}{\partial z} - \frac{v_\varphi B_r}{r}, \end{aligned} \quad (2.5)$$

$$\begin{aligned} \frac{\partial B_z}{\partial t} = & -B_z\frac{v_r}{r} - B_z\frac{\partial v_r}{\partial r} - \frac{1}{r}B_z\frac{\partial v_\varphi}{\partial\varphi} + B_r\frac{\partial v_z}{\partial r} \\ & + \frac{1}{r}B_\varphi\frac{\partial v_z}{\partial\varphi} - v_r\frac{\partial B_z}{\partial r} - \frac{v_\varphi}{r}\frac{\partial B_z}{\partial\varphi} - v_z\frac{\partial B_z}{\partial z}. \end{aligned} \quad (2.6)$$

These equations can be simplified to get a first idea of how magnetic fields will evolve in a galactic disc. For a differentially rotating disc ( $\partial v_\varphi/\partial r \approx 0$ ) with a perfectly axisymmetric velocity field,  $\mathbf{v}$  does not depend on  $\varphi$ . The same holds for an axisymmetric magnetic field. If we also assume that changes of all quantities in the  $z$  direction are small compared with those in the radial direction and  $B_z \simeq 0$ , the equations for the regular field, i.e. the field in the plane of the disc, read:

$$\frac{\partial B_r}{\partial t} = -B_r\frac{v_r}{r}, \quad (2.7)$$

$$\frac{\partial B_\varphi}{\partial t} = -B_\varphi\frac{\partial v_r}{\partial r} - \frac{v_\varphi B_r}{r} = -B_\varphi\frac{\partial v_r}{\partial r} + B_r r \frac{\partial\Omega}{\partial r}, \quad (2.8)$$

where  $\Omega$  is the angular velocity.

In the absence of radial flows, the last term of eq. 2.8 describes the generation of a toroidal magnetic field from the radial component of the already present magnetic field by differential rotation. This effect is the so called  $\Omega$ -effect already mentioned above. Since  $v_\varphi \gg (v_r, v_z)$  this term is dominant and one would expect any initial magnetic field to be first wound up by differential rotation. However, this effect alone cannot be responsible for a significant amplification of the magnetic field, as the amplification stops when all of the radial field is wound up. However, if a gas flow in the negative radial direction (i.e. towards the centre of the disc) is present the radial field can be amplified and then be converted into a toroidal field. These radial gas flows occur when angular momentum is transported in the gas out of the disc, e.g. by spiral arms or bars. The toroidal magnetic field can be amplified further if the radial gas flow velocity decreases with increasing galactocentric radius.

Therefore, a good understanding of the evolution of magnetic fields in galactic discs requires full information of the three-dimensional velocity field of the gas which is naturally provided by self-consistent numerical simulations. We will discuss the velocity field in our simulations and the resulting values of the different terms of the induction equation in section 2.5.

## 2.3 Numerical methods

### 2.3.1 Vine

The equations presented below are implemented within the OpenMP parallel  $N$ -body/SPH evolution code VINE. For all details we refer the reader to Wetzstein et al. (2009) and Nelson et al. (2009).

#### 2.3.1.1 SPH basics

Within the SPH formulation a hydrodynamic quantity  $A$  is interpolated by a kernel function  $W(\mathbf{r} - \mathbf{r}', h)$  with  $\int W d\mathbf{r} = 1$  and  $\lim_{h \rightarrow 0} W = \delta(\mathbf{r} - \mathbf{r}')$ , where the so called smoothing length  $h$  defines the spatial extent of the function  $W$ . This interpolation is then discretised, so that

$$A_i = \sum_j m_j \frac{A_j}{\rho_j} W(\mathbf{r}_i - \mathbf{r}_j, h), \quad (2.9)$$

where  $i$  ( $j$ ) is the index of the particle at position  $\mathbf{r}_i$  ( $\mathbf{r}_j$ ) and  $A_i$  ( $A_j$ ) the value of the quantity  $A$  at the position of particle  $i$  ( $j$ ).  $\rho_j$  and  $m_j$  denote the density and mass at position of particle  $j$ , respectively.

The VINE code uses the common W4 kernel defined by Monaghan and Lattanzio (1985) as

$$W_{ij} = W(\mathbf{r}_{ij}, h) = \frac{\sigma}{\bar{h}_{ij}^\nu} \begin{cases} 1 - \frac{3}{2}\varrho^2 + \frac{3}{4}\varrho^3 & 0 \leq \varrho < 1 \\ \frac{1}{4}(2 - \varrho)^3 & 1 \leq \varrho < 2 \\ 0 & \text{else} \end{cases}, \quad (2.10)$$

where values with index  $ij$  denote differences (e.g.  $\mathbf{r}_{ij} = \mathbf{r}_i - \mathbf{r}_j$ ) and arithmetic means (e.g.  $\bar{h}_{ij} = 0.5 \cdot (h_i + h_j)$ ), respectively,  $\varrho = |\mathbf{r} - \mathbf{r}'|/h$ ,  $\nu$  is the number of spatial dimensions of the system and  $\sigma$  is a constant of order unity. See Monaghan (1992), Monaghan (2001) or Price (2005) for more details.

#### 2.3.1.2 Continuity equation

As long as the kernel itself is differentiable, every function  $A$  can be interpolated to a differentiable function by the procedure described above. The most common formulation of derivatives in SPH is (see e.g. Monaghan, 1992, Price, 2005)

$$(\nabla A)_i = \frac{1}{\rho_i} \sum_j m_j (A_j - A_i) \nabla_i W_{ij}. \quad (2.11)$$

Using the continuity equation, the total time derivative of the density thus reads

$$\frac{d\rho_i}{dt} = -\rho_i (\nabla \cdot \mathbf{v})_i = \sum_j m_j (\mathbf{v}_i - \mathbf{v}_j) \cdot \nabla_i W_{ij}. \quad (2.12)$$

### 2.3.1.3 Momentum and Energy equation

A natural ansatz to derive a conservative form of the momentum equation comprising the force due to pressure gradients (in addition to the force due to the gravitational potential) is to use the Lagrange formalism together with the first law of thermodynamics. This leads to the following SPH variant of its ideal form ( $\frac{d\mathbf{v}}{dt} = -\frac{\nabla P}{\rho}$ ):

$$\frac{d\mathbf{v}_i}{dt} = -\frac{\nabla P_i}{\rho_i} = -\sum_j m_j \left( \frac{P_i}{\rho_i^2} + \frac{P_j}{\rho_j^2} \right) \nabla_i W_{ij}. \quad (2.13)$$

In this formulation momentum is conserved exactly, since the contribution of particle  $j$  to the momentum of particle  $i$  is equal and negative to the contribution of particle  $i$  to the momentum of particle  $j$ .

The change in the thermodynamical state of the gas requires an evolution equation for a state variable corresponding to the internal energy or entropy of the gas. VINE employs an equation for the specific internal energy ( $u$ ) of the gas. Without external heating or cooling terms, only compressional heating and cooling are important and the SPH variant of the ideal form ( $\frac{du}{dt} = -\frac{P}{\rho} \nabla \cdot \mathbf{v}$ ) reads:

$$\frac{du_i}{dt} = \frac{P_i}{\rho_i^2} \sum_j m_j \mathbf{v}_{ij} \cdot \nabla_i W_{ij}. \quad (2.14)$$

To close the set of equations, an isothermal equation of state is used throughout this paper.

### 2.3.1.4 Artificial viscosity

Artificial viscosity is required to model shocks and angular momentum transport properly, where the latter is important to be able to simulate spiral arm formation. The VINE code uses the most common form of the artificial viscosity. It is described by the tensor  $\mathbf{\Pi}_{ij}$  as in Monaghan (1992).

Since the value of  $\mathbf{\Pi}_{ij}$  depends on the difference in velocity between the considered particles (i.e. the velocity gradient) the viscosity increases with increasing velocity gradient. Moreover, the viscosity is only applied if particles are approaching each other.

Balsara (1995) suggested a viscosity limiter to avoid spurious angular momentum and vorticity transport in gas disks. However, a lower viscosity leads to a higher velocity dispersion of the gas and therefore to higher divergence of the velocity and magnetic field. As will be shown and discussed in section 2.5, this higher divergence causes a more violent magnetic field amplification.

The viscous terms within the momentum and energy equations read:

$$\left( \frac{d\mathbf{v}_i}{dt} \right)_{diss} = -\sum_j m_j \mathbf{\Pi}_{ij} \nabla_i W_{ij} \quad (2.15)$$

$$\left( \frac{du_i}{dt} \right)_{diss} = \frac{1}{2} \sum_j m_j \mathbf{\Pi}_{ij} \mathbf{v}_{ij} \cdot \nabla_i W_{ij} \quad (2.16)$$

This treatment of viscous forces allows for a sensible description of the behaviour of gas in a spiral galaxy. However, eqs. 2.14 and 2.16 are not applied when using isothermal equation of state.

### 2.3.1.5 Induction equation

In order to follow the evolution of the magnetic field we have additionally implemented equation 2.3 discretised as

$$\begin{aligned} \frac{dB_i^\mu}{dt} &= \frac{1}{\rho_i} \sum_j m_j [ \underbrace{B_i^\mu (\mathbf{v}_{ij} \cdot \nabla_i W_{ij})}_{\hat{=} -\mathbf{B}(\nabla \cdot \mathbf{v})} - \underbrace{v_{ij}^\mu (\mathbf{B}_i \cdot \nabla_i W_{ij})}_{\hat{=} (\mathbf{B} \cdot \nabla) \mathbf{v}} ] \\ &= \frac{1}{\rho_i} \sum_j m_j (B_i^\mu \mathbf{v}_{ij} - v_{ij}^\mu \mathbf{B}_i) \nabla_i W_{ij}. \end{aligned} \quad (2.17)$$

with  $\mu, \nu$  denoting the spatial directions.

### 2.3.1.6 Euler potentials

A well known problem related to magnetic fields within SPH is the maintenance of  $\nabla \cdot \mathbf{B} = 0$  throughout the simulation. Different attempts to solve this problem have been made (see Price and Monaghan, 2005), examples include source term approaches (Powell et al., 1999) and projection methods.

Theoretically, the problem can be avoided if the magnetic field is represented by Euler potentials (Stern, 1970, Price and Bate, 2007, Rosswog and Price, 2007), an approach we have also implemented into the VINE code.

The magnetic field is expressed as a function of two scalar potentials  $\alpha_E$  and  $\beta_E$  as:

$$\mathbf{B} = \nabla \alpha_E \times \nabla \beta_E. \quad (2.18)$$

Taking the divergence of  $\mathbf{B}$  we get:

$$\begin{aligned} \nabla \cdot \mathbf{B} &= \nabla \cdot (\nabla \alpha_E \times \nabla \beta_E) \\ &= \underbrace{\nabla \beta_E (\nabla \times \nabla \alpha_E)}_{=0} - \underbrace{\nabla \alpha_E (\nabla \times \nabla \beta_E)}_{=0} = 0. \end{aligned} \quad (2.19)$$

Thus, the divergence constraint is fulfilled by construction.

Moreover, for the ideal case ( $\eta = 0$ ) the Euler potentials for each particle (i.e. the convective values of the potentials) are direct tracers of the magnetic field and stay constant with time,

$$\frac{d\alpha_E}{dt} = 0, \quad (2.20)$$

$$\frac{d\beta_E}{dt} = 0, \quad (2.21)$$

thus one does not need to perform an additional integration when following magnetic fields, leading to a higher accuracy of the calculation. The variation of magnetic field is only due to the motion of the particles, which corresponds to the advection of magnetic field lines by Lagrangian particles (frozen flow) (Stern, 1970).

Moreover, the formulation by Euler potentials guarantees conservation of magnetic helicity,

$$H = \int_V \mathbf{A} \cdot \mathbf{B} d^3 \mathbf{x}, \quad (2.22)$$

which is again reasonable for ideal treatment. Actually, the magnetic helicity is zero, since for  $\mathbf{A} = \alpha_E \nabla \beta_E$  and equivalently  $\mathbf{A} = -\beta_E \nabla \alpha_E$ , respectively,  $\mathbf{B} = \nabla \alpha_E \times \nabla \beta_E = \nabla \times \mathbf{A}$  and therefore  $\mathbf{A} \cdot \mathbf{B} = 0$ .

The gradients of  $\alpha_E$  and  $\beta_E$  can be expressed as

$$\chi_i^{\mu\nu}(\nabla\alpha_E)_i^\mu = -\sum_j m_j(\alpha_{E,i} - \alpha_{E,j})(\nabla_i W_{ij}(h_i))^\nu, \quad (2.23)$$

$$\chi_i^{\mu\nu}(\nabla\beta_E)_i^\mu = -\sum_j m_j(\beta_{E,i} - \beta_{E,j})(\nabla_i W_{ij}(h_i))^\nu, \quad (2.24)$$

where

$$\chi_i^{\mu\nu} = \sum_j m_j(\mathbf{r}_j - \mathbf{r}_i)^\mu(\nabla_i W_{ij}(h_i))^\nu, \quad (2.25)$$

which is exact for linear functions (Price and Bate, 2007), i.e. for initial conditions with an uniform field. However, the difference in using this exact-linear interpolation compared to the usual gradient operator is marginal (D. Price, private communication).

Unfortunately, not all magnetic field configurations can be expressed in terms of Euler potentials easily as they enter eq. 2.18 in a nonlinear way, and they are not unique for certain field configurations (Stern, 1970, Yahalom and Lynden-Bell, 2006). The former problem restricts only the choice of the initial magnetic field, whereas the latter can be crucial. If there are field configurations which can be expressed by different sets of Euler potentials, then this implies, that some other field configurations cannot be expressed at all using Euler potentials. However, since the fields considered in this work are topologically ‘simple’, we do not expect to encounter these problems.

Furthermore, Euler potentials do not allow to follow the winding of magnetic fields beyond a certain point. This constraint is due to the fact that using the Euler potentials, the magnetic field is essentially mapped on the initial particle arrangement. If the initial arrangement evolves too much during the simulation, particles carrying conflicting values of Euler potentials (i.e. values, which do no longer allow for a finite and unambiguous calculation of their gradients) can come close. Then, the ability of the Euler potentials to represent the magnetic field correctly is lost. This conflict is expected to occur when the magnetic field is wound up more than once, which poses a problem especially towards the central region of a simulated galaxy.

### 2.3.1.7 Timestepping

In VINE, there are basically three different time step criteria, based on changes in the acceleration of a particle,

$$\Delta t_a^{n+1} = \tau_{\text{acc}} \sqrt{\frac{\epsilon}{|\mathbf{a}|}}, \quad (2.26)$$

its velocity,

$$\Delta t_v^{n+1} = \tau_{\text{acc}} \frac{\epsilon}{|\mathbf{v}|}, \quad (2.27)$$

or both in combination,

$$\Delta t_{va}^{n+1} = \tau_{\text{acc}} \frac{|\mathbf{v}|}{|\mathbf{a}|}, \quad (2.28)$$

where  $\epsilon$ ,  $\mathbf{a}$  and  $\mathbf{v}$  are the gravitational softening length, the acceleration and velocity of a particle in the previous time step ( $n$ ), respectively, and  $\tau_{\text{acc}}$  is an accuracy parameter.

Two additional time step criteria are applied in SPH simulations: First, the Courant-Friedrichs-Lewy criterion as suggested by Monaghan (1989),

$$\Delta t_{\text{CFL}}^{n+1} = \tau_{\text{CFL}} \frac{h_i}{c_s + 1.2(\alpha_i c_s + \beta_i h_i \max_j \mu_{ij})}, \quad (2.29)$$

where  $\alpha_i$  and  $\beta_i$  are artificial viscosity parameters,  $c_s$  is the sound speed,  $h_i$  the SPH softening length for gas particle  $i$ , and  $\mu_{ij}$  corresponds to the velocity divergence between particles  $i$  and  $j$  with the maximum taken over all neighboring particles  $j$  of particle  $i$  (see Wetzstein et al., 2009 for more details). Secondly, there is a limit on how much the SPH softening lengths are allowed to change during one timestep:

$$\Delta t_h^{n+1} = \tau_h \frac{h_i}{\dot{h}_i}, \quad (2.30)$$

where  $\tau_h$  is again an accuracy parameter. Usually, we apply  $\tau_{\text{acc}} = 1$ ,  $\tau_{\text{CFL}} = 0.5$  and  $\tau_h = 0.15$ . The timestep actually employed in the simulation is the minimum of the timesteps in eqs. 2.26-2.30.

### 2.3.2 Gadget

A somewhat different treatment of hydrodynamics and magnetic fields is realised within the MPI parallel  $N$ -body/SPH code GADGET (Springel et al., 2001, Springel, 2005, Dolag and Stasyszyn, 2009). There are two significant differences in the implementation relevant even for non-radiative simulations:

First, VINE follows a classical implementation which is integrating the internal energy, whereas GADGET utilises what is generally called the entropy conserving formulation. The important difference thereby is not the fact that GADGET integrates the entropy instead of the internal energy. The crucial differences are rather the way in which the smoothing length  $h_i$  is defined (in GADGET,  $h_i$  is defined based on the mass within the kernel instead of the number of particles) and the inclusion of correction terms arising from the varying smoothing length. Also, the entropy conserving formulation uses a way of symmetrizing the kernel given by the derivation of the SPH equations, which in sum leads to conservation of energy and entropy at the same time (Springel and Hernquist, 2002).

The second difference originates in an alternative formulation of the artificial viscosity. In GADGET, artificial viscosity is based on the signal velocity instead of sound speed (Monaghan, 1997) and apt to incorporate magnetic waves in a natural way (Price and Monaghan, 2004b).

This different implementation was shown to bring measurable improvements specially for MHD applications (Dolag and Stasyszyn, 2009), but should not make too much of a difference for passive magnetic fields. The implementation of the induction equation and the Euler potentials formalism is the same in both codes.

The integration in GADGET is also performed using the leapfrog integration scheme, but GADGET utilises a kick-drift-kick-scheme whereas VINE uses a drift-kick-drift-scheme.

The timestep is given by

$$\Delta t^{n+1} = \sqrt{\frac{2\eta\epsilon}{|\mathbf{a}|}}, \quad (2.31)$$

where  $\eta$  translates to the accuracy parameter  $\tau_{\text{acc}}$  in eq. 2.26 via  $\tau_{\text{acc}} = \sqrt{2\eta}$ . For SPH particles, also a Courant-like condition in the form

$$\Delta t_{\text{cour}}^{n+1} = \frac{C_{\text{cour}} h_i}{\max_j v_{ij}^{\text{sig}}} \quad (2.32)$$

total mass	$M_{\text{tot}}$	=	$1.34 \cdot 10^{12} M_{\odot}$
disc mass	$M_{\text{disc}}$	=	$0.041 \cdot M_{\text{tot}}$
bulge mass	$M_{\text{bulge}}$	=	$0.01367 \cdot M_{\text{tot}}$
mass of the extended gas disc	$M_{\text{gas}}$	=	$0.2 \cdot M_{\text{disc}}$
exponential disc scale length	$l_D$	=	3.5 kpc
scale height of the disc	$h$	=	$0.2 \cdot l_D$
bulge scale length	$l_B$	=	$0.2 \cdot l_D$
extent of flat gas disc	$l_G$	=	$6 \cdot l_D$
spin parameter	$\lambda$	=	0.033
virial velocity of the halo	$v_{\text{vir}}$	=	160 km s <sup>-1</sup>
half mass circular velocity	$v_{\text{half}}$	≈	200 km s <sup>-1</sup>
half mass rotation period	$T_{\text{half}}$	≈	150 Myr
isothermal sound speed	$c_s$	≈	15 km s <sup>-1</sup>
initial magnetic field	$B_0$	=	$10^{-9}$ G

Table 2.1: Parameters of initial disc setup

is applied, where  $h_i$  is the SPH softening length for gas particle  $i$  and  $v_{ij}^{\text{sig}}$  the signal velocity between particles  $i$  and  $j$  as defined in Price and Monaghan (2004b) with the maximum taken over all neighboring particles  $j$  of particle  $i$ .  $C_{\text{cour}}$  is an accuracy parameter which does not translate one-to-one to  $\tau_{\text{CFL}}$  in eq. 2.29 due to the different definition of the Courant criterion. We commonly use values of  $\eta = 0.02$  and  $C_{\text{cour}} = 0.15$  to ensure that the timestep  $\Delta t$  in GADGET does not get too large compared to VINE. However, changing the accuracy parameters by a factor of two does not affect the overall evolution and amplification of the magnetic field in the simulated systems (not shown).

Beside that, the codes differ in details of the tree construction for calculating gravitational forces. For more details we refer the reader to the code papers for VINE (Wetzstein et al., 2009, Nelson et al., 2009) and GADGET (Springel, 2005, Dolag and Stasyszyn, 2009).

## 2.4 Simulations

### 2.4.1 Setup

The initial conditions for our Milky Way like galaxy are realised using the method described by Springel et al. (2005a) which is based on Hernquist (1993) (see also Johansson et al., 2009b). The galaxy consists of an exponential stellar disc and a flat extended gas disc, a stellar bulge and a dark matter halo of collisionless particles. The gas is represented by SPH particles adopting an isothermal equation of state with a fixed sound speed of  $c_s \approx 15$  km s<sup>-1</sup>, which corresponds to a temperature of  $T \approx 2 \cdot 10^4$  K for a molecular weight of  $1.4/1.1 \cdot m_{\text{proton}}$ . We briefly note that by using an isothermal equation of state only one component of the ISM is modeled, typically this is a reasonably good approximation for the warm gas phase in disc galaxies (e.g. Barnes, 2002, Li et al., 2005, Naab et al., 2006). Assuming an isothermal equation of state implies that additional heat created in shocks by adiabatic compression and feedback processes (e.g. by SNII) is radiated away immediately. In addition, substantial heating processes prevent the gas from cooling below its effective temperature predefined by its sound speed.

The parameters describing the initial conditions can be found in Table 2.1. The particle numbers and the gravitational and SPH softening lengths used in the different runs can be found in Table 2.2.

Before we include magnetic fields we allow the galaxy to evolve for approximately three half mass rotation periods. For simplicity we choose an initial magnetic field in the  $x$  direction. Its value,  $B_0 = 10^{-9}$  G, corresponds to the typical value of intergalactic magnetic fields (Kronberg et al., 1999).

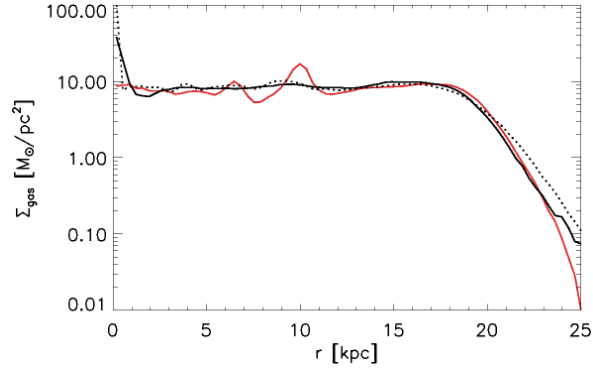


Figure 2.2: Surface densities  $\Sigma_{\text{gas}}$  of the extended gas discs as a function of radius before the inclusion of the magnetic fields after 0.5 Gyr (red line) and after 2 Gyr (black lines) for simulations with GADGET (solid line) and VINE (dotted line). The gas discs are stable for more than ten half mass rotation periods.

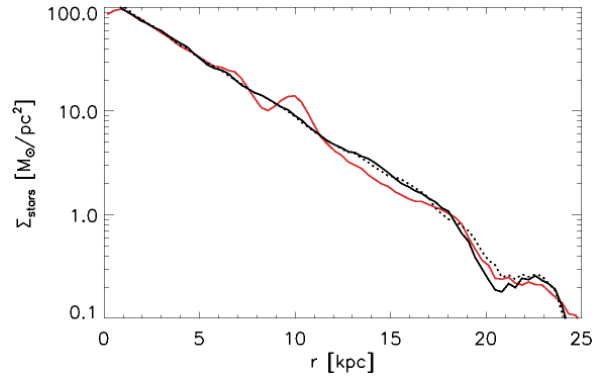


Figure 2.3: Same as Fig. 2.2 but for the stellar surface densities  $\Sigma_{\text{stars}}$ . Both the stellar and the gas discs are stable for more than ten half mass rotation periods.

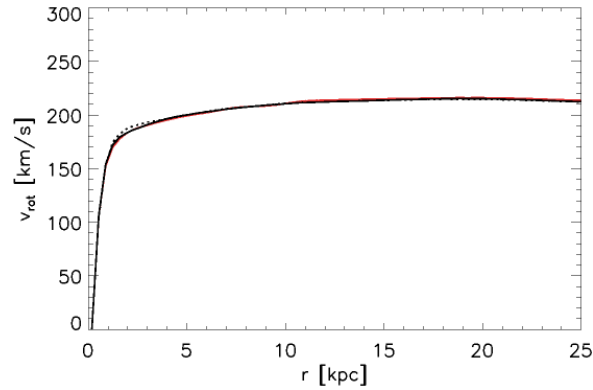


Figure 2.4: Circular velocity curves of the simulated galaxies at two different times. The colour coding is the same as in Figs. 2.2 and 2.3. Again, the circular velocity curves are stable over more than ten half mass rotation periods.

	low resolution		normal resolution		high resolution	
	number of particles					
Halo	$6 \cdot 10^4$		$6 \cdot 10^5$		$6 \cdot 10^6$	
Disc	$3 \cdot 10^4$		$3 \cdot 10^5$		$3 \cdot 10^6$	
Bulge	$1 \cdot 10^4$		$1 \cdot 10^5$		$1 \cdot 10^6$	
Gas	$3 \cdot 10^4$		$3 \cdot 10^5$		$3 \cdot 10^6$	
Total	$13 \cdot 10^4$		$13 \cdot 10^5$		$13 \cdot 10^6$	
fixed gravitational softening lengths $\epsilon$ [kpc]						
	VINE	GADGET	VINE	GADGET	VINE	GADGET
Halo	0.934/2	0.934	0.434/2	0.434	-	0.199
Disc	0.248/2	0.248	0.114/2	0.114	-	0.052
Bulge	0.269/2	0.269	0.127/2	0.127	-	0.059
Gas	0.248/2	0.248	0.114/2	0.114	-	0.052
minimum SPH softening lengths $h_{\min}$						
Gas	0.01 $\epsilon$	0.01 $\epsilon$	0.01 $\epsilon$	0.01 $\epsilon$	-	0.01 $\epsilon$

Table 2.2: Particles numbers and softening lengths. The factor two accounts for the different definition of the Kernel extent in VINE ( $\varrho < 2$ ) and GADGET ( $\varrho < 1$ ).

To set up the corresponding Euler potentials, we choose

$$\alpha_E = B_0 \cdot y, \quad (2.33)$$

$$\beta_E = y + z. \quad (2.34)$$

We have checked the stability of our discs in independent simulations without magnetic fields. Figs. 2.2 and 2.3 show the surface densities  $\Sigma_{\text{gas}}$  of the extended gaseous discs and  $\Sigma_{\text{stars}}$  of the exponential stellar discs, respectively, as a function of radius for  $t = 0.5$  Gyr (red), i.e. the time at which the magnetic field is switched on, and  $t = 2.0$  Gyr (black). Fig. 2.4 shows the circular velocity curves of the simulated galaxies at the same times. The discs simulated with VINE (dotted line) and GADGET (solid line) show similar results and stay stable over more than ten half mass rotation periods.

## 2.4.2 Direct magnetic field simulations

Figs. 2.5 and 2.6 show the face on view of the magnetic field energy and gas density of the simulated galaxy at different output times. The magnetic field was switched on at  $t = 510$  Myr. The viscosity limiter was not applied. Fig. 2.5 shows the simulation performed with VINE and Fig. 2.6 the same initial conditions simulated with GADGET. The magnetic field energy  $B^2/8\pi$  is colour coded and normalised to the initial value of  $\frac{1}{8\pi} \cdot 10^{-18}$  erg cm $^{-3}$  on a logarithmic scale from 1 (blue) to  $1.5 \cdot 10^8$  (red). The contours overplotted indicate physical densities of 23, 37 and 52  $M_{\odot}$  pc $^{-3}$ , respectively. We use a grid with a cell size of 0.3 kpc for the calculation of the mean values of the densities and the magnetic field energies, averaging in the vertical direction from  $-h$  to  $h$ , where  $h$  is the local height of the gas disc.

In both simulations we see that the magnetic field energy pattern is tightly connected to the density pattern of the gas. Moreover, both simulated galaxies show a very similar morphology in the gas and magnetic field distributions. The magnetic field energy in the spiral arms is amplified by up to five orders of magnitude in both codes and even more in the central region (see also Fig. 2.13). Furthermore, the SPH smoothing lengths  $h_{\text{gas}}$  are similar for both codes (Fig. 2.9), indicating that the performance of the hydrodynamic calculations is concerted. The smoothing lengths in VINE are initially set to a constant value of  $h_{\text{gas}} \approx 0.3$  kpc at the time of the magnetic field inclusion.

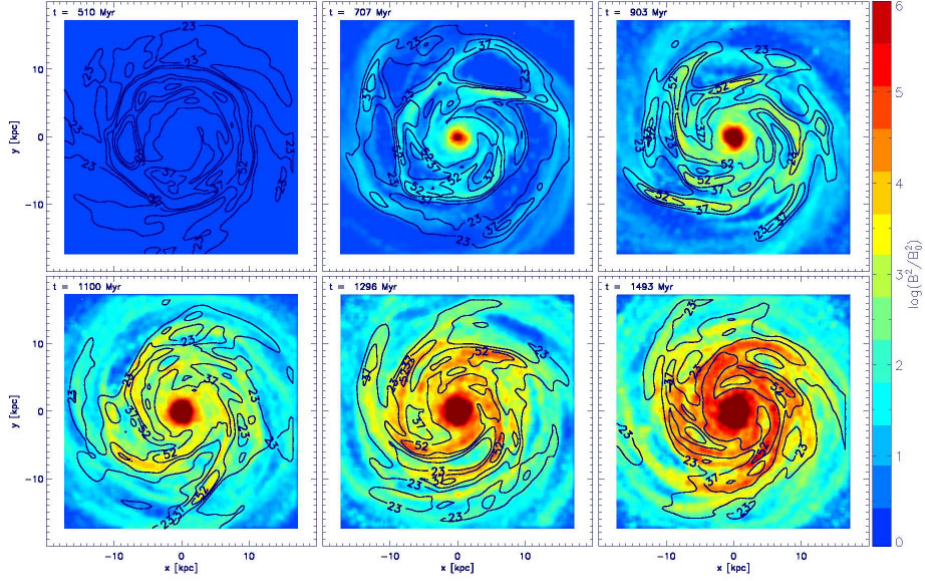


Figure 2.5: Face-on magnetic field energy and gas density as a function of time for the simulation performed with VINE using direct magnetic field description and without applying the viscosity limiter. The colours correspond to the magnetic field energy  $B^2/8\pi$  on a logarithmic scale, normalised to the initial value of  $\frac{1}{8\pi} \cdot 10^{-18} \text{ erg cm}^{-3}$ . The contour lines indicate physical densities of  $23$ ,  $37$  and  $52 M_{\odot} \text{ pc}^{-3}$ , respectively.

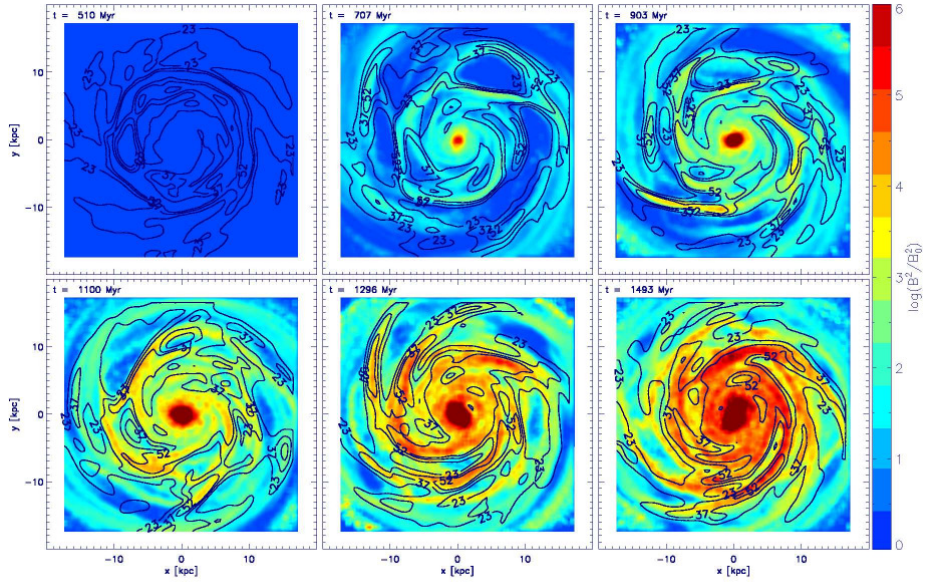


Figure 2.6: Same as Fig. 2.5 for identical initial conditions simulated with GADGET. The morphology is very similar but the magnetic field reaches higher values in the spiral arms in the GADGET simulation compared to the simulation with VINE.

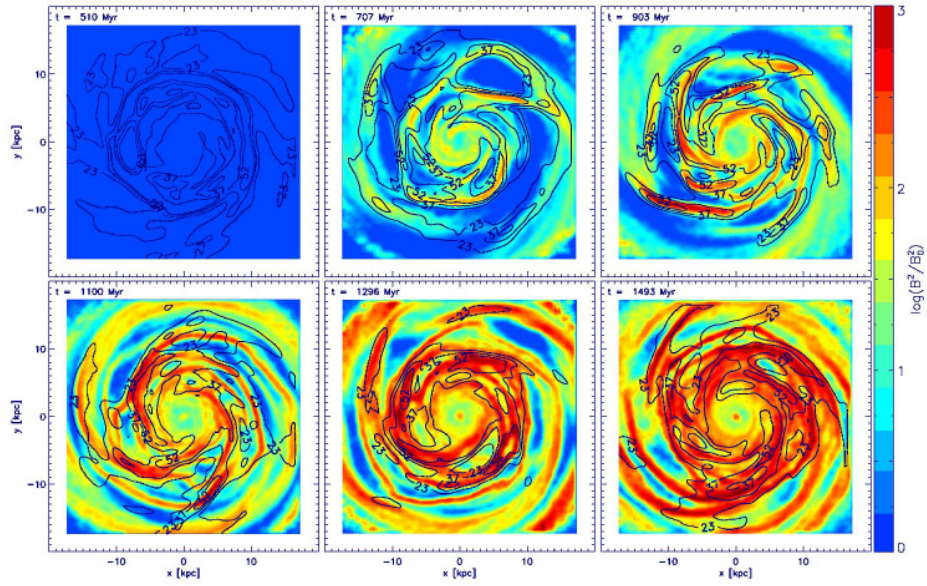


Figure 2.7: Same as Fig. 2.5, this time the magnetic field is followed using Euler potentials implemented in VINE. In contrast to the direct simulation the magnetic field is more strongly amplified in the spiral arms than at the centre. The maximum amplification of the magnetic field energy is only three orders of magnitude. Note that the colour scaling is different to Figs. 2.5 and 2.6.

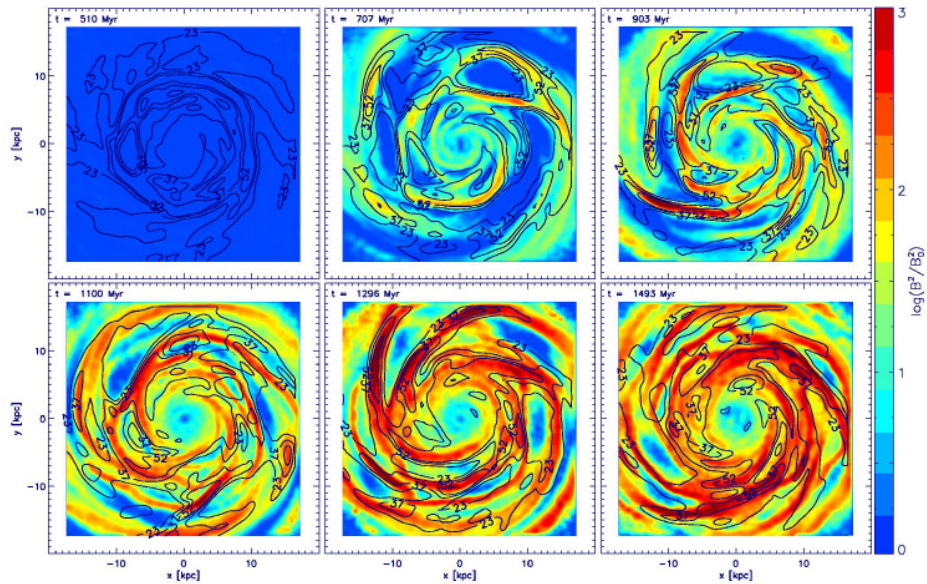


Figure 2.8: Same as Fig. 2.6, this time the magnetic field is followed using Euler potentials implemented in GADGET. The energies and morphology of the magnetic field is now similar to the VINE simulation.

### 2.4.3 SPH with Euler Potentials

Figs. 2.7 and 2.8 show simulations starting from the same initial conditions as before. However, this time the evolution of the magnetic field was followed using the Euler potentials. Again, we show magnetic field energies and gas densities. This time the amplification of the magnetic field energy in the spiral arms is only three orders of magnitude for both simulations with VINE and GADGET, with both showing a remarkably similar evolution. The most notable difference to the simulations with direct magnetic field treatment shown in Fig. 2.5 and 2.6 is at the centre of the galaxies, where in the direct simulations the field amplification was strongest. With Euler potentials the magnetic field grows mostly in the spiral arms of the galaxy (see also Fig. 2.13).

Since the magnetic fields in our simulations are passive, the density profiles (Figs. 2.2 and 2.3) of the disc are the same for all runs. Thus, the different profiles of the magnetic field energy cannot be traced back to the density profiles. In fact, it is the numerical  $\nabla \cdot \mathbf{B}$  which presumably causes the high amplification of the magnetic field at the centre in simulations with the direct magnetic field treatment. Fig. 2.10 shows the radial profile of the numerical  $h \cdot |\nabla \cdot \mathbf{B}|/|\mathbf{B}|$  at time  $t \approx 1.5$  Gyr for simulations using direct magnetic field treatment (blue for simulations without applying the viscosity limiter and orange where the limiter was applied) and Euler potentials (black) performed using GADGET (solid lines) and VINE (dotted line). Utilising the direct magnetic field description, the numerical  $\nabla \cdot \mathbf{B}$  is highest at small radii, and much larger than for the Euler potential formalism. As will be discussed in the following section, high  $\nabla \cdot \mathbf{B}$  corresponds to high amplification of the magnetic field.

Fig. 2.11 shows the magnetic field vectors for the normal resolution VINE simulation utilising Euler potentials at the time  $t \approx 0.9$  Gyr. This time the colours correspond to the gas density on a logarithmic scale from  $0.3 \cdot 10^{-3}$  to  $2.3 \cdot 10^3 M_{\odot} \text{ pc}^{-3}$ , overplotted with the field vectors. The length  $l$  of the vectors is normalised to the initial value and displayed logarithmically as  $l = 3 \cdot \log(B/B_0)$ , i.e.  $l = 0$  corresponds to  $B \approx B_0$  or smaller,  $l = 1$  to  $B \approx 2 \cdot B_0$ ,  $l = 2$  to  $B \approx 5 \cdot B_0$  and  $l = 3$  to  $B = 10 \cdot B_0$ . The magnetic field lines follow the spiral structure of the gas. They have been amplified by contraction in regions of higher density and restructured by differential rotation of the galaxy. Their orientation is caused by the motion of the gas. These characteristics are very similar to typical observations of magnetic fields in galactic discs (e.g. Fig. 2.1).

Qualitatively, this behaviour is the same for all simulations using both codes. Only the central region in simulations using direct magnetic field treatment shows chaotic orientation of the magnetic field lines, indicating artificial amplification of the magnetic field due to high numerical  $\nabla \cdot \mathbf{B}$ .

## 2.5 Evaluation

### 2.5.1 Magnetic field growth

Figs. 2.5 (2.6) and 2.7 (2.8), respectively, reveal the differences in the magnetic field amplification for the direct magnetic field treatment and the Euler potentials formalism: Using the direct description, the amplification of the magnetic field energy in the spiral arms is higher by at least two orders of magnitude, and at the centre even more than six orders of magnitude compared to the Euler potentials method. This difference is probably caused by the numerical  $\nabla \cdot \mathbf{B}$  in these simulations (Fig. 2.10), but possibly also by the fact that field winding is not traced beyond a certain evolutionary state in the Euler potentials formulation (see section 2.3.1.6). Since the Euler potentials are free from physical divergence by construction (i.e. the divergence is zero to measurements errors), the numerical divergence in simulations using the Euler potentials is due to the SPH derivative approximation when calculating the magnetic field from the potentials (Eq. 2.18). In this sense, the numerical divergence found in simulations using Euler potentials reflects the ability of SPH operators to measure the gradient of a curl to zero. Thus, the fact that  $\nabla \cdot \mathbf{B}$  is higher by approximately one order of magnitude in

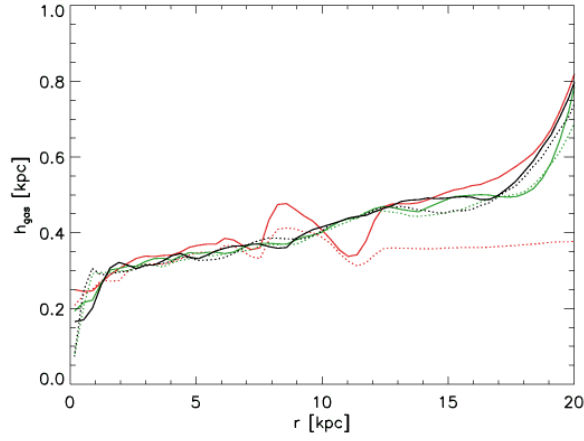


Figure 2.9: SPH softening lengths  $h_{\text{gas}}$  as a function of radius shortly after the inclusion of the magnetic fields at 0.55 Gyr (red line), at 1.25 Gyr (green lines) and at 2 Gyr (black lines) for simulations with GADGET (solid lines) and VINE (dotted lines). The SPH smoothing lengths are very similar for both codes.

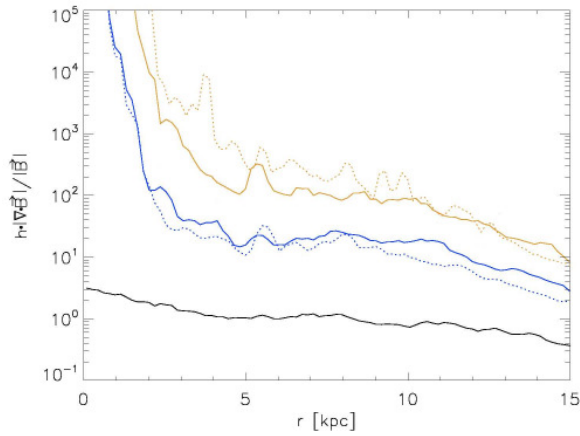


Figure 2.10: Numerical  $h \cdot \nabla \cdot \mathbf{B} / |\mathbf{B}|$  at  $t \approx 1.5$  Gyr as a function of radius for simulations without applying the viscosity limiter using direct magnetic field treatment (blue) and using Euler potentials (black) in GADGET (solid lines) and VINE (dotted lines). Direct magnetic field simulations for which the viscosity limiter was applied are also shown (orange). Using direct magnetic field description, the numerical  $h \cdot \nabla \cdot \mathbf{B}$  is highest at small radii, and much larger than in the Euler potentials formalism.

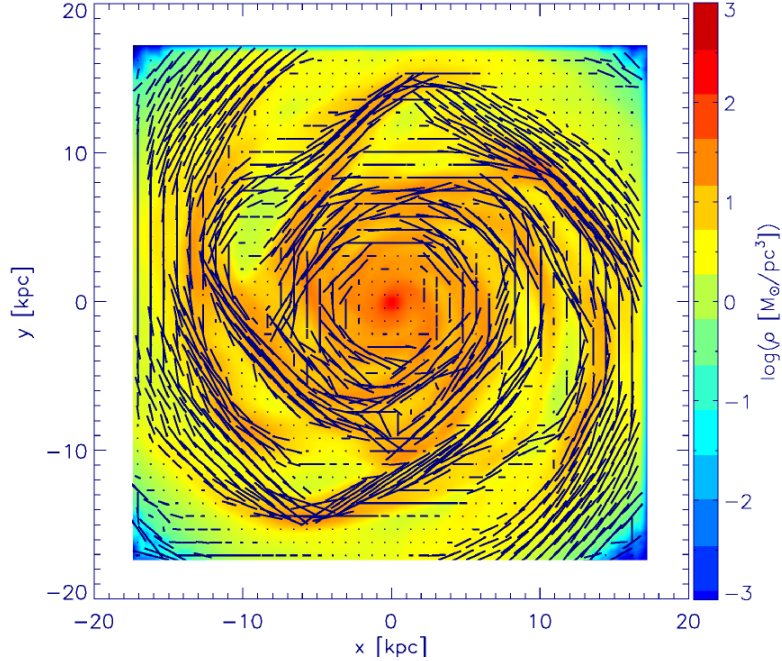


Figure 2.11: Gas density (colour coded) and magnetic field vectors for the normal resolution simulation with VINE using the Euler potentials formalism at  $t \approx 1$  Gyr, i.e.  $\approx 500$  Myr after the inclusion of the magnetic field. The length of the vectors is normalised to the initial value and displayed logarithmically.  $l = 0$  corresponds to  $B \approx B_0$  or smaller and  $l = 3$  to  $B = 10 \cdot B_0$ .

the disc (i.e. within  $\approx 5$  to 15 kpc) and by several orders of magnitude at the centre (Fig. 2.10), presumably causes the different magnetic field amplification in these simulations. This is the case at least in the disc region, where the winding of the field is not strong enough to constrain the Euler potentials formulation.

To get a better idea of the influence of numerical  $\nabla \cdot \mathbf{B}$  on the amplification of the magnetic field, we have performed simulations applying magnetic field smoothing, a technique allowing for reduction of small scale fluctuations and therefore also the numerical divergence (Dolag and Stasyszyn, 2009). Within this method, the magnetic field is smoothed periodically as suggested by Børve et al. (2001). Fig. 2.12 shows again the magnetic field energies and gas densities for a GADGET simulation starting from the same initial conditions as before and without applying the viscosity limiter. This time, the magnetic field was smoothed every 30 timesteps. Applying the smoothing scheme, the amplification of the magnetic field energy is reduced to approximately three orders of magnitude within the spiral arms, which is the same as the amplification seen in simulations using the Euler potentials, and it is also lowered towards the centre of the galaxy. The structure of the magnetic field is despite the smoothing still very similar to the other runs and again correlates well with the structure of the gas density, however, the magnetic field energy is more concentrated within the spiral arms.

Fig. 2.13 shows the total magnetic field at  $t \approx 1.5$  Gyr as a function of radius for the normal resolution GADGET (solid line) and VINE (dotted line) simulations using Euler potentials (black) and the direct magnetic field description without applying the viscosity limiter (blue) and with the limiter turned on (orange), respectively. The direct magnetic field simulations including field smoothing are shown in red and green. They have been performed with a smoothing interval of 30 (red) and

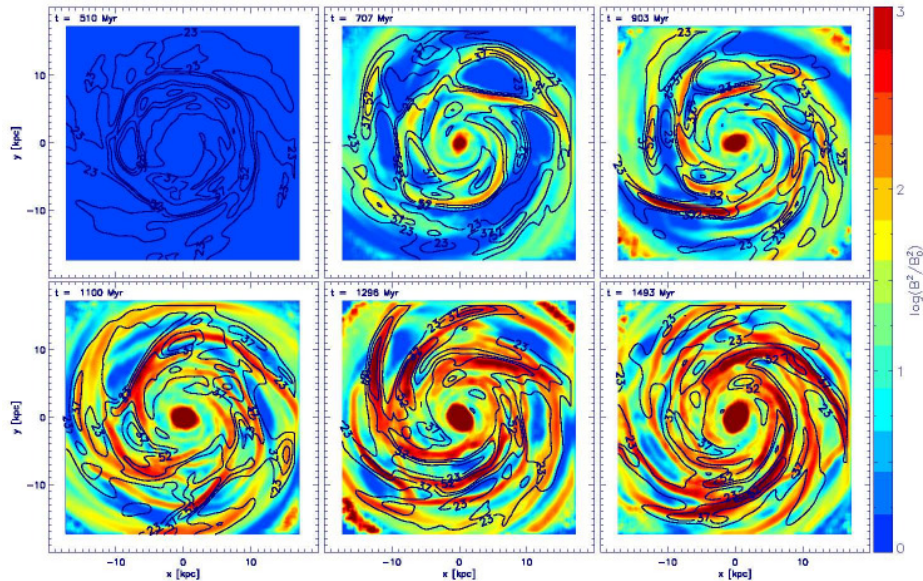


Figure 2.12: Same as Fig. 2.6, this time the magnetic field is smoothed every 30 timesteps. The field morphology is similar to the morphology in Fig. 2.6 and 2.5, respectively, but the magnetic field values in the spiral arms are now more similar to the values in the Euler implementation.

5 timesteps (green), respectively, and without applying the viscosity limiter. As discussed before, the most notable difference between simulations with direct magnetic field treatment and the Euler implementation is at the centre of the galaxies. There, the amplification in the direct simulations is much stronger than in the Euler simulations. This behaviour could be at least partly physical, as there are high radial velocities and strong in- and outflows of gas in the central region (fig. 2.17), resulting according to Eqs. 2.7 and 2.8 in an amplification of the magnetic field. In addition, also the azimuthal derivatives of the radial and toroidal velocity components are large at the very centre, which also could account for the violent amplification (see section 2.5.3). On the other hand, the second term of eq. 2.8 does not play an important role, since  $dv_\varphi/dr$  is large and therefore  $d\Omega/dr$  small in the central region (by reason of solid body rotation). However, the high  $\nabla \cdot \mathbf{B}$  values at the centre make it difficult to distinguish between physical growth and numerical errors. Since the Euler potentials are also unreliable in this region (see section 2.3.1.6), it is not easy to decide which formalism is the most capable in describing the physics in the centre of the galaxy correctly. This is also true for the simulations including smoothing. Increasing the frequency of smoothing tends to decrease the amplitude of the magnetic field between 3 and 10 kpc, but has relatively little effect for larger radii. Interestingly, the large increase of  $\mathbf{B}$  in the centre is never smoothed away, which could indicate, that this behaviour is actually partly physical. For the simulation which applies smoothing every 30 timesteps (red), the amplification of the field at  $r > 3$  kpc is similar to the simulations with Euler potentials. Applying smoothing every 5 timesteps (green), the amplification is considerably weaker than in the Euler potentials simulations, indicating that by such strong smoothing essential physics is lost, in agreement with earlier findings by Dolag and Stasyszyn (2009).

In the following, we only consider the disc region (from 5 to 15 kpc), since the high numerical divergence in the centre makes it difficult to lower it to the value of the divergence seen in simulations with Euler potentials (i.e.  $h \cdot |\nabla \cdot \mathbf{B}|/|\mathbf{B}| \approx 1$ ), without smoothing the magnetic field structure too

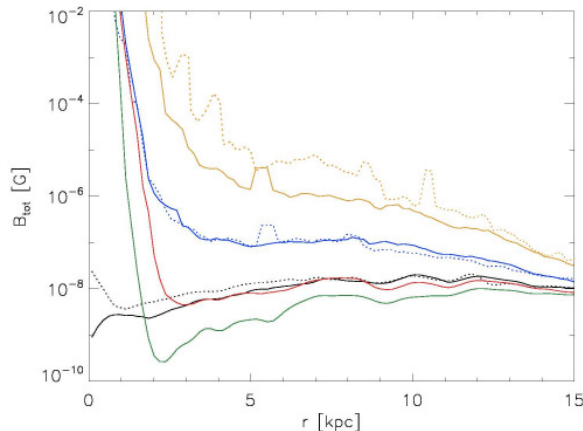


Figure 2.13: Total magnetic field ( $B_{\text{tot}} = \sqrt{B_x^2 + B_y^2 + B_z^2}$ ) at  $t \approx 1.5$  Gyr as a function of radius for the normal resolution GADGET (solid lines) and VINE (dotted lines) simulations without applying the viscosity limiter using Euler potentials (black) and the direct magnetic field description (blue). Direct magnetic field simulations for which the viscosity limiter was applied are also shown (orange). Two direct magnetic field implementations including field smoothing to reduce the numerical  $\nabla \cdot \mathbf{B}$  contribution are shown in red and green. The simulations including smoothing have been run with a smoothing interval of 30 (red) and 5 timesteps (green), respectively. Increasing the frequency of smoothing tends to decrease the amplitude of the magnetic field between 3 and 10 kpc, but has relatively little effect for larger radii.

much.

Fig. 2.14 shows the evolution of the total magnetic field ( $B_{\text{tot}} = \sqrt{B_x^2 + B_y^2 + B_z^2}$ ) within the disc with time for the different implementations. The colour coding is the same as in Fig. 2.13. As before, for the simulation which applies smoothing every 30 timesteps (red), the amplification of the field is similar to the simulation with Euler potentials. However, the performance of these simulation is not very convincing due to the “jumps” in the evolution caused by the artificial periodic smoothing. Applying smoothing every 5 timesteps (green), the amplification is as discussed before lower than in the Euler potentials simulations.

This behaviour can be understood by considering the corresponding numerical divergence of the magnetic field. Fig. 2.15 shows  $h \cdot |\nabla \cdot \mathbf{B}|/|\mathbf{B}|$  as a function of time for all simulations. In all cases, the growth of  $h \cdot |\nabla \cdot \mathbf{B}|/|\mathbf{B}|$  behaves similar to the amplification of the total magnetic field, i.e. the higher the divergence, the stronger the amplification of the field. Though the numerical divergence in the simulation using Euler potentials (black) is higher than in the simulation with a smoothing interval of 5 timesteps (green), its value does not directly correlate with the field growth. That is because the (defective) magnetic field itself is not used for calculating the magnetic field evolution within the Euler potential formalism as is the case for the direct magnetic field description (compare eqs. 2.17 and 2.18). Using the smoothing scheme lowers the divergence (in case of smoothing every 5 timesteps even below the numerical divergence of the Euler potential formalism) and lowers also the field amplification, leading (if applied not too often) to an amplification of the total field much more similar to that using the Euler potentials, which are free from *physical* divergence by construction.

Interestingly, for simulations applying the viscosity limiter suggested by Balsara (1995), the magnetic field amplification using the direct magnetic field description is in both codes much higher than without applying this limiter (orange lines in Figs. 2.13 and 2.14). The reason for this higher amplification is the higher velocity dispersion in these simulations. The viscosity limiter lowers the viscosity in regions of strong shear flows, thus suppressing velocity diffusion and leading to higher velocity gradients. Consistently, also the numerical divergence of the magnetic field is higher (and consider-

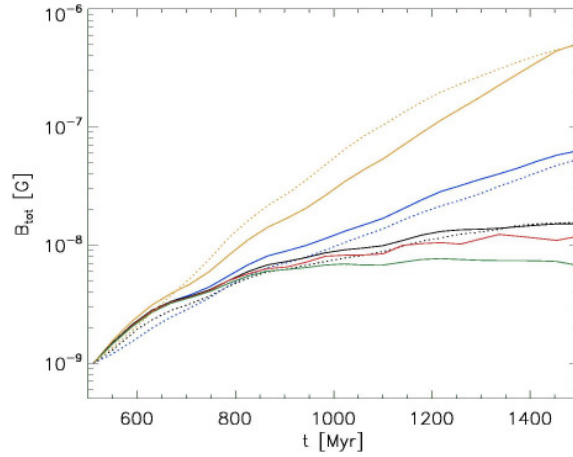


Figure 2.14: Total magnetic field ( $B_{\text{tot}} = \sqrt{B_x^2 + B_y^2 + B_z^2}$ ) within the disc (between 5 and 15 kpc) as a function of time for different implementations. The colour coding is the same as in Fig. 2.13. Applying the smoothing scheme reduces the amplification of the magnetic field.

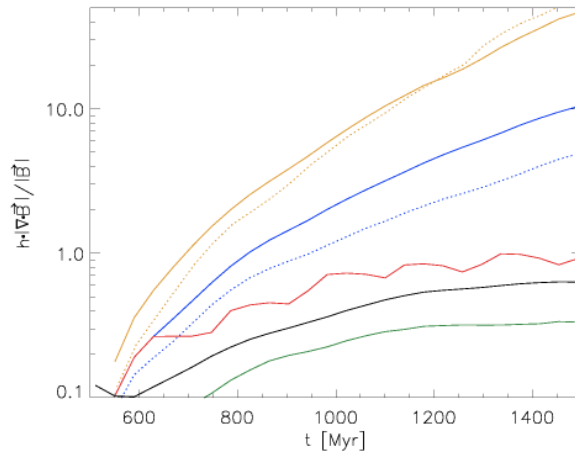


Figure 2.15: Total divergence of the magnetic field within the disc (between 5 and 15 kpc) as a function of time for different implementations. The colour coding is the same as in Fig. 2.13. The higher the divergence, the stronger the amplification of the magnetic field.

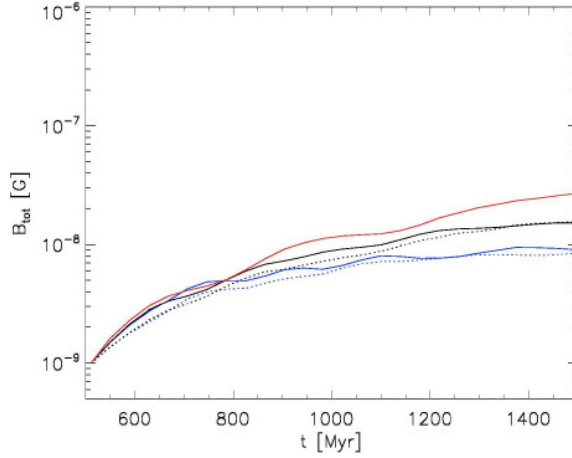


Figure 2.16: Resolution study: Total magnetic field ( $B_{\text{tot}} = \sqrt{B_x^2 + B_y^2 + B_z^2}$ ) as a function of time for the GADGET (solid line) and VINE (dotted line) simulations without applying the viscosity limiter using Euler potentials. The total numbers of particles are  $1.3 \cdot 10^5$  (blue),  $1.3 \cdot 10^6$  (black) and  $1.3 \cdot 10^7$  (red).

ably higher than the “unavoidable” value of approximately one) in these simulations (orange lines in Figs. 2.10 and 2.15). Applying the viscosity limiter in simulations using Euler potentials, however, does not change the evolution of the magnetic field significantly (not shown). Therefore, again, it is probable that the higher numerical  $\nabla \cdot \mathbf{B}$  terms lead via the induction equation (eq. 2.3) to an enhanced magnetic field growth.

In summary, the field amplification in case of direct magnetic field description correlates with the non-vanishing, numerical  $\nabla \cdot \mathbf{B}$ . The Euler potential formalism also has its shortcomings (like the non-uniqueness and the dependence of the magnetic field on two derivatives (Eq. 2.18) leading to lower numerical accuracy). Thus there is a strong need for simulations with different  $\nabla \cdot \mathbf{B}$  cleaning techniques and even higher resolution in order to be able to distinguish the best description for simulations of magnetic fields in galactic discs.

However, since the physical divergence is zero in the case of the Euler potentials, we believe this method (for the time being) to be the best one for our studies of magnetic convection in disc galaxies. The following discussion therefore concentrates on simulations using Euler potentials.

## 2.5.2 Numerical resolution

Fig. 2.16 shows the total magnetic field as a function of time for different resolutions (see Table 2.2) in simulations with GADGET (solid lines) and VINE (dashed lines) without applying the viscosity limiter.

One Gyr after its initialization the magnetic field has been amplified from  $10^{-9}$  to approximately  $9 \cdot 10^{-9}$  G in the low resolution simulation (blue), whereas the final magnetic field strength in the normal resolution simulation is slightly more than 1.5 times higher ( $1.5 \cdot 10^{-8}$  G). The final magnetic field strength in the high resolution run is again approximately 1.5 times higher than in the normal resolution run (i.e.  $\approx 2.5 \cdot 10^{-8}$ ). The numerical  $h \cdot |\nabla \cdot \mathbf{B}|/|\mathbf{B}|$  values are of the same order for all resolutions (not shown). Thus, we have not yet reached numerical convergence in the magnetic field evolution.

### 2.5.3 Inspection of the induction equation

By analyzing the velocity and magnetic field in our simulation we can identify the single terms of the induction equation responsible for the behaviour of the magnetic field. Dropping all dependencies on  $z$ , the equations for the evolution of the radial and toroidal magnetic fields read

$$\begin{aligned}
 \frac{\partial B_r}{\partial t} &= \underbrace{-B_r \frac{v_r}{r}}_{(1)} \quad \underbrace{-\frac{1}{r} B_r \frac{\partial v_\varphi}{\partial \varphi}}_{(2)} \quad + \underbrace{\frac{1}{r} B_\varphi \frac{\partial v_r}{\partial \varphi}}_{(3)} \\
 &\quad \underbrace{-v_r \frac{\partial B_r}{\partial r}}_{(4)} \quad \underbrace{-\frac{v_\varphi}{r} \frac{\partial B_r}{\partial \varphi}}_{(5)}, \\
 \frac{\partial B_\varphi}{\partial t} &= \underbrace{-B_\varphi \frac{\partial v_r}{\partial r}}_{(6)} \quad \underbrace{+ B_r \frac{\partial v_\varphi}{\partial r}}_{(7)} \quad \underbrace{-v_r \frac{\partial B_\varphi}{\partial r}}_{(8)} \\
 &\quad \underbrace{-\frac{v_\varphi}{r} \frac{\partial B_\varphi}{\partial \varphi}}_{(9)} \quad \underbrace{-\frac{v_\varphi}{r} B_r}_{(10)},
 \end{aligned}$$

where we have labelled the single terms with numbers for easier reference.

The radial and toroidal components of the velocity and the magnetic field and their corresponding derivatives are shown in Fig. 2.17 after approximately three half mass rotation periods after the onset of the magnetic field. The radial velocity (top left) is typically negative, leading to an effective gas inflow towards the centre of the galaxy. This negative radial velocity mirrors the angular momentum transport to large radii of the galaxy by spiral arm formation. The mean circular velocity (second row, left) is  $210 \text{ km s}^{-1}$  at large radii, and drops to zero towards the centre (see also Fig. 2.4). The toroidal magnetic field (bottom left) is wound up by differential rotation, leading to a structure of altering positive and negative magnetic field values from centre to the edge of the galaxy. Consequently the derivatives with respect to  $\varphi$  (right panel) are smaller than the radial derivatives (middle panel), mirroring the approximate axial symmetry. However, since the terms of the induction equation depend always on a product between a derivative and a velocity or magnetic field component, one cannot a priori neglect the terms depending on azimuthal derivatives.

In order to quantify the influence of the different terms 1-10 during the simulation we calculated their values in cylindrical bins within the disc (5 to 15 kpc) and their mean value at different times. We have taken the negative values of each term in case of negative magnetic field to distinguish between amplifying and attenuating terms. The result of this calculation is shown in Fig. 2.18. The upper plot shows the temporal evolution of the terms responsible for amplification/attenuation of the radial magnetic field (terms 1 to 5) and the lower of the toroidal magnetic field (terms 6 to 10). Positive values imply amplification, and negative attenuation of the corresponding  $\mathbf{B}$ -component. The non-axisymmetric terms are shown in red.

Looking at Fig. 2.18, the most important term for the evolution of the radial magnetic field is term 5, i.e.  $-\frac{v_\varphi}{r} \frac{\partial B_r}{\partial \varphi}$ . Since the toroidal velocity dominates the velocity field, this term is most important although  $\frac{\partial B_r}{\partial \varphi}$  is comparatively small. This can be seen following the evolution of the circular velocity and the radial magnetic field more closely: The radial magnetic field is strongest where the circular velocity has its highest value, with a delay of roughly 40 Myr. All other terms lie in the same range and therefore compete with each other. Since their values are positive as well as negative, one should not expect a significant amplification on their account. This analysis shows, that even small deviations from axial symmetry are very important for the evolution of the magnetic field in spiral galaxies.

One reaches the same conclusion looking at the terms of the evolution equation for  $B_\varphi$ . Except

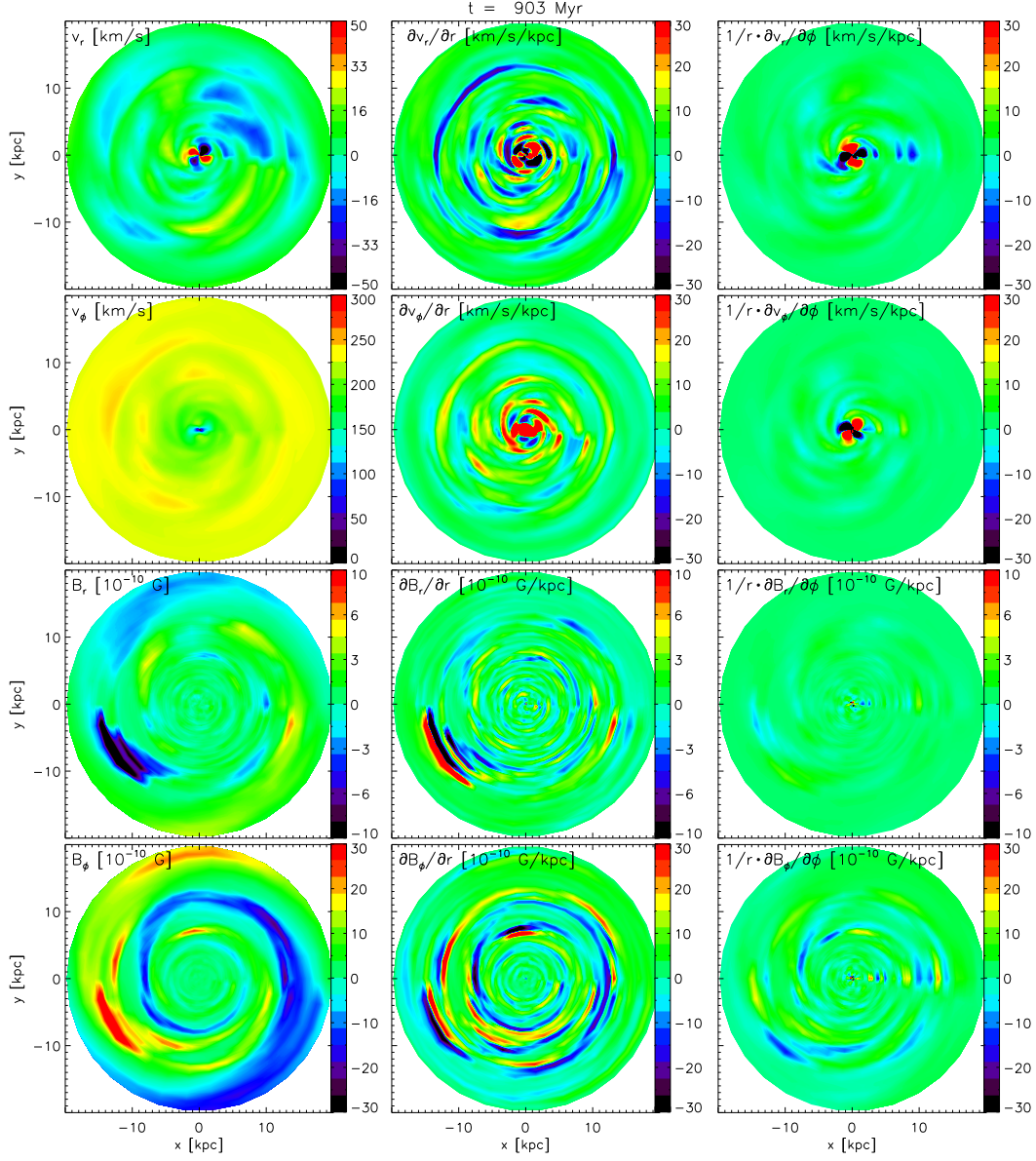


Figure 2.17: Radial and toroidal components of the velocity and the magnetic field and their derivatives at  $t \approx 900$  Myr for the normal resolution GADGET simulation. From left to right and top to bottom:  $v_r$ ,  $\frac{\partial v_r}{\partial r}$ ,  $\frac{1}{r} \cdot \frac{\partial v_r}{\partial \phi}$ ,  $v_\phi$ ,  $\frac{\partial v_\phi}{\partial r}$ ,  $\frac{1}{r} \cdot \frac{\partial v_\phi}{\partial \phi}$ ,  $B_r$ ,  $\frac{\partial B_r}{\partial r}$ ,  $\frac{1}{r} \cdot \frac{\partial B_r}{\partial \phi}$ ,  $B_\phi$ ,  $\frac{\partial B_\phi}{\partial r}$  and  $\frac{1}{r} \cdot \frac{\partial B_\phi}{\partial \phi}$ .

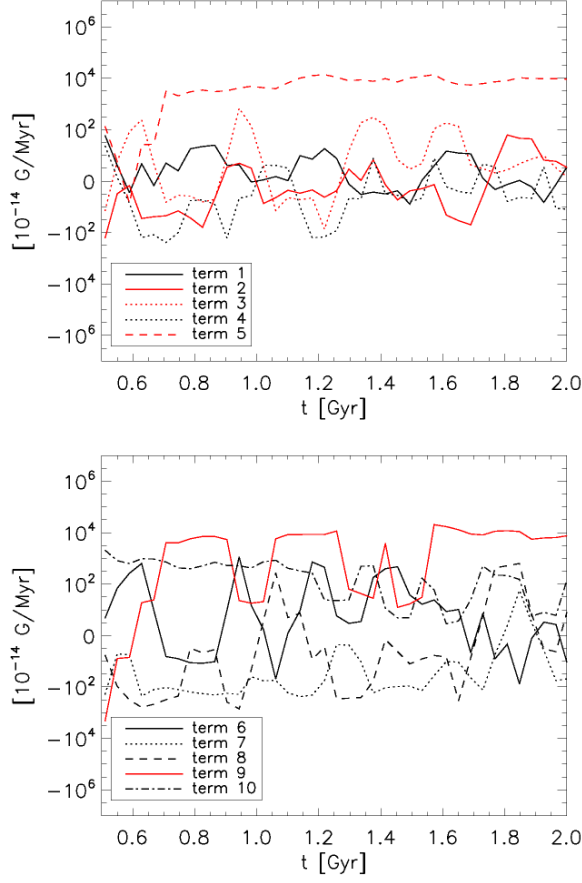


Figure 2.18: Values of the different terms of the induction equation with time for the normal resolution GADGET simulation using Euler potentials. Upper plot: temporal evolution of the terms responsible for amplification/attenuation of the radial magnetic field (terms 1 to 5). Lower plot: Evolution of terms 6-10, responsible for the evolution of the toroidal magnetic field. Positive values imply amplification, and negative attenuation of the corresponding  $\mathbf{B}$ -component. The non-axisymmetric terms are shown in red, the axisymmetric terms are shown in black.

for the beginning of the simulation, the leading term here is clearly term 9,  $-\frac{v_\varphi}{r} \frac{\partial B_\varphi}{\partial \varphi}$ , i.e. the only non-axisymmetric term in this equation. Term 10, which was our candidate for the most important term for axial symmetry, is only the second most important. Both terms depend on the toroidal velocity component, thus demonstrating the importance of the differential rotation for the evolution of the toroidal component of the magnetic field.

Neglecting all non-axisymmetric terms (plotted in red) one finds term 1 ( $-B_r \frac{v_r}{r}$ ) to be largely dominant over term 4 ( $-v_r \frac{\partial B_r}{\partial r}$ ), in agreement with the theory for the evolution of  $B_r$ . Also the term responsible for the evolution of  $B_\varphi$  is as expected: Term 10 ( $-\frac{v_\varphi}{r} B_r$ ) is the leading term and followed by term 6 ( $-B_\varphi \frac{\partial v_r}{\partial r}$ ). However, term 1 and 6 are both of order  $10^{-13}$  G Myr $^{-1}$ , thus not being able to account for any significant amplification of our initial magnetic field, and term 10 can only amplify  $B_\varphi$  effectively if  $B_r$  is amplified.

This behaviour is qualitatively the same also for runs with the direct implementation of the induction equation. We conclude that the non-axisymmetry of the system is the driving force for the observed field amplification in our simulations.

## 2.6 Conclusion and Outlook

We have presented a set of self-consistent simulations of the evolution of magnetic fields in galactic discs performed with the  $N$ -body codes VINE and GADGET. Hydrodynamics was treated using the SPH method. The evolution of magnetic fields within the framework of ideal MHD was followed by both a direct implementation of the induction equation and a formalism using Euler potentials.

The presented set of simulations shows the importance of a sensible treatment of  $\nabla \cdot \mathbf{B}$  when simulating magnetic fields in spiral galaxies. Since artificial magnetic monopoles can be responsible for unphysical amplification of the field, more studies of possibilities to avoid or inhibit numerical  $\nabla \cdot \mathbf{B}$  terms are still needed. Although the description using Euler potentials avoids (physical) magnetic monopoles by construction, the drawback in using them is that they lead to constraints on magnetic helicity. Since helicity fluxes can affect the dynamo process within a mean field theory (Brandenburg and Subramanian, 2005), Euler potentials would probably not be suitable for simulations including the  $\alpha$ -effect. Furthermore, Euler potentials do not allow for all initial field configurations, since they are not necessarily single valued and in addition, their derivation can become quite complex. Nevertheless, using topologically simple initial conditions for the magnetic field, the Euler potential formalism seems to be the best tool to follow the ideal evolution of magnetic fields in simulations of spiral galaxies with SPH.

A possible alternative to Euler potentials is the vector potential  $\mathbf{A}$ . The disadvantages are the need for a time integration of  $\mathbf{A}$  when evolving magnetic fields and the occurrence of second derivatives in the force equation when calculating magnetic forces ( $F_{\text{mag}} \propto \mathbf{j} \times \mathbf{B} \propto (\nabla \times \mathbf{B}) \times \mathbf{B} \propto (\nabla \times (\nabla \times \mathbf{A})) \times (\nabla \times \mathbf{A})$ ), both leading to lower accuracy in the calculation. On the other hand, the advantages are a somewhat easier derivation of  $\mathbf{A}$  for a given magnetic field and that there are no constraints on magnetic helicity using a vector potential. It would be definitely interesting to study the differences between simulations utilizing a vector potential and the Euler description, although it could be hard to overcome the problems related to numerical intricacies within a SPH implementation of the vector potential.

The analysis of the different terms of the induction equation applied to our simulations clearly show that the non-axisymmetry of the velocity and magnetic field cannot be ignored in any consideration of the kinematic dynamo. There are two main processes leading to angular momentum transport and hence non-axisymmetry in spiral galaxies: Internal driving due to spiral structure and bar formation (the former considered in the presented paper) and external driving due to interaction with other galaxies. Simulations of interacting systems would therefore enrich our understandings even further on how large scale magnetic fields evolve due to large scale velocity fields.

Our simulations show only a weak amplification of the initial magnetic field. Observations of spirals galaxies at high redshifts suggest that their magnetic field strengths were at least as strong as the magnetic fields at the current epoch within few Gyrs of the Big Bang (Kronberg et al., 2008). Assuming initial strengths of order  $B_{\text{IGM}} = 10^{-9}$  G an amplifying process should therefore account for four orders of magnitude of increase within few Gyrs in order to reach the observed values of  $\approx 10 \mu\text{G}$ . Since our simulations of a purely kinematic dynamo account at best for one order of magnitude, there is still need for a more complete scenario with additional subgrid physics. Such subgrid physics should comprise the  $\alpha$ -effect due to turbulent gas motions below the resolution limit, estimated from local high-resolution MHD simulations and observations of turbulent motions in nearby galaxies. Hereby, potentially the most promising ansatz is the cosmic ray driven dynamo (Lesch and Hanasz, 2003, Hanasz et al., 2005). Given the fact, that the presented simulations reveal the complete three dimensional velocity field to fully account for the large-scale structure of the magnetic field, we believe that  $N$ -body SPH together with sensible subgrid physics will be apt to test our understanding of the evolution of magnetic fields in spiral galaxies numerically.

---

## Acknowledgements

We thank the referee Daniel Price for numerous very helpful comments and suggestions which improved the paper a lot. HK is grateful for interesting discussions with Michal Hanasz, Daniel Price and Axel Brandenburg. The authors also greatly thank Rainer Beck for providing Fig. 2.1. This research was supported by the DFG cluster of excellence ‘Origin and Structure of the Universe’ ([www.universe-cluster.de](http://www.universe-cluster.de)).



# Chapter 3

## Paper II: Simulating magnetic fields in the Antennae galaxies

H. Kotarba, S. J. Karl, T. Naab, P. H. Johansson, K. Dolag, H. Lesch & F. A. Stasyszyn, 2010, *The Astrophysical Journal*, 716, 1438-145

### ABSTRACT

We present self-consistent high-resolution simulations of NGC4038/4039 (the "Antennae galaxies") including star formation, supernova feedback and magnetic fields performed with the *N*-body/SPH code GADGET, in which magnetohydrodynamics are followed with the SPH method. We vary the initial magnetic field in the progenitor disks from  $10^{-9}$  to  $10^{-4}$  G. At the time of the best match with the central region of the Antennae system the magnetic field has been amplified by compression and shear flows to an equilibrium field value of  $\approx 10 \mu\text{G}$ , independent of the initial seed field. These simulations are a proof of the principle that galaxy mergers are efficient drivers for the cosmic evolution of magnetic fields. We present a detailed analysis of the magnetic field structure in the central overlap region. Simulated radio and polarization maps are in good morphological and quantitative agreement with the observations. In particular, the two cores with the highest synchrotron intensity and ridges of regular magnetic fields between the cores and at the root of the southern tidal arm develop naturally in our simulations. This indicates that the simulations are capable of realistically following the evolution of the magnetic fields in a highly non-linear environment. We also discuss the relevance of the amplification effect for present day magnetic fields in the context of hierarchical structure formation.

**Key words:** methods: *N*-body simulations — galaxies: spiral — galaxies: evolution — galaxies: magnetic fields — galaxies: kinematics and dynamics

### 3.1 Introduction

Within the framework of the hierarchical galaxy formation picture, galaxies assemble and evolve via mergers of smaller progenitor galaxies (e.g. White and Rees, 1978, White and Frenk, 1991). Thus, galaxy interactions are essential for the understanding of structure formation. In the bottom-up picture of structure formation dwarf galaxies merge to form the first galaxies at an early epoch of the universe. Later, there is still a continuous merging of fully evolved galaxies. The further growth of galaxies progresses through a combination of mergers and diffuse accretion of gas.

Interactions of galaxies change their dynamics drastically (see e.g. Toomre and Toomre, 1972, Barnes, 1992, Hernquist and Barnes, 1994, Barnes, 1999 and Burkert and Naab, 2003, González-García et al., 2006) as the gravitational potential is changing rapidly during the interaction. Since the gas component is dissipative and most sensitive to changes of the gravitational potential, it is strongly affected during the interaction and driven to the galaxy centers, eventually causing bursts of star formation (Barnes and Hernquist, 1992, Mihos and Hernquist, 1994, Barnes and Hernquist, 1996, Bekki and Shioya, 1998, Springel, 2000, Barnes, 2002, Bournaud et al., 2005, Cox et al., 2006, Naab et al., 2006, Robertson et al., 2006, Cox et al., 2008b, Hopkins et al., 2008). So far simulations of interactions and mergers of disk galaxies have only been investigated with respect to changes in stellar dynamics, gas flows, star formation (SF) or formation of central supermassive black holes (Di Matteo et al., 2005, Springel et al., 2005a, Springel et al., 2005b, Robertson et al., 2006, DeBuhr et al., 2010, Johansson et al., 2009a, Johansson et al., 2009b). However, the dramatic impact of mergers on the gas flows will directly affect the magnetic fields of the systems (and vice versa) via the induction equation of magnetohydrodynamics (MHD) and the Lorentz force. The magnetic fields will change their morphology following the motion of the gas and will be amplified by shocks and gas inflow.

Changes in the magnetic field structure, on the other hand, might influence gas flows, local collapse and the morphology as well as the star formation activity. Local, interacting galaxies are the perfect laboratories for investigating the effects associated with their magnetic fields. However, the timescales for galaxy mergers are far too long to observe these processes directly. The only observational possibility to study the time evolution of mergers is to consider different systems at different evolutionary stages. However, the available sample of interacting nearby galaxies is too small to investigate the evolution of magnetic fields in detail. Thus, numerical simulations pose a promising tool to study the magnetic field evolution in interacting systems.

The structure of an interacting system strongly depends on the properties of the progenitor galaxies. Thus, matching observed nearby interacting systems with simulations in space and time can give us an idea of the properties of their progenitors, e.g. their sizes, gas fractions and relative velocities. Furthermore, comparing simulated systems with observations helps to assess the performance of the applied numerical method. Numerical methods supported by these comparisons can then be used to study processes in the early universe, when galaxies were very different from present-day galaxies. High resolution simulations of the formation of individual galaxies in a full cosmological context (see e.g. Naab et al., 2007) including magnetic fields could help us in understanding the processes leading to the magnetization of the universe. This type of study would complement earlier semi-analytical studies that investigated the possibility of magnetic field seeding by galactic winds in a cosmological context (Bertone et al., 2006).

The standard theory of magnetic field amplification in galaxies is the so called Galactic Dynamo based on the mean field theory (see Kulsrud, 1999 for a review). Within this theory, turbulent motions of the ionized gas driven by stellar activity lead to the generation of a random magnetic field ( $\alpha$ -effect). This random magnetic field (particularly its radial component) can then be amplified by the differential rotation of the galaxy ( $\Omega$ -effect), leading to an efficient dynamo action which results in an exponential growth of the magnetic field (the  $\alpha\Omega$ -dynamo). However, dynamos may probably only work efficiently if magnetic helicity is transported away from the differentially ro-

tating disc (Brandenburg and Subramanian, 2005). Gressel et al. (2008) performed high-resolution box-simulations which demonstrate that a dynamo may operate if supernova explosions release magnetic helicity from the disc. However, for an efficient magnetic helicity transport out from a galactic disk, galactic winds or galactic fountains may be required. This might be a problem particularly for massive galaxies due to the deeper potential well. The fact that it is difficult to get an efficient dynamo is generally addressed as the dynamo problem. Different solutions, e.g. turbulence driven by large-scale SN-bubbles (Ferriere, 1992b) or the Cosmic Ray Dynamo (Hanasz et al., 2009c) have been proposed. These solutions describe the exponential growth of a small-scale magnetic seed field which is amplified up to present-day values within several Gyr. However, recent observations indicate that magnetic fields in galaxies have been already very strong (comparable to present-day galactic magnetic fields) at very high redshifts, at a time when the universe was only  $t \approx 6$  Gyr old ( $z \approx 1$ ) (Bernet et al., 2008). Former observations of damped Ly- $\alpha$  systems by Wolfe et al. (1992) indicate that progenitors of galactic discs had magnetic fields of a few  $\mu\text{G}$  even at  $z \approx 2$  ( $t \approx 3$  Gyr). The very fast amplification required to generate the strong magnetic fields at high redshifts can probably not be achieved with any Galactic Dynamo model (see e.g. Arshakian et al., 2009). Thus, alternative possibilities for the amplification of galactic magnetic fields on shorter timescales need to be explored. Lesch and Chiba (1995) have shown analytically that strong magnetic fields in high redshift objects can be explained by the combined action of an evolving protogalactic fluctuation and electrodynamic processes providing magnetic seed fields. Wang and Abel (2009) performed numerical simulations of the formation of disc galaxies within an collapsing halo imposing a uniform initial magnetic field of  $10^{-9}$  G. The initial field was amplified by three orders of magnitude within approximately 500 Myr of evolution. The amplification might be due to the combined effects of magnetic field compression during the collapse and amplification of the uniform initial field by differential rotation as studied also in Kotarba et al. (2009). These studies indicate, that the amplification of magnetic fields might be a natural part of the galaxy formation process. However, interactions of galaxies, which were more frequent at earlier times, pose another promising possibility.

Although it would be worthwhile to consider cosmological studies of structure formation including magnetic fields in the long run, numerical studies of interacting magnetized systems in the local universe may serve as a first step towards a more complete scenario. These studies help us in understanding the morphological evolution of galaxies, their star formation histories (Springel et al., 2005c, Cox et al., 2008b, Bournaud et al., 2007, Di Matteo et al., 2008, Jesseit et al., 2009, Naab and Ostriker, 2009), and as we will show in this paper also their magnetic histories. The system NGC 4038/39, also known as the Antennae galaxies, is one of the best examples for an ongoing local merger. It is also the by far best observed interacting galaxy system.

In this paper we present further steps towards a more complete numerical representation of the Antennae system as a prototype for interacting galaxies. For the first time we will follow the evolution of the magnetic field in a galaxy interaction simulation. We also address the general question whether smoothed particle magnetohydrodynamics (SPMHD) is capable of following the evolution of magnetic fields in interacting systems at reasonable accuracy. In a previous paper we have shown that SPMHD is well suited for following the evolution of magnetic fields in isolated disk galaxies (Kotarba et al., 2009) so the study of interacting systems is a natural extension of this earlier study.

The paper is organized as follows: Section 3.2 summarizes the properties of the Antennae system as known from observations and theory. In section 3.3 we describe our numerical methods (section 3.3.1), the setup of the isolated disks (section 3.3.2.1) and the match to the observed Antennae system (section 3.3.2.2). A detailed analysis of the evolution of the system is presented in section 3.3.3, where we discuss the evolution of the magnetic field (section 3.3.3.1) the numerical stability of our simulations (section 3.3.3.2) and the self-regulation of the magnetic field amplification (section 3.3.3.3). In section 3.4 we describe our method to calculate artificial radio maps (section 3.4.1) and present applications to the isolated disk and the Antennae simulations (section 3.4.2). The artificial radio maps derived from the simulations can be compared against the radio observations of the system, thus providing a

further tool for constraining the numerical model and method. We conclude in section 3.5 and briefly discuss the relevance of our simulations in the context of hierarchical structure formation.

## 3.2 Properties of the Antennae systems

The Antennae system is relatively nearby, the estimated distances range from 13 to 25 Mpc. The smaller distances are favored by methods based on photometry of the red giant branch (Saviane et al., 2008), whereas the larger distances are estimated from observations of the Type Ia supernova 2007sr in the southern tail (Schweizer et al., 2008). But note also that sometimes even values up to  $d = 29$  Mpc have been adopted in the literature (Fabbiano et al., 2001, Zezas and Fabbiano, 2002). In this paper, we apply the conventional distance of 22 Mpc for all relevant flux calculations. Given the large variety of high quality observations (Whitmore et al., 1999, Neff and Ulvestad, 2000, Wilson et al., 2000, Hibbard et al., 2001, Chyży and Beck, 2004, Wang et al., 2004, Brandl et al., 2005, Zezas et al., 2006, Brandl et al., 2009) several authors tried to find initial conditions for simulations representing the Antennae system. Toomre and Toomre (1972) first presented restricted three-body simulations which already explained the formation of tidal arms and bridges as a result of tidal interaction during the merger. Follow-up investigations confirmed the early results by studying the detailed galactic dynamics using self-consistent, multiple-component galaxy models (Barnes, 1988). Further studies added star-formation (Mihos et al., 1993) to the modeling process and aimed at constraining the influence of dark halo mass profiles on the development and morphology of the tidal tails (Dubinski et al., 1996).

Recently, Karl et al. (2010) developed a new model of the system, not only focussing on its plane-of-sky appearance, but also on fitting the observed line-of-sight velocity structure (see also Karl et al., 2008). This study, alongside with new observations (Zhang et al., 2010), suggests that the localized intense starburst sites observed in the overlap-region can be explained as the imprint of the interpenetrating process of the two merging disks following their second encounter. These results contrast with previous numerical simulations which find the current orbital phase of the Antennae system to lie somewhere between the first and the second closest encounters (e.g. Toomre and Toomre, 1972, Barnes, 1988, Dubinski et al., 1996).

In this paper we use the model of Karl et al. (2010) and focus on the central region of the Antennae system and its magnetic fields. Fig. 3.1 shows a DSS image (Digitized Sky Survey (Blue), conducted with the Palomar and UK Schmidt telescopes and digitized by the Catalogs and Surveys Group of the Space Telescope Science Institute) of the central region of the Antennae system, i.e. the galactic disks and bases of the tidal tails. Overlaid are contours of total radio synchrotron emission (tracing the total magnetic field energy) and magnetic field vectors (derived from polarized intensity). The strength of the magnetic field is  $20 \mu\text{G}$  on average. The highest values of more than  $30 \mu\text{G}$  are reached in the overlapping region and the centers of the galaxies (Chyży and Beck, 2004). Thus, the magnetic field is roughly twice as strong as the typical values of 5 to  $10 \mu\text{G}$  observed in isolated spiral galaxies (e.g. Beck et al., 1996, Beck, 2007, Krause, 2009). On the upper left (east), there is a large region with highly ordered magnetic field lines, most probably tracing the gas flow at the root of the lower (southern) tidal tail. This gas is also visible as a HI ridge which extends far out along the southern tail (Hibbard et al., 2001). The structure of the magnetic field most likely traces the recent gas motions induced by tidal forces during the merger. Apparently, not much of the magnetic field structure of the progenitor galaxies have survived the interaction. The progenitors were presumably typical spirals with a spiral magnetic field pattern (see e.g. Beck, 2009a). As the magnetic field is tightly linked to the motion of the gas, the structure of the field in a system which has recently undergone a violent interaction should mainly resemble the recent kinematic evolution. It does not depend on long-term processes like the Galactic Dynamo, which is believed to be important in isolated spiral galaxies (e.g. Brandenburg and Subramanian, 2005, Gressel et al., 2008, Beck, 2009a, Dubois and Teyssier, 2010, Elstner et al., 2009, Gissinger et al., 2009, Hanaasz et al., 2009c). In other words, nonlinear systems

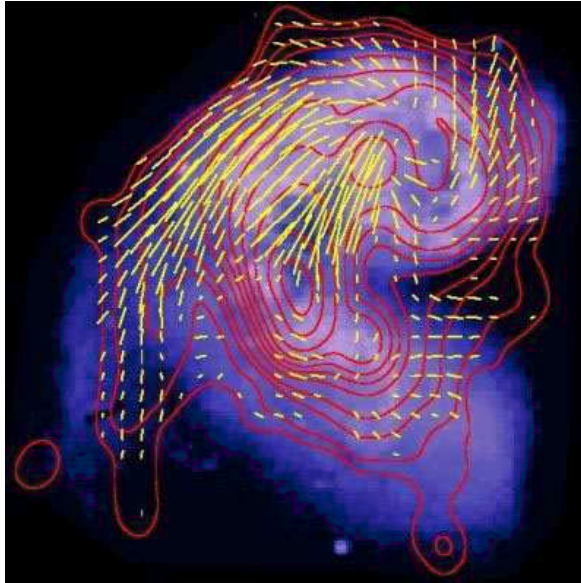


Figure 3.1: Total synchrotron emission (contours) and magnetic field vectors of polarized intensity at 4.86 GHz based on VLA data (yellow), overlaid on a DSS image (blue - white background) (Digitized Sky Survey, Palomar and UK Schmidt telescopes). The contour levels are 0.005, 0.12, 0.30, 0.53, 1.2, 2.1, 3.3, 5.3, 9.0, 17 and 24 mJy/beam-area. The resolution is  $17'' \times 14''$ . Credit: Chyzy (2005)

lose the memory of their initial conditions. Hence, numerical studies of the kinematics of merging systems including magnetic fields should be able to represent the observed magnetic fields in nearby interacting systems also without including long-term processes.

### 3.3 Simulations

#### 3.3.1 Numerical methods

All simulations were performed with the N-body/SPH-code GADGET (Springel, 2005). Gravitational interactions between the particles are evaluated with a hierarchical tree method (Barnes and Hut, 1986). The dynamics of Lagrangian fluid elements are followed using a SPH formulation which conserves both energy and entropy (Springel and Hernquist, 2002) including the evolution of magnetic fields which was implemented and tested by Dolag and Stasyszyn (2009). The code has already been used to investigate the evolution of magnetic fields in isolated spiral galaxies (Kotarba et al., 2009) and to compare different implementations of the SPH formulations and implementations in the SPH Code VINE (Wetzstein et al., 2009, Nelson et al., 2009). These studies demonstrated the importance of a sensible treatment of the numerical divergence of the magnetic field ( $\nabla \cdot \mathbf{B}$ ) in SPH simulations, as it can lead to artificial magnetic field growth. An implementation utilizing Euler potentials, which by construction poses a  $\nabla \cdot \mathbf{B}$ -free prescription of magnetic fields (see Price and Bate (2007) for more details) circumvents this problem. However, using the Euler potentials, the magnetic field is essentially mapped on the initial particle arrangement. Thus, if the initial configuration significantly changes shape during the simulation, regions carrying conflicting values of Euler potentials (i.e. values, which do no longer allow for a finite and unambiguous calculation of their gradients) can overlap and the ability of the Euler potentials to represent the magnetic field correctly is lost. This can lead to defec-

tive magnetic field calculations, especially in kinematically vigorous systems like interacting galaxies (see also Brandenburg, 2009). Therefore, all simulations presented in this paper have been performed using the standard (direct) magnetic field implementation. In contrast to Kotarba et al. (2009) we now also apply the Lorentz force and artificial magnetic dissipation applying an artificial magnetic dissipation constant of  $\alpha_B = 0.5$ . The latter does not only allow for magnetic field redistribution and reconnection, but also lowers the numerical divergence as it helps to smooth artificially high magnetic fields arising from intrinsic constraints of the numerical prescription. In this sense, it poses a regularization scheme similar to smoothing of the magnetic field. Both schemes reduce the numerical noise and  $\nabla \cdot \mathbf{B}$  errors by a similar amount (Dolag and Stasyszyn, 2009). However, the dissipation scheme is based on physical considerations, whereas the smoothing scheme is completely artificial. Thus, using the dissipation scheme, the factor  $h\nabla \cdot \mathbf{B}/|\mathbf{B}|$  (where  $h$  is the so called smoothing length, which poses the typical length scale of spatial derivatives in SPH calculations) is restricted to a value of approximately unity. Values of order unity have been shown to be low enough to guarantee a physically meaningful evolution of the magnetic fields in SPH simulations, particularly preventing artificial magnetic field growth. This threshold is actually defined by simulations using Euler potentials, for which the numerical divergence measure  $h\nabla \cdot \mathbf{B}/|\mathbf{B}|$  is of order unity although the physical divergence is zero by definition (see Kotarba et al., 2009 and section 3.3.3.2 for more details).

Furthermore, we do not use a viscosity limiter as suggested by Balsara (1998), because applying this limiter resulted in an increased growth of the magnetic field. This is most likely a numerical artefact, as the limiter lowers the viscosity in regions of strong shear flows, thus suppressing velocity diffusion and leading to a higher velocity dispersion and higher velocity gradients, which in turn lead to artificially enhanced magnetic field growth (Kotarba et al., 2009).

All simulations are performed including radiative cooling assuming a primordial gas composition together with a homogeneous and time-independent extragalactic UV background (Haardt and Madau, 1996). We include star formation and the associated supernova feedback, but exclude explicit supernova-driven galactic winds, following the sub-resolution multiphase model developed by Springel and Hernquist (2003), in which the ISM is treated as a two-phase medium (McKee and Ostriker, 1977, Johansson and Efstathiou, 2006): Cold clouds are embedded in a tenuous hot gas at pressure equilibrium. Stars form from the cold clouds in regions where  $n > n_{\text{th}} = 0.128 \text{ cm}^{-3}$  with the shortlived stars supplying an energy of  $10^{51}$  ergs to the surrounding gas by supernovae. The threshold density,  $n_{\text{th}}$ , is determined self-consistently in the model by requiring that the equation-of-state (EOS) is continuous at the onset of star formation. The parameters governing the model (see Tab. 3.1) are set to produce a star formation rate of  $\sim 1M_{\odot} \text{ yr}^{-1}$  for a Milky Way-like galaxy in isolation.

The implementation used in this paper has been tested in detail (Springel et al., 2001, Springel, 2005, Springel et al., 2005a, Dolag and Stasyszyn, 2009) and fulfills the established requirements for numerical methods. Particularly, Dolag and Stasyszyn (2009) have shown that the MHD-implementation performs well in various test problems, including different shock tube problems, the Fast Rotator (Balsara and Spicer, 1999), the Strong Blast (e.g. Balsara and Spicer, 1999) and the Orszag-Tang Vortex (Orszag and Tang, 1979).

### 3.3.2 Setup

#### 3.3.2.1 Isolated disks

The Antennae system has most likely formed through the interaction of two formerly isolated spiral galaxies. In this section we present the properties of the isolated progenitor model disks used in our simulations. The initial conditions for the spiral galaxies are realized using the method described by Springel et al. (2005a) which is based on Hernquist (1993). The galaxies consist of a Hernquist (1990) profile cold dark matter halo, a rotationally supported exponential stellar disk, an exponential gas

DISK PARAMETERS		
total mass	$M_{\text{tot}}$	$1.34 \times 10^{12} M_{\odot}$
disk mass	$M_{\text{disk}}$	$0.075 M_{\text{tot}}$
bulge mass	$M_{\text{bulge}}$	$0.025 M_{\text{tot}}$
mass of the gas disk	$M_{\text{gas}}$	$0.2 M_{\text{disk}}$
exponential disk scale length	$l_D$	8.44 kpc
scale height of the disk	$h_D$	$0.2 l_D$
bulge scale length	$l_B$	$0.2 l_D$
spin parameter	$\lambda$	0.1
virial velocity of the halo	$v_{\text{vir}}$	160 km s <sup>-1</sup>
half mass radius	$R_{\text{half}}$	$\approx 12$ kpc
half mass circular velocity	$v_{\text{half}}$	$\approx 249$ km s <sup>-1</sup>
half mass rotation period	$T_{\text{half}}$	$\approx 295$ Myr
initial magnetic field	$B_0$	$10^{-9}$ to $10^{-6}$ G
MULTI-PHASE MODEL PARAMETERS		
gas consumption timescale	$t_{\text{MP}}$	8.4 Gyr
mass fraction of massive stars	$\beta_{\text{MP}}$	0.1
evaporation parameter	$A_0$	4000
effective SN temperature	$T_{\text{SN}}$	$4 \times 10^8$ K
cold cloud temperature	$T_{\text{CC}}$	1000 K

Table 3.1: Parameters of initial setup

Component	initial particle number	fixed gravitational softening length $\epsilon$ [pc] <sup>a,b</sup>
Halo	$4.0 \times 10^5$	$80/h$
Disk	$4.8 \times 10^5$	$20/h$
Bulge	$2.0 \times 10^5$	$20/h$
Gas	$1.2 \times 10^5$	$20/h$
Stars	0	$20/h$
Total	$1.2 \times 10^6$	-

<sup>a</sup> The minimum SPH smoothing length for the gas particles is  $1.0\epsilon$ .

<sup>b</sup> The Hubble constant is assumed to be  $h = 0.71$  in this paper.

Table 3.2: Particle numbers and softening lengths

disk and a stellar Hernquist (1990) bulge component (see Karl et al., 2010 for more details). The halo, stellar disk and bulge particles are collisionless N-body particles. The gas is represented by SPH particles.

Possible initial conditions resulting in a good fit of the present-day properties of the Antennae galaxies have been tested in a large parameter study by Karl et al. (2010) (see also section 3.3.2.2). In this paper we present results using the initial condition parameters of this study which result in the best match to the central region of the Antennae system. The parameters describing the initial conditions of the two galaxies can be found in Table 3.1. Particle numbers and softening lengths are listed in Table 3.2. The disks are kinematically stable if evolved in isolation as has been shown in detail in Kotarba et al. (2009). In the following we thus only address the evolution of the magnetic fields.

For simplicity, the initial seed magnetic field is assumed to be homogeneous with only one non-vanishing component of  $B_x = B_0$ . This choice is justified, as it takes more than one Gyr of dynamic evolution until the present plane-of-sky-appearance of the system has developed in our simulations. Thus, the particular structure of the initial magnetic field should not be of significance for the final result. We use two different values for the initial field,  $B_0 = 10^{-9}$  G and  $B_0 = 10^{-6}$  G for the isolated galaxies, and additionally two intermediate values,  $B_0 = 10^{-8}$  G and  $B_0 = 10^{-7}$  G for the Antennae simulations. The smallest value of  $B_0 = 10^{-9}$  G is the typical value of the observed intergalactic

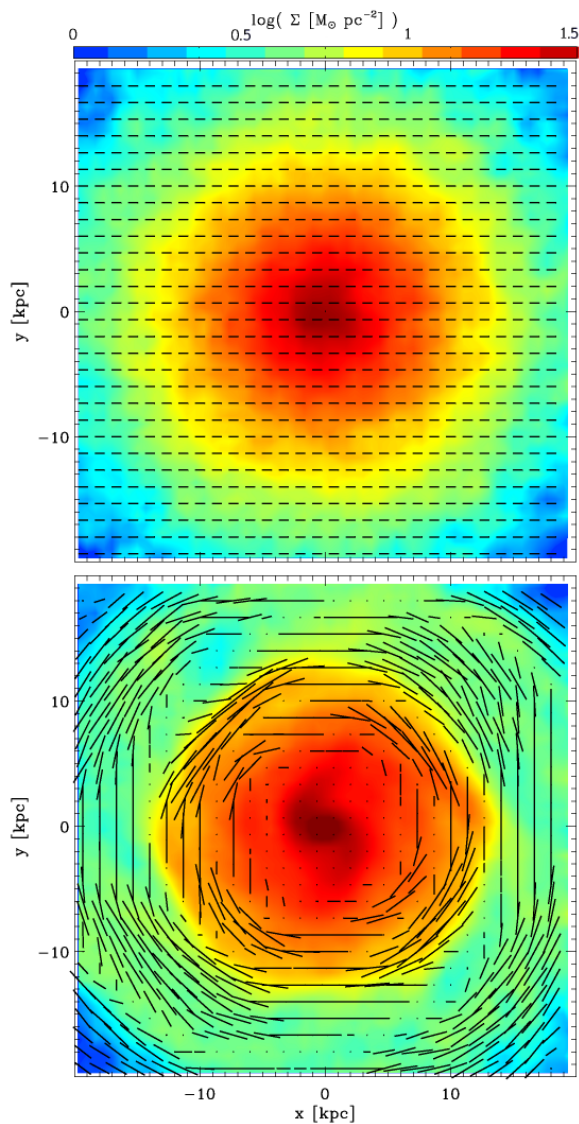


Figure 3.2: Gas surface density  $\Sigma$  at time  $t = 0$  Myr (upper panel) and  $t = 400$  Myr (lower panel), overlaid with magnetic field vectors for the simulation with  $B_0 = 10^{-6}$  G. The length  $l$  of the vectors is normalized to a minimal value  $B_{\text{min}} = B_0/\sqrt{2}$  and displayed logarithmically according to  $l = 5 \log(B/B_{\text{min}})$ , i.e.  $l = 0$  corresponds to  $B \approx B_{\text{min}}$  or smaller and  $l = 5$  to  $B = 10B_{\text{min}}$ .

magnetic field  $B_{\text{IGM}}$  (see e.g. Kronberg et al., 2008) and the highest,  $B_0 = 10^{-6}$  G, is motivated by the typical value of several  $\mu\text{G}$  observed in spiral galaxies. As much larger or much smaller values are not observed, these values cover the range of realistic initial fields. However, we have also performed a simulation of the Antennae system with an initial magnetic field value of  $B_0 = 10^{-4}$  G in order to study the physical behaviour of the system in an extreme situation. We do not include neither large-scale dynamo processes, nor turbulent motions on scales smaller than  $\approx 100$  pc which are not resolved in our simulations. The mean velocity dispersion  $\sigma = \sqrt{\langle \bar{v}^2 \rangle_{\text{n.n.}} - \langle \bar{v} \rangle_{\text{n.n.}}^2}$  (where the mean is taken over the nearest  $64 \pm 5$  neighbors within the smoothing kernel) during the isolated disc simulation is of order of  $5 \text{ km s}^{-1}$  with approximately 30% of the particles having dispersions  $> 5 \text{ km s}^{-1}$  and only a few percent  $> 10 \text{ km s}^{-1}$ . These values are somewhat lower than the values found in recent grid simulations by Wang and Abel (2009) (see Fig. 3 of their paper) and Agertz et al. (2009). They both find typical dispersion values of approximately  $10 \text{ km s}^{-1}$  in their comparable disc galaxy simulations. However, these authors use lower temperature floors for the dense gas component found in the star-forming regions, resulting in a clumpier disc structure and thus probably in an enhanced turbulence in the hot diffuse component of their discs. This may explain the discrepancy in the measured velocity dispersions. Since the dispersion values in our simulations are rather low, we do not expect any significant amplification of the magnetic field in the isolated galaxies. Consequently, the magnetic field gets only redistributed during the simulation, developing a spiral pattern as the differential rotation continues to wind it up (Fig. 3.2), while the overall value of  $|\vec{B}|$  remains of order  $B_0$  throughout the simulation. After the magnetic field has been wound up by differential rotation, it is highly ordered in the disc region ( $r > 5 \text{ kpc}$ ) and more "turbulent" in the inner region of the galaxy. Thus, the inner magnetic field is not visible in the lower panel of Fig. 3.2 due to the averaging calculation of our plotting routines.

The evolution of the absolute value of the magnetic field as a function of time is shown in Fig. 3.3 for  $B_0 = 10^{-6}$  G (red line) and  $B_0 = 10^{-9}$  G (orange line). In the beginning of the simulation, the initially homogeneous magnetic field gets wound up and thereby amplified due to the differential rotation and associated shear flows by roughly a factor of two (see also Kotarba et al., 2009). After approximately one half mass rotation period the magnetic field has been redistributed to a mostly toroidal pattern by the winding process, and the amplification ceases. In the subsequent evolution, the strength of the field decreases slowly due to magnetic dissipation, which is the only process causing magnetic field diminution in our simulations. The velocity dispersion of the gas also leads to the development of a  $z$ -component of the magnetic field (not shown) which, however, remains smaller than all other components by more than one order of magnitude throughout the simulation. In summary, the magnetic field gets redistributed to form a spiral pattern (Fig 3.2) and retains on average its initial value throughout one Gyr of evolution. This behaviour is the same for both the weaker and the stronger initial magnetic field.

Fig. 3.4 shows the mean numerical divergence  $h\nabla \cdot \mathbf{B}/|\mathbf{B}|$  as a function of time in isolated galaxy simulations (red line) with  $B_0 = 10^{-6}$  G. The mean was taken over three simulations with the magnetic field in the plane of the disk and inclined as in the setup of the Antennae simulation (see section 3.3.2.2), respectively. Although the numerical noise increases with time, it remains clearly below the tolerance value of unity (see also section 3.3.3.2).

The SFR in the isolated disks is roughly constant throughout the simulations (not shown). Starting at a value of approximately  $2 M_\odot \text{ yr}^{-1}$  and then decreasing slightly to approximately  $1.7 M_\odot \text{ yr}^{-1}$  after 1.3 Gyr of evolution due to gas consumption. There is no significant difference in the evolution of the SFR compared to the same simulation without any magnetic field, indicating that the presence of a global magnetic field of order  $10^{-6}$  G or lower does not affect the gas flow enough to hinder or abet the collapse of gas.

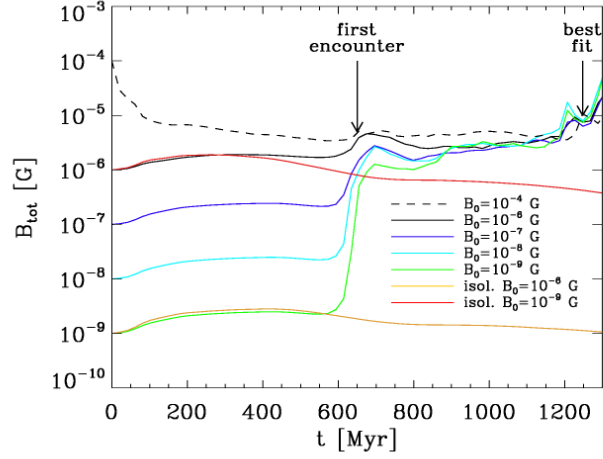


Figure 3.3:  $B_{tot} = \sqrt{B_x^2 + B_y^2 + B_z^2}$  as a function of time for the Antennae simulations with an initial field of  $B_0 = 10^{-9}$  G (green line),  $B_0 = 10^{-8}$  G (blue line),  $B_0 = 10^{-7}$  G (dark blue line),  $B_0 = 10^{-6}$  G (black line) and  $B_0 = 10^{-4}$  G (black dashed line), respectively, and for the progenitor disks simulations with  $B_0 = 10^{-9}$  G (orange line) and  $B_0 = 10^{-6}$  G (red line), respectively. The magnetic field of the isolated disks does not evolve significantly. For the mergers the field is amplified to  $\approx 10\mu\text{G}$  independent of the initial field strength in the disks.

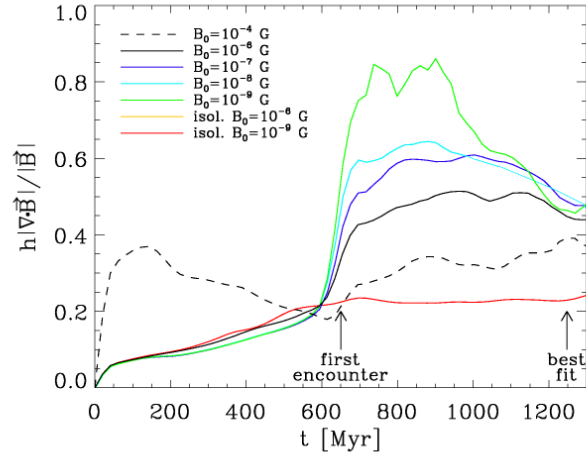


Figure 3.4:  $h|\nabla \cdot \mathbf{B}|/|\mathbf{B}|$  as a function of time for the Antennae simulations with an initial field of  $B_0 = 10^{-9}$  G (green line),  $B_0 = 10^{-8}$  G (blue line),  $B_0 = 10^{-7}$  G (dark blue line),  $B_0 = 10^{-6}$  G (black line) and  $B_0 = 10^{-4}$  G (black dashed line), respectively, and mean divergence for isolated simulations with  $B_0 = 10^{-6}$  G (red line). The values stay below the tolerance value of unity throughout the simulation in every run.

INITIAL ORBIT PARAMETERS		
disk orientation	NGC 4038	NGC 4039
$\iota$	$60^\circ$	$60^\circ$
$\omega$	$30^\circ$	$60^\circ$
ellipticity	$e$	0.96
pericenter distance	$r_p$	$7 \text{ kpc h}^{-1}$
initial separation	$r_{\text{sep}} = r_{\text{vir}}$	$160 \text{ kpc h}^{-1}$
ANALYSIS PARAMETERS		
time of best match	$t_{\text{BM}}$	1.25 Gyr
direction to observer <sup>a</sup>	$(\theta, \psi, \phi)$	(208, 282, 0)
distance scale	$\mathcal{L}$	2.0

<sup>a</sup> The viewing direction is specified by a series of rotations in the following order around the  $x$ -,  $y$ -, and  $z$ -axis.

Table 3.3: Antennae simulation parameters

### 3.3.2.2 The match to the Antennae system

The simulations presented here are taken out of a suit of self-consistent simulations designed as a large parameter study to match the morphological and kinematical properties of the Antennae (see Karl et al., 2010). In this study, we initially set two equal-mass galaxies, each modeled as in section 3.3.2.1 and residing in its own dark matter halo, on nearly-parabolic Keplerian two-body orbits with given ellipticity  $e$ , pericenter distance  $r_p$ , and initial separation  $r_{\text{sep}}$ . The disk orientation in the orbital plane is given by a pair of angles  $(\iota, \omega)$ , which, for each galaxy, specify the adopted inclination with respect to the orbital plane and the pericentric argument (Toomre and Toomre, 1972). There is no hot gas component surrounding the galaxies initially. The initial field is assumed to be homogeneous with only one non-vanishing component of  $B_x = B_0$ . After the simulation has finished we determine the time of best match, the viewing direction of the observer, a common center-of-mass, and a distance scale factor  $\mathcal{L}$  in order to create a mock observation which can be compared to projections of the HI data cube from Hibbard et al. (2001). If the result does not prove satisfactory up to a level admissible by optical inspection, the simulation is repeated choosing a different set of initial parameters. Several key parameters regarding the elliptical orbit, the relative orientation of the galaxy disks, and the internal structure of the progenitor galaxies are varied in order to find the best match (for details, see Karl et al., 2010). The final parameters used in this study are shown in Tab. 3.3.

Starting on their initially set orbit, both galaxies evolve corresponding to their isolated evolution (section 3.3.2.1) until they reach the point of their first closest approach ( $t \approx 650 \text{ Myr}$ ). At this time, the prominent tidal arms, which we use as tracers for the dynamical history of the encounter, start to develop. On the other hand, the detailed structure of the galactic main bodies can only be seen in our simulations resulting from the recent splash during the second encounter ( $t \approx 1180 \text{ Myr}$ ). The time of best fit, i.e. the time, at which the simulation matches the appearance of the Antennae system in the sky and the observed line-of-sight velocities, is reached at  $t_{\text{BM}} \approx 1250 \text{ Myr}$ .

### 3.3.3 Evolution of the Antennae system

#### 3.3.3.1 Magnetic field evolution

We have run several simulations using the setup described in section 3.3.2.2. The initial field was again assumed to be homogeneous with only one non-vanishing component of  $B_x = B_0$  at the beginning of the simulation. We performed simulations with five different initial magnetic field strengths of  $B_0 = 10^{-9}, 10^{-8}, 10^{-7}, 10^{-6}$  and  $10^{-4} \text{ G}$  for comparison.

Fig. 3.5 shows the line-of-sight magnetic pressure  $P_{\text{mag}} = B^2/8\pi$  in the simulation with  $B_0 = 10^{-6} \text{ G}$  at different time steps, overlaid with contours of the stellar surface density  $\Sigma_{\text{stars}}$ . The particle data

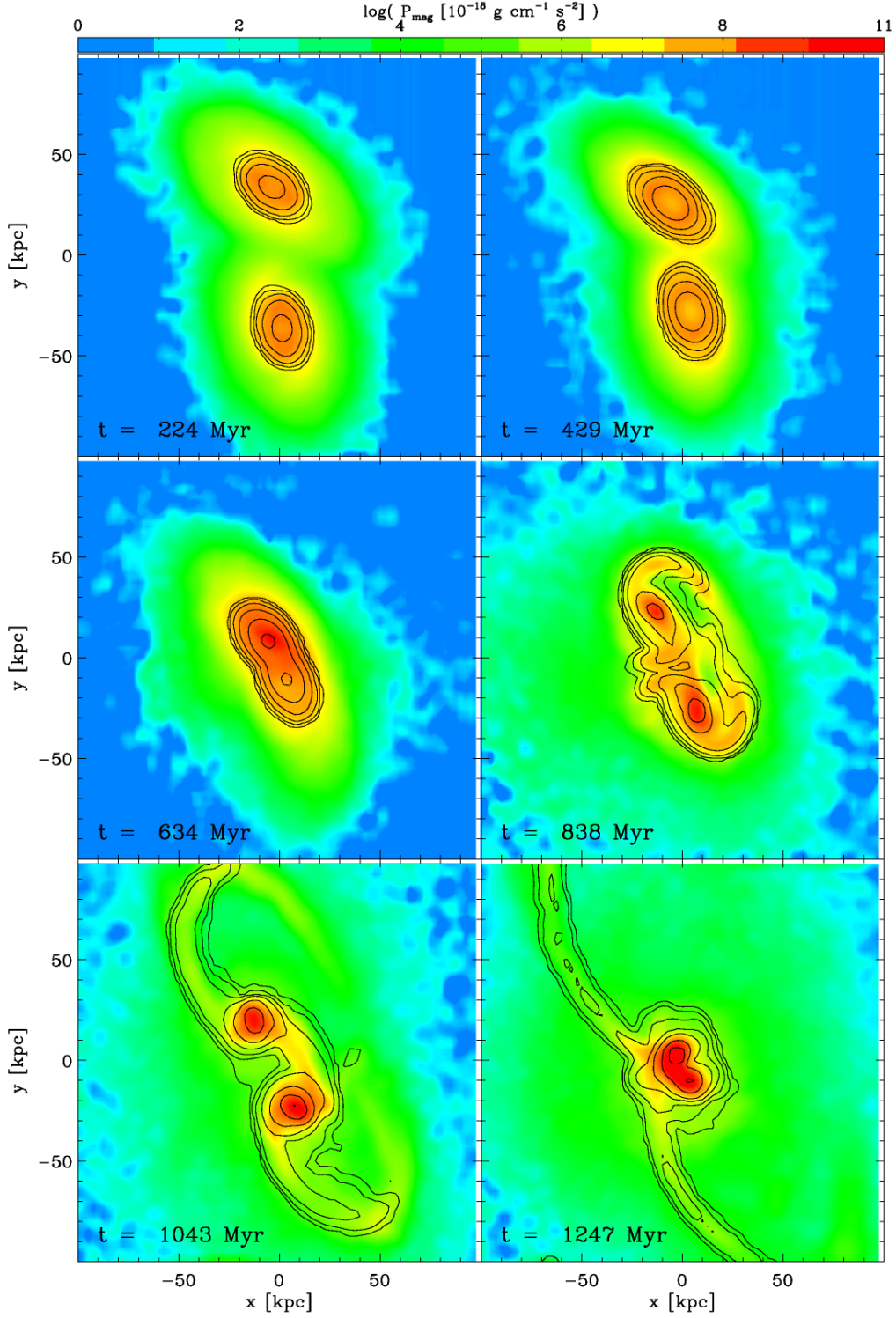


Figure 3.5: The Antennae simulation with an initial field of  $B_0 = 10^{-6}$  G. Colors visualize the line-of-sight magnetic pressure  $P_{\text{mag}} = B^2/8\pi$  (in units of  $10^{-18} \text{ g cm}^{-1} \text{ s}^{-2}$ ) and contours correspond to stellar surface density  $\Sigma_{\text{stars}}$ . The contour levels are 0.005, 0.02, 0.08, 0.32, 1.28, 5.12 and  $20.48 M_{\odot} \text{ pc}^{-2}$ .

has been transferred to a grid of  $80 \times 80$  cells using the TSC procedure (Triangular Shaped Cloud, see e.g. Hockney and Eastwood, 1988). As it takes roughly 600 Myr (i.e. approximately two half mass rotation periods) before the first encounter of the galaxies, the magnetic field has enough time to redistribute and form a realistic configuration in each of the galaxies prior to the merger (upper left and right panel, see also section 3.3.2.1 and Fig. 3.2). The formation of the tidal arms is visible in the stellar density distribution but also in the distribution of magnetic pressure (central right and lower left panel). At time of best fit (lower right panel) most of the gas has been driven into the central region of the Antennae system. Thus, the magnetic pressure reaches its highest values in this region.

The temporal evolution of the absolute values of the magnetic fields for the simulations with different initial field values is shown in Fig. 3.3 (black dashed, black, dark blue, blue and green lines). In all cases (except for the run with  $B_0 = 10^{-4}$  G), similarly to the simulations of the isolated galaxies (red and yellow lines), we see a mild amplification of the initial magnetic field in the beginning of the simulation due to the winding process. However, as the disks are not oriented parallel to the  $xy$ -plane, this initial amplification is slightly weaker than in the isolated disks. The reason is that the initial magnetic field now does not lie in the plane of the disks and thus the radial component of the magnetic field is weaker compared to the simulations of the isolated galaxy. In the case with the weakest initial field the magnetic field gets amplified by more than two orders of magnitude during the interaction, whereby the most violent amplification occurs during the first encounter at  $t \approx 650$  Myr. In the case with  $B_0 = 10^{-6}$  G, however, the amplification is relatively modest. The evolution of the magnetic field for the simulation with the highest initial field (dashed line) is different: At the very beginning of the simulation, the high magnetic overpressure drives the gas out of the galaxies, thus "blowing" them up. Consequently, the magnetic field decreases by one order of magnitude within 100 Myrs due to attenuation and continues to decrease until the first encounter. At the time of the first encounter, it is only very weakly amplified. At the time of best match, the value of the magnetic field is approximately  $10 \mu\text{G}$  within the numerical precision, independent of the initial seed field. This is roughly half the value derived from observations. The origin of this discrepancy might be observational as well as numerical and will be briefly addressed in section 3.4.2.

### 3.3.3.2 Numerical stability

Fig. 3.4 shows the arithmetic mean of the numerical divergence  $h \nabla \cdot \mathbf{B} / |\mathbf{B}|$  as a function of time for the Antennae simulations with the different initial magnetic field strengths (black dashed, black, dark blue, blue and green lines). For each simulation, there is an increase of the divergence during the first encounter, whereby the value of the numerical divergence increases with decreasing initial magnetic field. This is not surprising: If the magnetic tension is strong enough to overcome the gas pressure, the Lorentz force acts on the particles in a way that magnetic tension is released. On the other hand, if the magnetic pressure is significantly weaker than the gas pressure, chaotic motions of the particles driven by the encounter can fold the magnetic field on small scales - as small as the smoothing length - until the magnetic tension becomes dominant. This leads to a more irregular magnetic field and a higher numerical divergence. Thus, the numerical divergence is lowered in the presence of a stronger magnetic field.

Fig. 3.6 shows the mean line-of-sight numerical divergence  $h \nabla \cdot \mathbf{B} / |\mathbf{B}|$  in the simulation with  $B_0 = 10^{-6}$  G at different time steps, overlaid with contours of the stellar surface density  $\Sigma_{\text{stars}}$  to indicate the morphology of the galaxies. The particle data has been transferred to a grid using the TSC procedure as before in Fig. 3.5. Before the first encounter (central left panel), there are regions of high (of the order of 10) numerical divergence at the "edges" of the galaxies (upper panels, compare also Fig. 3.5). This high numerical divergence measures can be ascribed to defective SPH calculations in these regions. The particle density there decreases to zero due to the vacuum boundary conditions (which are usually used in this type of simulations). Thus, the particle distribution within one smoothing length changes rather abruptly. Some SPH operators, including the divergence operator, are not well

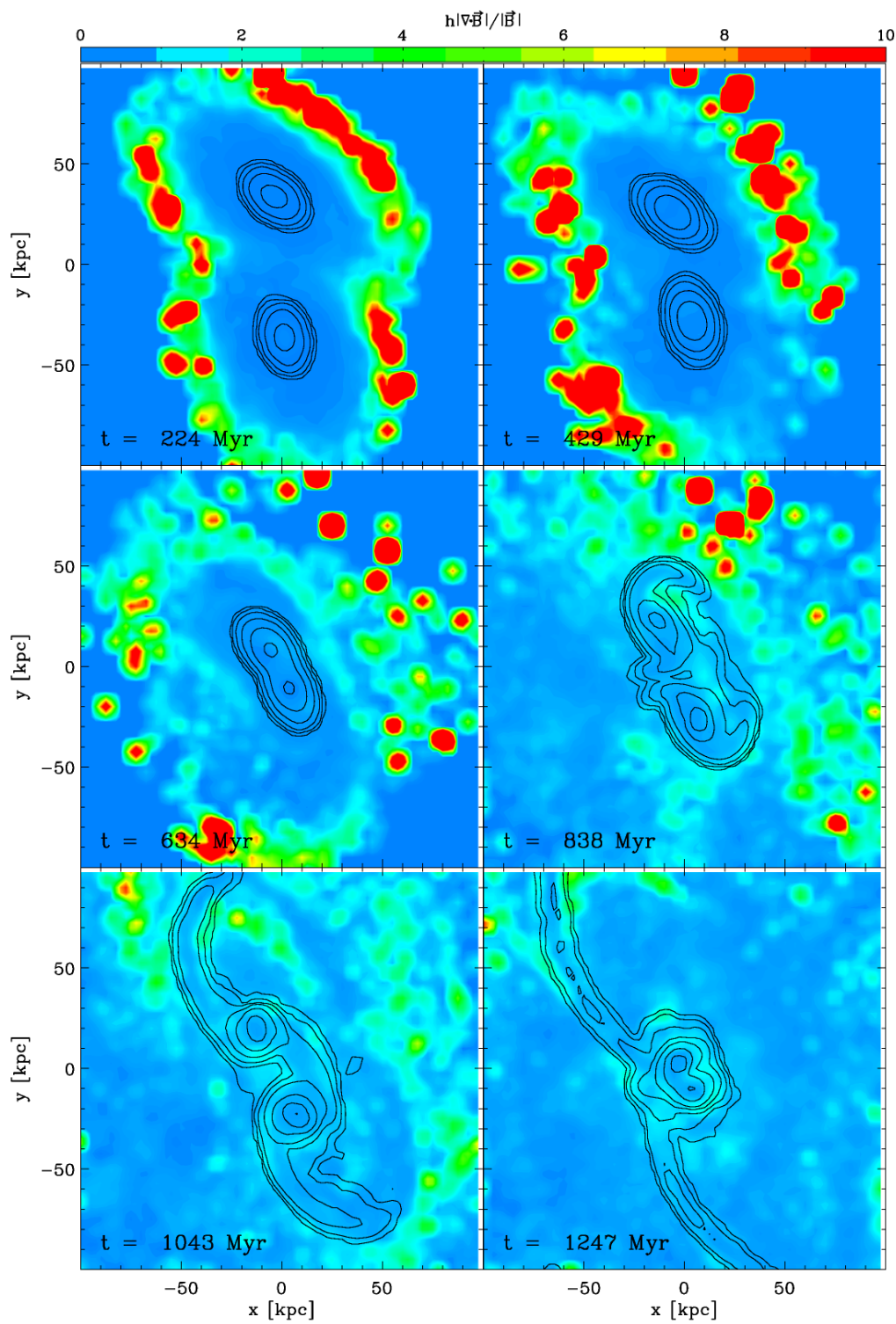


Figure 3.6: The Antennae simulation with an initial field of  $B_0 = 10^{-6}$  G. Colors visualize the mean line-of-sight numerical divergence  $h\nabla\cdot\mathbf{B}/|\mathbf{B}|$  and contours correspond to stellar surface density  $\Sigma_{\text{stars}}$ . The contour levels are 0.005, 0.02, 0.08, 0.32, 1.28, 5.12 and  $20.48 M_{\odot} \text{pc}^{-2}$ .

sampled in such a situation, leading to high numerical errors in these estimators. As soon as the particle distribution is smoothed out as a consequence of the interaction (central left to last panel, compare also Fig. 3.5), this effect vanishes. However, it is only a small fraction of particles which are affected by this defective calculation. Thus, the arithmetic mean of the numerical divergence is lower in the beginning of the simulation than after the first encounter (Fig. 3.4). Furthermore, comparing Fig. 3.5 with Fig. 3.6 shows that in regions with the highest magnetic field values the numerical divergence is relatively low.

We have performed the same simulation with an initial magnetic field of  $10^{-6}$  G but without applying the Lorentz force (not shown). In this simulation the magnetic field got amplified extremely violently by orders of magnitude to clearly unphysical values after the first encounter. The magnetic field got amplified much above the maximal value seen in the simulations presented above, and did not converge. This behaviour shows, that it is actually the Lorentz force, i.e. the backreaction of the magnetic field on the gas, which constrains the amplification. The unrealistic violence of the amplification can be traced back to the high  $\nabla \cdot \mathbf{B}$  values of several hundreds developing in this simulation. However, as applying the Lorentz force helps to lower the divergence in SPMHD simulations, these results are not surprising.

This can also be seen in simulations including the Lorentz force, but starting with an initially very weak magnetic field. We have performed an additional simulation with  $B_0 = 10^{-20}$  G (not shown). In this simulation, the divergence grew to a maximal value of 2.5 during the first encounter, subsequently dropping again to values below unity. The magnetic field - and thus the Lorentz force - was very weak in this simulation, nevertheless, the divergence was still lowered to values of order unity. The magnetic field was amplified by ten orders of magnitude to a value of  $10^{-10}$  G during the first encounter, which is still four orders of magnitude lower than the maximal value seen in Fig. 3.3. This demonstrates that one can not start with an arbitrary low magnetic field and end up at micro-gauss levels after the first encounter. However, as the subsequent interaction between the two galaxies drives further turbulence, the magnetic field continued to grow after the first encounter at a rate of approximately one order of magnitude per 100 Myr. Thus, at a time of 1.1 Gyr, the magnetic field reached a value of  $\approx 10^{-6}$  G and slowly converged towards the maximal value seen in Fig. 3.3. Note that during this steady growth of the magnetic field the numerical divergence was actually decreasing.

In the simulation with  $B_0 = 10^{-4}$  G, the numerical divergence measure grows up to a value of approximately 0.4 already at the beginning of the simulation. This is because the high magnetic pressure "blows up" the galaxies and thus excites strong turbulent motions which in turn result in a more irregular magnetic field. We note that this behaviour shows that the value of the numerical divergence mainly depends on the irregularity of the magnetic field, which is also the reason why the numerical divergence remains relatively small in the simulations of the quiescent evolution of the isolated galaxies (red line). This can also be understood theoretically: The numerical SPH divergence-operator calculates the weighted sum of the differences of the magnetic field of a particle and its neighbouring particles within a smoothing length. Thus, the higher the degree of irregularity of the magnetic field, the higher the numerical divergence. However, the numerical divergence should not be mistaken for a physical divergence, as it is only a measure of numerical small-scale (i.e. smaller than one smoothing length) fluctuations of the field. This can be seen in simulations using Euler-Potentials, where the physical divergence is zero by definition, but the numerical divergence has still values of order unity (see Kotarba et al., 2009) for a tangled magnetic field. Thus, lowering the numerical divergence below this tolerance value of unity should be sufficient to guarantee a physically meaningful evolution of the magnetic field. Using the Euler-Potentials in the Antennae simulations would most probably result in a much weaker amplification of the magnetic field which should not be considered physical, because Euler-Potentials are not suitable for simulations of kinematically vigorous system (see section 3.3.1).

Moreover, the applied SPH implementation is geared to ensure that the numerical divergence measure does not alter the evolution equations for the magnetic field (see Dolag and Stasyszyn, 2009).

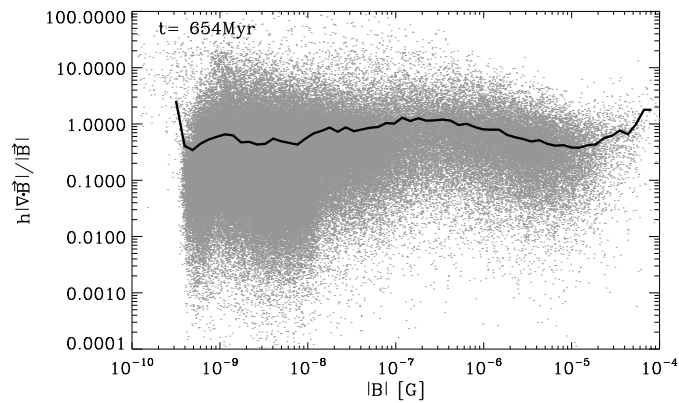


Figure 3.7:  $h\nabla \cdot \mathbf{B}/|\mathbf{B}|$  as a function of the total magnetic field for the Antennae simulation with  $B_0 = 10^{-9}$  G at time of the first encounter ( $t \approx 650$  Myr). Grey dots correspond to the values of each particle, the solid line is the mean value for a given magnetic field strength. The values of the numerical divergence are widely distributed over the range of magnetic field strength.

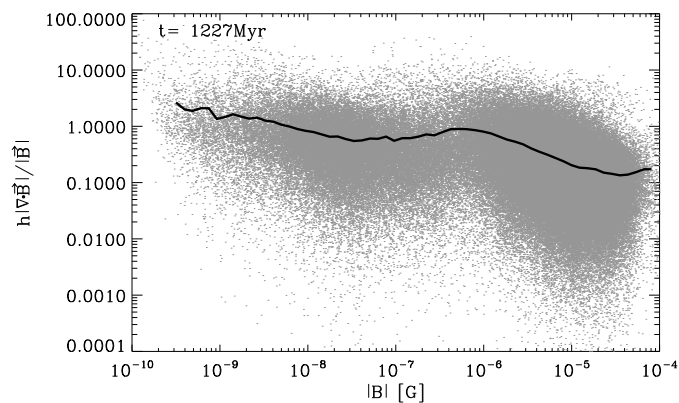


Figure 3.8: Same as Fig. 3.7, but at the time of best fit ( $t_{\text{BM}} \approx 1250$  Myr). The values of the numerical divergence are widely distributed over the range of magnetic field strength and even lower for higher magnetic field values.

Thus, even if the divergence operator measures a numerical divergence, it does not influence the magnetic field evolution directly. This has been shown by Price and Monaghan (2005), who demonstrated that a magnetic monopole can be advected without causing numerical instabilities. It can also be seen comparing Fig. 3.3 and Fig 3.4: The lower the initial magnetic field, the weaker the magnetic field shortly after the first encounter, although the numerical divergence is higher for lower initial fields. Thus, there is no direct dependance of the magnetic field strength on the value of the numerical divergence. Fig. 3.7 and 3.8 show the numerical divergence as a function of the magnetic field strength at the time of the first encounter and at the time of the best fit, respectively. We show the plots for the simulation with  $B_0 = 10^{-9}$  G, as the amplification of the magnetic field is the most efficient and the numerical divergence is the highest in this simulation. Thus, a possible dependance of the magnetic field on the divergence measure should be the best visible in this simulation. However, there is no significant correlation, and the values of the numerical divergence are widely distributed over the range of magnetic field strength. At the time of best fit, they are even lower for higher magnetic field values (see also Fig. 3.6). This behaviour is qualitatively the same for all initial magnetic field values. Of course, the amplification is more efficient for lower initial fields, thus one could argue that it is the amplification efficiency which depends on the numerical divergence value. However, in the beginning of the simulation with  $B_0 = 10^{-4}$  G the magnetic field actually *decreases* with increasing numerical divergence showing that non-vanishing numerical divergence not necessarily leads to an amplification of the magnetic field. Rather, the amplification efficiency is restricted by the strength of the Lorentz force: The higher the magnetic field, the stronger the Lorentz force braking the motions which lead to an amplification of the magnetic field. Thus, the lower the initial field, the more efficient its amplification. Hence we conclude that as long as the numerical divergence remains as low as the numerical divergence seen in simulations with Euler-Potentials (i.e. lower than unity), the evolution of magnetic fields in SPH simulations is physically meaningful.

### 3.3.3.3 Self-regulation of the amplification

The magnetic field is expected to get enhanced through field line compression in shocks and field line stretching in shear flows. However, in the framework of MHD, any motion of gas leading to an amplification of the magnetic field will be suppressed by the magnetic field itself via the Lorentz force as soon as the magnetic energy gets comparable to the kinetic energy of the gas. The magnetic energy is then converted into kinetic energy of the gas, thus maintaining equipartition between the magnetic and gas kinetic energy density, or equivalently, the magnetic and the hydrodynamic pressure  $P_{\text{hyd}} = 1/2\rho v^2$ . In particular, the magnetic field is expected to be in equipartition with the turbulent energy of the gas (see e.g. Beck, 2007 and Chyży et al., 2007b), as only velocity gradients can lead to an amplification of the magnetic field via the induction equation. Thus, the self-regulation of the strength of the magnetic field seen in our simulations can be ascribed to equipartition between the turbulent and magnetic pressures. In order to analyze this behavior, we have examined the central region of the system in more detail, and also performed a comparison simulation without magnetic fields. We define the turbulent pressure as  $P_{\text{turb}} = 1/2\rho v_{\text{turb}}^2$ , with the turbulent velocity of the  $i$ -th particle defined as

$$v_{\text{turb}}(i) = \frac{1}{3} \sqrt{\sum_k v_{\text{turb}}^k(i)^2}, \quad (3.1)$$

where  $k = x, y, z$  and

$$v_{\text{turb}}^k(i) = \sqrt{\frac{\sum_{j=1}^N v^k(j) - v^k(i)}{N}}, \quad (3.2)$$

with  $N = 64 \pm 5$  being the number of the nearest neighbors.

We briefly note that the thermal pressure does not directly affect the evolution of the magnetic fields. According to the induction equation of MHD, the magnetic field evolution is determined by the velocity field alone.

Fig. 3.9 shows from left to right and top to bottom the gas number density  $n$ , the turbulent pressure  $P_{\text{turb}}$ , the stellar surface density  $\Sigma_{\text{stars}}$ , the velocity dispersion  $\sigma$  (calculated as before in section 3.3.2.1), the magnetic pressure  $P_{\text{mag}}$  and  $\beta = P_{\text{turb}}/P_{\text{mag}}$  in the inner region (innermost 28 kpc) of the system at time of best fit for the simulation with  $B_0 = 10^{-6}$  G. This value of  $B_0$  is comparable to the typical magnetic field value observed in spiral galaxies, which is why we have chosen this simulation for our analysis. Assuming a distance of 22 Mpc this region would comprise approximately  $4.37'$ . Chyży and Beck, 2004 use a distance of 19.2 Mpc and observe an area of  $\approx 3.5'$ , scaled to a distance of 22 Mpc this gives an area of approximately 22.4 kpc across. Thus, our model has a bigger extent by a factor  $\approx 28/22.4 = 1.25$ , which still is in qualitative agreement with observations (see section 3.2). The particle data has been transferred to a spatial grid using the TSC procedure and averaged over the  $z$ -direction (i.e. the line-of-sight) with  $z \in [-14 \text{ kpc}, 14 \text{ kpc}]$  and  $z = 0$  defined as the center of mass of the system. The turbulent and magnetic pressures are given in units of  $10^{-15} \text{ g cm}^{-1} \text{ s}^{-2}$ , corresponding to  $6.242 \times 10^{-4} \text{ eV cm}^{-3}$ , i.e. the highest values are approximately  $100 \text{ eV cm}^{-3}$ .

In order to be able to recognize whether the magnetic field itself has a significant effect on the turbulent pressure in the system, we have applied the same analysis to a simulation without magnetic fields. Fig. 3.10 displays from left to right the mean line-of-sight gas number density  $n$ , turbulent pressure  $P_{\text{turb}}$  and stellar surface density  $\Sigma_{\text{stars}}$  in the inner region (innermost 28 kpc) of the not magnetized system at time of best fit (calculated as before in Fig. 3.9).

Comparing Fig. 3.9 and Fig. 3.10 shows that in the simulation with magnetic fields (Fig. 3.9) the gas distribution is more compact, whereas the turbulent pressure distribution is "disrupted". Particular in the northern (upper) galaxy the turbulent pressure distribution is more extended in the magnetized case (Fig. 3.9) than in the simulation without magnetic fields (Fig. 3.10). These differences probably develop because the gas is more likely to move along magnetic field lines than perpendicular to them and thus the velocity distribution is altered. The gas distribution is in both cases more extended than the stellar distribution, with the stellar density being highest in the centers of the galaxies ( $\approx 10^3 M_{\odot} \text{ pc}^{-2}$ ). The stellar distribution is not significantly changed in the presence of a magnetic field. Since the galaxies have a low gas fraction (20%), the total gravitational potential is dominated by the stellar component in the inner region of the Antennae system. Thus, the distribution of the high density gas ( $> 10 \text{ cm}^{-3}$ ) is almost unaffected by the presence of the field. As stars are expected to form in high density regions, it is not surprising that the distribution of stars formed in our simulations is also independent on the presence of the field. In the magnetized case (Fig. 3.9), the gas velocity dispersion  $\sigma$  (lower left panel) is of the order of 10 to 20  $\text{km s}^{-1}$  within the galaxies. The distribution of magnetic pressure (lower central panel in Fig. 3.9) is slightly different compared to the distribution of the turbulent pressure (upper central panel): The highest turbulent pressures are reached in the centers of the galaxies, whereas the magnetic pressure is highest in the overlapping region of the galaxies. Moreover, there is a ridge of magnetic pressure at the root of the southern tidal tail (indicated by the black oval) which is not visible in the distribution of turbulent pressure. This differences most probably originate in the magnetic field being a vector instead of a scalar quantity. A fully random magnetic field is not amplified efficiently by isotropic compression. Thus, only in regions with strong shear flows which stretch and therefore straighten the magnetic field it can be amplified efficiently. However, the energy range of the magnetic pressure is overall comparable to the energy range of the turbulent pressure. Thus,  $\beta = P_{\text{turb}}/P_{\text{mag}}$  (lower right panel) is in the range 1 to 10 almost everywhere, which means that the magnetic pressure is of the order of the turbulent pressure or slightly lower.

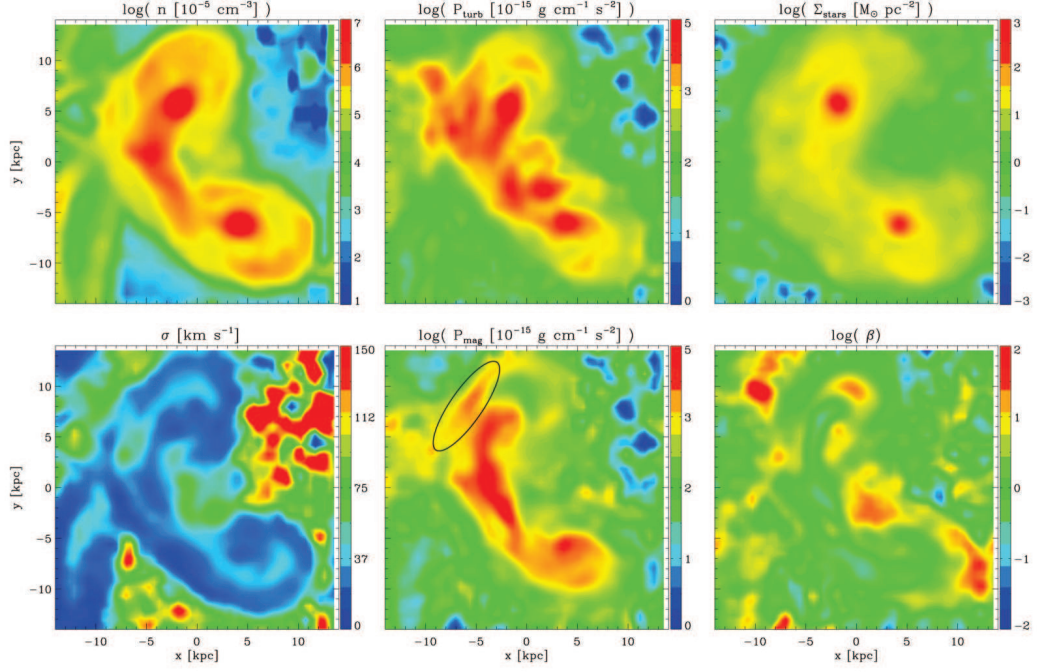


Figure 3.9: The Antennae simulation with an initial magnetic field of  $B_0 = 10^{-6}$  G. From left to right and top to bottom: Mean line-of-sight gas number density  $n$ , turbulent pressure  $P_{\text{turb}} = 1/2\rho v_{\text{turb}}^2$ , stellar surface density  $\Sigma_{\text{stars}}$ , gas velocity dispersion  $\sigma$ , magnetic pressure  $P_{\text{mag}} = B^2/8\pi$  and  $\beta = P_{\text{turb}}/P_{\text{mag}}$  in the inner region (innermost 28 kpc) of the system at time of best fit ( $t_{\text{BM}} \approx 1250$  Myr).

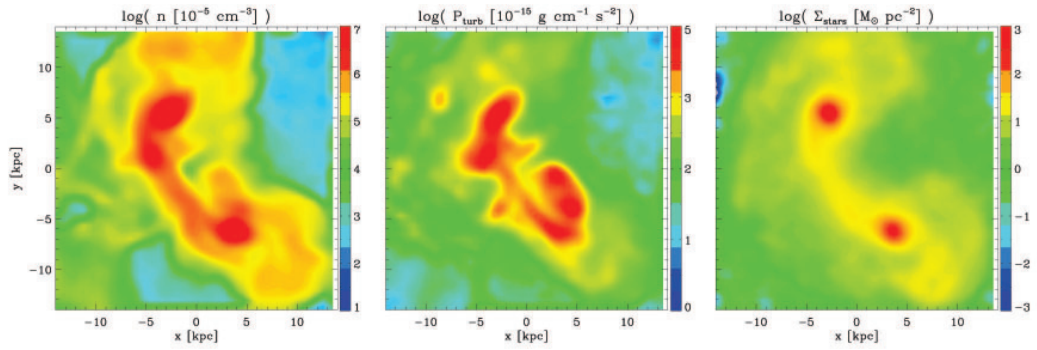


Figure 3.10: The Antennae simulation without including magnetic fields. From left to right: Mean line-of-sight gas number density  $n$ , turbulent pressure  $P_{\text{turb}} = 1/2\rho v_{\text{turb}}^2$  and stellar surface density  $\Sigma_{\text{stars}}$  in the inner region (innermost 28 kpc) of the system at time of best fit ( $t_{\text{BM}} \approx 1250$  Myr). The turbulent pressure is highest in the overlapping region between the two merging galaxies.

Fig. 3.11 shows the temporal evolution of the turbulent pressure  $P_{\text{turb}} \sim v_{\text{turb}}^2$  (black line), the hydrodynamic pressure  $P_{\text{hyd}} \sim v^2$  (blue line) the magnetic pressure  $P_{\text{mag}} \sim B^2$  (red line) and the "dispersion pressure", corresponding to the velocity dispersion, i.e.  $P_{\sigma} = 1/2\rho\sigma^2$  (green line) for gas particles with a number density  $> 0.005 \text{ cm}^{-3}$  in the simulation with  $B_0 = 10^{-6} \text{ G}$ . The hydrodynamic pressure is higher than the magnetic pressure by roughly three orders of magnitude throughout the simulation, which should be expected from theory as it is not the value of the velocity itself, but the velocity gradients which determine the evolution of magnetic fields. The turbulent, dispersion and the magnetic pressures are of the same order of magnitude until the first encounter (except of the beginning of the simulation). After the encounter, the turbulent and the dispersion pressures are always slightly higher (by a factor of approximately five and ten, respectively) than the magnetic pressure. At time of best fit the turbulent and magnetic pressures are again of the same order of magnitude, as already indicated in the last panel in Fig. 3.9. The fact, that the magnetic pressure never exceeds the turbulent pressure indicates, that the magnetic field amplification is restricted to magnetic field values corresponding to the equipartition level between turbulent and magnetic pressure. This is exactly what is expected from theory and explains the self-regulated saturation of the magnetic field strength in our simulations (Fig. 3.3)

Fig. 3.12 shows the same quantities as in Fig 3.11 but for the more extreme simulation with  $B_0 = 10^{-4} \text{ G}$ . In the beginning of this simulation, the magnetic pressure is three orders of magnitude higher than the turbulent pressure (because this initial magnetic field is two orders of magnitude higher than the expected equipartition value of several  $\mu\text{G}$  and  $P_{\text{mag}} \propto B^2$ ). Within the first 50 Myr of evolution the magnetic pressure drops by one order of magnitude. Simultaneously, the turbulent and dispersion pressures increase by the same amount. This is because the high magnetic pressure "blows up" the galaxies in the very beginning of the simulation and thus drives a lot of turbulent (or chaotic) motions. After the first 50 Myr, the difference between the turbulent and the magnetic pressure is only one order of magnitude and the system is able to relax again. Thus, the turbulent and dispersion pressures start to decrease, and the magnetic pressure continues to decrease further. After approximately 400 Myr the magnetic pressure is of the order of the turbulent and dispersion pressures. Shortly before the first encounter, it has reached a value slightly below the turbulent pressure. In the subsequent evolution, similar to the simulation with  $B_0 = 10^{-6} \text{ G}$ , the magnetic pressure always stays below the turbulent pressure. However, the evolution of the pressure components is altered compared to the simulation with  $B_0 = 10^{-6} \text{ G}$ . Particularly, the second encounter (visible as a temporary increase of the pressure values) preceding the time of best fit in Fig. 3.11 is shifted by approximately 100 Myr to later times in the simulation with  $B_0 = 10^{-4} \text{ G}$ . This difference develops because the strong magnetic field in the beginning of the simulation with  $B_0 = 10^{-4} \text{ G}$  alters the gas distribution significantly and thus changes the evolution of the whole system. In summary, this comparison clearly shows that interacting galactic systems always tend to reach equipartition, independent of the initial ratio of magnetic to turbulent pressure.

As already discussed in section 3.3.3.2, without applying the Lorentz force the magnetic field gets amplified much above the value of equipartition between magnetic and turbulent pressure, and does not converge. Thus, it is actually the Lorentz force, i.e. the backreaction of the magnetic field on the gas, which yields the self-regulation.

Finally, we compared the SF rates in the simulations with different initial magnetic field strengths with the SF rate in a simulation without any magnetic field (not shown). The SFR after the first encounter in the simulation with  $B_0 = 10^{-6} \text{ G}$  showed to be slightly lower (by a factor of approximately two) than in the simulation without or with a weak magnetic field, indicating that the presence of the magnetic field hinders the collapse of gas. However, this influence is not strong enough to alter the SF history significantly.

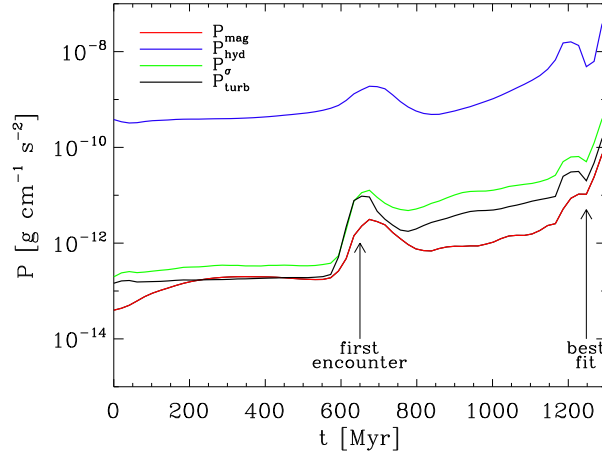


Figure 3.11: Temporal evolution of  $P_{\text{turb}}$  (black line),  $P_{\text{hyd}}$  (blue line),  $P_{\sigma}$  (green line) and  $P_{\text{mag}}$  (red line) for gas particles with a number density  $> 0.005 \text{ cm}^{-3}$  in the simulation with  $B_0 = 10^{-6} \text{ G}$ .  $P_{\text{turb}}$  and  $P_{\text{mag}}$  are of a comparable order of magnitude throughout the simulation and almost in equipartition at time of best fit.

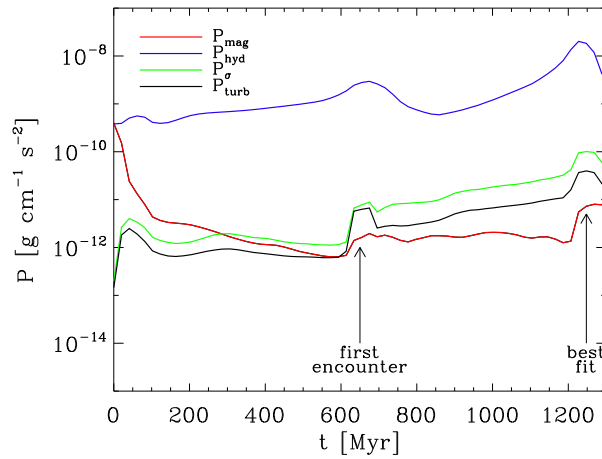


Figure 3.12: Same as Fig. 3.11 but for the simulation with  $B_0 = 10^{-4} \text{ G}$ .  $P_{\text{mag}}$  is much higher than  $P_{\text{turb}}$  in the beginning of the simulation, but decreases to the level of equipartition within 400 Myr.  $P_{\text{turb}}$  and  $P_{\text{mag}}$  are almost in equipartition at time of best fit.

## 3.4 Simulated radio emission and polarization maps

### 3.4.1 Computation method

In order to compare our results directly with observations, we compute artificial radio emission and polarization maps from our simulation data. For this purpose, the magnetic field components and the stellar density from the SPMHD simulations have been again transferred to a three-dimensional grid. The following calculations have been performed with an IDL code developed by Wiatr (2006). The calculations of the total and polarized synchrotron intensity and the calculation of the polarisation angle have been performed in the standard way according to the following formulae (see Longair, 1994 and Rybicki and Lightman, 1986 for more details):

The total synchrotron emission  $J_\nu$  at a given frequency  $\nu$  is given by

$$J_\nu = \left[ \frac{4}{3} \frac{\sigma_T c^3}{\mu_0} \sqrt{\frac{\pi^3 m_e^5}{2e^3}} \left( \sqrt{\frac{2\pi m_e^3}{e} c^2} \right)^{-p} \right] \times \kappa \sqrt{B^{1+p} \nu^{1-p}}, \quad (3.3)$$

where the magnetic field  $B$  is the only input from our simulations. The frequency  $\nu$  and the index of the power spectrum of the relativistic cosmic ray (CR) electrons  $p$  are input parameters. The latter is assumed to be 2.6 in this paper, corresponding to the value given by Chyży and Beck, 2004. The constants are the Thompson cross section  $\sigma_T = 0.665 \times 10^{-24}$  cm<sup>2</sup>, the magnetic permeability  $\mu_0 = 1$  (in CGS units), the speed of light  $c$  and the electron mass  $m_e \approx 9.1 \times 10^{-28}$  g. The constant normalization factor  $\kappa$  of the cosmic ray energy spectrum can be derived for a given total CR energy  $E_{CR}$  via

$$E_{CR} = \kappa \int_{E_{min}}^{E_{max}} E^{1-p} dE. \quad (3.4)$$

The observed CR energies in the Milky Way follow a steep spectrum from  $10^9$  to  $10^{20}$  eV, whereby supernova remnants (SNR) are the most likely source for CRs with energies  $< 10^{18}$  eV. CRs with higher energies may be produced in Jets of pulsars or black holes, and are probably of extragalactic origin (see The Pierre AUGER Collaboration et al., 2008). Given the steep fall-off of CR abundance with energy we assume an energy range of  $E_{min} = 10^9$  eV to  $E_{max} = 10^{15}$  eV in our calculations. Furthermore, as CRs in this energy range are most likely produced in SNRs, we assume the CR distribution to be proportional to the stellar density, with a typical value of the mean specific energy density of  $e_{CR} = 1$  MeV m<sup>-3</sup> for CR protons (see e.g. Ferrière, 2001). However, we apply a cutoff at an energy density of  $e_{CR} = 100$  MeV m<sup>-3</sup>. The energy density of CR electrons is roughly 100 times lower than the energy density of CR protons, thus the mean energy density for CR electrons is assumed to be 10 keV m<sup>-3</sup>.

$J_\nu$  is calculated within every grid cell at a frequency of  $\nu = 4.86 \times 10^9$  Hz (corresponding to the observed frequency). The total intensity  $I_{tot}$  of the synchrotron radiation is subsequently obtained by integration of the emission along the line-of-sight.

The degree of polarization  $\Pi$  of any electromagnetic radiation is defined as the amount of its polarized intensity  $I_p$  compared to the amount of its total intensity  $I_{tot}$ . The synchrotron emission of a single radiating charge is always polarized elliptically, because the light component for which polarization is parallel to the magnetic field projected onto the plane of sky ( $I_{\parallel}$ ) has a different refraction index than the perpendicular component ( $I_{\perp}$ ). However, as charges gyrate along the magnetic field lines, the elliptical components will cancel, as emission cones will contribute equally from both sides of the line-of-sight. Thus, for any reasonable distribution of particles that varies smoothly with pitch

angle, the radiation will be partially linearly polarized and thus characterized by the terms  $I_{\parallel}$  and  $I_{\perp}$ . The degree of linear polarization for particles of a single energy can then be expressed as

$$\Pi(\nu) = \frac{I_{\perp}(\nu) - I_{\parallel}(\nu)}{I_{\perp}(\nu) + I_{\parallel}(\nu)}, \quad (3.5)$$

where  $I_{tot}(\nu) = I_{\perp}(\nu) + I_{\parallel}(\nu)$ . If the energy spectrum of the radiating particles follows a power-law (here  $N(E) = \kappa E^{-p} dE$ ), it can be shown that

$$\Pi = \frac{p+1}{p+\frac{7}{3}}. \quad (3.6)$$

Thus, in a homogeneous magnetic field, the degree of polarization is very high (approximately 73% for  $p = 2.6$ ). However, when integrated along the line-of-sight, opposite polarization cancels out and the observed degree of polarization is therefore usually much lower than the theoretically expected value.

The polarized intensity  $I_p$  depends on the Stokes parameters  $Q$  and  $U$  according to

$$I_p = \sqrt{Q^2 + U^2}, \quad (3.7)$$

with

$$Q = \Pi \int J_{\nu} \cos(2\psi) ds, \quad (3.8)$$

$$U = \Pi \int J_{\nu} \sin(2\psi) ds, \quad (3.9)$$

where the integration is performed along the line-of-sight and  $\psi$  is the polarization angle, defined as the angle between the electric field vector of the radiation perpendicular to the magnetic field ( $\vec{E}_{\perp}$ ) and the  $x$ -axis in the  $xy$ -plane (the plane of sky), i.e.:

$$\sin(2\psi) = -\frac{2B_x B_y}{B_x^2 + B_y^2}, \quad (3.10)$$

$$\cos(2\psi) = \frac{B_x^2 - B_y^2}{B_x^2 + B_y^2}. \quad (3.11)$$

Finally, the observed degree of polarization is

$$\Pi_{\text{obs}} = \frac{I_p}{I_{\text{tot}}}. \quad (3.12)$$

All calculated values are subsequently convolved with a telescope beam corresponding to the  $17'' \times 14''$  beam in the observations of Chyży and Beck (2004), i.e. the beam-diameter is approximately 1.5 kpc at the distance of the Antennae system (assuming a distance of 22 Mpc). The shape and sensitivity of the beam is specified by a 2D gaussian function.

### 3.4.2 Applications

Fig. 3.13 shows an simulated face-on radio map of the isolated disk at  $t = 400$  Myr for the simulation with  $B_0 = 10^{-6}$  G. The particle data of a domain with  $x \in [-20 \text{ kpc}, 20 \text{ kpc}]$ ,  $y \in [-20 \text{ kpc}, 20 \text{ kpc}]$  and  $z \in [-10 \text{ kpc}, 10 \text{ kpc}]$  (with the zero-point defined as the center of mass of the system) has been transferred to a spatial grid with  $60 \times 60 \times 30$  cells. Thus, the displayed domain comprises  $40 \times 40$

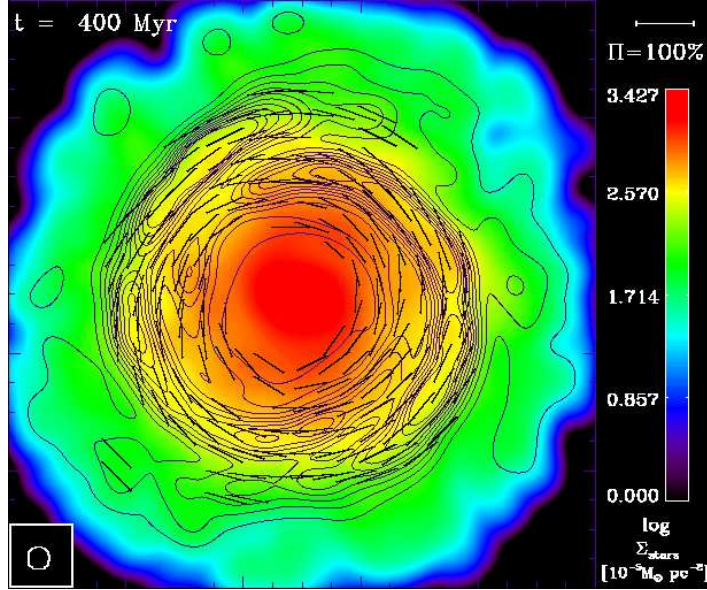


Figure 3.13: Face on view of the isolated galaxy. Colors correspond to the logarithm of stellar surface density (in units of  $10^{-5} M_{\odot} \text{pc}^{-2}$ ), overlaid with contours of total synchrotron power. The contour levels are 0.001 to 0.01 mJy in ten equally spaced steps. Magnetic field lines derived from calculations of polarization are shown in black.

$\text{kpc}^2$ . The colours correspond to the stellar surface density, overlaid with contours of total synchrotron power. Magnetic field lines derived from calculations of polarization are shown in black. To account for the spatial isotropy of the emission from any emitting volume element, the total flux has been multiplied by the factor

$$f_{\text{obs}} = \frac{\pi \cdot r_{\text{beam}}^2}{4\pi \cdot d^2}, \quad (3.13)$$

with  $d = 22 \text{ Mpc}$  the distance to the observer and  $r_{\text{beam}}$  the assumed radius of the beam. Thus, the artificial flux, given in mJy, corresponds to what is expected to reach the earth from the distance of the Antennae system.

As already discussed above, the initially homogeneous magnetic field gets redistributed by the differential rotation of the disk, thus developing a spiral pattern which is clearly visible in the total emission. The magnetic field lines trace this spiral pattern. Altogether, the structure of the magnetic field is similar to what is observed in typical disk galaxies. A similar result has been also obtained independently by Kulesza-Żydzik et al. (2009), who have performed 3D MHD simulations of barred spiral galaxies using a grid code.

Interestingly, the distribution of the magnetic field lines derived from the polarization calculations (Fig. 3.13) does not extend as far out in the disk as the magnetic field itself (Fig. 3.2). This difference occurs because we can only observe polarization where enough CR particles are present, which is not the case in the outer parts of the galaxy. However, the structure of the magnetic field is comparable.

Fig. 3.14 shows a simulated radio map of the inner region of the Antennae system for the simulation with  $B_0 = 10^{-6} \text{ G}$  at the time of best match ( $t_{\text{BM}} \approx 1.25 \text{ Gyr}$ ). The particle data of a domain with  $x \in [-14 \text{ kpc}, 14 \text{ kpc}]$ ,  $y \in [-14 \text{ kpc}, 14 \text{ kpc}]$  and  $z \in [-56 \text{ kpc}, 56 \text{ kpc}]$  (with the zero-point again defined as the center of mass of the system) has been transferred to a spatial grid with  $75 \times 75 \times 300$  cells. The total flux was again corrected to the isotropy of the emission by multiplying by the factor

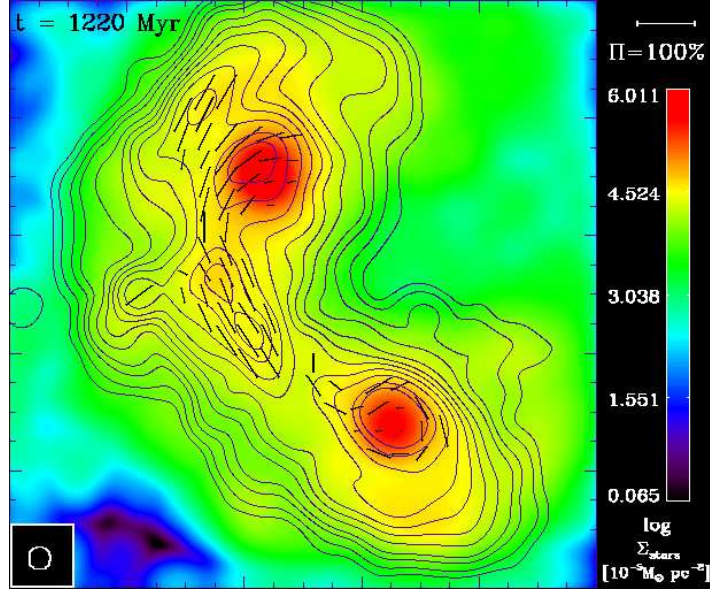


Figure 3.14: Inner region (innermost 28 kpc) of the simulated Antennae system. Colors correspond to the stellar surface density (in units of  $10^{-5} M_{\odot} \text{pc}^{-2}$ ), overlaid with contours of total synchrotron power. The contour levels are 0.005, 0.12, 0.30, 0.53, 1.2, 2.1, 3.3, 5.3, 9.0, 17 and 24 mJy. Magnetic field lines derived from calculations of polarization are shown in black. The simulated systems compares very well to the observed system (Fig. 3.1).

$f_{\text{obs}}$ . The contour levels of total synchrotron emission have been chosen to be as given in Fig. 3 in Chyży and Beck (2004). Thus, they are the same levels as displayed in Fig. 3.1.

Given the fact that our simulations are fully self-consistent, the similarity between the simulated and the observed system is astonishing. The spatial extent and distribution of the total synchrotron flux compares very favorably with the observations. Also, the highest values of total synchrotron emission are reached in the overlapping region and at the centers of the interacting galaxies. Furthermore, two ridges of ordered magnetic field lines, one reaching from one galaxy to the other along the overlap region, and one corresponding to the root of the southern tidal tail, naturally develop in our simulation. However, there are also several differences: There is a lack of magnetic fields in the southern tidal tail, i.e. the ordered magnetic field structure is not as prominent as in the observations, which may be caused by a lack of CRs in this region. Also, there is no western spiral arm in NGC4038 (the upper galaxy), which is probably because the spiral structure of the progenitors in our simulation is not pronounced enough. Furthermore, there is too little polarized emission in the outskirts of the galaxies and the overlap region is shifted north (down) compared to the observations. Moreover, the pitch angle of the magnetic field in the isolated galaxy (Fig. 3.13) is rather small. The latter can probably be explained by the absence of a dynamo process in this simulation. Despite these differences the satisfactory match between observation and our simulation is encouraging. Thus, our numerical method already seems to capture the most essential basic processes relevant in investigating interactions of magnetized galaxies. In particular, our model of the Antennae system seems to provide a fair description of how this system may have formed.

A further discrepancy between observation and our simulation is the value of the magnetic field itself. The magnetic field strength in our simulations saturates at a mean value of roughly  $10 \mu\text{G}$ , only 10% of the simulated particles carry magnetic field values of  $|B| > 20 \mu\text{G}$  and only 1% have  $|B| > 50 \mu\text{G}$ . On the other hand, the mean magnetic field strength derived from observations of synchrotron

radiation is approximately  $20 \mu\text{G}$ . However, the observed value is derived assuming equipartition between the CR energy and the energy of the magnetic field, an assumption which does not necessarily have to hold. Furthermore, the assumed CR energy density and the magnetic dissipation factor in our calculations are only approximate estimates. Given these uncertainties, a difference by a factor of two between the observed magnetic field and the field strength in our simulations is admissible.

### 3.5 Conclusion and Discussion

We have presented the first fully self-consistent  $N$ -body/SPH simulations of the interacting Antennae galaxy system including magnetic fields. We show that weak magnetic seed fields in the isolated disk galaxies are amplified by the gravitational interaction throughout the two galactic encounters. Thereby the magnetic pressure saturates at a level corresponding to equipartition between the turbulent and the magnetic pressure, independent of the initial field strength. Particularly, magnetic fields with an initial value higher than the equipartition value diminish during the evolution, demonstrating that the state of equipartition is the natural state for magnetized galactic systems. An analysis of artificial total synchrotron emission and polarization maps provides a convincing agreement with the observations. Summarizing, the method of  $N$ -body/SPH simulations including magnetic fields reproduces quite conclusively the complicated dynamics of the amplification and spatial design of magnetic fields in interacting galaxies.

Moreover, a detailed discussion of the numerical divergence of the magnetic field in SPH simulations has been presented in section 3.3.3.2. Our analysis strongly suggests that numerical divergence measures which are smaller than a certain threshold can be considered as measures of sub-resolution fluctuations which do not affect the overall evolution of the magnetic field. Considering simulations using the Euler-Potentials, which pose a  $\nabla \cdot \mathbf{B}$ -free prescription by definition, this threshold can be assessed to be  $h\nabla \cdot \mathbf{B}/|\mathbf{B}| \approx 1$  (see also Kotarba et al., 2009).

What can we learn from these simulations for the global evolution of cosmic magnetic fields? Within the framework of standard CDM hierarchical clustering models the formation of large disk galaxies as well as elliptical galaxies is characterized by more or less intense merging of smaller galactic subunits, e.g. dwarf galaxies, collapsing gas clouds or globular clusters. If we assume that at least some of the accreted subunits have been magnetized by stellar activity (e.g. supernova explosions, stellar winds or T-Tauri-jets), the merging of such subunits to larger galaxies must have been accompanied by a significant amplification and restructuring of the magnetic field on galactic scales. The amplification and ordering of small-scale magnetic fields to a toroidal configuration during the evolution of isolated galaxies was recently shown by Hanasz et al. (2009c) and Dubois and Teyssier (2010) independently. Hanasz et al. (2009c) considered an axially symmetric galactic disk in which stellar seed fields were amplified by a cosmic ray driven dynamo. Dubois and Teyssier (2010) demonstrated the amplification and ordering of small-scale fields seeded by SF activity in the context of the formation of a dwarf galaxy with significant galactic winds. Complementary to these findings, our simulations prove that amplification via non-axisymmetric three dimensional gravitational interaction alone may provide an alternative channel for galactic as well as intergalactic magnetic field evolution. In other words, given that the structure formation is characterized by a galactic bottom-up architecture, we would expect that within one or two Giga-years the Universe has been globally magnetized by the combination of dynamo action in isolated galaxies and dynamical amplification by interacting galactic objects. However, dynamo action is supposed not to be very efficient in dwarf galaxies since their differential rotation is not strong enough (Gressel et al., 2008). Thus, at an early epoch of the universe, when most of the galaxy population consists of dwarfs, magnetic field amplification due to interactions may be even more significant.

With their study of the formation of dwarf galaxies including magnetic fields and galactic winds, Dubois and Teyssier (2010) demonstrate an alternative scenario based on the ideas of Bertone et al.

(2006) which they call the “Cosmic Dynamo”. According to their findings, galactic winds from young dwarf galaxies eject magnetic field energy into the intergalactic medium, leading to a mean intergalactic field  $B_{\text{IGM}}$  of  $10^{-11}$  to  $10^{-10}$  G. The preceding amplification of the magnetic field inside the dwarf galaxy by the combined action of stellar activity and differential rotation (i.e. the Galactic Dynamo) is thereby restricted by the IGM magnetic field already present at the formation time of the galaxy. For an IGM magnetic field of  $B_{\text{IGM}} \approx 10^{-10}$  G, the Lorentz force may prevent the formation of a new generation of dwarf galaxies and subsequent star formation. As a consequence, the IGM magnetic field never grows significantly above  $10^{-10}$  G. Since dwarf galaxies are characteristic in the early phase of the evolution of the universe, this Cosmic Dynamo may have been very efficient in magnetizing the IGM. However, besides the accretion of IGM material previously enriched with magnetic fields, Dubois and Teyssier (2010) also point out the importance of accretion of satellite galaxies for the evolution and amplification of the magnetic field in galaxies at later times.

Our simulations emphasize the Cosmic Dynamo scenario proposed by Dubois and Teyssier (2010). The efficient amplification of the magnetic field during the equal-mass-merger presented here clearly shows that interactions of galaxies should be taken into account in studies of the magnetic evolution of the universe. We would also expect an intergalactic medium which is not only enriched with heavy elements by stellar activity, but also magnetized on large scales by galaxy interactions. Our simulations may help to understand the observationally well established facts that very young galaxies already exhibit magnetic field strengths comparable with nearby fully developed spiral galaxies and the rotation measure estimates of intergalactic magnetic fields (e.g. Bernet et al., 2008).

## Acknowledgements

We thank the referee for very helpful comments which improved the paper significantly. H. Kotarba is grateful for interesting discussions with Krzysztof Chyży and Michal Hanasz. The authors also thank Krzysztof Chyży for providing Fig. 3.1. This research was supported by the DFG Cluster of Excellence “Origin and Structure of the Universe” ([www.universe-cluster.de](http://www.universe-cluster.de)). S. Karl and T. Naab acknowledge support from the DFG priority program SPP1177.



# Chapter 4

## Paper III: Galactic ménage à trois: Simulating magnetic fields in colliding galaxies

H. Kotarba, H. Lesch, K. Dolag, T. Naab, P. H. Johansson, J. Donnert & F. A. Stasyszyn, 2011, accepted for publication by the *Monthly Notices of the Royal Astronomical Society*, *ArXiv e-prints*: 1011.5735

### ABSTRACT

We present high resolution simulations of a multiple merger of three disk galaxies including the evolution of magnetic fields performed with the  $N$ -body/SPH code GADGET. For the first time, we embed the galaxies in a magnetized, low-density medium, thus modeling an ambient IGM. The simulations include radiative cooling and a model for star formation and supernova feedback. Magnetohydrodynamics is followed using the SPH method. The progenitor disks have initial magnetic seed fields in the range of  $10^{-9}$  to  $10^{-6}$  G and the IGM has initial fields of  $10^{-12}$  to  $10^{-9}$  G. The simulations are compared to a run excluding magnetic fields. We show that the propagation of interaction-driven shocks depends significantly on the initial magnetic field strength. The shocks propagate faster in simulations with stronger initial field, suggesting that the shocks are supported by magnetic pressure. The Mach numbers of the shocks range from approximately  $M = 1.5$  for the non-magnetized case up to  $M = 6$  for the highest initial magnetization, resulting in higher temperatures of the shock heated IGM gas. The magnetic field in the system saturates rapidly after the mergers at  $\sim 10^{-6}$  G within the galaxies and  $\sim 10^{-8}$  G in the IGM independent of the initial value. These field strengths agree with observed values and correspond to the equipartition value of the magnetic pressure with the turbulent pressure in the system. We also present synthetic radio and polarization maps for different phases of the evolution showing that shocks driven by the interaction produce a high amount of polarized emission. These idealized simulations indicate that magnetic fields play an important role for the hydrodynamics of the IGM during galactic interactions. We also show that even weak seed fields are efficiently strengthened during multiple galactic mergers. This interaction driven amplification might have been a key process for the magnetization of the Universe.

**Key words:** methods:  $N$ -body simulations — galaxies: spiral — galaxies: evolution — galaxies: magnetic fields — galaxies: kinematics and dynamics

## 4.1 Introduction

Radio observations have revealed that most late type galaxies in the local Universe - isolated grand design spirals, irregulars and dwarf galaxies - are permeated by magnetic fields (Beck et al., 1985; Hummel and Beck, 1995; Beck and Hoernes, 1996; Chyży et al., 2007a; Vollmer et al., 2010). The field strengths in all of these objects do not vary by more than one order of magnitude from a few  $\mu\text{G}$  in dwarfs (e.g. Chyży et al., 2003) to 30  $\mu\text{G}$  in the star-forming regions of grand-design spiral galaxies (Fletcher et al., 2004). Magnetic fields have also been observed at redshifts up to  $z \approx 2$  in damped Ly- $\alpha$  systems. These systems, which might be interpreted as large progenitors of present-day galaxies (e.g. Wolfe et al., 1995, 2005), seem to host magnetic fields of similar strength as local late-type galaxies (e.g. Bernet et al., 2008 and references therein).

These observations invite the question about the origin and the evolution of the magnetic fields in the early universe. Different scenarios have been suggested: Lesch and Chiba (1995) have shown analytically that strong magnetic fields in high redshift objects can be explained by the combined action of an evolving protogalactic fluctuation and electrodynamic processes providing magnetic seed fields (i.e. battery processes). Wang and Abel (2009) performed numerical simulations of the formation of disc galaxies within an collapsing halo imposing a uniform initial magnetic field of  $10^{-9}$  G. The initial field grew by three orders of magnitude within approximately 500 Myr of the evolution. The amplification might be due to the combined effects of magnetic field compression during the collapse and amplification of the uniform initial field by differential rotation as studied also in Kotarba et al. (2009). These studies indicate, that the growth of magnetic fields might be a natural part of the galaxy formation process.

A key ingredient in galaxy formation studies, however, is the consideration of galaxy interactions. Within the standard cold dark matter (CDM) models present-day galaxies have undergone several major and minor mergers at earlier epochs of the universe, and thereafter continued accreting gas and smaller galactic subunits (White and Rees, 1978; White and Frenk, 1991). Interactions of galaxies change their dynamics drastically (Toomre and Toomre, 1972; Barnes, 1992; Hernquist and Barnes, 1994; Barnes, 1999; Naab and Burkert, 2003; González-García et al., 2006) as the gravitational potential is varying rapidly during the interaction. Since the gas component is dissipative and most sensitive to variations of the gravitational potential, it is strongly affected by the interaction and driven towards the galaxy centers, eventually causing bursts of star formation (Barnes and Hernquist, 1992; Mihos and Hernquist, 1994; Barnes and Hernquist, 1996; Bekki and Shioya, 1998; Springel, 2000; Barnes, 2002; Bournaud et al., 2005; Cox et al., 2006; Naab et al., 2006; Robertson et al., 2006; Cox et al., 2008a; Hopkins et al., 2008; Teyssier et al., 2010). We can crudely estimate the amount of free energy during an interaction of two galactic subunits to be proportional to their relative velocity squared, i.e.  $E_{\text{free}} \sim v_{\text{rel}}^2$ . Obviously some of this energy released during the interaction is converted into thermal energy of hot gas. High energy particles also carry away some of the energy. However, it is reasonable to assume that at least some of this energy is converted into magnetic field energy during the compression of gas and the formation of tidal structures. As the amount of  $E_{\text{free}}$  can be very large during a major merger, the amount of energy converted into magnetic energy might be significant. Moreover, gas which is heated by the interaction and driven into the IGM should carry magnetic energy out of the galactic units, thus magnetizing the IGM. This process should be similar to what was found by Dubois and Teyssier (2010) in their study of the formation of dwarf galaxies including magnetic fields and galactic winds.

So far, simulations of interactions and mergers of disk galaxies have been mainly investigated with respect to changes in stellar dynamics, gas flows, star formation (SF) and the formation of central supermassive black holes (Di Matteo et al., 2005; Springel et al., 2005b,a; Robertson et al., 2006; Johansson et al., 2009a,b). However, the dramatic impact of mergers on the gas flows will directly affect the dynamics of the magnetic field of the systems. Since gas and magnetic field are tightly coupled, the magnetic field traces the gas motion and will be strengthened by shocks and gas in-

flow. A perfect example for the strong coupling of gas and magnetic fields is the interacting system NGC4038/4039 (the "Antennae galaxies") which has been recently simulated (Karl et al., 2010) by Kotarba et al. (2010a) including magnetic fields. It was shown that even an initial magnetic field as small as  $10^{-9}$  G grows significantly during the interaction of two equal-mass spiral galaxies. The magnetic field strength thereby saturates at a value of  $\approx 10 \mu\text{G}$ , in good agreement with observations (Chyży and Beck, 2004). This saturation value was reached independently of the initial magnetic field strength in the range of  $B_0 = 10^{-9} - 10^{-4}$  G. We emphasize that Kotarba et al. (2010a) found the saturation level to correspond to near equipartition between magnetic and turbulent gas pressure, which is in good agreement with theoretical considerations of the turbulent dynamo (e.g. Arshakian et al., 2009 and references therein, see also section 4.4.3.3). Furthermore, Kotarba et al. (2010a) provided synthetic radio maps calculated at time of best match between the simulated gas and stellar distributions and observations. These synthetic radio maps are in convincing morphological agreement with synchrotron observations of the Antennae system and the underlying numerics of the applied  $N$ -body/SPH code GADGET showed to be capable of following the evolution of magnetic fields in a highly nonlinear environment.

High resolution simulations of the formation of individual galaxies in a full cosmological context (see e.g. Naab et al., 2007; Sawala et al., 2010; Piontek and Steinmetz, 2011) including magnetic fields could help us in understanding the processes leading to the magnetization of the Universe. Although it would be worthwhile to consider cosmological studies in the long run, the simulations of three interacting galaxies presented in this paper are an additional further step towards a more complete scenario and a natural extension of the previous study presented in Kotarba et al. (2010a). With this study we show that the magnetic field growth accompanying a galactic interaction and its saturation at the equipartition level between magnetic and turbulent pressure holds also for a more general setup of interacting galaxies including IGM gas.

The paper is organized as follows: We briefly describe our numerical method in section 4.2. In section 4.3, we present a detailed description of the setup of the three colliding galaxies. The temporal evolution of the simulated systems and particularly the magnetic fields is described in section 4.4. In section 4.5, we present synthetic radio and  $RM$  maps of our simulated system. Finally, we summarize our results and conclude in section 4.6.

## 4.2 Numerical Method

The simulations presented here were performed with the  $N$ -body/SPH-code GADGET (Springel, 2005). Gravitational interactions between the particles are evaluated with a hierarchical tree method (Barnes and Hut, 1986). The dynamics of the Lagrangian fluid elements are followed using a SPH formulation which conserves both energy and entropy (Springel and Hernquist, 2002) including the evolution of magnetic fields which was implemented and tested by Dolag and Stasyszyn (2009). The code has already been used to investigate the evolution of magnetic fields in isolated spiral galaxies (Kotarba et al., 2009) and during the collision of two equal mass spiral galaxies resembling the nearby Antennae galaxies (Kotarba et al., 2010a).

The simulations presented in this paper have been performed using the standard (direct) magnetic field implementation. We apply the Lorentz force and artificial magnetic dissipation with an artificial magnetic dissipation constant of  $\alpha_B = 0.5$ . Artificial magnetic dissipation is included in order to reduce numerical errors arising from the SPH approximation rather than to capture any physical dissipation correctly (Dolag and Stasyszyn, 2009). Thereby, only a small fraction of the magnetic field within the volume defined by the SPH particle is allowed to leave this volume within the local dynamical time (defined via the local signal velocity). This limitation ensures that even strong shocks are well captured. Yet, of course, the artificial dissipation also leads to an effective slow diffusion of the magnetic field. This can be seen in the simulations of isolated disk galaxies presented in

Kotarba et al. (2010a) (Fig. 3 in their paper, the yellow and red lines). However, the value of  $\alpha_B$  is chosen such that on the one hand the numerical errors are efficiently reduced, and on the other hand, the magnetic diffusion is preferably low. Hence, the numerical dissipation does not reflect the true physical dissipation. Physical magnetic dissipation arises either due to electric conductivity, in which case it is very small and thus negligible, or due to turbulent diffusion, which can be significantly higher. However, turbulent diffusion would have to be modeled within the simulations, because it reflects processes on sub-resolution scales. We do not include any sub-resolution turbulent diffusion model in our simulations.

In addition to Kotarba et al. (2010a), we now also apply the subtraction of the effect of numerical magnetic divergence (the “divergence force”) in the momentum equation as suggested by Børve et al. (2001) (see Dolag and Stasyszyn, 2009 for more details). However, as a refinement of the method presented in Dolag and Stasyszyn (2009), we define a threshold for the divergence force subtraction: Whenever the correction becomes larger than the half of the current Lorentz force, it is limited to that level. In this way we avoid situations in which the divergence force could become the main source of acceleration and thus instabilities due to temporal high numerical divergence, e.g. during strong interactions (see also section 4.4.3.2). This limitation of the divergence force also helps to maintain energy conservation (for details see Stasyszyn & Dolag (2011), in preparation). The basic method of divergence force subtraction is not conservative, however, by limiting the correction we reduce possible transfer of energy associated with the numerical divergence to kinetic energy.

Similarly to Kotarba et al. (2010a), we apply radiative cooling, star formation and the associated supernova feedback, but exclude explicit supernova-driven galactic winds, following the sub-resolution multiphase model developed by Springel and Hernquist (2003), in which the ISM is treated as a two-phase medium (McKee and Ostriker, 1977, Johansson and Efstathiou, 2006).

The implementation used in this paper has been tested in detail (Springel et al., 2001; Springel, 2005; Springel et al., 2005a; Dolag and Stasyszyn, 2009). We refer the reader to these studies for further details on the applied method. Detailed discussions on the numerical divergence of the magnetic field ( $\nabla \cdot \mathbf{B}$ ) in SPH simulations of isolated and interacting galaxies can be found in Kotarba et al. (2009) and Kotarba et al. (2010a).

## 4.3 Setup

### 4.3.1 Galaxies

The initial conditions for the spiral galaxies are produced using the method described by Springel et al. (2005a) which is based on Hernquist (1993). The galaxies consist of a cold dark matter halo, a rotationally supported exponential stellar disk, an exponential gas disk and a stellar bulge component. The profiles of the halo and bulge are based on Hernquist (1990). The halo, stellar disk and bulge particles are collisionless N-body particles. The gas is represented by SPH particles.

The parameters used for the initial setup of the three identical galaxies can be found in Table 4.1. The magnetic field in each disc is set to  $B_x = B_{0,\text{disk}}$  and  $B_y = B_z = 0$  with the  $z$ -axis being the axis of rotation. The particle numbers and fixed gravitational softening lengths  $\epsilon$  for each galaxy can be found in Table 4.2. The minimum SPH smoothing length for the gas particles is thereby  $h_{\text{SPH}}^{\text{min}} = 1.0\epsilon = 25 \text{ pc}/h$ , with  $h = 0.71$  being the Hubble constant. This choice of parameters results in particle masses of  $m_{\text{gas}} = m_{\text{disk}} = m_{\text{bulge}} \approx 1.19 \cdot 10^5 M_{\odot}/h$  and  $m_{\text{halo}} \approx 21.43 \cdot 10^5 M_{\odot}/h$ , respectively, with the Hubble constant  $h = 0.71$ . More details on the properties, evolution and stability of the disks evolved in isolation can be found in Kotarba et al. (2009, 2010a).

DISK PARAMETERS		
total mass	$M_{\text{tot}}$	$1.34 \times 10^{12} M_{\odot}$
disk mass	$M_{\text{disk}}$	$0.075 M_{\text{tot}}$
bulge mass	$M_{\text{bulge}}$	$0.025 M_{\text{tot}}$
mass of the gas disk	$M_{\text{gas}}$	$0.2 M_{\text{disk}}$
exponential disk scale length	$l_D$	8.44 kpc
scale height of the disk	$h_D$	$0.2 l_D$
bulge scale length	$l_B$	$0.2 l_D$
spin parameter	$\lambda$	0.1
virial velocity of the halo	$v_{\text{vir}}$	160 km s <sup>-1</sup>
half mass radius	$R_{\text{half}}$	$\approx 12$ kpc
half mass circular velocity	$v_{\text{half}}$	$\approx 249$ km s <sup>-1</sup>
half mass rotation period	$T_{\text{half}}$	$\approx 295$ Myr
initial temperature	$T_{\text{disk}}$	$\approx 10\,000$ K
initial magnetic field	$B_0$	$0 - 10^{-6}$ G
MULTI-PHASE MODEL PARAMETERS		
gas consumption timescale	$t_{\text{MP}}$	8.4 Gyr
mass fraction of massive stars	$\beta_{\text{MP}}$	0.1
evaporation parameter	$A_0$	4000
effective SN temperature	$T_{\text{SN}}$	$4 \times 10^8$ K
cold cloud temperature	$T_{\text{CC}}$	1000 K

Table 4.1: Parameters of initial disk setup

Component	initial particle number	fixed gravitational softening length $\epsilon$ [pc] <sup>a</sup>
Dark Matter	$4.0 \times 10^5$	$110/h$
Disk - stars	$4.8 \times 10^5$	$25/h$
Bulge - stars	$2.0 \times 10^5$	$25/h$
Gas	$1.2 \times 10^5$	$25/h$
Total	$1.2 \times 10^6$	-

(a) The Hubble constant is assumed to be  $h = 0.71$  in this paper.

Table 4.2: Particle numbers and softening lengths

### 4.3.2 Orbits

We want to study a general case of a galactic interaction. Thus, the initial orbital setup of the three colliding galaxies has been chosen arbitrarily without the aim of matching a particular observed system. In creating the initial conditions, the galaxies (including their magnetic field) are first rotated with respect to the plane of sky ( $xy$ -plane) around the  $x$ -,  $y$ - and  $z$ -axes by the angles  $\theta$ ,  $\psi$  and  $\phi$ , respectively. In order to guarantee a final merger of the three galaxies, two of them (galaxy 1 (G1) and galaxy 2 (G2)) are set on a nearly parabolic Keplerian two-body orbit with an initial separation of the centers of mass of  $r_{\text{sep}}^a$  and a pericenter distance of  $r_p^a$ . Then, the third galaxy (G3) and the center of mass of the combined system G1 and G2 are set on a nearly parabolic orbit with  $r_{\text{sep}}^b$  and  $r_p^b$ . The values of the rotation angles, the initial separations, the pericenter distances and the initial velocities can be found in Table 4.3.

### 4.3.3 IGM

As an extension compared to our previous study in Kotarba et al. (2010a), we now also include an ambient IGM surrounding the galaxies in order to be able to realistically study the magnetic field evolution in this IGM. The IGM is set up by placing additional gas particles in a regular hexagonal close-packed lattice (hcp) arrangement. Close-packed lattice arrangements have been shown to be

initial separation [kpc/h] <sup>a</sup>	$r_{\text{sep}}^a =$	160	
	$r_{\text{sep}}^b =$	320	
pericenter distance [kpc/h] <sup>a</sup>	$r_p^a =$	12	
	$r_p^b =$	24	
	G1	G2	G3
rotation around $x$ ( $\theta$ )	45	90	30
rotation around $y$ ( $\psi$ )	45	90	0
rotation around $z$ ( $\phi$ )	0	0	0
initial $v_x$ [km s <sup>-1</sup> ]	-145	73	18
initial $v_y$ [km s <sup>-1</sup> ]	-157	-95	63

(a) The Hubble constant is assumed to be  $h = 0.71$  in this paper.

Table 4.3: Collision setup parameters

more stable for the particles than simple grid arrangements (see Price and Bate, 2007 and references therein). The particle mass is again  $m_{\text{IGM}} = m_{\text{gas}} \approx 1.19 \cdot 10^5 M_{\odot}/h$ . The volume filled by the IGM is  $500 \times 700 \times 300$  (kpc/h)<sup>3</sup> and centered at the center-of-mass of the initial setup of the discs. The density is  $\rho_{\text{IGM}} = 10^{-29}$  g cm<sup>-3</sup> (equivalent to  $\approx 6 \cdot 10^{-6}$  H-atoms cm<sup>-3</sup>), resulting in a particle number of  $N_{\text{IGM}} = 43 \times 70 \times 31 = 93310$ .

The initial morphology of our galaxies corresponds to fully evolved disk galaxies residing in their dark matter haloes, hence, we assume that the IGM in each scenario is already virialized. However, for simplicity, we assume a common temperature for the IGM, which we set to the virial temperature at the virial radius of the simulated galactic haloes:

$$T_{\text{vir}} = \frac{\langle v^2 \rangle \mu m_p}{3k_B} = \frac{GM\mu m_p}{3r_{\text{vir}}k_B} = T_{\text{IGM}} \approx 6 \cdot 10^5 \text{ K}, \quad (4.1)$$

where  $\mu \approx 0.588$  is the molecular weight (for fully ionized gas of primordial composition),  $m_p$  the proton mass,  $k_B$  the Boltzmann constant,  $G$  the gravitational constant,  $M$  the mass of the halo and  $r_{\text{vir}}$  its virial radius. We assume the initial magnetic field of the IGM gas to be directed in the  $x$  direction (where the  $x$ – $y$ -plane is the orbital plane) with  $B_x = B_{0,\text{IGM}}$ . Thus, altogether, the galaxies are permeated by a homogeneous magnetic field lying in the planes of the disks, and the IGM hosts a homogeneous field lying in the orbital plane.

The addition of an ambient IGM has a further, numerical advantage: As the field is not dropping to zero at the disk edges, spurious calculations of the numerical divergence  $h_{\text{SPH}} \nabla \cdot \mathbf{B}/|\mathbf{B}|$  (where  $h_{\text{SPH}}$  is the SPH smoothing length) are avoided, resulting in higher numerical stability.

#### 4.3.4 Magnetic fields

A detailed study of the cosmological seeding and evolution of magnetic fields in the early universe is beyond the scope of this paper. Rather, we want to gain better understanding of how magnetic fields might have evolved during the epoch of galaxy formation by considering three different scenarios of the magnetization of the colliding galaxies in the local universe, and, additionally, a further scenario excluding magnetic fields for comparison.

The initial magnetic field strengths for each scenario are summarized in Table 4.4. With the first scenario (G6-IGM9), we aim to simulate a present-day galactic merger. Hence, within this scenario, we assume that the galaxies already host an initial magnetic field of  $B_{0,\text{disk}} = 10^{-6}$  G, and that the IGM is interspersed with an initial magnetic field of  $B_{0,\text{IGM}} = 10^{-9}$  G. With our second scenario (G9-IGM9), we want to study the general situation of a common magnetic field strength in the IGM and the galaxies. Within this scenario, the galaxies as well as the IGM host an initial magnetic field of  $10^{-9}$  G. In the third scenario (G9-IGM12), we assume that the magnetic field strengths are weaker by roughly three orders of magnitude than today, i.e.  $B_{0,\text{disk}} = 10^{-9}$  G, and  $B_{0,\text{IGM}} = 10^{-12}$  G.

Scenario	$B_{0,\text{disk}}$ [G]	$B_{0,\text{IGM}}$ [G]
G6-IGM9	$10^{-6}$	$10^{-9}$
G9-IGM9	$10^{-9}$	$10^{-9}$
G9-IGM12	$10^{-9}$	$10^{-12}$
G0-IGM0	-	-

Table 4.4: Initial uniform magnetic field strengths for the different scenarios in the plane of the disks ( $B_{0,\text{disk}}$ ) and in the  $x$ -direction of the orbital plane ( $B_{0,\text{IGM}}$ ), respectively.

In the last scenario (G0-IGM0), we exclude any magnetic field. For simplicity, all initial magnetic fields are assumed to be homogeneous with only one non-vanishing component at the beginning of the simulations (which lies in the plane of the disks for the galaxies, and in the orbital plane for the IGM). The choice of the initial configuration is not important, as the timescales of the simulations are much longer than e.g. the turbulent timescales of the gas. Moreover, it takes more than 0.5 Gyr until the first encounter between the galaxies and the magnetic field within the galaxies has enough time to redistribute and form a realistic configuration prior to the first encounter (see also Kotarba et al., 2009, 2010a).

Finally, we let the system evolve for 200 Myr in order to allow possible numerical discontinuities introduced by the setup to relax before considering its physical properties.

## 4.4 Simulations

### 4.4.1 Morphological evolution

Figs. 4.1, 4.2 and 4.3 show the mean line-of-sight total magnetic field  $|\mathbf{B}|$ , the mean line-of-sight temperature  $T$  and the mean line-of-sight rms velocity  $v_{\text{rms}}$ , respectively, at nine different time steps for the G6-IGM9 scenario (i.e. the present-day merger)<sup>1</sup>. To generate the images, the particle data in the  $500^3$  (kpc/h)<sup>3</sup> volume was binned to a  $512^2$  image using the code P-SMAC2 (Donnert et al., in preparation), which applies the gather approximation (see Dolag et al., 2005). In each case, the color maps are overlaid with contours of the stellar surface density  $\Sigma_*$  in order to indicate the stellar morphology of the system. The stellar density was binned using the TSC procedure (Triangular Shaped Cloud, see e.g. Hockney and Eastwood, 1988). Here and hereafter,  $v_{\text{rms}}$  of each particle is defined as the rms velocity around the *mean velocity* inside the SPH kernel of the particle (i.e. inside its smoothing length  $h_{\text{SPH}}$ ). This value is different from the rms velocity around the *central velocity* (i.e. the velocity of the particle considered) inside the kernel. The latter was defined as the “turbulent” velocity in Kotarba et al. (2010a). However,  $v_{\text{rms}}$  is a more conservative estimator for the local turbulent velocity on the kernel scale. By averaging over all particles inside the kernel to obtain the mean we reduce the influence of SPH sampling noise, which is present on subkernel scales, on the estimate. Hence, we use  $v_{\text{rms}}$  as the estimate of the turbulent velocity in this paper.

At  $t = 300$  Myr, the initial magnetic field has been redistributed and forms a realistic configuration in each galaxy (upper left panel in Fig. 4.1). Due to the winding of the initially uniform magnetic field by differential rotation, the magnetic field in each galaxy forms a non-axisymmetric pattern, which can be recognized from the two magnetic arms extending from the galactic disc (best visible at the later times  $t = 654$  Myr and  $t = 715$  Myr in G3, see also Kotarba et al., 2009, 2010a for a more detailed discussion of the winding process). As a consequence of their mutual gravitational attraction, G1 and G2 are moving towards each other and collide at  $t \approx 0.7$  Gyr. Due to the lower ram pressure within the IGM than within the galaxies, the interaction-driven shocks (which are analyzed in more detail in section 4.4.2) are propagating favorably into the IGM, thus heating the IGM gas (upper

<sup>1</sup>See <http://www.usm.uni-muenchen.de/people/kotarba/public.html> for the corresponding movies.

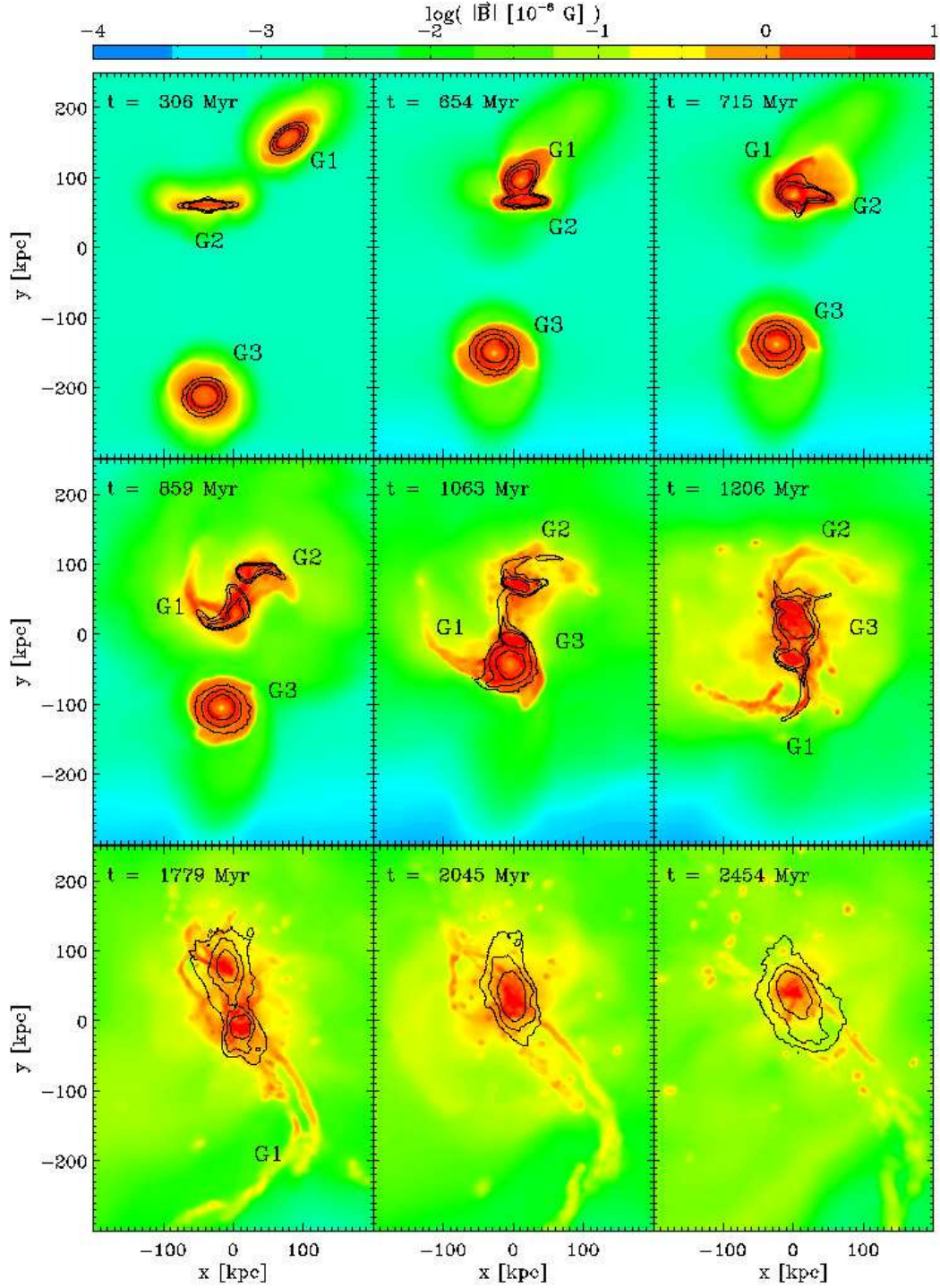


Figure 4.1: The evolution of the magnetic field as a function of time for the G6-IGM9 scenario. Colours visualize the mean line-of-sight total magnetic field  $|\mathbf{B}|$  (in units of  $10^{-6}$  G) and contours correspond to stellar surface density  $\Sigma_{\text{stars}}$ . The contour levels are 10, 20 and  $50 M_{\odot} \text{pc}^{-2}$ .

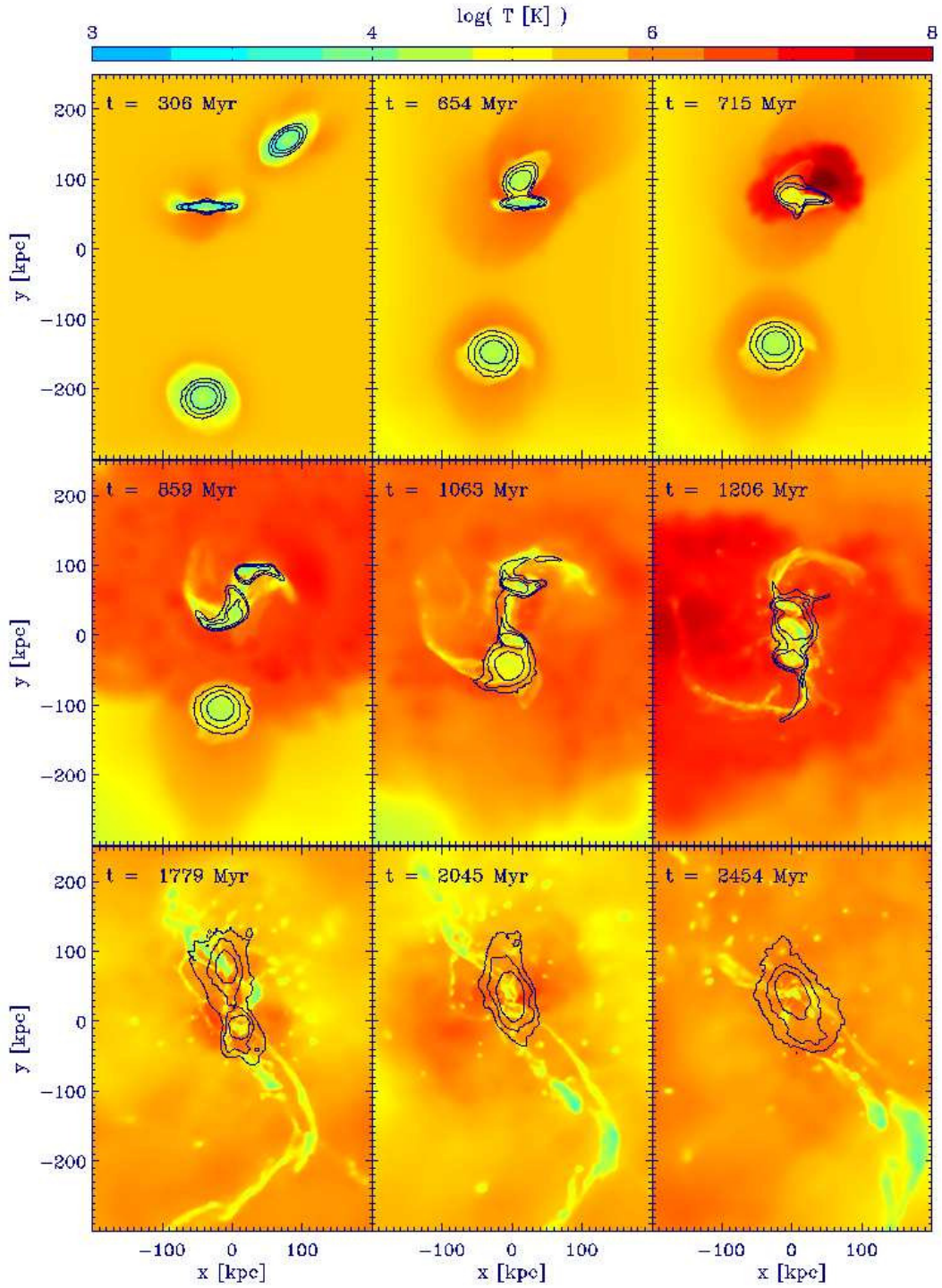


Figure 4.2: The evolution of the temperature as a function of time for the G6-IGM9 scenario. Colours visualize the mean line-of-sight temperature  $T$  (in K). Contours correspond to stellar surface density as in Fig. 4.1.

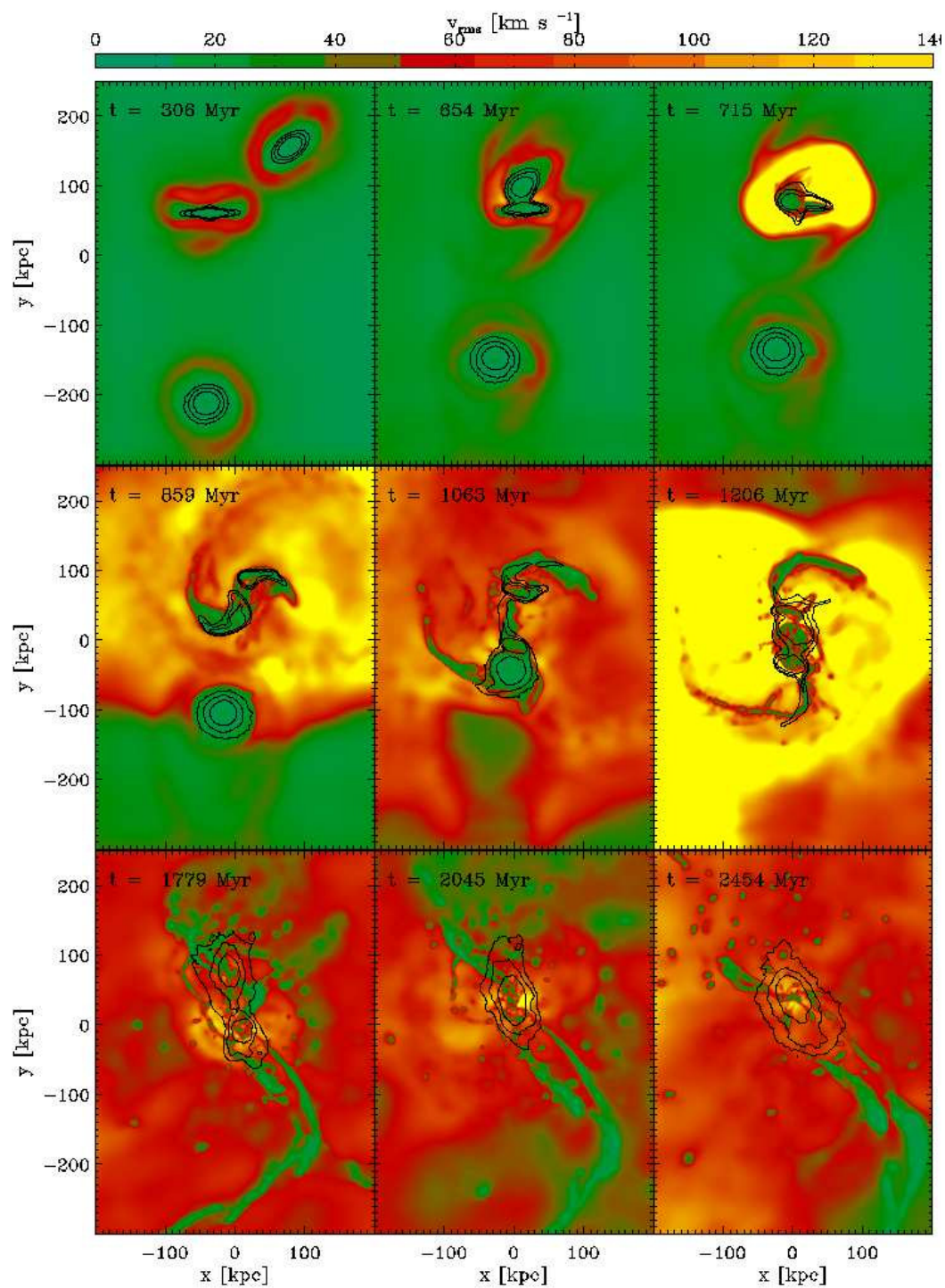


Figure 4.3: The evolution of the rms velocity as a function of time for the G6-IGM9 scenario. Colours visualize the mean line-of-sight rms velocity  $v_{\text{rms}}$  (in  $\text{km s}^{-1}$ ). Contours correspond to stellar surface density as in Fig. 4.1.

central and right panels in Fig. 4.2). Simultaneously, the rms velocity is enhanced and the magnetic field is strengthened in the shocked regions (upper right panels in Figs. 4.1 and 4.3). During the collision, prominent tidal arms are developing (middle left panels in Figs. 4.1 - 4.3). At  $t \approx 1.1$  Gyr a second collision between G1 and G3 takes place, again accompanied by shocks and interaction-driven outflows. During the subsequent violent collision between G2 and G3 at  $t \approx 1.2$  Gyr, further shocks and outflows are driven into the pre-shocked gas of the IGM (middle right panel in Fig. 4.3). The pre-shocked gas is now ejected by the cumulative shock fronts of this interaction, thus magnetizing the IGM. At  $t \approx 1.8$  Gyr, the IGM within several 100 kpc around the collision debris is magnetized and highly turbulent (lower left panels in Figs. 4.1 and 4.3). The debris continues to interact until their mutual final merger at  $t \approx 2.5$  Gyr (lower right panels in Figs. 4.1 - 4.3). By the end of the simulation, the galactic magnetic field has an average value of approximately  $10^{-6}$  G, thus retaining its initial value, and the average IGM magnetic field reached a final strength of roughly  $10^{-8}$  G (lower right panel in Fig. 4.1).

The global morphological evolution of the system within the G9-IGM9, G9-IGM12 and the G0-IGM0 scenarios is similar to the evolution within the G6-IGM9 scenario presented above, i.e. the evolution of the stellar distribution does not change significantly, and the collisions and merger events take place at the same times.<sup>2</sup> For clarity, we do not show the corresponding figures to Figs. 4.1 - 4.3 for the other scenarios here (see appendix 4.A), but rather highlight the main differences below.

#### 4.4.2 Differences between the scenarios

The most prominent differences between the different scenarios are the evolution of the magnetic field and, simultaneously, the behaviour of the shocks driven into the IGM during the interactions. Thereby, the shocks are propagating faster (and gain higher Mach numbers, section 4.4.2.2) for stronger initial magnetic fields. This is best visible during and shortly after the first collision ( $t \approx 700 - 900$  Myr), when shocks are driven into the IGM for the first time. After the second collision, multiple shocks are propagating through the IGM which are additionally moving with different velocities depending on the scenario considered. Thus, even if it is possible to identify a single shock within one scenario, it is not possible to find the corresponding shock structure within the other scenarios. Therefore, within this section, we confine our analysis to the time before the second collision, where we can identify and compare the shocks within every scenario.

##### 4.4.2.1 Differences in the shock propagation

Fig. 4.4 shows the shock propagation within the different scenarios, which is best visibly traced by the rms velocity. From top to bottom: the mean line-of-sight rms velocity at  $t = 715$  Myr (left panels) and  $t = 859$  Myr (right panels) for the G6-IGM9, G9-IGM9, G9-IGM12 and the G0-IGM0 scenario, respectively. The color table is the same as in Fig. 4.3, whereby we only show the upper two galaxies G1 and G2.

The energy initially released in form of shocks by the subsequent interactions should be comparable within each scenario, as the setup of the galaxies and thus the impact parameters are the same. Nevertheless, Fig. 4.4 clearly shows that the stronger the initial magnetic field (decreasing from top to bottom), the faster the shocks propagate (note that the different scenarios differ *only* in the value of the initial field). The shock is the slowest for the scenario excluding magnetic fields (G0-IGM0, bottom panels). This behaviour suggests that the magnetic pressure associated with the magnetic field is able to additionally push the gas driven out by the interaction and thus accelerate the shocks.

<sup>2</sup>This is not surprising, as it is commonly believed that the global morphological evolution of interacting galactic systems is determined mainly by gravity and associated tidal action. However, it is interesting to note that in the early sixties, some authors believed that the filaments and tails observed in interacting galactic systems have nothing to do with tidal phenomena and even considered magnetic fields as the driving force for the morphological appearance of those systems (Vorontsov-Velyaminov, 1960, 1962).

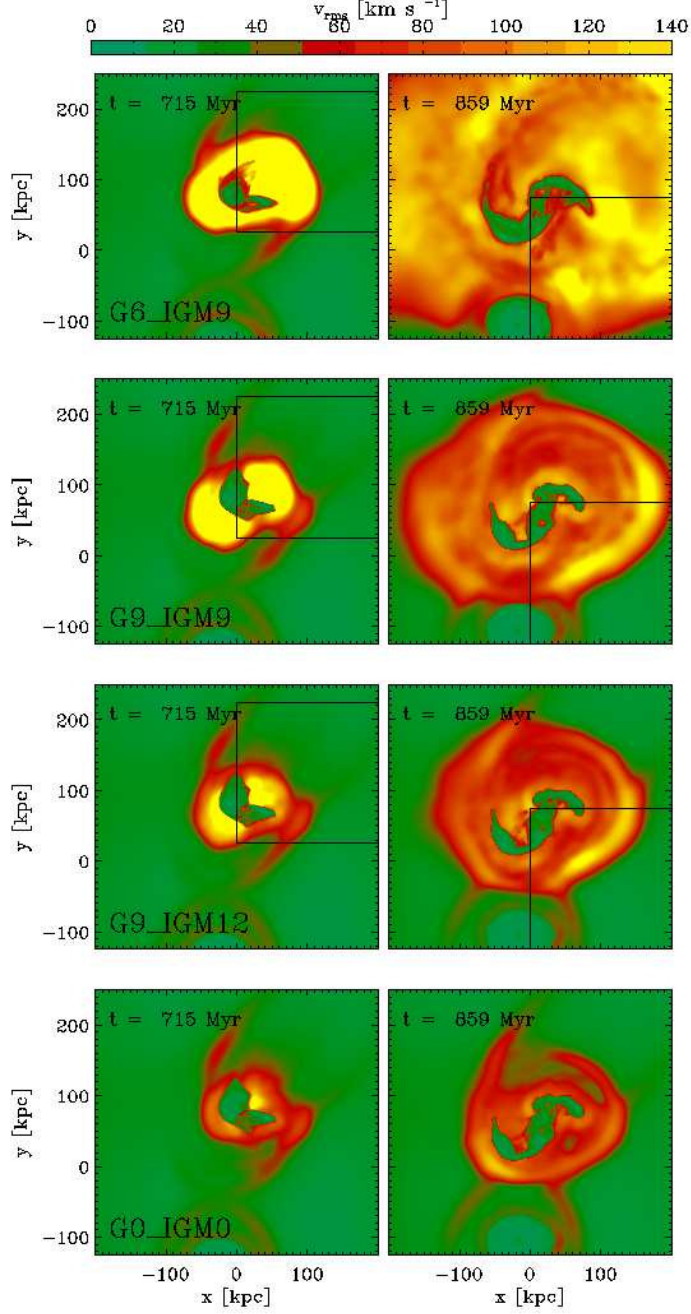


Figure 4.4: Shock propagation within the different scenarios, traced by the rms velocity. From top to bottom: the mean line-of-sight rms velocity at  $t = 715$  Myr (left panels) and  $t = 859$  Myr (right panels) for the G6-IGM9, G9-IGM9, G9-IGM12 and the G0-IGM0 scenario, respectively. The color table is the same as in Fig. 4.3, whereby we only show the upper two galaxies G1 and G2. The higher the initial magnetic field (decreasing from top to bottom), the faster the shock propagation. The black boxes indicate the regions within which we analyse the shocks in more detail (see below).

#### 4.4.2.2 Differences in the magnetic field evolution

Fig. 4.5 shows zoom-ins on the shock region at  $t = 715$  Myr (black boxes in the left panels in Fig. 4.4) for the G6-IGM9 scenario (left panel), the G9-IGM9 scenario (central panel) and the G9-IGM12 scenario (right panel), respectively. Colours give the total magnetic field strength applying the same colour coding as in Fig. 4.1. Black vectors show the gas velocity whereby a length of ten on the given spatial scale corresponds to  $500 \text{ km s}^{-1}$ . The white line indicates the line-of-sight  $r_{\text{los}}$  used for the shock analysis presented below. The higher the initial magnetic field, the faster the shock (see also Fig. 4.4), and the magnetic field is significantly strengthened behind the shock front. Independent of the initial magnetization model, the magnetic field strength behind the shock reaches values of the order of  $10^{-6}$  G, thus showing that the growth is more efficient for lower initial magnetic fields.

Fig. 4.6 shows zoom-ins on the shock at  $t = 859$  Myr (black boxes in the right panels in Fig. 4.4), similar to Fig. 4.5, but with vector length of ten corresponding to  $200 \text{ km s}^{-1}$ . As before, the magnetic field strengths behind the shock reach a common value. However, within the tenuous IGM gas, the magnetic field reaches strengths of only  $10^{-8}$  G.

Fig. 4.7 shows the hydrodynamic values along the line-of-sight  $r_{\text{los}}$  for the shock at  $t = 715$  Myr. The values are calculated using the SPH interpolation formalism. We show the shock properties for the G6-IGM9 scenario (blue lines), the G9-IGM9 scenario (red lines), the G9-IGM12 scenario (black lines), and the G0-IGM0 scenario (green lines), respectively. From left to right and top to bottom: The number density  $n$ ; the sound velocity  $c_s$ , the Alfvén velocity  $v_{\text{Alfvén}} = B/\sqrt{4\pi\rho}$  and the magnetosonic velocity  $c_{\text{ms}} = \sqrt{c_s^2 + v_{\text{Alfvén}}^2}$ , respectively (whereby we do not show  $v_{\text{Alfvén}}$  and  $c_{\text{ms}}$  for the G0-IGM0 scenario); the gas velocity projected onto the line-of-sight  $v_{\text{pro}}$ ; and, finally, the magnetic pressure  $P_{\text{mag}}$  (except for the G0-IGM0 scenario), the thermodynamical pressure  $P_{\text{therm}}$  and the shock energy density  $e_{\text{shock}}$ , respectively. We estimate the shock energy density by considering the difference between the projected downstream (ds) peak velocity  $v_{\text{pro,peak}}^{\text{ds}}$  (i.e. the shock velocity) and the average upstream (us) velocity  $v_{\text{pro}}^{\text{us}}$ , i.e.  $e_{\text{shock}} = 1/2\rho^{\text{ds}} \cdot (v_{\text{pro,peak}}^{\text{ds}} - v_{\text{pro}}^{\text{us}})^2$ . Magnetosonic Mach numbers  $M_{\text{ms}} = (v_{\text{pro,peak}}^{\text{ds}} - v_{\text{pro}}^{\text{us}})/c_{\text{ms}}^{\text{us}}$  for the magnetized scenarios, and the Mach number  $M = (v_{\text{pro,peak}}^{\text{ds}} - v_{\text{pro}}^{\text{us}})/c_s^{\text{us}}$  for the G0-IGM0 scenario are given in the upper left panel.

Again, Fig. 4.7 clearly shows that the shock is propagating faster the stronger the initial magnetic field (e.g. lower left panel). Thus, it is the fastest within the G6-IGM9 scenario, and the slowest within the G0-IGM0 scenario. This increase in the shock intensity is also reflected in the projected gas velocities (lower left panel) and the corresponding Mach numbers, which range from 1.7 for the G0-IGM0 scenario to 6.0 for the G6-IGM9 scenario.<sup>3</sup> Within each scenario (except for the G0-IGM0 scenario), the magnetic field gets strengthened behind the shock (solid lines in the lower right panel). Thereby, the magnetic pressure behind the shock is of order of the energy density of the shock itself (between  $10^{-13}$  and  $10^{-12} \text{ erg cm}^{-3}$ ) within each scenario, thus confirming that the growth of the magnetic field is the more efficient the lower the initial magnetic field.

Fig. 4.8 shows the same quantities as in Fig. 4.7 but for the shock at  $t = 859$  Myr. Again, the shock is propagating faster the stronger the initial magnetic field. However, the Mach numbers are lower than at  $t = 715$  Myr, ranging from 1.4 for the G0-IGM0 scenario to only 2.8 for the G6-IGM9 scenario. Thus, also the shock energies are lower by roughly one order of magnitude (lower left panel). As before, the magnetic field gets strengthened behind the shock (lower left panel). However, for this weaker subsequent shock which is propagating through a pre-shocked gas further outside the galaxies, the growth is not as efficient as at  $t = 715$  Myr. Hence, the magnetic pressure behind the shock does not reach the shock energy density.

However, given the different sound speeds (or magnetosonic velocities) within the different scenarios, also the hydrodynamical timescales ( $\sim c_s/l$ , where  $l$  is a typical length-scale) are different.

<sup>3</sup>Mach numbers of approximately 2-5 have also been found by Johansson et al. (2009c) in their numerical studies of gravitational heating through the release of potential energy from infalling stellar clumps on galaxies.

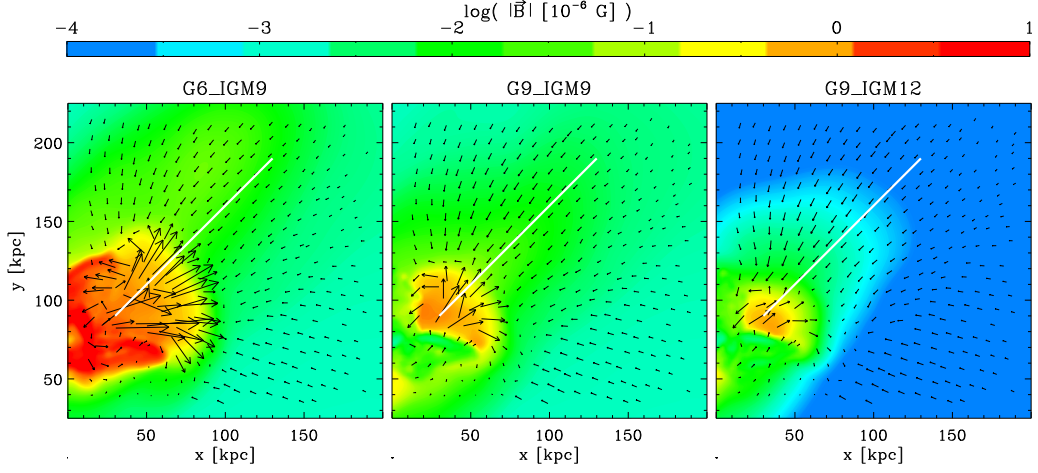


Figure 4.5: Zoom-ins on the shock region at  $t = 715$  Myr (black boxes in the left panels in Fig. 4.4) for the G6-IGM9 scenario (left), the G9-IGM9 scenario (central) and the G9-IGM12 scenario (right). Colours give the total magnetic field strength similar to Fig. 4.1 and black vectors show the gas velocity (a length of ten on the given spatial scale correspond to  $500 \text{ km s}^{-1}$ ). The white line indicates the line-of-sight  $r_{\text{los}}$  used for the shock analysis. The magnetic field strength reaches  $\approx 10^{-6} \text{ G}$  behind the shock within each scenario.

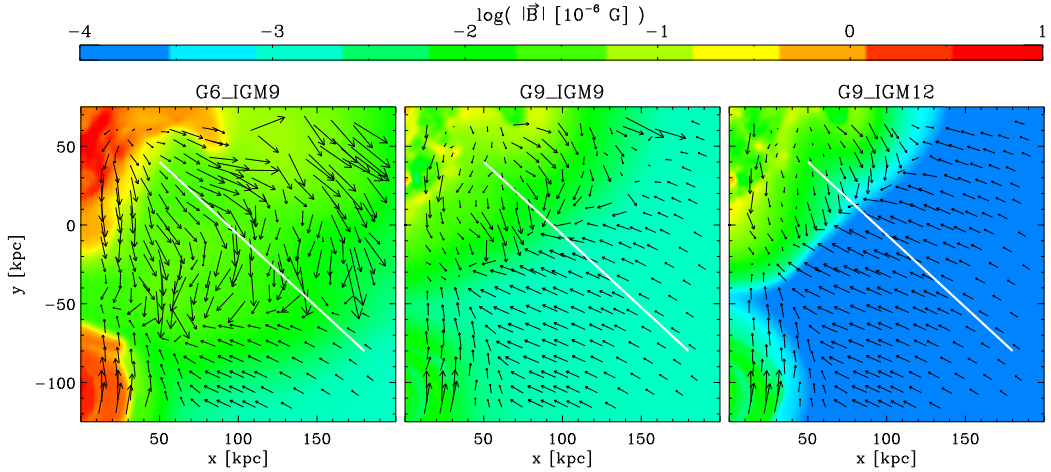


Figure 4.6: Zoom-ins on the shock region at  $t = 859$  Myr (black boxes in the right panels in Fig. 4.4), similar to Fig. 4.5, but with a vector length of ten corresponding to  $200 \text{ km s}^{-1}$ . The IGM magnetic field strength behind the shock front reaches  $\approx 10^{-8} \text{ G}$  within each scenario.

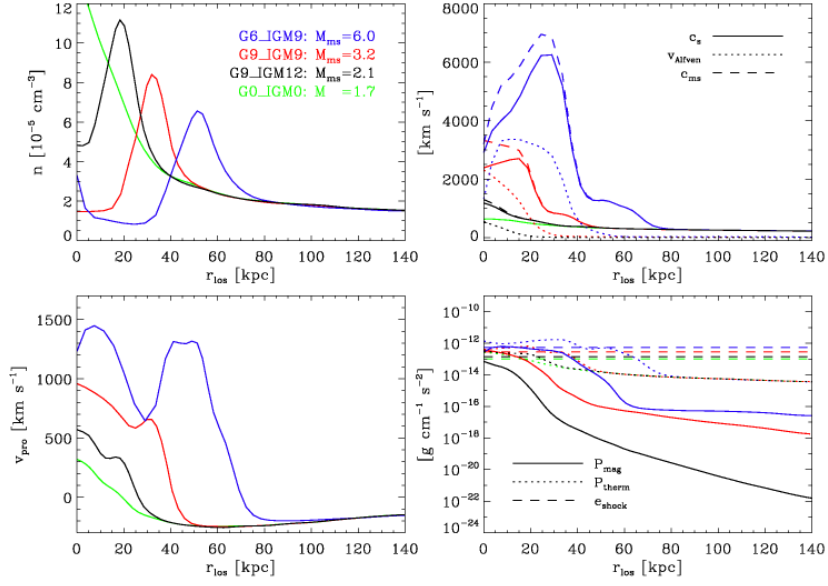


Figure 4.7: Hydrodynamic values along the line-of-sight  $r_{\text{los}}$  at  $t = 715$  Myr for the G6-IGM9 scenario (blue lines), the G9-IGM9 scenario (red lines), the G9-IGM12 scenario (black lines), and the G0-IGM0 scenario (green lines), respectively. From left to right and top to bottom: The number density  $n$ ; the sound velocity  $c_s$ , the Alfvén velocity  $v_{\text{Alfvén}}$  and the magnetosonic velocity  $c_{\text{ms}}$ , respectively; the gas velocity projected onto the line-of-sight  $v_{\text{pro}}$ ; and, eventually, the magnetic pressure  $P_{\text{mag}}$ , the thermodynamical pressure  $P_{\text{therm}}$  and the shock energy density  $e_{\text{shock}}$ , respectively. Magnetosonic Mach numbers  $M_{\text{ms}}$  for the magnetized scenarios are given in the upper left panel. For the G0-IGM0 scenario, we give the Mach number  $M$  and do not show  $v_{\text{Alfvén}}$ ,  $c_{\text{ms}}$  and  $P_{\text{mag}}$ , respectively.

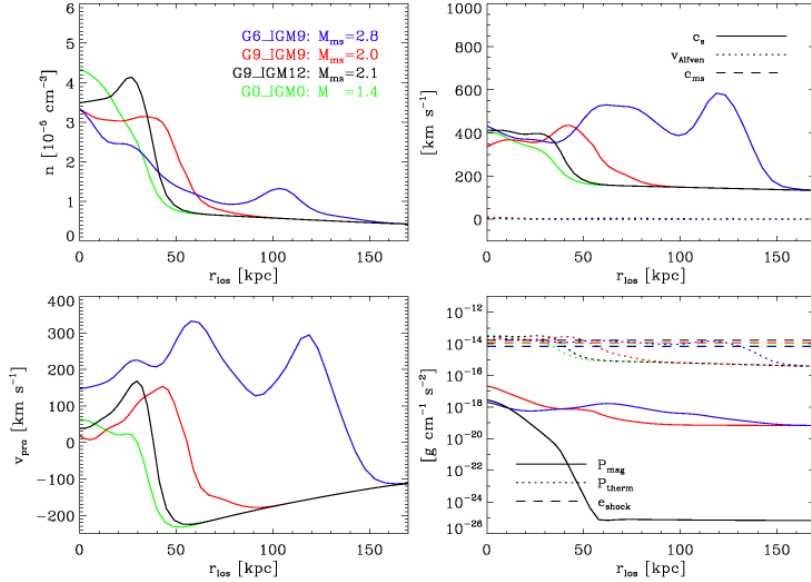


Figure 4.8: Same as Fig. 4.7, but for the shock at  $t = 859$  Myr. Note the different  $y$ -ranges compared to Fig. 4.7.

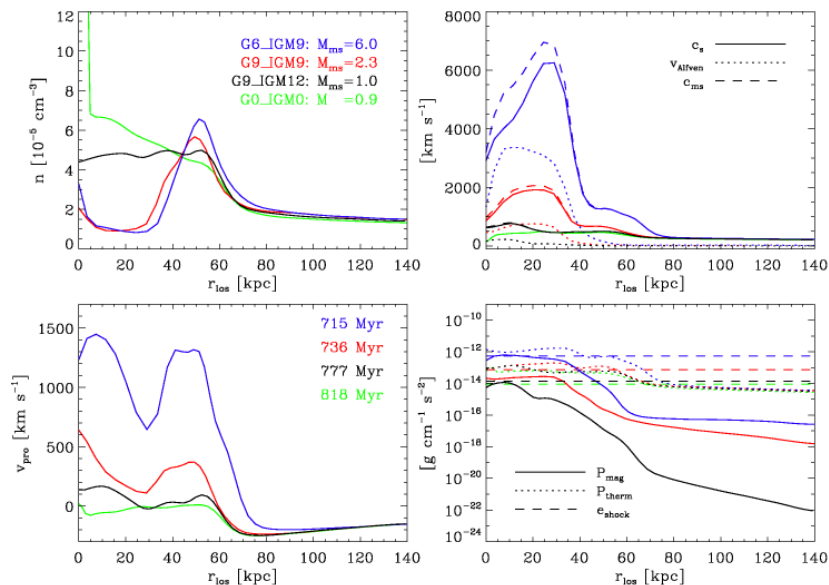


Figure 4.9: Same as Fig. 4.7, but for these moments in time, at which the density peaks of the shocks driven by the first collision within each scenario have covered the same distance (the different times for each scenario are given in the lower left panel). The even greater difference in the Mach numbers compared to Fig. 4.7 confirms the conclusion that the shocks are supported by magnetic pressure.

Thus, the comparison of the shocks at the same global dynamical time (defined by the gravitational interaction) might be questioned. In order to verify our conclusions drawn on the basis of Figs. 4.7 and 4.8, we show how the shocks within each scenario compare when the density peaks of the shocks driven by the first collision have covered the same distance (Fig. 4.9). The corresponding different global dynamical times for each scenario are given in the lower left panel of Fig. 4.9. The lower the sound speed (upper right panel), the later in time the morphological agreement with the G6-IGM9 scenario (blue lines) is reached (upper left panel). The difference in the shock behaviour, i.e. the fact that the projected velocities are smaller for a smaller initial magnetization (lower left panel), is even more pronounced as before in Fig 4.7. This is reflected also in the Mach numbers (upper left panels in Fig. 4.7 and 4.9) and in the energies of the shocks (lower right panels in Fig. 4.7 and 4.9), and confirms our conclusion that the shocks are stronger for a stronger initial magnetization.

In summary, when shocks and outflows are driven by the interactions, the magnetic fields get strengthened. Thereby, the weaker the initial magnetic field, the more efficient the growth of the field (except for scenario G0-IGM0, where we exclude magnetic fields). The magnetic fields are thereby most efficiently strengthened behind the shocks. By the end of the simulations, the magnetic field strengths and distributions within every scenario are comparable (see section 4.4.3.1 and the appendix 4.A.1).

#### 4.4.2.3 Differences in the temperature evolution

According to the Rankine-Hugoniot shock jump conditions, the temperature behind the shock is proportional to the Mach number of the shock (more precisely, for  $\gamma = 5/3$ ,  $T_{\text{ds}}/T_{\text{us}} \propto 5M^2 + 14 - 3/M^2$ , see Landau and Lifshitz, 1959). Thus, the higher Mach numbers within the different scenarios are reflected in the temperatures of the IGM behind the shock fronts (best visible for  $t = 715$  Myr, Fig.

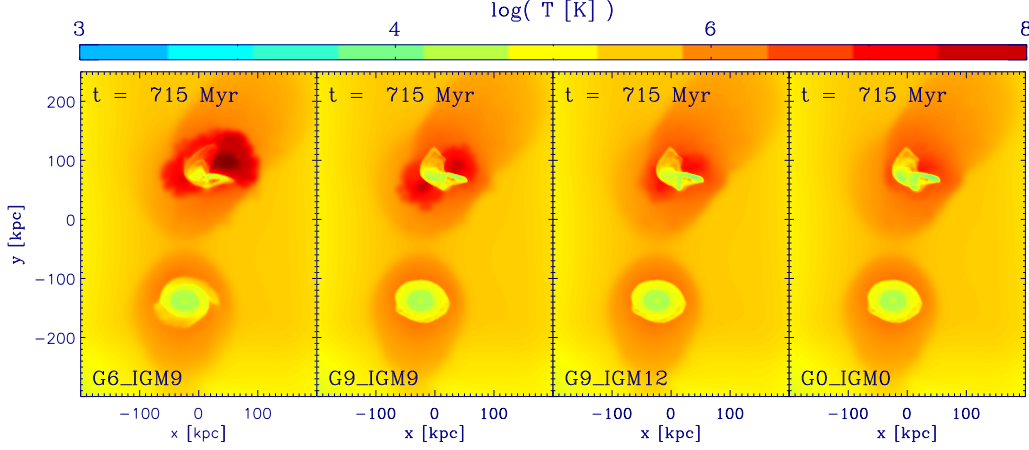


Figure 4.10: Comparison of the temperatures at  $t = 715$  Myr within the different scenarios. From left to right: the G6-IGM9, G9-IGM9, G9-IGM12 and the G0-IGM0 scenario. The color table is the same as in Fig. 4.2. The higher the Mach numbers (decreasing from left to right), the higher the temperature.

4.10). Simultaneously, the region of shock heated gas is larger the stronger the shock (see also appendix 4.A.2). Thereby, the IGM temperatures reach values up to  $10^8$  K. Gas of this temperature can be expected to give rise to significant X-ray emission by thermal bremsstrahlung. This was shown by e.g. Cox et al. (2006), who performed hydrodynamical simulations of mergers of gas-rich disk galaxies. They showed that the hot diffuse gas that is produced by strong shocks attending the merger process can produce appreciable X-ray emission. Hence, it is interesting to note that the expected X-ray emission during galactic interactions increases with increasing magnetic field.

As the nature of the presented galactic interaction is highly non-linear, our conclusions should be taken as general trends. The behaviour of the shocks in our simulations strongly indicates that in the presence of a magnetic field the shocks driven by an interaction are supported by the magnetic pressure, thus resulting in higher Mach numbers. Simultaneously, the magnetic field evolution in our simulations is a strong indication for a shock driven magnetic field amplification. As most of the gas in the Universe is magnetized and shocks can be driven by different processes, we want to emphasize that the “magnetic shock acceleration” seen in our simulations might have implications within many astrophysical settings, e.g. galaxy clusters.

### 4.4.3 Global evolution

#### 4.4.3.1 Magnetic fields

Fig. 4.11 shows the rms magnetic field  $B_{\text{rms}} = \sqrt{\langle B_x^2 + B_y^2 + B_z^2 \rangle}$  as a function of time for the G6-IGM9 scenario (blue lines), the G9-IGM9 scenario (red lines), and the G9-IGM12 scenario (black lines). We separately plot the IGM values (dotted lines) and the values inside the galaxies (solid lines). We distinguish between the IGM and the galaxies applying a density threshold of  $10^{-29}$  g  $\text{cm}^{-3}$ .

Within all magnetized scenarios, the galactic magnetic field saturates at several  $\mu\text{G}$  by the end of the simulation, independent of the initial magnetic field strength. The first collision between G1 and

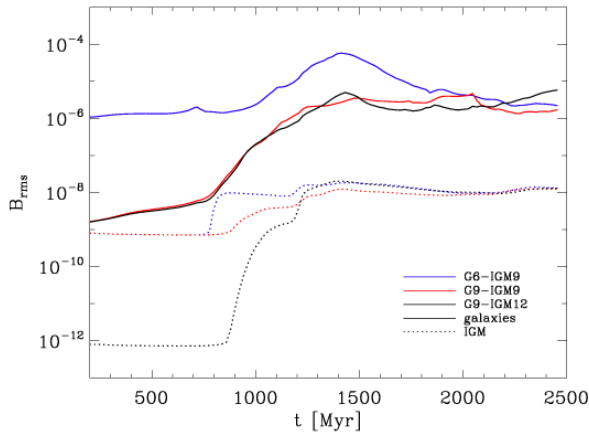


Figure 4.11:  $B_{\text{rms}} = \sqrt{\langle B^2 \rangle}$  as a function of time for the G6-IGM9 scenario (blue lines), the G9-IGM9 scenario (red lines), and the G9-IGM12 scenario (black lines). We separately show the IGM values (dotted lines) and the values inside the galaxies (solid lines). We distinguish between the IGM and the galaxies applying a density threshold of  $10^{-29} \text{ g cm}^{-3}$ . The final values for the galactic and the IGM magnetic field, respectively, are the same within all scenarios.

G2 initiates within all scenarios a steady growth of the galactic rms magnetic field, which continues throughout the second and third collision. This growth starts at a later time and is less efficient within the G6-IGM9 scenario (where the initial galactic field is already of order of the final value) than within the other scenarios. This indicates that it is easier to enhance a magnetic field which is not yet of the order of the saturation value. In the subsequent evolution, the galactic rms magnetic field strength within the G6-IGM9 scenario decreases again. Thus, at time of the intermediate merger ( $t \approx 1.8 \text{ Gyr}$ ), the galactic magnetic field has a rms value between 1 and  $10 \mu\text{G}$  within all scenarios. The intermediate and the final mergers ( $t \approx 2 \text{ Gyr}$ ) do not lead to further growth of the field.

The evolution of the IGM rms magnetic field (dotted lines) results in a common final value of approximately  $10^{-8} \text{ G}$  within all scenarios. Again, the first collision initiates a growth of the IGM magnetic field. Within the G9-IGM12 scenario, where the initial IGM field is four orders of magnitude smaller than the final value, this growth continues throughout the second and third collision until the final value is reached after approximately 500 Myrs. Within the G6-IGM9 scenario, the initial IGM field of  $10^{-9} \text{ G}$  grows by a factor of 10 at time of the first collision, thus reaching the final value shortly after this collision. None of the further collision and merger events lead to a significant further growth of the field. Most interestingly, the same initial IGM field of  $10^{-9} \text{ G}$  does not grow as efficiently at time of the first collision within the G9-IGM9 scenario. Rather, within the G9-IGM9 scenario, the IGM field grows more slowly and reaches the final value only after the final merger. The only difference between the G9-IGM9 and G6-IGM9 scenarios is the different initial galactic magnetic field, which is three order of magnitude higher within the G6-IGM0 scenario. Thus, the faster growth of the IGM field within the G6-IGM9 scenario shows that interaction-driven outflows transport magnetic field energy from the galaxies into the IGM, resulting in a more efficient growth of the IGM magnetic field.

The fundamental source of energy for the general strengthening of the magnetic field is the gravitational energy released during the interaction of the galaxies. This gravitational energy is converted into kinetic energy of the particles, particularly, turbulence which is expected to be driven on kpc scales. The kinetic energy in turn is partly converted into magnetic energy by compression, shearing and folding of the magnetic field lines. This behaviour results from the basic thermodynamical principle according to which the free energy of a system will always be distributed among all available

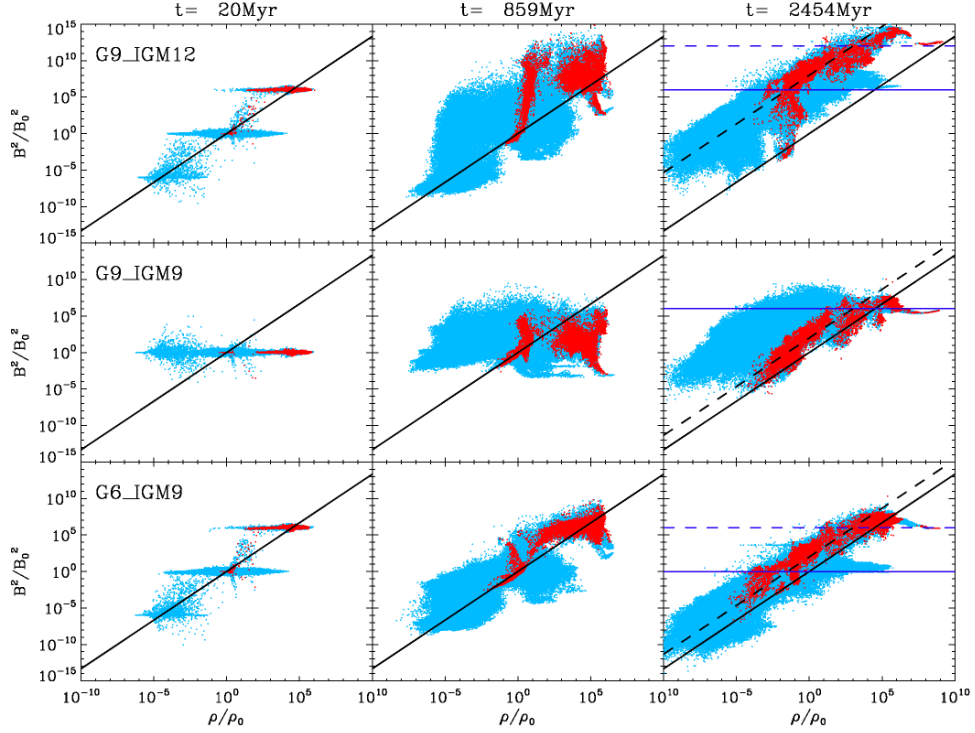


Figure 4.12:  $B^2/B_0^2$  as a function of  $\rho/\rho_0$  at three different timesteps (from left to right:  $t = 20$  Myr,  $t = 859$  Myr and  $t = 2454$  Myr) for the G9-IGM12 scenario (upper panels), the G9-IGM9 scenario (central panels) and the G6-IGM9 scenario (lower panels). The light blue dots correspond to particles with an initial density  $\rho \geq 10^{-29}$  g cm $^{-3}$  (i.e. galactic particles), and the residual particles (IGM) are marked in red. The black solid lines follow the relation  $B^2/B_0^2 = (\rho/\rho_0)^{4/3}$ , which is valid for isotropic compression. The final distributions of the magnetic field strengths (right panels) lie above this relation, showing that compression is not the only process responsible for the growth of the magnetic field. The black dashed lines (right panels) show the same relation but shifted by the factor by which the IGM magnetic field has been strengthened within each scenario (not fitted to the distribution). The horizontal solid and dashed dark blue lines (right panels) correspond to the difference between, respectively, the initial galactic and IGM magnetic field ( $B_{0,\text{disk}}$  and  $B_{0,\text{IGM}}$ ) within each scenario, and the common final galactic rms value of  $10^{-6}$  G (for the G9-IGM9 scenario, these lines lie on top of each other). These are the saturation levels of the magnetic field in the different scenarios.

energy channels. Given the high variability of the simulated system and the limited resolution, however, detailed studies of the small-scale processes responsible for this distribution (e.g. the turbulent dynamo) are beyond the scope of this paper. Yet, simple magnetic field line compression would result in a tight correlation between the magnetic field strength and the gas density. Thus, it is possible to demonstrate the presence of the other processes, i.e. the shearing and folding of the magnetic field lines in the course of turbulent amplification, by analyzing the distribution of the magnetic field strength as a function of the gas density.

Fig. 4.12 shows  $B^2/B_0^2$  as a function of  $\rho/\rho_0$  at three different timesteps (from left to right:  $t = 20$  Myr,  $t = 859$  Myr and  $t = 2454$  Myr) for the G9-IGM12 scenario (upper panels), the G9-IGM9 scenario (central panels) and the G6-IGM9 scenario (lower panels). The light blue dots correspond to particles with an initial density  $\rho \geq 10^{-29}$  g cm $^{-3}$  (i.e. galactic particles), and the residual particles (IGM) are marked in red. The “trimodality” of the distribution of the G9-IGM12 and the G6-IGM9 scenarios at  $t = 20$  Myr is a result of the initial conditions: At the edges of the galaxies,

IGM particles carrying a weak magnetic field overlap with galactic particles having a stronger field. Magnetic diffusion redistributes the field among these edge particles, leading to an increase of the IGM field and a decrease of the galactic field in these regions. This effect is of course not seen for the G9-IGM9 scenario, where all particles carry the same initial magnetic field.

The black solid lines crossing all panels of Fig. 4.12 follow the equation  $B^2/B_0^2 = (\rho/\rho_0)^{4/3}$ , which is valid for isotropic compression of a turbulent magnetic field. If compression would be the only process responsible for the magnetic field growth, the distribution could evolve only along this line. Yet, the intermediate and final distributions of the magnetic field strengths (middle and right panels) lie above this relation, showing that turbulent amplification has additionally strengthened the field (this is least prominent for the G6-IGM9 scenario, where the initial magnetic field strength is already of the order of the final strength). On the other hand, the final distributions (right panels) follow the 4/3 inclination, thus showing that compression has to be a part of the overall strengthening process. The factor by which the IGM magnetic field (squared) gets strengthened is approximately  $(10^4)^2$  for the G9-IGM12 scenario and  $(10)^2$  for the G9-IGM9 and the G6-IGM9 scenarios, respectively. The black dashed lines (right panels) correspond to the black solid lines but shifted by this factor (not fitted to the distribution), thus additionally demonstrating the importance of non-compressive processes for the magnetic field evolution.

The horizontal solid and dashed dark blue lines in Fig. 4.12 (right panels) indicate the difference between, respectively, the initial galactic and IGM magnetic field ( $B_{0,\text{disk}}$  and  $B_{0,\text{IGM}}$ ) within each scenario, and the common final galactic rms value of  $10^{-6}$  G (for the G9-IGM9 scenario, these lines lie on top of each other). As this final galactic rms value is the maximal magnetic field strength which can be acquired by both, the galactic and the IGM particles, the dark blue lines actually show the saturation levels of the magnetic field in the different scenarios. This is also visible from the “noses” on the right-hand side of the final distributions, which show that particles which have already reached the saturation level can not acquire higher magnetic field strengths even if the density increases.

In summary, Fig. 4.12 shows that the magnetic field growth driven by the interactions is due to both, the compression and the folding and stretching of the magnetic field lines in turbulent flows. It also confirms the saturation level of the magnetic field strength as shown in Fig. 4.11. However, we note that the presented simulations are not designed to study the process of turbulent amplification in detail, wherefore our results should be interpreted in terms of general thermodynamics and magnetohydrodynamics.

#### 4.4.3.2 Numerical divergence

Fig. 4.13 shows the mean numerical divergence measure  $\langle h_{\text{SPH}} |\nabla \cdot \mathbf{B}| / |\mathbf{B}| \rangle$  as a function of time for the G6-IGM9 scenario (blue lines), the G9-IGM9 scenario (red lines), and the G9-IGM12 scenario (black lines). We separately show the IGM values (dotted lines) and the values inside the galaxies (solid lines). A numerical divergence is expected to arise from the SPH divergence operator even for a field which is divergence free in the first place, but tangled on sub-resolution scales. This numerical divergence arises also in simulations where the magnetic field is expressed in terms of Euler potentials, which avoid physical divergence by definition. Comparisons of simulations using the Euler potentials with simulations using the direct implementation (as in this paper) have shown that the numerical divergence does not influence the evolution of the magnetic field significantly as long as the divergence measure is  $\leq 1$  (Kotarba et al., 2009). For the simulations presented here, the mean numerical divergence of all gas particles stays always below this tolerance value, except for the IGM value within the G9-IGM12 scenario during the third collision. Note, however, that this comparatively high divergence does not lead to an enhanced magnetic field growth (Fig. 4.11). Generally, the higher the initial magnetic field, the lower the numerical divergence. This trend is consistent with previous studies (Kotarba et al., 2010a). The reason for this behaviour is the Lorentz force acting on the particles, which is always opposing the motions leading to a change (growth) of the magnetic field.

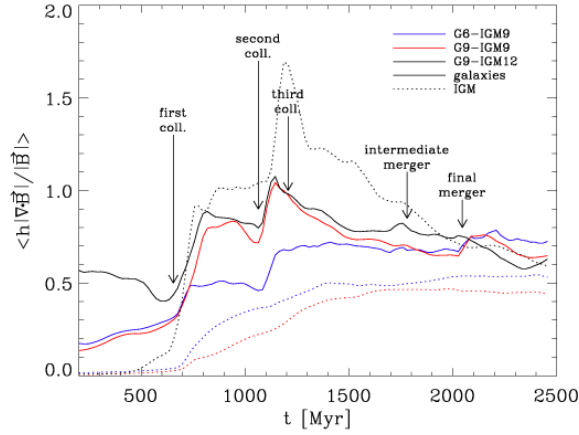


Figure 4.13: The mean  $\langle h \nabla \cdot \mathbf{B} / |\mathbf{B}| \rangle$  as a function of time for the G6-IGM9 scenario (blue lines), the G9-IGM9 scenario (red lines), and the G9-IGM12 scenario (black lines). We separately show the IGM values (dotted lines) and the values inside the galaxies (solid lines). We distinguish between the IGM and the galaxies applying a density threshold of  $10^{-29} \text{ g cm}^{-3}$ . The numerical divergence is small enough to guarantee numerical stability.

The stronger the field, the stronger this force. Thus, in the presence of a stronger field, random particle motions on sub-resolution scales are more efficiently suppressed. These motions result in a sub-resolution tangling of the magnetic field, and by reducing the motions, the numerical divergence is simultaneously reduced. Altogether, the numerical divergence should not influence the general conclusions on the magnetic field evolution presented in this paper (see also Kotarba et al., 2009, 2010a).

#### 4.4.3.3 Pressures

Saturation phenomena as seen for the magnetic fields in our simulations (Fig. 4.11) usually suggest some kind of energy equipartition. Given enough time, a thermodynamical system will always distribute its free energy to all the degrees of freedom available. A particular saturation value is thereby reached when the energy which is increasing balances the energy of the source responsible for the increase. For example, in case of the galactic dynamo, the main source for the amplification of the magnetic field is the energy of the particles which have a velocity component perpendicular to the galactic disc. The corresponding rising and descending particle motions are expected to become helical under the influence of the Coriolis force, resulting in the so-called  $\alpha$ -effect (see e.g. Kulsrud (1999) for a review). Assuming these particles to be cosmic ray (CR) particles rises the expectation of equipartition between the magnetic and the CR pressure (Hanasz et al., 2009a). This equipartition was recently shown by Hanasz et al. (2009b). More generally, in the framework of MHD, any motion of the gas leading to a growth of the magnetic field will be suppressed by the magnetic field itself via the Lorentz force as soon as the magnetic energy gets comparable to the kinetic energy of the gas. The magnetic energy is then converted into kinetic energy of the gas, thus maintaining equipartition between the magnetic and gas kinetic energy. In particular, the magnetic field is expected to be in equipartition with the turbulent energy of the gas, as only velocity gradients can lead to a growth of the magnetic field. This concept of a “turbulent dynamo” is well known from theory (see e.g. Brandenburg and Subramanian, 2005 for a review). Thus, within this section, we analyse our simulations with respect to the different pressure components within the galaxies and within the IGM.

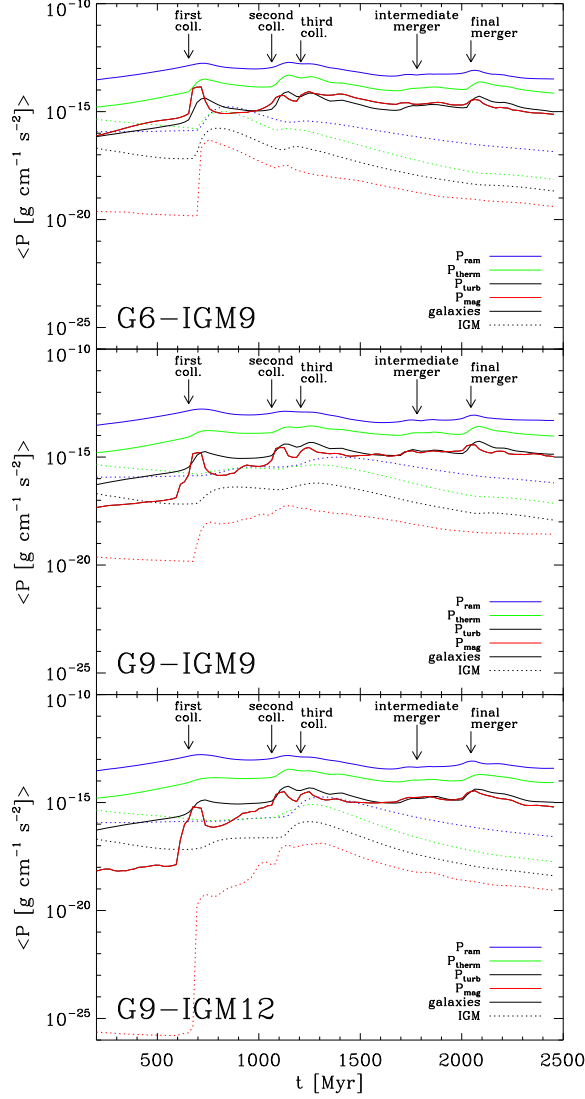


Figure 4.14: Evolution of the volume weighted mean of different pressure components as a function of time for the G6-IGM9 scenario (upper panel), the G9-IGM9 scenario (central panel) and the G9-IGM12 scenario (lower panel). We plot the following pressures: magnetic pressure  $P_{\text{mag}}$  (red lines), thermal pressure  $P_{\text{therm}}$  (green lines), turbulent pressure  $P_{\text{turb}}$  (black lines) and ram pressure  $P_{\text{ram}}$  (blue lines). We distinguish between the IGM (dotted lines) and the galaxies (solid lines) applying a density threshold of  $10^{-29} \text{ g cm}^{-3}$ . By the end of the simulations, the magnetic pressure is of the same order of magnitude as the turbulent pressure within all scenarios.

Fig. 4.14 shows the evolution of the volume weighted mean of different pressure components as a function of time for the G6-IGM9 scenario (upper panel), the G9-IGM9 scenario (central panel) and the G9-IGM12 scenario (lower panel). We plot the following pressures: magnetic pressure  $P_{\text{mag}} = B^2/8\pi$  (red lines), thermal pressure  $P_{\text{therm}} = 1/2\rho c_s^2$  (green lines, with  $c_s$  being the sound speed and  $\rho$  the gas density), turbulent pressure  $P_{\text{turb}} = 1/2\rho v_{\text{rms}}^2$  (black lines) and ram pressure  $P_{\text{ram}} = 1/2\rho v^2$  (blue lines, with  $v$  the total velocity of the gas particle considered, i.e. including turbulent components). Again, we distinguish between the IGM (dotted lines) and the galaxies (solid lines) applying a density threshold of  $10^{-29} \text{ g cm}^{-3}$ .

Within the galaxies (solid lines), the thermal and ram pressures within each scenario evolve smoothly with time, whereby the thermal pressure stays always below the ram pressure by roughly one order of magnitude. By the end of the simulations, these pressure components have the same values as at the beginning. The turbulent pressure (black lines) within each scenario increases by slightly more than one order of magnitude during the simulations, whereby each collision and merger event tends to increase the turbulent pressure.

The galactic magnetic pressures (red solid lines) within each scenario evolve in a similar way as the turbulent pressures, increasing at the times of collision and merger events and partly decreasing afterwards (due to the dilatation of the shocked region and the corresponding dilution of the magnetic field energy). After the second collision, the magnetic pressure is in approximate equipartition with the turbulent pressure within all scenarios. Before, the evolution of the magnetic pressures within the different scenarios differs because of the different initial magnetization. Within the G6-IGM9 scenario (upper panel), where the initial magnetic pressure is already of the order of the turbulent pressure, it increases by roughly one order of magnitude during the first collision, thus even exceeding the turbulent pressure. However, it decreases again to its initial value shortly after the first collision. Within the other scenarios, where the initial magnetic pressure is lower than the turbulent pressure, the galactic magnetic pressure increases during the first collision only up to the equipartition level, and does not decrease to its initial value after this collision.

Within the IGM (dotted lines), the thermal and ram pressures within each scenario are near equipartition until the third collision. This is reasonable, as we assume the IGM temperature to be the same as the virial temperature of the haloes at the beginning of the simulations. However, at roughly the time of the third collision, the thermal pressure begins to decrease more efficiently than the ram pressure, and, in the subsequent evolution, stays below the ram pressure by a factor 10 - 30. This behaviour is similar for each scenario. The IGM turbulent pressure (black dotted lines) differs from the IGM ram pressure by roughly two orders of magnitude during the whole simulation within each scenario, which is comparable to the ratios between the turbulent and ram pressures within the galaxies.

The evolution of the IGM magnetic pressure (red dotted lines) follows the evolution of the turbulent pressure within each scenario after the second collision. This parallel evolution indicates a correlation between these pressure components. However, contrary to what is seen in the galaxies (solid lines), the IGM magnetic pressure stays by roughly one order of magnitude below the IGM turbulent pressure until the end of the simulations. This difference is most probably a result of the numerical method by which we estimate the turbulence, within which shearing and inhomogeneous motions can lead to an overestimate of the turbulence. This can particularly happen within the IGM, where shocks propagate in a nongeneric direction. Thus, the similarity of the evolution of the IGM magnetic and turbulent pressures may be interpreted as equipartition between these components.

Before the second collision, the evolution of the IGM magnetic pressure within the different scenarios again differs because of the different initial magnetization. Within the G6-IGM9 scenario (upper panel), the “quasi” equipartition with the turbulent pressure is reached already after the first collision, whereas it is reached only after the second collision within the other scenarios. Particularly, the IGM magnetic pressure within the G9-IGM9 (central panel) scenario does not grow as efficiently as within the G6-IGM9 scenario, although the initial IGM magnetization is the same within both scenarios.

This difference is due to the stronger initial galactic magnetic field within the G6-IGM9 scenario: The strong galactic field is transported by interaction-driven outflows into the IGM, thus enhancing the IGM magnetic field more efficiently than within the G9-IGM9 scenario (see also section 4.4.3.1).

Summing up, we conclude that the saturation value within the galaxies of several  $\mu\text{G}$  seen in all simulations corresponds to the equipartition between turbulent and magnetic pressure, a result which was also achieved by Kotarba et al. (2010a). Also, the saturation value within the IGM ( $\approx 10^{-8}$  G) supports the assumption of equipartition between magnetic and turbulent pressure.

## 4.5 Synthetic radio emission, polarization and $RM$ maps

Radio observations of local galaxies and galaxy groups provide maps of the distribution and structure of the magnetic fields in these systems. However, the radio maps are always only one snapshot in time and observers face the problem of explaining the origin of the observed magnetic field strengths and structures. For example, observations of the compact group of galaxies Stephan's Quintet, which consists of four interacting spiral galaxies and was recently modeled by means of  $N$ -body simulations by Renaud et al. (2010), show a prominent ridge of radio emission crossing through the system in between the galaxies (Xu et al., 2003). It is commonly believed that this ridge of radio emission corresponds to a shock front driven by a former interaction between two of the galaxies of the group. Due to the shock compression, the magnetic field of the ambient gas might have been amplified. Moreover, electrons are expected to get Fermi-accelerated within the shock, thus giving rise to the enhanced radio emission.

It is the aim of this section to show how our simulated system of three merging galaxies might look like when observed at a typical radio frequency. As we are able to provide synthetic radio maps at every snapshot, we can assess the evolution and thus the origin of the magnetic field pattern seen in the synthetic maps. As detailed radio observations are available only for local groups of galaxies, we have chosen the G6-IGM9 scenario for the calculation of the synthetic maps.

Kotarba et al. (2010a) have already presented such synthetic radio maps for an isolated galaxy and the Antennae system. Compared to their calculations, in this paper, we use a more precise formula for the synchrotron emission, which, however, does not change the results qualitatively (see e.g. Ginzburg and Syrovatskii, 1965, Rybicki and Lightman, 1986 or Longair, 1994 for more details on the standard theory of synchrotron radiation). Assuming an energy distribution of the relativistic CR electrons of a power-law form

$$n(E)dE = \kappa E^{-p}dE \quad (4.2)$$

(where  $n(E)$  is the number density of electrons,  $\kappa$  a constant normalization factor and  $p$  the index of the power spectrum), the synchrotron emissivity  $J_\nu$  at a given frequency  $\nu$  is given by

$$J_\nu = \frac{\sqrt{3}e^2 B_\perp \kappa}{m_e c^2 (p+1)} \left( \frac{m_e^3 c^5 2\pi\nu}{3eB_\perp} \right)^{-\frac{p-1}{2}} \times \Gamma\left(\frac{p}{4} + \frac{19}{12}\right) \Gamma\left(\frac{p}{4} - \frac{1}{12}\right), \quad (4.3)$$

where  $\Gamma$  denotes the Gamma function. The magnetic field component perpendicular to the line of sight  $B_\perp$  is taken from the simulation. The frequency  $\nu$  and the index  $p$  are input parameters. Similar to Kotarba et al. (2010a) we assume  $p = 2.6$  and  $\nu = 4.86 \times 10^9$  Hz, corresponding also to the values given by Xu et al. (2003). The value of  $p$  gives a spectral index of the radio emission of  $\alpha = (p-1)/2 = 0.8$ , which is typical for spiral galaxies (Gioia et al., 1982), and given also by Xu et al. (2003) and Chyży and Beck (2004). Also, this value is close to the power-law slope of 2.7 of the all-particle spectrum of CRs in the energy range of  $10 \times 10^9 \text{ eV} \leq E \leq 3 \times 10^{15} \text{ eV}$  (e.g. Blasi,

2008 and references therein). The constants are the speed of light  $c$ , the electron mass  $m_e$  and the electron charge  $e$ . For a given CR energy density  $e_{\text{CR}}$ ,  $\kappa$  can be derived using Eqs. 4.2:

$$e_{\text{CR}} = \int_{E_{\text{min}}}^{E_{\text{max}}} En(E)dE = \kappa \int_{E_{\text{min}}}^{E_{\text{max}}} E^{1-p}dE. \quad (4.4)$$

Similar to Kotarba et al. (2010a) we assume an energy range of  $E_{\text{min}} = 10^9$  eV to  $E_{\text{max}} = 10^{15}$  eV in our calculations. The cutoff at  $10^9$  eV is justified, since for a magnetic field strength of  $10 \mu\text{G}$  (which is the typical maximum field strength in our simulations) synchrotron emission is radiated mainly by particles with an energy of  $\approx 7 \times 10^9$  eV (Longair, 1994, eq. 18.51). For lower magnetic fields, the energy of the electrons responsible for the observed radiation is even higher.

CRs with energies between  $10^9$  eV and  $10^{15}$  eV are produced mainly through particle acceleration within the shocks of SN remnants. They propagate by advection and diffusion along the magnetic field lines throughout the galaxy or the IGM. Given the non-triviality of the physics involved in these processes (e.g. Blasi, 2008), the distribution of CRs within a galactic system is not easily modeled. However, CRs are bound to the magnetic field, which, in turn, is coupled to the (ionized) thermal gas. Thus, as a reasonable but simple assumption, the CR energy distribution may be expected to be proportional to the thermal energy distribution. Particularly, we assume that  $e_{\text{CR}} = 0.01 \cdot e_{\text{therm}}$ .

$J_\nu$  is calculated for every particle, and the total synchrotron intensity  $I_{\text{tot}}$  is subsequently obtained by integrating along the line-of-sight. The polarized emission  $I_{\text{pol}}$ , the predicted observed degree of polarization  $\Pi_{\text{obs}}$  and the polarization angles  $\psi$  are calculated in the same way as in Kotarba et al. (2010a).

The calculations are implemented within the code P-SMAC2 (Donnert et al., in preparation), which subsequently bins the values of  $I_{\text{tot}}$ ,  $I_{\text{pol}}$ ,  $\Pi_{\text{obs}}$  and  $\psi$  on a grid using the gather approximation as before for Figs. 4.1 to 4.3. In order to account for the spatial isotropy of the emission, we multiply the calculated total and polarized intensities by the factor

$$f_{\text{obs}} = \frac{d_{\text{pix}}^2}{4\pi \cdot d^2}, \quad (4.5)$$

with  $d$  the assumed distance to the observer and  $d_{\text{pix}}$  the pixel size (corresponding to a beam diameter) of  $\approx 0.98$  kpc/h. We assume  $d = 80$  Mpc, which is a typical distance for local groups, e.g. the Stephan's Quintet (Xu et al., 2003). Thus,  $d_{\text{pix}}$  corresponds to an angular resolution of  $\approx 1''.3$ . For comparison, the maximum resolution of the Very Large Array (VLA) at  $\nu = 4.86 \times 10^9$  Hz ( $\lambda \approx 6$  cm) is  $0''.4$ , and for the Effelsberg telescope  $2''.4$ . However, observations performed with these telescopes are usually presented with a lower resolution of  $\approx 5'' - 15''$ , e.g. the Stephan's Quintet (Xu et al., 2003), the Antennae galaxies (Chyży and Beck, 2004) or M51 (Beck, 2009b). The upcoming Square Kilometer Array (SKA) is expected have 50 times the sensitivity of the VLA with a maximum angular resolution of  $0''.02$  at 1.4 GHz ( $\lambda \approx 21$  cm) (Gaensler, 2009).

Fig. 4.15 shows synthetic radio maps for the same nine time steps as in Figs. 4.A2 - 4.A6. Colours visualize the total intensity (in  $\mu\text{J}/\text{pixel}$ ). White contours show the polarized intensity, whereby the contour levels are 0.001, 0.01, 0.1, 1, 10 and 50  $\mu\text{J}/\text{pixel}$ . The direction of the magnetic field is indicated by the black lines which are inclined by  $\psi + \pi/2$ , whereby the data of the  $512^2$  array has been rebinned to a  $50^2$  array, thus lowering the assumed angular resolution to  $\approx 13''$ . The length of this lines is scaled according to the degree of polarization  $\Pi_{\text{obs}}$ , the length-scale is given in the lower right corner of each plot. We show the magnetic field lines only where the polarized intensity is higher than 0.01 times the maximum polarized intensity in the beginning of the simulation, corresponding to a threshold of  $\approx 0.001 \mu\text{Jy}/\text{pixel}$ .

At the beginning of the simulation, the initially unidirectional magnetic field lines within the galaxies are wound up by the differential rotation of the disks. Hence, the magnetic field vectors derived from polarization are showing a nearly toroidal pattern at  $t \approx 300$  Myr (upper left panel).

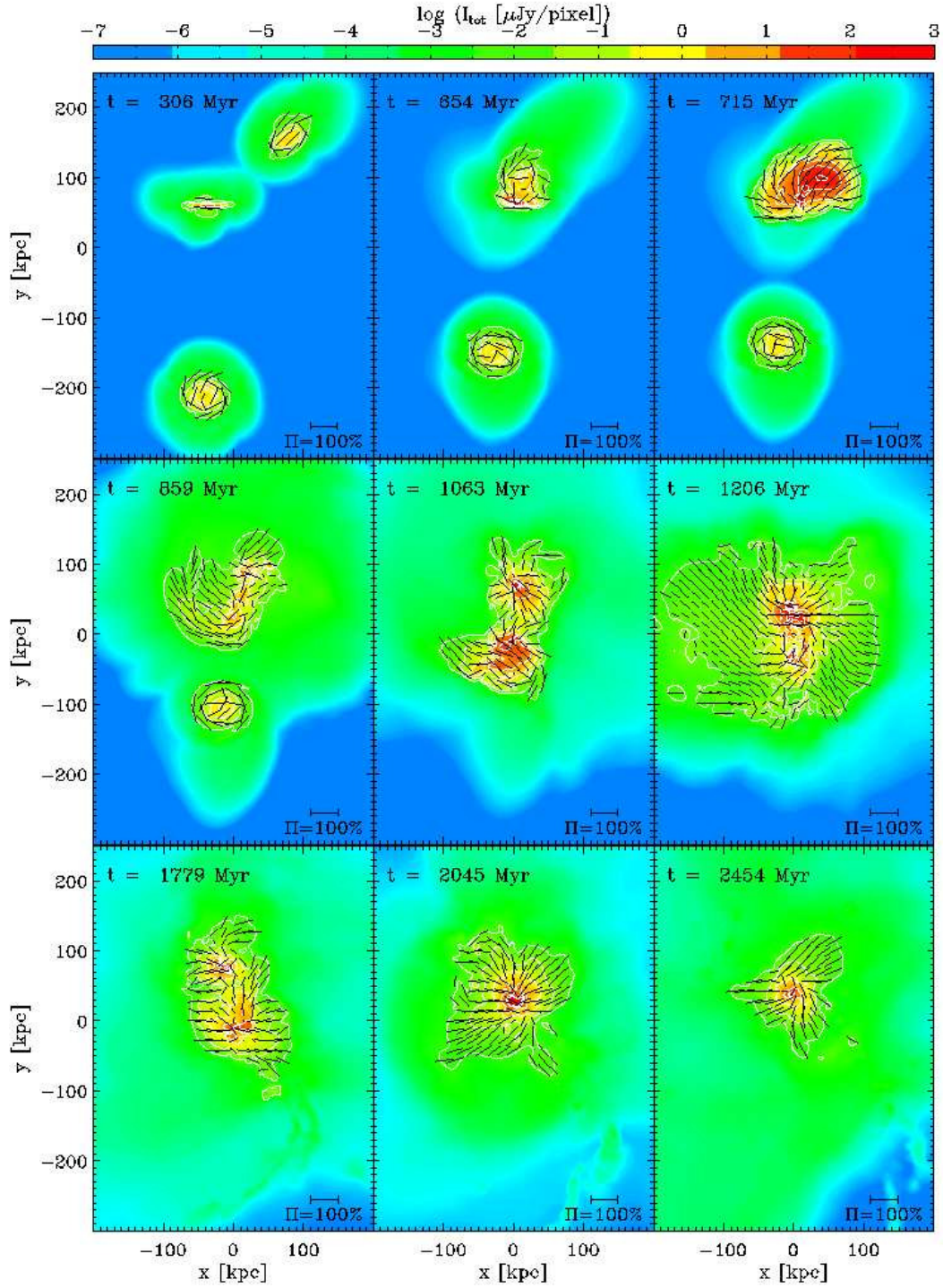


Figure 4.15: Synthetic radio maps for the G6-IGM9 scenario at the same nine time steps as in Figs. 4.A2 - 4.A6. Colours visualize the total intensity (in  $\mu\text{J}/\text{pixel}$ ). White contours show the polarized intensity, whereby the contour levels are 0.001, 0.01, 0.1, 1, 10 and  $50 \mu\text{J}/\text{pixel}$ . Magnetic field lines derived from calculations of polarization are shown in black.

After the first collision (upper central panel), when shocks are driven into the IGM, the total and polarized intensities are considerably enhanced behind the shocks (upper right panel). Thereby, the magnetic field exhibits a regular pattern aligned with the direction of the outflow. In the subsequent evolution, prominent tidal arms are developing (middle left panel). These tidal arms are also visible in the total and polarized radio emission and are traced by the magnetic field lines. Presumably, the magnetic field lines have been stretched by the shear flows of the tidal structure. At time of and after the second collision (middle central and right panels), the polarized synchrotron emission is also visible outside the disks, showing that the interaction driven shocks and outflows have already magnetized parts of the IGM. During the subsequent evolution (lower left panel), the gas motions inside the galaxies become more random and thus the polarization of the radio emission generally decreases. At time of the final merger (lower central panel) shock driven gas flowing out of the merging system again gives rise to a high degree of polarization. By the end of the simulation, when most of the gas has been driven to the central core of the merged system (lower right panel), the total emission is concentrated around this core, and the polarization is tracing the weak outflows which are still driven into the IGM.

Fig. 4.15 does not reveal whether the polarized emission originates from an unidirectional or a reversing magnetic field configuration. Therefore, below we also present synthetic rotation measure ( $RM$ ) maps of the simulated system. The value of  $RM$  gives the strength by which the polarization vector of polarized radiation passing a magnetized plasma is rotated, whereby the rotation angle is  $\phi = RM \cdot \lambda^2$ . The  $RM$  value for each simulated particle is calculated according to (cf. Rybicki and Lightman, 1986)

$$RM(\text{particle}) = \frac{e^3}{2\pi m_e^2 c^4} n_e B_{\parallel}, \quad (4.6)$$

with  $n_e$  the number density of thermal electrons (equal to the number density of thermal protons and thus proportional to the gas density) and  $B_{\parallel}$  the magnetic field component along the line-of-sight.  $RM$  is positive (negative) for a magnetic field directed toward (away from) the observer. The cumulative  $RM$  is obtained by integrating along the line-of-sight, whereby individual  $RM$  values may add or cancel. Thus,  $RM$  distributions which show reversals on small scales indicate a reversing magnetic field. The cumulative  $RM$  is binned on a grid as before in Fig. 4.15.

Fig. 4.16 shows  $RM$  maps for the G6-IGM9 scenario at the same nine time steps as in Fig. 4.15. Colors visualize the  $RM$  (in  $10^{-2}$  rad  $\text{m}^{-2}$ ) on a asinh-scale for a better visibility of the small  $RM$  values in the IGM (caused by the low electron density in these regions). Note that on this scale values of 1, 5 and 10 correspond to  $RM \approx 0.01, 0.74$  and  $110$  rad  $\text{m}^{-2}$ , respectively.

In the very beginning of the simulation ( $t = 0$  Myr, not shown), the lower galaxy (G3), which is seen exactly face-on, does not show any  $RM$  because of the lack of a  $B_{\parallel}$  component. The two other galaxies, which are inclined with respect to the line-of-sight, show a positive  $RM$ . The subsequent initial infall of IGM gas onto the galaxies and the winding of the initial magnetic field due to differential rotation lead to the development of the  $RM$  patterns seen at  $t = 306$  Myr (upper left panel). E.g., the  $RM$  is positive at both sides of the galaxy seen edge-on because the winding of the initially homogeneous magnetic field results in a field pattern with the field lines directed towards the observer at both sides of the galaxy. The lack of  $RM$  in the central parts of the galaxies results from the cancellation of the (symmetric) contributions from both sides of the galaxies along the line-of-sight. Generally, the  $RM$  does not show reversals on small scales, showing that the magnetic field is unidirectional on scales  $\geq 10$  kpc. This regularity is a result of the homogeneity of the initial magnetic field. After the first collision ( $t = 654$  Myr), the  $RM$  values within the regions of polarized emission (upper right panel, cf. Fig. 4.15) are all negative, strongly indicating an unidirectional magnetic field configuration. This is also true for the interaction-driven outflows at later times (middle left to lower right panels), whereby the sign of the  $RM$  may change depending on whether the outflow is driven predominantly towards or away from the observer. This large-scale homogeneity of the  $RM$  distribution is most probably a relic

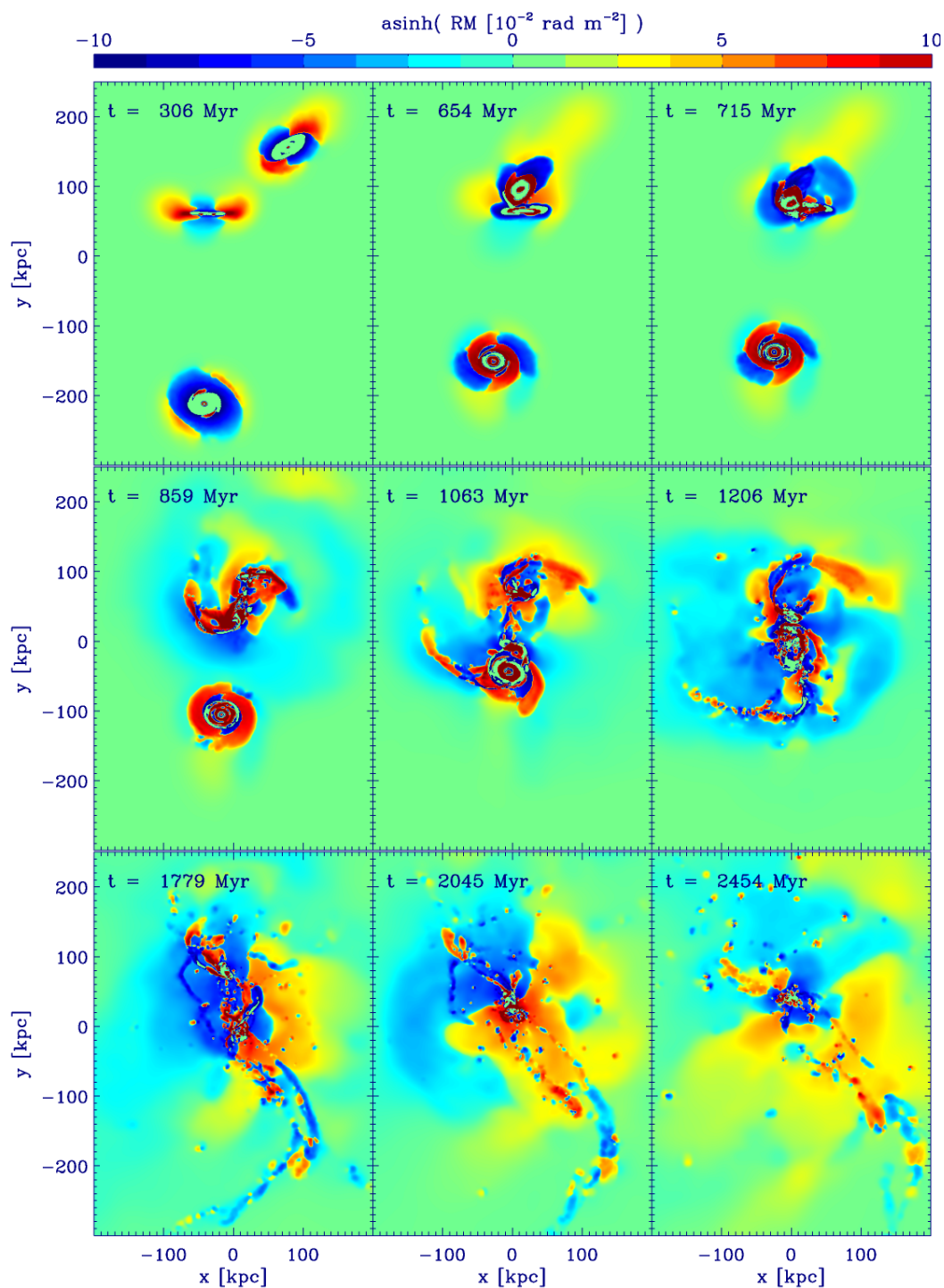


Figure 4.16: RM maps for the G6-IGM9 scenario at the same nine time steps as in Fig. 4.15. Colors visualize the RM value (in  $10^{-2}$  rad  $m^{-2}$ ) on a asinh-scale for a better visibility of the small RM values in the IGM.

of the homogeneous initial IGM magnetic field. Furthermore, the  $RM$  tends to change sign on the edges of tidal arms (e.g. middle central panel,  $t = 1063$  Myr), showing that the magnetic field within the arms is predominantly of galactic origin in contrast to the IGM magnetic field. At later times, the  $RM$  distribution within the galaxies and the tidal arms shows frequent reversals, originating in the reversing magnetic field tangled by interaction-driven turbulence.

In summary, when shocks and outflows are driven out of the galaxies or tidal structures are forming, a high amount of polarized emission can be expected due to the stretching of the magnetic field lines by the gas flows. Thereby, the magnetic field structure may be unidirectional or reversing depending on the precedent magnetic field. Generally, high synchrotron intensity corresponds to high density regions, except for periods of intensive shock ejection. During these periods, the magnetic field is enhanced by the shocks and transported from the galaxies into the IGM by interaction-driven outflows.<sup>4</sup>

Given the importance of shocks for the synthetic polarization in our simulations it is reasonable to ascribe observed prominent regular magnetic field structures like the magnetic field ridge observed in the Stephan's Quintet to shock activity. This assumption holds even better, as electrons are accelerated within shocks (which we do not model in our calculations), thus giving rise to an even higher synchrotron emissivity.

## 4.6 Conclusions and Outlook

We have presented for the first time high resolution simulations of a merger of three disk galaxies within an ambient, magnetized IGM. We have studied three different models for the initial magnetic field strengths within the galaxies and the IGM, respectively, and compared these models to a simulation excluding magnetic fields. The initial magnetic field strength range from  $10^{-12}$  G to  $10^{-9}$  G within the IGM, and from  $10^{-9}$  G to  $10^{-6}$  G within the galaxies. We find that the magnetic field saturates at a value of several  $\mu\text{G}$  within the galaxies and at roughly  $10^{-8}$  G within the IGM, independent of the initial magnetic field. This saturation levels correspond to equipartition between the magnetic and the turbulent pressure in the system. This result is in agreement with previous studies of Kotarba et al. (2010a), who have presented simulations of the interaction of two disk galaxies, particularly the Antennae system. However, Kotarba et al. (2010a) did not include an ambient IGM, wherefore they could not study the behaviour of shock propagation within the IGM and its magnetization. The simulations presented in this paper show that the shock propagation within the IGM is changed significantly depending on the initial magnetic field model. Thereby, the stronger the initial magnetic field, the stronger the shocks driven into the IGM. This result suggests that the shocks are supported by the magnetic pressure, resulting in higher Mach numbers in the presence of a strong magnetic field.

The main findings presented in this paper can be summarized as follows:

- The magnetic field within the galaxies grows to the equipartition value between the turbulent and magnetic energy density during the subsequent interactions between the merging galaxies. The IGM is magnetized by outflows and multiple shocks driven by the interactions up to nearly equipartition with the turbulent energy density within the IGM.
- The final saturation value for the galaxies is of order of several  $\mu\text{G}$ , and the final IGM magnetic field strength has an average value of  $10^{-8}$  G, independent of the applied initial magnetic field. As the setup of the system was chosen arbitrarily and the system was allowed to evolve freely in time, it is very interesting that the final magnetic field values are consistent with observations.

---

<sup>4</sup>See <http://www.usm.uni-muenchen.de/people/kotarba/public.html> for a movie of the polarization and  $RM$  maps of the G6-IGM9 scenario.

- The growth of the IGM field is more efficient, the higher the galactic magnetic field, suggesting that magnetic energy is transported from the galaxies into the IGM.
- The initial values of the magnetic field in the galaxies and in the IGM affect the propagation of shocks in the IGM: The stronger the initial field, the faster the shock propagation, suggesting that the shocks are gaining higher Mach numbers due to magnetic pressure support. This effect might be referred to as “magnetic shock acceleration”.
- The higher Mach numbers are also reflected in the higher temperatures of the shock heated IGM gas, and the shock-heated region is larger the stronger the shock.
- Shocks play an important role for the polarized emission of an interacting system. Always when shocks are driven into the ambient IGM by an interaction, a high amount of polarized emission can be expected.

The presented simulations of a merger of three disk galaxies do not only provide insights in the evolution and significance of magnetic fields in a highly nonlinear environment, but also agree well with observations. The typical observed value of several  $\mu\text{G}$  in different types of local galaxies shows to be a typical value which arises naturally in merging systems. Also, the typical observational estimates for the upper limit of IGM magnetic fields of approximately  $10^{-9} - 10^{-8}$  G (Kronberg et al., 2008 and references therein) are in agreement with the IGM magnetic field in our simulations.

Given the complexity of the simulated system, for a future project, it would be worthwhile to perform detailed shock simulations in a magnetized IGM setting. Parameter studies of the dependence of shock characteristics on the applied magnetic field strength and structure would lead to a deeper understanding of the evolution of magnetic fields during galactic interactions.

Finally, we emphasize that the efficient strengthening of magnetic fields during subsequent galaxy interactions up to levels consistent with observations is of particular interest within the framework of CDM clustering models. On the basis of the simulations presented in this paper and in Kotarba et al. (2010a), we can assume that every galactic interaction contributes to the magnetization of the affected galaxies and the ambient IGM. As the phase of structure formation in the Universe is accompanied by frequent, subsequent interactions of galaxies and galactic subunits, the observed present-day magnetic fields might at least to some extent be the result of interaction-driven amplification processes in the early universe. Furthermore, the transport of magnetic energy from the galaxies into the IGM by interaction-driven outflows could explain the existence of IGM magnetic fields of order  $10^{-9} - 10^{-8}$  G already at high redshifts. We note, however, that the simulations presented here picture the interaction of three fully evolved present-day galaxies, wherefore they can not be compared directly with interactions in the early universe. High redshift galaxies are known to be very different than present-day galaxies. However, subsequent galaxy interactions were more frequent in the early universe. Thus, it is reasonable to assume that the cumulative interaction-driven magnetic field amplification of even small initial seed fields might have magnetized young galaxies and their environment already at high redshifts. More studies of magnetic field evolution during the early phases of the Universe, preferably in a cosmological context, would thus be of particular interest for the whole astronomical community.

## Acknowledgments

We thank the referee Anvar Shukurov for his valuable comments and suggestions which helped us to improve this paper significantly. This research was supported by the DFG Cluster of Excellence ”Origin and Structure of the Universe” ([www.universe-cluster.de](http://www.universe-cluster.de)). K.D. acknowledges the support by the DFG Priority Programme 1177.

## 4.A Appendix

In Figs. 4.1, 4.2 and 4.3 we showed the evolution of the magnetic field, the temperature and the rms velocity as a function of time for the G6-IGM9 scenario. Below, we show the corresponding figures for the G9-IGM9, G9-IGM12 and G0-IGM0 scenarios, respectively (see table 4.4).

### 4.A.1 Magnetic fields

Figs. 4.A1 and 4.A2 show the evolution of the mean line-of-sight magnetic field as a function of time similar to Fig. 4.1, but for the G9-IGM9 and G9-IGM12 scenarios, respectively. The final distributions and strengths of the magnetic fields are comparable within every scenario.

### 4.A.2 Temperatures

Figs. 4.A3, 4.A4 and 4.A5 show the evolution of the mean line-of-sight temperature as a function of time similar to Fig. 4.1, but for the G9-IGM9, G9-IGM12 and G0-IGM0 scenarios, respectively. The stronger the shocks driven into the IGM, the higher the temperatures.

### 4.A.3 RMS velocities

Figs. 4.A6, 4.A7 and 4.A5 show the evolution of the mean line-of-sight rms velocity as a function of time similar to Fig. 4.1, but for the G9-IGM9, G9-IGM12 and G0-IGM0 scenarios, respectively. The higher the initial magnetic field, the faster the shock propagation within the IGM.

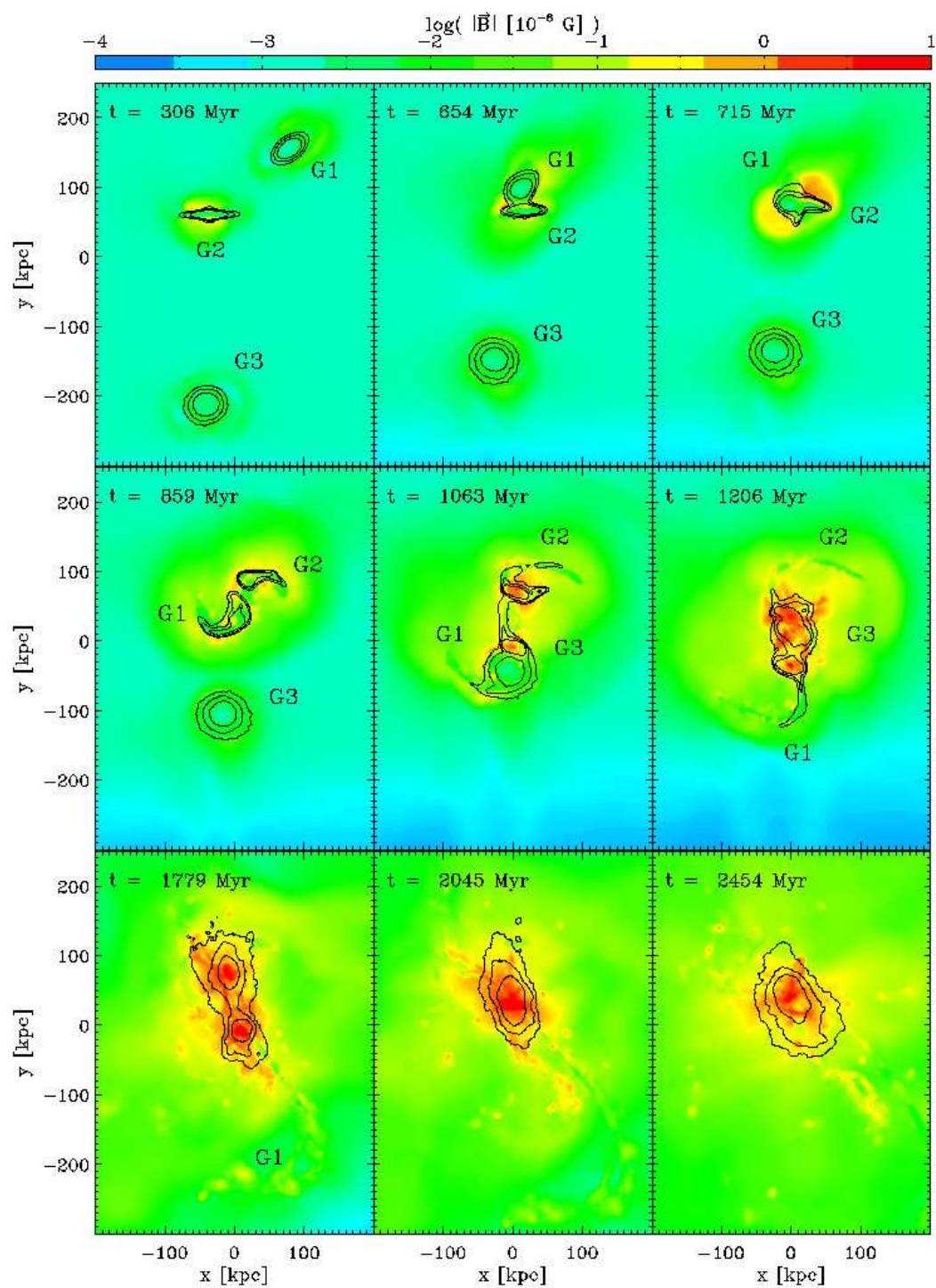


Figure 4.A1: Same as Fig. 4.1, but for the G9-IGM9 scenario.

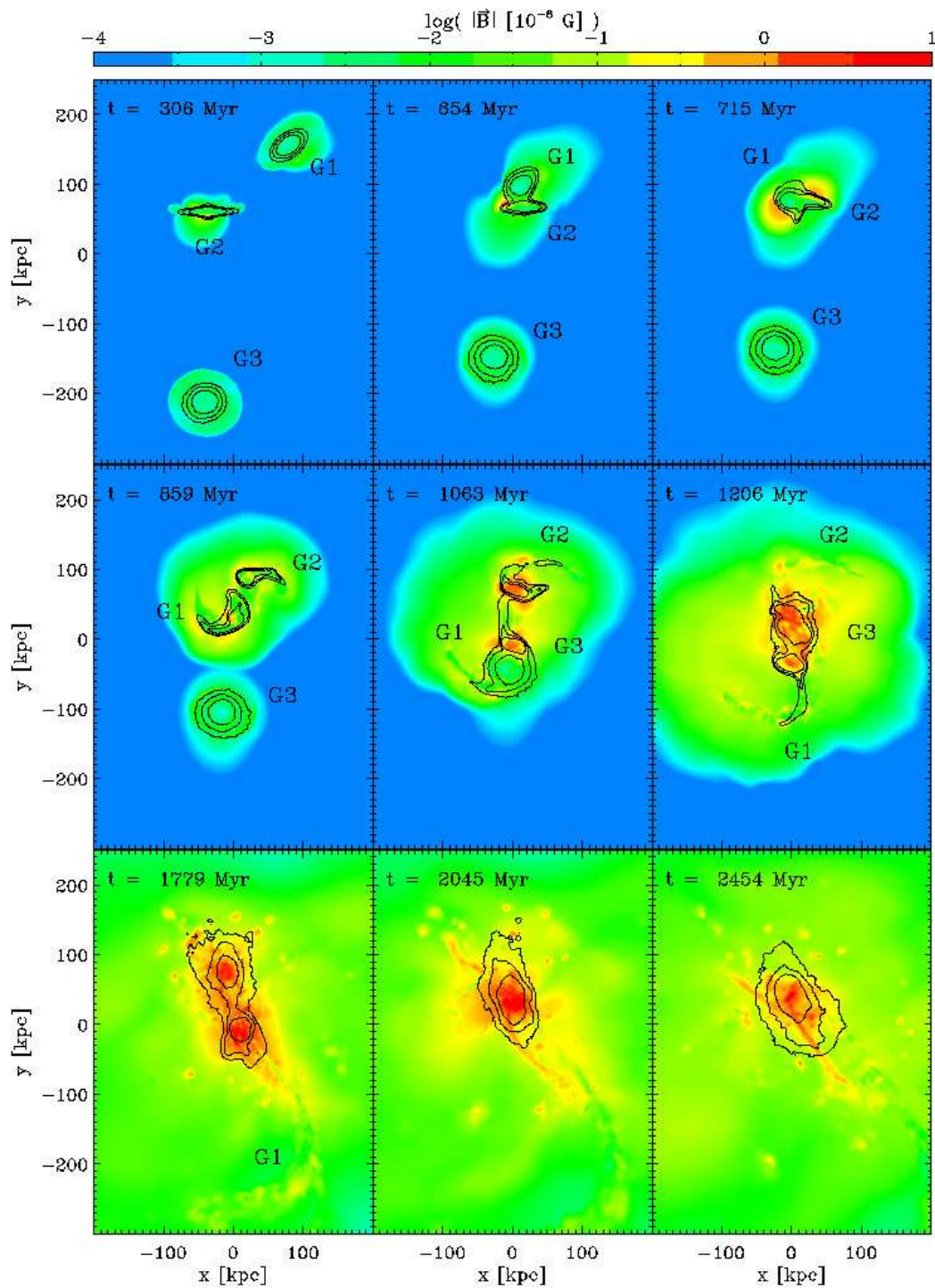


Figure 4.A2: Same as Fig. 4.1, but for the G9-IGM12 scenario.

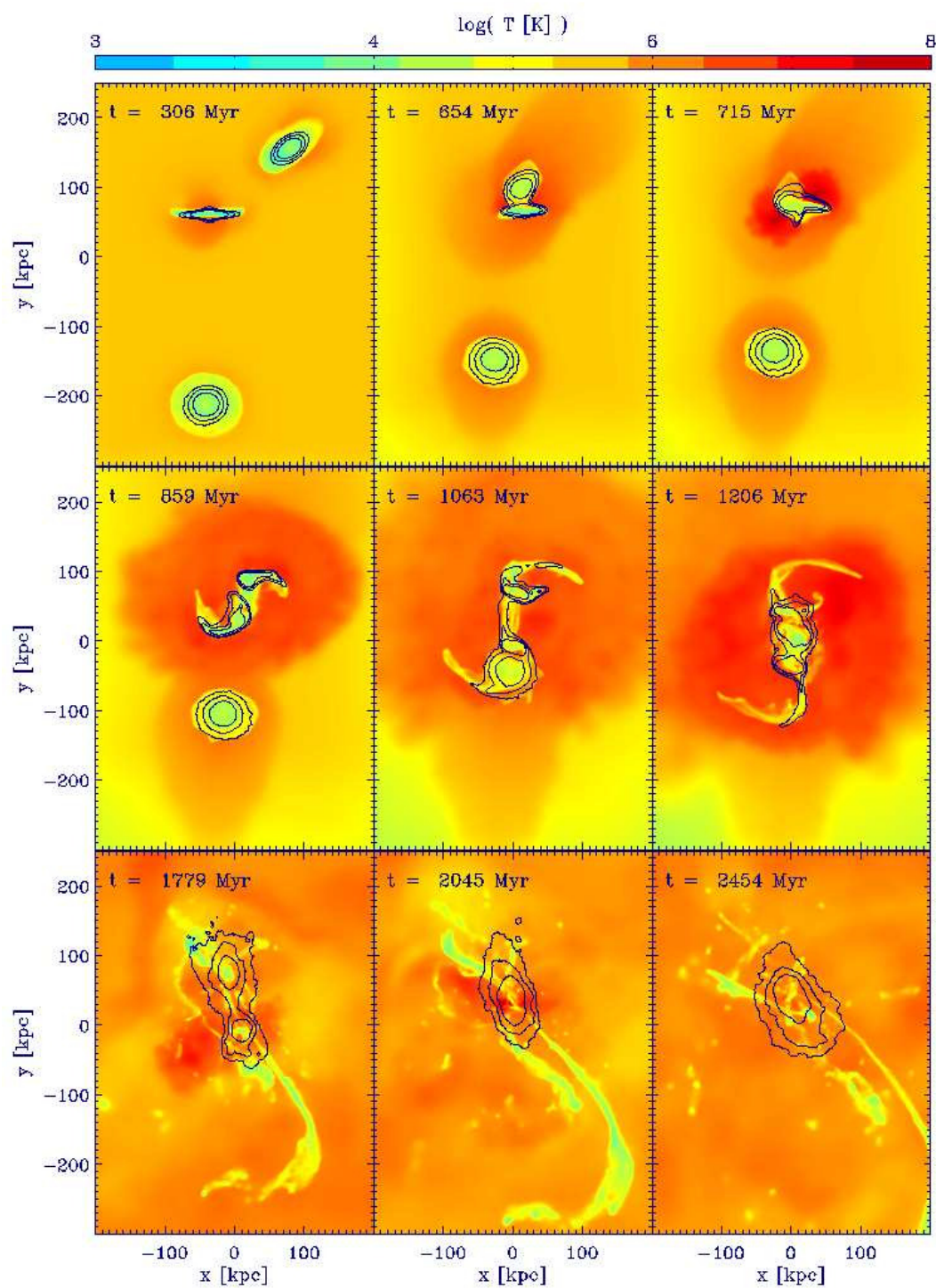


Figure 4.A3: Same as Fig. 4.2, but for the G9-IGM9 scenario.

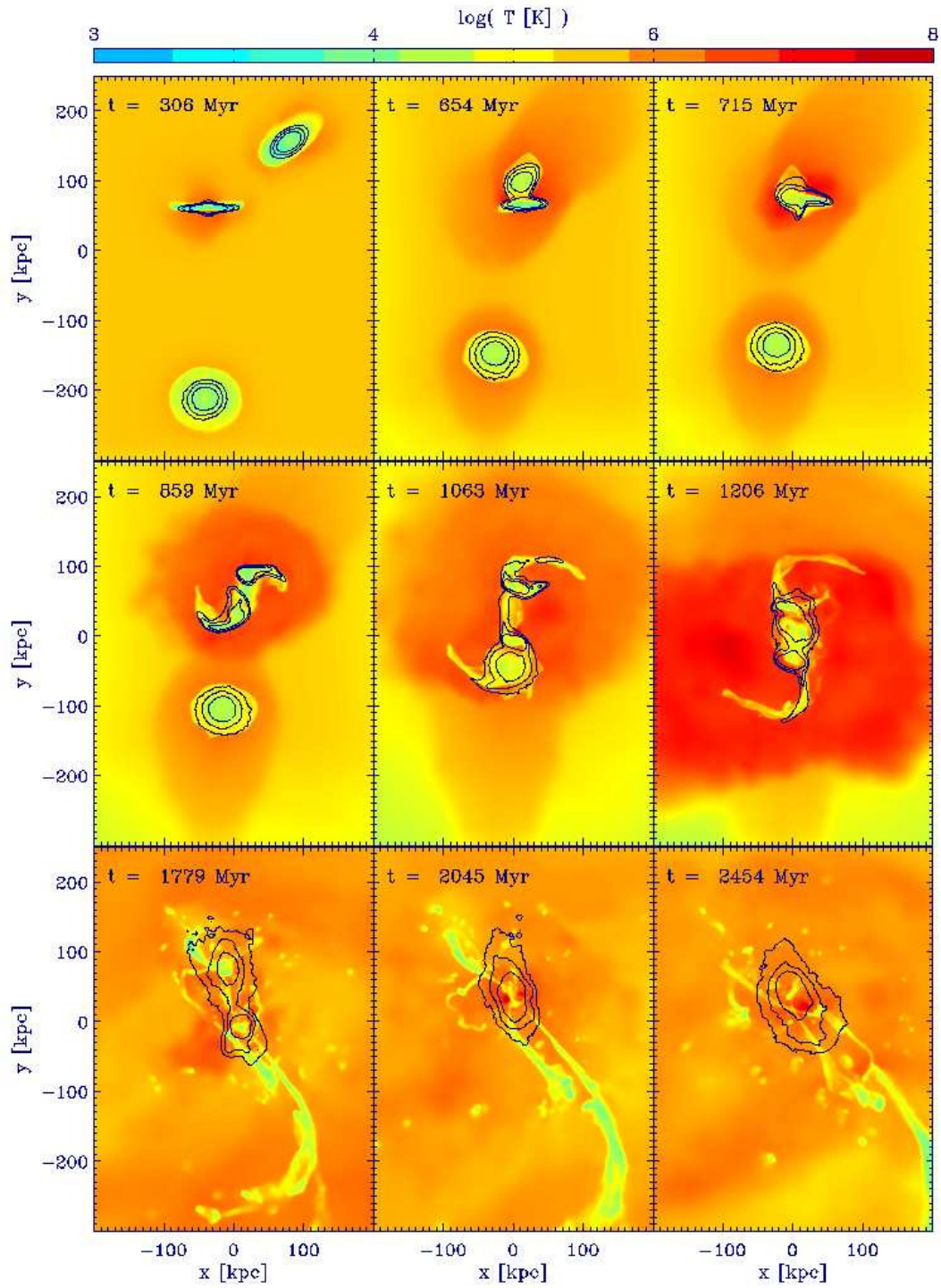


Figure 4.A4: Same as Fig. 4.2, but for the G9-IGM12 scenario.

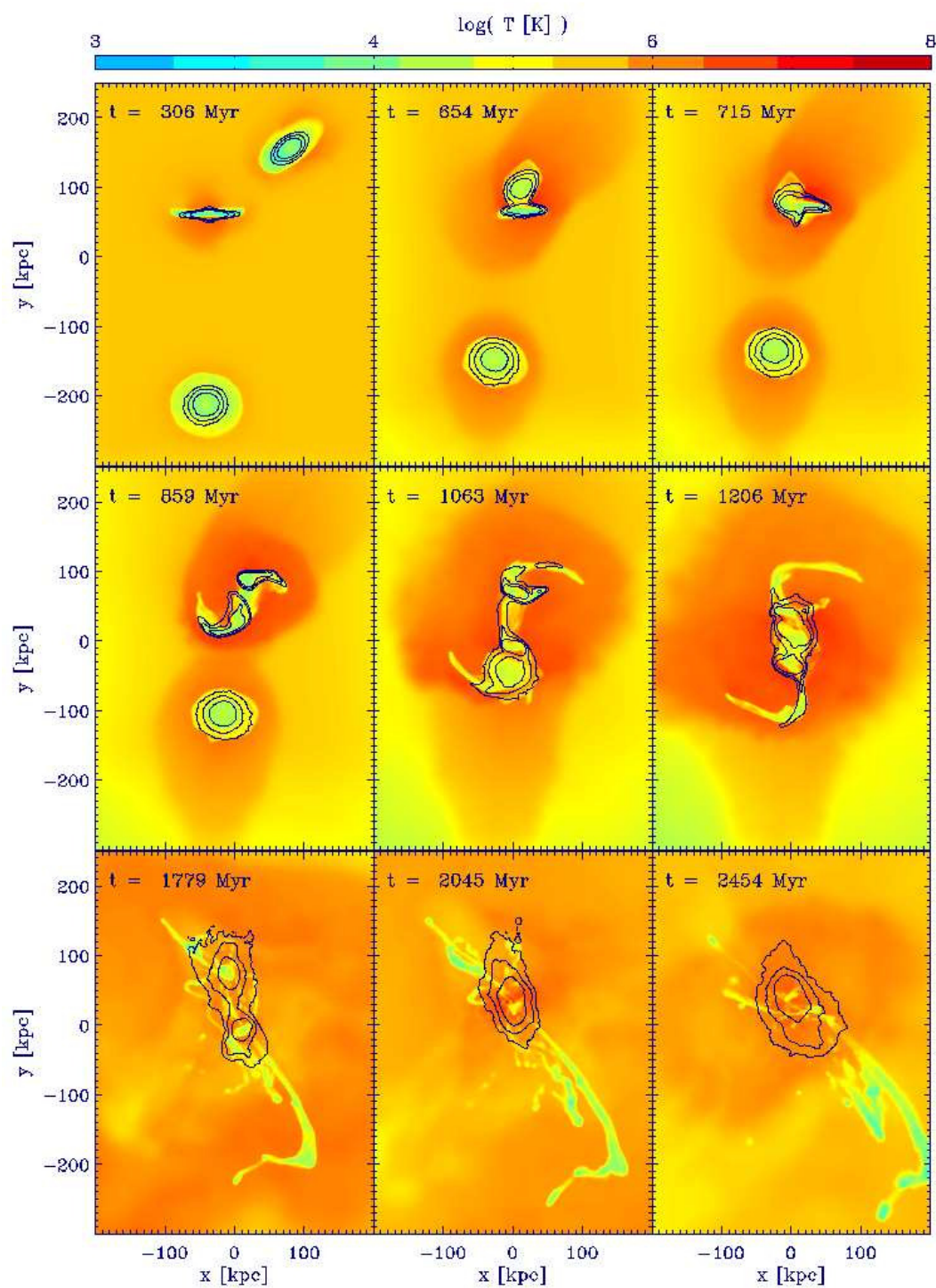


Figure 4.A5: Same as Fig. 4.2, but for the G0-IGM0 scenario.

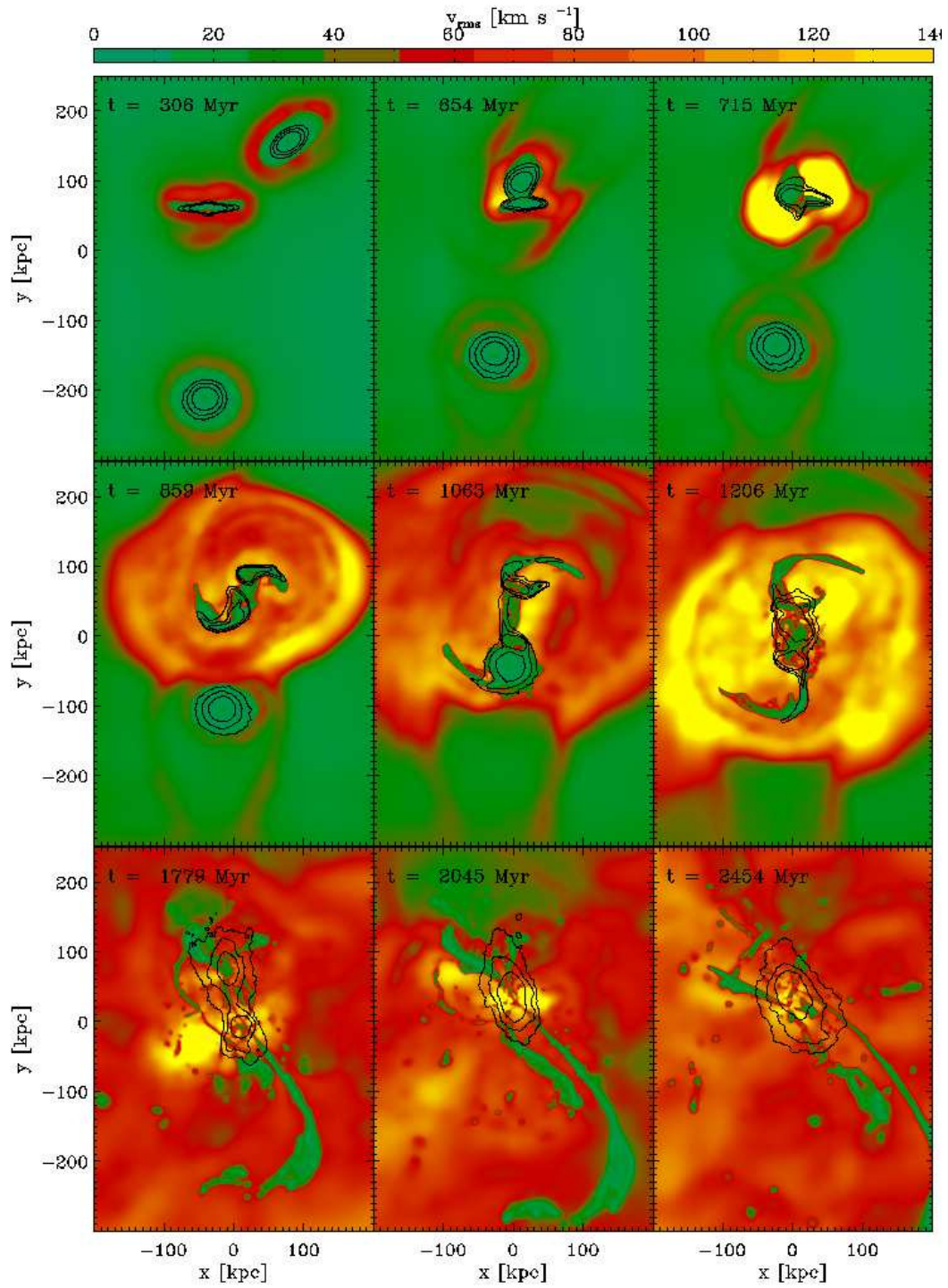


Figure 4.A6: Same as Fig. 4.3, but for the G9-IGM9 scenario.

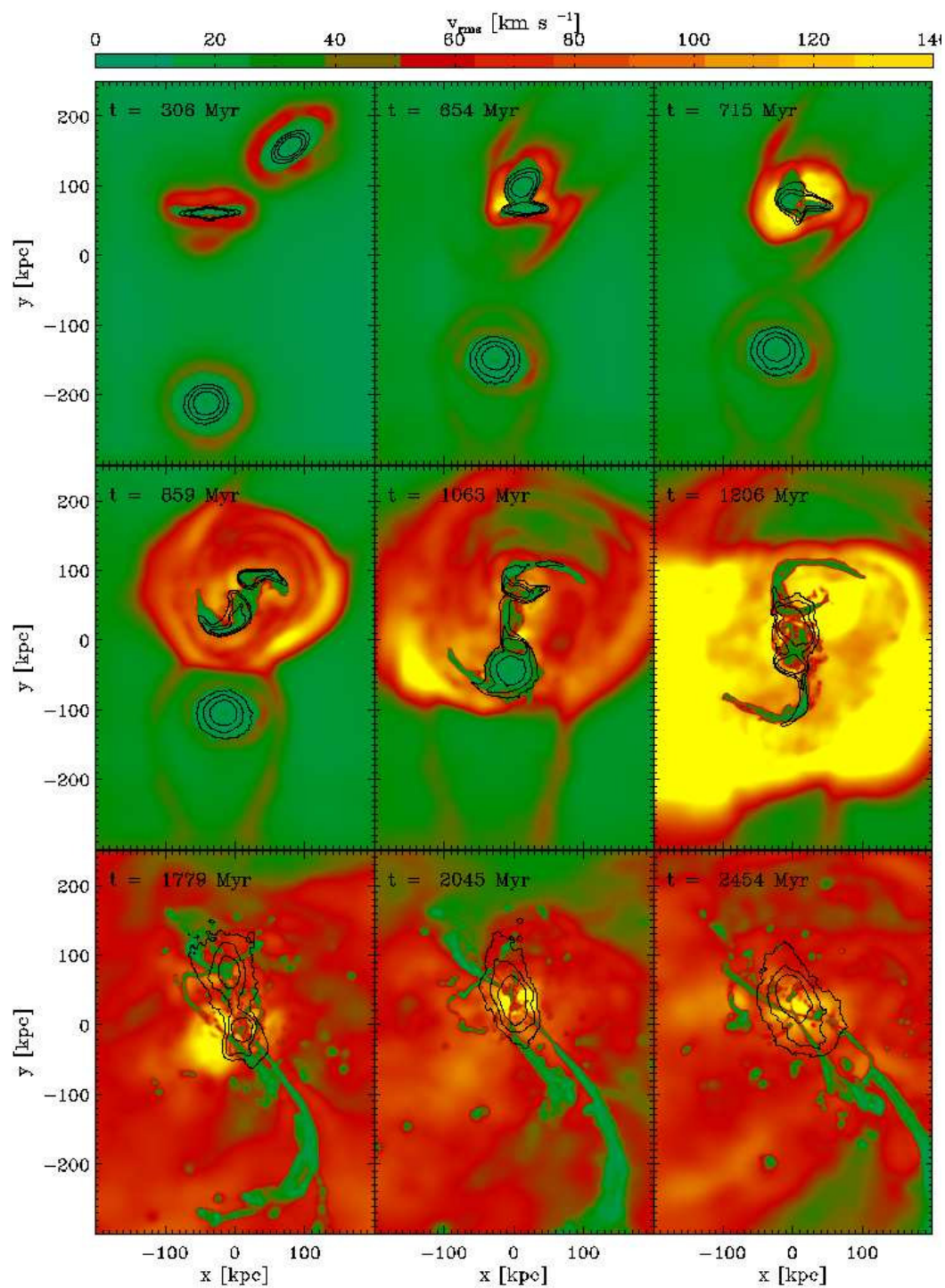


Figure 4.A7: Same as Fig. 4.3, but for the G9-IGM12 scenario.

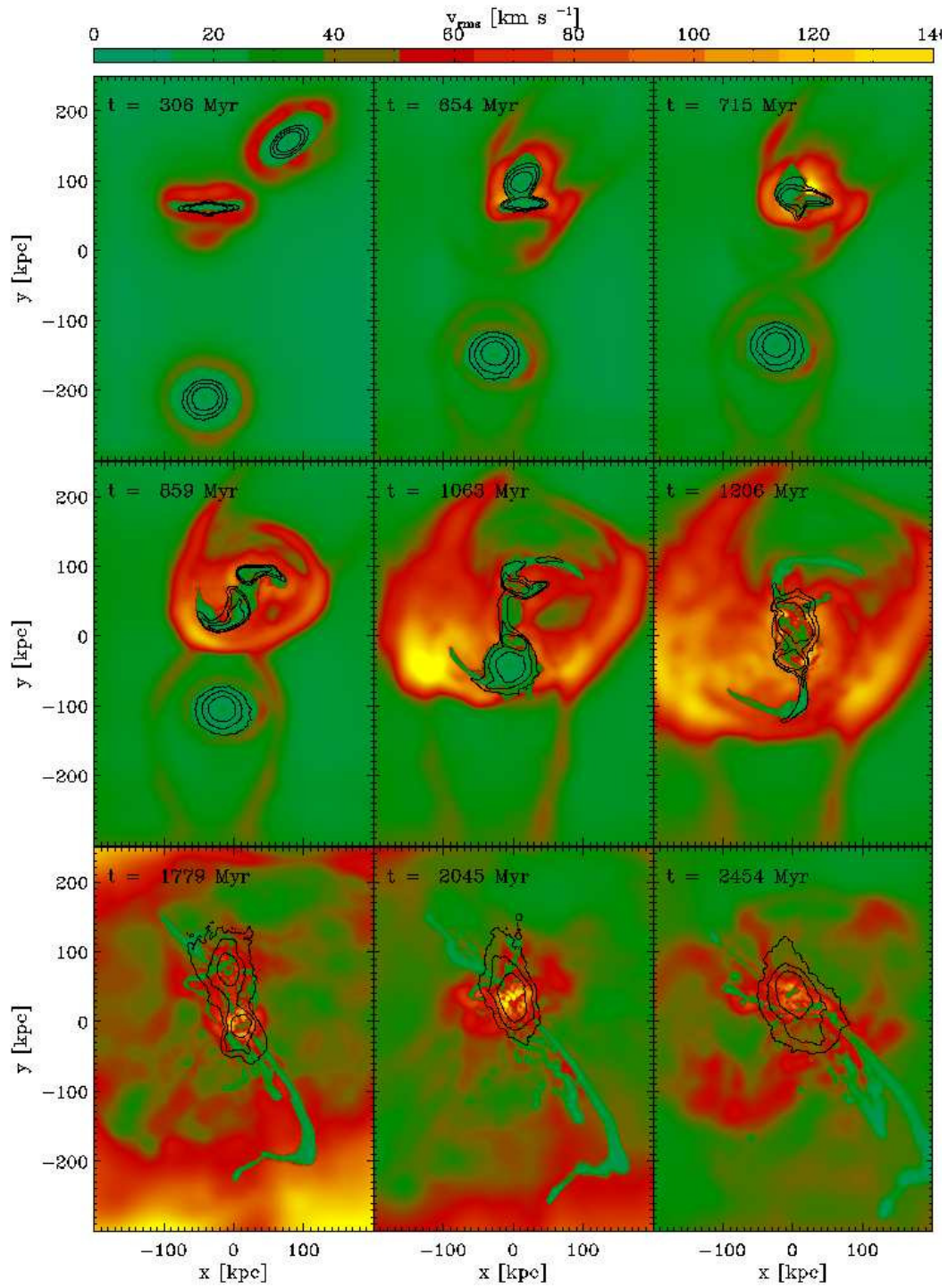


Figure 4.A8: Same as Fig. 4.3, but for the G0-IGM0 scenario.



# Chapter 5

## Discussion and Outlook

The articles presented within this thesis cover high-resolution state-of-the-art numerical investigations of the magnetic field evolution in local isolated and interacting disc galaxies. The presented simulations are the first self-consistent and full MHD galactic-scale  $N$ -body/SPH investigations ever attempted. Particularly, the evolution of magnetic fields during galactic interactions, which change the dynamics and thus the hydro- and magnetohydrodynamics of the galaxies drastically, has never been studied numerically before.

The first of the presented articles (section 2) discusses the kinematic evolution of a given initial magnetic field in an evolving spiral galaxy, which, in contrast to most former studies, is forming a spiral structure self-consistently. These studies examine the question about the response of the magnetic field to the realistic, three-dimensional velocity field of a spiral galaxy. It is shown that such a velocity field alone is not able to amplify a weak initial magnetic field up to the observed level, thus showing the necessity of other amplification mechanisms. Furthermore, comparison simulations making use of a description of the magnetic field based on Euler potentials, which guarantees a vanishing physical divergence of the magnetic field by definition, allowed for an estimate of an upper limit of the numerical divergence within SPH/MHD simulations (cf. section 2.5). This upper limit has already been a useful guide within studies of the proto-stellar collapse and fragmentation using  $N$ -body/SPH (Bürzle et al., 2011).

The question about an efficient magnetic field amplification mechanism within galaxies led to the idea of an interaction-driven amplification. During galactic interactions, huge amounts of gravitational potential energy are released. This energy is partly converted into heat and kinetic energy (turbulence) of the gas. The kinetic energy is in turn expected to be converted into magnetic energy by turbulent magnetic field amplification until an equipartition state between the magnetic and turbulent energy is reached (section 1.4.5). This equipartition is also confirmed by observations. Therefore, the theoretical expectation of an interaction-driven magnetic field amplification up to the equipartition level is studied in the two subsequent articles (sections 3 and 4).

The first of these articles (section 3) examines the magnetic field evolution in the Antennae galaxies, which are the prime example of an observed interaction of two galaxies. This system has been observed in many bandwidths, particularly in the radio band, wherefore detailed comparisons of the simulated Antennae system with the observations were possible. It is shown that during the interaction of the two galaxies a given initial magnetic field is indeed amplified efficiently up to the equipartition level, independent of the initial field strength, which was varied between  $10^{-9}$  and  $10^{-4}$  G (section 3.3.3.1). The equipartition value of several  $\mu\text{G}$  is thereby in very good agreement with observations (section 1.3.1). Interestingly, the system tends to the same turbulent and magnetic equipartition energy even in case of an initial magnetic field which is by two orders of magnitude stronger than the observed value, thus showing that the equipartition at a magnetic field value of several  $\mu\text{G}$  is a natural state for

galactic systems. Furthermore, synthetic radio maps, calculated on the basis of the simulated data at time of the best morphological fit to the observed system, reveal that also the overall distribution and structure of the magnetic field compares very well to the observations (section 3.4.2). This agreement clearly shows the ability of the underlying numerical scheme to follow the highly non-linear evolution of magnetic fields in interacting galactic systems, a result which is also important in view of future studies of cosmic magnetism with the  $N$ -body/SPH method.

In the continuative article (section 4), a more general interaction of three spiral galaxies is presented. Thereby, an ambient IGM surrounding the interacting galaxies is additionally included in order to study the effects of the magnetic field on the interaction-driven shocks and outflows within the ambient medium. Again, this is the first time that the behaviour of a magnetized IGM during a galactic interaction has been studied in detail. The efficient amplification of the galactic magnetic field up to the equipartition level is confirmed. Also, the magnetic field within the IGM is shown to get amplified due to the interaction-driven shocks and galactic outflows. Thereby, the IGM magnetic field energy does also reach equipartition with the turbulent energy within the IGM. The corresponding magnetic field strengths of several  $\mu\text{G}$  within the galaxies and  $\approx 10^{-8}$  G within the IGM are again in excellent agreement with the observed magnetic field strengths in the local Universe (section 4.4.3.1). Furthermore, it is shown that the magnetic field already present within the galaxies and the IGM before the interaction has a strong influence on the propagation and strength of the interaction-driven shocks and outflows. Thereby, the stronger the initial field, the higher the Mach numbers of the shocks and the stronger the outflows, suggesting that the shocks are supported by the magnetic pressure. Consequently, also the temperature of the shock-heated gas increases with increasing initial magnetic field. This difference of the shock behaviour has been studied in detail in section 4.4.2. Moreover, synthetic radio and  $RM$  maps (cf. section 1.2.3), calculated at different evolutionary times of the simulated system, give clues about the nature and origin of the observed polarized emission in interacting galaxies (section 4.5). Thereby, a high amount of polarized emission can be expected whenever shocks and outflows are driven into the IGM, because the magnetic field is stretched by the motion of the outflowing gas. These results may be important for future studies of the magnetization of the IGM and the ICM (cf. section 1.5.2).

The presented studies have fundamental implications for the evolution of magnetic fields in the early universe. Magnetic fields of  $\mu\text{G}$  strength are not only observed in local galaxies, but also in young galactic objects with redshifts up to  $z \approx 2$  (section 1.3.3). These observations challenge the standard model of magnetic field amplification via the relatively slow galactic dynamo (section 1.4.3), as this dynamo would not have had enough time to amplify the magnetic field in these high redshift objects up to the observed strength (section 1.5.3). Yet, interactions between galaxies and galactic subunits were much more common during the phase of structure formation in the early Universe. Hence, the interaction-driven amplification of magnetic fields studied in this thesis may be a key issue for the magnetization of young galactic objects.

However, the simulations presented within this thesis deal with equal-mass, well-evolved, present-day spiral galaxies and their interactions. High redshift galaxies are known to be much different than those present-day galaxies. Generally, galaxies are born within DM haloes forming according to the CDM clustering models of structure formation (e.g. White and Frenk, 1991; Mo et al., 1998; Benson, 2010). Gas which falls into the potential wells of these haloes is shock heated and then cools radiatively from the inside out. As long as the cooling time is shorter than the global free-fall time, gas is gradually accreted onto a central disk forming at the center of the DM halo, where quiescent star formation starts to take place. Hence, high-redshift galaxies are predicted to be small and dense, with gaseous disks which may not yet be well established. They contain much higher gas fractions than present-day galaxies and are still accreting more gas and smaller galactic subunits. Simultaneously, the clustering of DM haloes to larger structures continues, resulting in subsequent galactic interactions. Mutual mergers of young disk galaxies might result in the observed population of elliptical galaxies. Furthermore, continuous gas accretion and interactions between the young galaxies

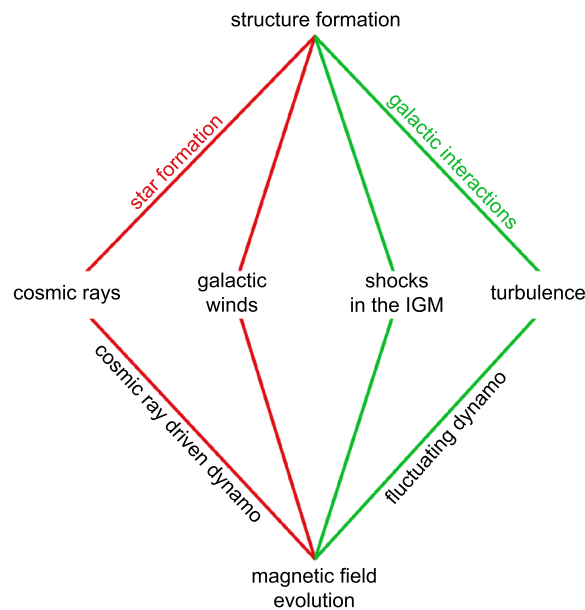


Figure 5.1: A schematic view of the connection between structure formation and magnetic field evolution. The seeding of magnetic fields is thereby not considered. Also, turbulence due to star formation, CR driven winds and the classical mean field dynamo are neglected for simplicity. This thesis concentrated on processes induced by galactic interactions, which are highlighted in green.

are expected to drive enhanced star formation due to the compression of gas and additional gas supply. These bursts of star formation lead to galactic outflows into the ambient IGM as well as an increase of the associated SN and CR production rates. Thus, complementary to the expected interaction-driven magnetic field amplification, the SN remnants can provide additional seed magnetic fields (section 1.5.1) and the supplementary CR production can support the CR driven dynamo (section 1.4.4) and galactic outflows which can magnetize the IGM. On the other hand, magnetic fields already present before and during the time of structure formation may influence the star formation history, confine the CRs produced by the first SN remnants and additionally support galactic outflows (cf. section 1.5.3).

Thus, during the phase of structure formation, an interdependent network of processes is expected to control the evolution of magnetic fields in the Universe (Fig. 5.1). Due to the complexity arising from the interdependency, the cumulative effect of these processes is accessible only through advanced numerical simulations in a full cosmological context (cf. section 1.6). Those simulations are only now beginning to come into reach. Donnert et al. (2009) are the first who have performed full MHD cosmological simulations of the evolution of magnetic fields in galaxy clusters. They showed that the strength and structure of magnetic fields observed in galaxy clusters are well reproduced applying a simple model for the seeding of cluster-scale magnetic fields by magnetized galactic outflows. On a galactic scale, cosmological MHD simulations of the formation of a single galaxy have yet only been performed by Alexander Beck within his ongoing Diploma thesis at the University Observatory of the LMU in Munich. Hence, it is definitely important to further leverage the modern numerical possibilities to advance our knowledge about the evolution of magnetic fields with cosmic time.

The main questions which could be answered by numerical investigations are the following:

1. How does the magnetic field evolve with cosmological redshift?
2. How much does the magnetic evolution of the Universe depend on the strength of the very first magnetic seed fields?
3. How does the presence of a magnetic field influence the star formation rates in different objects?
4. Is the (interaction-driven) magnetic field amplification accompanying the phase of structure formation efficient enough to explain the observed magnetic field values, particularly in DLAS (section 1.3.3), or
5. are there other processes (like subsequent seeding of magnetic fields by SN remnants and AGN or dynamo action) needed to explain the observed magnetic field strengths at different redshifts?

Of course, a cosmological simulation including all of the processes mentioned above – the hierarchical build up of structure comprising mutual interactions between the forming substructures; star burst driven winds; magnetic field seeding and CR production by SN remnants; and the CR driven dynamo – would be most desirable. Apart from the huge CPU power necessary to carry out such a simulation, however, still a lot of code development is necessary. The following ideas of research would therefore be important steps towards a more realistic modeling using fully cosmological simulations.

- Simulations of unequal mass mergers in the local universe. Those simulations are currently carried out by Annette Geng within her Ph.D. studies at the University of Konstanz in collaboration with our group at the University Observatory in Munich (Geng et al., in preparation). They will reveal the dependence of the interaction-driven amplification of a given initial magnetic field on the mass ratio of the interacting galaxies. Given that unequal mass mergers are expected to have been much more common in the early Universe than equal-mass mergers, these studies will give further clues on the magnetic field evolution in the early Universe.
- Simulations of galaxy mergers until the formation of elliptical galaxies. As described in section 1.5.2, the presence of  $\mu\text{G}$  magnetic fields in elliptical galaxies is still an area of active research. Simulations of the formation of elliptical galaxies from the merger of already magnetized disk galaxies would reveal whether a given magnetization of the progenitor galaxies is sufficient to explain the magnetization of elliptical galaxies. If the progenitors host only very weak magnetic fields, or if these fields diminish significantly due to turbulent diffusion during the merger, those studies could also show whether the merger process can drive enough turbulence to result in an efficient fluctuating dynamo.
- Incorporation of magnetic field seeding by SN remnants. Apart from the PIERNIK code (Hanasz et al., 2010a,b), most current MHD codes are only able to follow the evolution of a given initial magnetic field. In a more realistic scenario, however, magnetic fields could be seeded by SN remnants (section 1.5.1), which number density and spatial distribution should depend on the local star formation rate. With the assumption that SN release a fraction of their energy in form of magnetic dipolar fields filling some cubic parsecs, magnetic field seeding by SN remnants could be implemented in numerical codes like GADGET, which are already capable of following the star formation history self-consistently (section 3.3.1). Thus, studies of magnetic field evolution including continuous seeding of magnetic fields would be possible.
- Incorporation of CR production and the CR-driven dynamo. Together with the release of magnetic energy, each SN may be assumed to result in a local population of CR protons with a total energy of a fraction of the SN energy. The propagation of these CRs within the simulated galaxy can thereby be modeled as a combination of advection and diffusion along the magnetic field. The associated CR pressure can be incorporated into the momentum equation of the

---

plasma, thus influencing the motion of the plasma and simultaneously the magnetic field lines via the frozen-in condition (section 1.4.1). In this way, a CR driven dynamo could be modeled. The simultaneous evolution of the CR population within an evolving galaxy would reveal the impact of the CR-driven dynamo on the evolution of the galactic magnetic field. Moreover, synthetic radio maps could be calculated without additional assumptions of the CR distribution, but rather on the basis of the self-consistently evolving CR population. Thereby, the energy of CR electrons can be assumed to be a fraction of the CR protons (or, in a further step, also the release and propagation of CR electrons could be implemented). The models could thus be tested by comparisons of the resulting synthetic radio maps with observations in local galaxies.

- Model simulations of DLAS. DLAS are believed to be an agglomeration of proto-galactic gas clouds in the process of merging within a common DM halo (section 1.5.3). Birk et al. (2002) have shown that in self-gravitating proto-galactic clouds magnetic fields of  $\approx 10^{-14}$  G may be generated within  $\approx 7 \cdot 10^6$  years. Thus, such a magnetization can be assumed for the individual clouds falling into the potential well of a DM halo. During the formation of a DLAS, the initial magnetic field of the clouds might have been amplified by their mutual interactions to the observed  $\mu$ G level (section 1.3.3). This scenario could be tested by model simulations of the formation of DLAS from the successive capture of proto-galactic clouds within a DM halo.
- Finally, the models developed during the research projects proposed above can be incorporated into cosmological MHD codes, thus leading to a more realistic treatment of magnetic fields within cosmological simulations. For example, the incorporation of the CR driven dynamo would help to answer the question whether galactic winds supported by CR and magnetic pressure can explain the observed bulge to disk ratios in galaxies (cf. section 1.5.3).

In a nutshell, the origin and evolution of magnetic fields in our Universe still rises interesting and challenging scientific questions, thus offering exciting research opportunities. I can only encourage future students to take up this interesting field of studies.



# Bibliography

- O. Agertz, G. Lake, R. Teyssier, B. Moore, L. Mayer, and A. B. Romeo. Large-scale galactic turbulence: can self-gravity drive the observed HI velocity dispersions? MNRAS, 392:294–308, January 2009.
- H. Alfvén. Cosmical electrodynamics. Oxford: Clarendon Press, 1950.
- T. G. Arshakian, R. Beck, M. Krause, and D. Sokoloff. Evolution of magnetic fields in galaxies and future observational tests with the Square Kilometre Array. A&A, 494:21–32, January 2009.
- R. M. Athreya, V. K. Kapahi, P. J. McCarthy, and W. van Breugel. Large rotation measures in radio galaxies at  $Z > 2$ . A&A, 329:809–820, January 1998.
- H. W. Babcock. A Catalog of Magnetic Stars. ApJS, 3:141–+, January 1958.
- D. S. Balsara. von Neumann stability analysis of smooth particle hydrodynamics—suggestions for optimal algorithms. Journal of Computational Physics, 121:357–372, 1995.
- D. S. Balsara. Total Variation Diminishing Scheme for Adiabatic and Isothermal Magnetohydrodynamics. ApJS, 116:133–+, May 1998.
- D. S. Balsara and D. S. Spicer. A Staggered Mesh Algorithm Using High Order Godunov Fluxes to Ensure Solenoidal Magnetic Fields in Magnetohydrodynamic Simulations. Journal of Computational Physics, 149:270–292, March 1999.
- J. Barnes and P. Hut. A Hierarchical  $O(N \log N)$  Force-Calculation Algorithm. Nature, 324:446–449, December 1986.
- J. E. Barnes. Encounters of disk/halo galaxies. ApJ, 331:699–717, August 1988.
- J. E. Barnes. Transformations of galaxies. I - Mergers of equal-mass stellar disks. ApJ, 393:484–507, July 1992.
- J. E. Barnes. Galaxy Interactions. In D. R. Merritt, M. Valluri, & J. A. Sellwood, editor, Galaxy Dynamics - A Rutgers Symposium, volume 182 of Astronomical Society of the Pacific Conference Series, pages 463–+, August 1999.
- J. E. Barnes. Formation of gas discs in merging galaxies. MNRAS, 333:481–494, July 2002.
- J. E. Barnes and L. Hernquist. Dynamics of interacting galaxies. ARA&A, 30:705–742, 1992.
- J. E. Barnes and L. Hernquist. Transformations of Galaxies. II. Gasdynamics in Merging Disk Galaxies. ApJ, 471:115–+, November 1996.

- G. K. Batchelor. On the Spontaneous Magnetic Field in a Conducting Liquid in Turbulent Motion. Royal Society of London Proceedings Series A, 201:405–416, April 1950.
- E. Battaner and E. Florido. The Rotation Curve of Spiral Galaxies and its Cosmological Implications. Fund. Cosmic Phys., 21:1–154, 2000.
- R. Beck. Observations of galactic magnetic fields. Highlights of Astronomy, 12:712–715, 2002.
- R. Beck. The Role of Magnetic Fields in Spiral Galaxies. Ap&SS, 289:293–302, February 2004.
- R. Beck. Magnetism in the spiral galaxy NGC 6946: magnetic arms, depolarization rings, dynamo modes, and helical fields. A&A, 470:539–556, August 2007.
- R. Beck. Galactic and Extragalactic Magnetic Fields. In F. A. Aharonian, W. Hofmann, & F. Rieger, editor, American Institute of Physics Conference Series, volume 1085, pages 83–96, December 2008.
- R. Beck. Galactic dynamos and galactic winds. Ap&SS, 320:77–84, April 2009a.
- R. Beck. Galactic and extragalactic magnetic fields - a concise review. Astrophysics and Space Sciences Transactions, 5:43–47, October 2009b.
- R. Beck and P. Hoernes. Magnetic spiral arms in the galaxy NGC6946. Nature, 379:47–49, January 1996.
- R. Beck, M. Krause, and U. Klein. M81 at high radio frequencies. A&A, 152:237–249, November 1985.
- R. Beck, A. D. Poezd, A. Shukurov, and D. D. Sokoloff. Dynamos in evolving galaxies. A&A, 289: 94–100, September 1994.
- R. Beck, A. Brandenburg, D. Moss, A. Shukurov, and D. Sokoloff. Galactic Magnetism: Recent Developments and Perspectives. ARA&A, 34:155–206, 1996.
- R. Beck, V. Shoutenkov, M. Ehle, J. I. Harnett, R. F. Haynes, A. Shukurov, D. D. Sokoloff, and M. Thierbach. Magnetic fields in barred galaxies. I. The atlas. A&A, 391:83–102, August 2002.
- R. Beck, A. Fletcher, A. Shukurov, A. Snodin, D. D. Sokoloff, M. Ehle, D. Moss, and V. Shoutenkov. Magnetic fields in barred galaxies. IV. NGC 1097 and NGC 1365. A&A, 444:739–765, December 2005.
- S. Begall, J. Cervený, J. Neef, O. Vojtech, and H. Burda. Magnetic alignment in grazing and resting cattle and deer. Proc. Natl. Acad. Sci. USA, 105:13451–+, September 2008.
- K. Bekki and Y. Shioya. Stellar Populations in Gas-rich Galaxy Mergers. I. Dependence on Star Formation History. ApJ, 497:108–+, April 1998.
- A. J. Benson. Galaxy formation theory. Phys. Rep., 495:33–86, October 2010.
- M. L. Bernet, F. Miniati, S. J. Lilly, P. P. Kronberg, and M. Dessauges-Zavadsky. Strong magnetic fields in normal galaxies at high redshift. Nature, 454:302–304, July 2008.
- S. Bertone, C. Vogt, and T. Enßlin. Magnetic field seeding by galactic winds. MNRAS, 370:319–330, July 2006.
- L. Biermann. Über den Ursprung der Magnetfelder auf Sternen und im interstellaren Raum (mit einem Anhang von A. Schlüter). Zeitschrift Naturforschung Teil A, 5:65–+, 1950.

- J. Binney and S. Tremaine. Galactic dynamics. Princeton University Press, 1987.
- G. T. Birk, H. Wiechen, and H. Lesch. Generation of magnetic seed fields in self-gravitating protogalactic clouds. A&A, 393:685–691, October 2002.
- R. Blandford and D. Eichler. Particle acceleration at astrophysical shocks: A theory of cosmic ray origin. Phys. Rep., 154:1–75, October 1987.
- P. Blasi. Direct Measurements, Acceleration and Propagation of Cosmic Rays. ArXiv e-prints, January 2008. arXiv:0801.4534.
- H. Bloemen. The high-energy component of the ISM - Cosmic-ray phenomena. In D. J. Hollenbach & H. A. Thronson Jr., editor, Interstellar Processes, volume 134 of Astrophysics and Space Science Library, pages 143–168. D. Reidel Publishing Co., Dordrecht, 1987.
- G. R. Blumenthal, S. M. Faber, J. R. Primack, and M. J. Rees. Formation of galaxies and large-scale structure with cold dark matter. Nature, 311:517–525, October 1984.
- S. Børve, M. Omang, and J. Trulsen. Regularized Smoothed Particle Hydrodynamics: A New Approach to Simulating Magnetohydrodynamic Shocks. ApJ, 561:82–93, November 2001.
- W. Bothe and W. Kolhörster. Das Wesen der Höhenstrahlung. Zeitschrift für Physik, 56:751–777, November 1929.
- A. Boulares and D. P. Cox. Galactic hydrostatic equilibrium with magnetic tension and cosmic-ray diffusion. ApJ, 365:544–558, December 1990.
- F. Bournaud, C. J. Jog, and F. Combes. Galaxy mergers with various mass ratios: Properties of remnants. A&A, 437:69–85, July 2005.
- F. Bournaud, C. J. Jog, and F. Combes. Multiple minor mergers: formation of elliptical galaxies and constraints for the growth of spiral disks. A&A, 476:1179–1190, December 2007.
- A. Brandenburg. Magnetic field evolution in simulations with Euler potentials. MNRAS, pages 1492–+, October 2009.
- A. Brandenburg and A. Nordlund. Astrophysical turbulence modeling. ArXiv e-prints, December 2009. arXiv:0912.1340.
- A. Brandenburg and K. Subramanian. Astrophysical magnetic fields and nonlinear dynamo theory. Phys. Rep., 417:1–4, October 2005.
- B. R. Brandl, D. M. Clark, S. S. Eikenberry, J. C. Wilson, C. P. Henderson, D. J. Barry, J. R. Houck, J. C. Carson, and T. L. Hayward. Deep Near-Infrared Imaging and Photometry of the Antennae Galaxies with WIRC. ApJ, 635:280–289, December 2005.
- B. R. Brandl, L. Snijders, M. den Brok, D. G. Whelan, B. Groves, P. van der Werf, V. Charmandaris, J. D. Smith, L. Armus, R. C. Kennicutt, and J. R. Houck. Spitzer-IRS Study of the Antennae Galaxies NGC 4038/39. ApJ, 699:1982–2001, July 2009.
- D. Breitschwerdt, J. F. McKenzie, and H. J. Voelk. Galactic winds. I - Cosmic ray and wave-driven winds from the Galaxy. A&A, 245:79–98, May 1991.
- D. Breitschwerdt, J. F. McKenzie, and H. J. Voelk. Galactic winds. II - Role of the disk-halo interface in cosmic ray driven galactic winds. A&A, 269:54–66, March 1993.

- A. Burkert and T. Naab. Major Mergers and the Origin of Elliptical Galaxies. In G. Contopoulos and N. Voglis, editors, Galaxies and Chaos, volume 626 of Lecture Notes in Physics, pages 327–339. Berlin Springer Verlag, 2003.
- F. Bürzle, P. C. Clark, F. Stasyszyn, T. Greif, K. Dolag, R. S. Klessen, and P. Nielaba. Protostellar collapse and fragmentation using an MHD GADGET. MNRAS, 412:171–186, March 2011.
- C. L. Carilli and G. B. Taylor. Cluster Magnetic Fields. ARA&A, 40:319–348, 2002.
- F. Cattaneo and S. I. Vainshtein. Suppression of turbulent transport by a weak magnetic field. ApJ, 376:L21–L24, July 1991.
- S. Chapman. Solar Plasma, Geomagnetism and Aurora. Gordon and Breach, New-York, 1964.
- S. Chapman and J. Bartels. Geomagnetism, volume I,II. Oxford : Clarendon Press, 1940.
- K. T. Chyży. Magnetic fields and starbursts: from irregulars to mergers. In R. de Grijs & R. M. González Delgado, editor, Starbursts: From 30 Doradus to Lyman Break Galaxies, volume 329 of Astrophysics and Space Science Library, pages 12P–+, May 2005.
- K. T. Chyży and R. Beck. Magnetic fields in merging spirals - the Antennae. A&A, 417:541–555, April 2004.
- K. T. Chyży and R. J. Buta. Discovery of a Strong Spiral Magnetic Field Crossing the Inner Pseudoring of NGC 4736. ApJ, 677:L17–L20, April 2008.
- K. T. Chyży, J. Knapik, D. J. Bomans, U. Klein, R. Beck, M. Soida, and M. Urbanik. Magnetic fields and ionized gas in the local group irregular galaxies IC 10 and NGC 6822. A&A, 405:513–524, July 2003.
- K. T. Chyży, D. J. Bomans, M. Krause, R. Beck, M. Soida, and M. Urbanik. Magnetic fields and ionized gas in nearby late type galaxies. A&A, 462:933–941, February 2007a.
- K. T. Chyży, M. Ehle, and R. Beck. Magnetic fields and gas in the cluster-influenced spiral galaxy NGC 4254. I. Radio and X-rays observations. A&A, 474:415–429, November 2007b.
- D. A. Clarke, J. O. Burns, and M. L. Norman. VLA observations of the inner lobes of Centaurus A. ApJ, 395:444–452, August 1992.
- J. J. Condon. Radio emission from normal galaxies. ARA&A, 30:575–611, 1992.
- T. G. Cowling. The Electrical Conductivity of an Ionized Gas in a Magnetic Field, with Applications to the Solar Atmosphere and the Ionosphere. Royal Society of London Proceedings Series A, 183: 453–479, June 1945.
- T. G. Cowling. Solar Electrodynamics, pages 532–+. In: The Sun. Edited by Gerard P. Kuiper. The University of Chicago Press, 1953.
- T. J. Cox, S. N. Dutta, T. Di Matteo, L. Hernquist, P. F. Hopkins, B. Robertson, and V. Springel. The Kinematic Structure of Merger Remnants. ApJ, 650:791–811, October 2006.
- T. J. Cox, S. N. Dutta, P. F. Hopkins, and L. Hernquist. Galaxy Mergers: Driving Galaxy Formation. In T. Kodama, T. Yamada, and K. Aoki, editors, Astronomical Society of the Pacific Conference Series, volume 399, pages 284–+, October 2008a.

- T. J. Cox, P. Jonsson, R. S. Somerville, J. R. Primack, and A. Dekel. The effect of galaxy mass ratio on merger-driven starbursts. *MNRAS*, 384:386–409, February 2008b.
- L. Davis, Jr. and J. L. Greenstein. The Polarization of Starlight by Aligned Dust Grains. *ApJ*, 114:206–+, September 1951.
- M. Davis, G. Efstathiou, C. S. Frenk, and S. D. M. White. The evolution of large-scale structure in a universe dominated by cold dark matter. *ApJ*, 292:371–394, May 1985.
- E. M. de Gouveia Dal Pino. Cosmic Magnetic Fields: from Stars and Galaxies to the Primordial Universe. *ArXiv e-prints*, March 2010. arXiv:1003.3884.
- J. DeBuhr, E. Quataert, C.-P. Ma, and P. Hopkins. Self-regulated black hole growth via momentum deposition in galaxy merger simulations. *MNRAS*, 406:L55–L59, July 2010.
- P. Di Matteo, F. Bournaud, M. Martig, F. Combes, A.-L. Melchior, and B. Semelin. On the frequency, intensity, and duration of starburst episodes triggered by galaxy interactions and mergers. *A&A*, 492:31–49, December 2008.
- T. Di Matteo, V. Springel, and L. Hernquist. Energy input from quasars regulates the growth and activity of black holes and their host galaxies. *Nature*, 433:604–607, February 2005.
- C. L. Dobbs and D. J. Price. Magnetic fields and the dynamics of spiral galaxies. *MNRAS*, 383:497–512, January 2008.
- K. Dolag and F. Stasyszyn. An MHD GADGET for cosmological simulations. *MNRAS*, 398:1678–1697, October 2009.
- K. Dolag, F. K. Hansen, M. Roncarelli, and L. Moscardini. The imprints of local superclusters on the Sunyaev-Zel’dovich signals and their detectability with Planck. *MNRAS*, 363:29–39, October 2005.
- J. Donnert, K. Dolag, H. Lesch, and E. Müller. Cluster magnetic fields from galactic outflows. *MNRAS*, 392:1008–1021, January 2009.
- T. Doumler and A. Knebe. Investigating the influence of magnetic fields upon structure formation with AMIGA - a C code for cosmological magnetohydrodynamics. *MNRAS*, 403:453–473, March 2010.
- A. Dubey, R. Fisher, C. Graziani, G. C. Jordan, IV, D. Q. Lamb, L. B. Reid, P. Rich, D. Sheeler, D. Townsley, and K. Weide. Challenges of Extreme Computing using the FLASH code. In N. V. Pogorelov, E. Audit, & G. P. Zank, editor, *Numerical Modeling of Space Plasma Flows*, volume 385 of *Astronomical Society of the Pacific Conference Series*, pages 145–+, April 2008.
- J. Dubinski, J. C. Mihos, and L. Hernquist. Using Tidal Tails to Probe Dark Matter Halos. *ApJ*, 462:576–+, May 1996.
- Y. Dubois and R. Teyssier. Magnetised winds in dwarf galaxies. *A&A*, 523:A72+, November 2010.
- G. Efstathiou. A model of supernova feedback in galaxy formation. *MNRAS*, 317:697–719, September 2000.
- D. Elstner, K. Otmianowska-Mazur, S. von Linden, and M. Urbanik. Galactic magnetic fields and spiral arms. 3D dynamo simulations. *A&A*, 357:129–138, May 2000.
- D. Elstner, O. Gressel, and G. Rüdiger. Galactic dynamo simulations. In *IAU Symposium*, volume 259, pages 467–478, April 2009.

- B. Evans. Magnetism and archaeology: Magnetic oxides in the first American civilization. Physica B+C, 86:1091–1099, January 1977.
- V. F. Hess. über Beobachtungen der durchdringenden Strahlung bei sieben Freiballonfahrten. Physikalische Zeitschrift, 13:1084–1091, November 1912.
- G. Fabbiano. X rays from normal galaxies. ARA&A, 27:87–138, 1989.
- G. Fabbiano, A. Zezas, and S. S. Murray. Chandra Observations of “The Antennae” Galaxies (NGC 4038/9). ApJ, 554:1035–1043, June 2001.
- M. Fatuzzo, F. C. Adams, and F. Melia. Enhanced Cosmic-Ray Flux and Ionization for Star Formation in Molecular Clouds Interacting with Supernova Remnants. ApJ, 653:L49–L52, December 2006.
- A. M. N. Ferguson, R. F. G. Wyse, J. S. Gallagher, and D. A. Hunter. Discovery of Recent Star Formation in the Extreme Outer Regions of Disk Galaxies. ApJ, 506:L19–L22, October 1998.
- C. Ferrari, F. Govoni, S. Schindler, A. M. Bykov, and Y. Rephaeli. Observations of Extended Radio Emission in Clusters. Space Sci. Rev., 134:93–118, February 2008.
- K. Ferriere. Effect of the explosion of supernovae and superbubbles on the Galactic dynamo. ApJ, 391:188–198, May 1992a.
- K. Ferriere. Effect of an ensemble of explosions on the Galactic dynamo. I - General formulation. ApJ, 389:286–296, April 1992b.
- K. M. Ferrière. The interstellar environment of our galaxy. Reviews of Modern Physics, 73:1031–1066, October 2001.
- A. Fletcher, R. Beck, E. M. Berkhuijsen, C. Horellou, and A. Shukurov. Magnetic Fields and Spiral Structure. In E. J. Alfaro, E. Pérez, & J. Franco, editor, How Does the Galaxy Work?, volume 315 of Astrophysics and Space Science Library, pages 299–+, October 2004.
- B. Fryxell, K. Olson, P. Ricker, F. X. Timmes, M. Zingale, D. Q. Lamb, P. MacNeice, R. Rosner, J. W. Truran, and H. Tufo. FLASH: An Adaptive Mesh Hydrodynamics Code for Modeling Astrophysical Thermonuclear Flashes. ApJS, 131:273–334, November 2000.
- B. M. Gaensler. Cosmic magnetism with the Square Kilometre Array and its pathfinders. In IAU Symposium, volume 259, pages 645–652, April 2009.
- B. M. Gaensler, R. Beck, and L. Feretti. The origin and evolution of cosmic magnetism. NewAR, 48:1003–1012, December 2004.
- W. Gilbert. On the Magnet. Basic Books, New York, 1958. Edited by D.J. Price, in original form from 1600.
- V. L. Ginzburg and S. I. Syrovatskii. Cosmic Magnetobremstrahlung (synchrotron Radiation). ARA&A, 3:297–+, 1965.
- I. M. Gioia, L. Gregorini, and U. Klein. High frequency radio continuum observations of bright spiral galaxies. A&A, 116:164–174, December 1982.
- C. Gisinger, S. Fromang, and E. Dormy. Direct numerical simulations of the galactic dynamo in the kinematic growing phase. MNRAS, 394:L84–L88, March 2009.

- G. A. Glatzmaier, R. S. Coe, L. Hongre, and P. H. Roberts. The role of the Earth's mantle in controlling the frequency of geomagnetic reversals. Nature, 401:885–890, October 1999.
- N. Y. Gnedin, A. Ferrara, and E. G. Zweibel. Generation of the Primordial Magnetic Fields during Cosmological Reionization. ApJ, 539:505–516, August 2000.
- A. C. González-García, M. Balcells, and V. S. Olshevsky. Line-of-sight velocity distributions of elliptical galaxies from collisionless mergers. MNRAS, 372:L78–L82, October 2006.
- F. Govoni and L. Feretti. Magnetic Fields in Clusters of Galaxies. International Journal of Modern Physics D, 13:1549–1594, 2004.
- O. Gressel, D. Elstner, U. Ziegler, and G. Rüdiger. Direct simulations of a supernova-driven galactic dynamo. A&A, 486:L35–L38, August 2008.
- A. P. Guimarães. Mexico and the early history of magnetism. Revista Mexicana de Física, Vol. E50, p.51–53, 50:51–53, June 2004.
- F. Haardt and P. Madau. Radiative Transfer in a Clumpy Universe. II. The Ultraviolet Extragalactic Background. ApJ, 461:20–+, April 1996.
- M. G. Haehnelt, M. Steinmetz, and M. Rauch. Damped Ly alpha Absorber at High Redshift: Large Disks or Galactic Building Blocks? ApJ, 495:647–+, March 1998.
- G. E. Hale. On the Probable Existence of a Magnetic Field in Sun-Spots. ApJ, 28:315–+, November 1908.
- J. S. Hall. Observations of the Polarized Light from Stars. Science, 109:166–167, February 1949.
- J. L. Han, R. Beck, and E. M. Berkhuijsen. New clues to the magnetic field structure of M 31. A&A, 335:1117–1123, July 1998.
- M. Hanasz and H. Lesch. Magnetic buoyancy and the galactic dynamo. A&A, 278:561–568, November 1993.
- M. Hanasz and H. Lesch. The galactic dynamo effect due to Parker-shearing instability of magnetic flux tubes. I. General formalism and the linear approximation. A&A, 321:1007–1020, May 1997.
- M. Hanasz and H. Lesch. The galactic dynamo effect due to Parker-shearing instability of magnetic flux tubes. III. The fast dynamo model. A&A, 332:77–87, April 1998.
- M. Hanasz and H. Lesch. Cosmic-Ray Evolution in Parker-unstable Galactic Magnetic Fields. ApJ, 543:235–244, November 2000.
- M. Hanasz, H. Lesch, K. Otmianowska-Mazur, and G. Kowal. Cosmic ray driven dynamo in galactic disks. In K. T. Chyzy, K. Otmianowska-Mazur, M. Soida, and R.-J. Dettmar, editors, The Magnetized Plasma in Galaxy Evolution, pages 162–170, June 2005.
- M. Hanasz, K. Otmianowska-Mazur, G. Kowal, and H. Lesch. Cosmic-ray-driven dynamo in galactic disks. A parameter study. A&A, 498:335–346, May 2009a.
- M. Hanasz, K. Otmianowska-Mazur, H. Lesch, G. Kowal, M. Soida, D. Wóltański, K. Kowalik, R. K. Pawłaszek, and B. Kulesza-Żydzik. Cosmic-ray driven dynamo in galactic disks. In IAU Symposium, volume 259, pages 479–484, April 2009b.

- M. Hanasz, D. Wóltański, and K. Kowalik. Global Galactic Dynamo Driven by Cosmic Rays and Exploding Magnetized Stars. ApJ, 706:L155–L159, November 2009c.
- M. Hanasz, K. Kowalik, D. Wóltański, and R. Pawłaszek. The PIERNIK MHD code - a multi-fluid, non-ideal extension of the relaxing-TVD scheme (I). In K. Goździewski, A. Niedzielski, & J. Schneider, editor, EAS Publications Series, volume 42, pages 275–280, April 2010a.
- M. Hanasz, K. Kowalik, D. Wóltański, R. Pawłaszek, and K. Kornet. The PIERNIK MHD code - a multi-fluid, non-ideal extension of the relaxing-TVD scheme (II). In K. Goździewski, A. Niedzielski, & J. Schneider, editor, EAS Publications Series, volume 42, pages 281–285, April 2010b.
- E. R. Harrison. Generation of magnetic fields in the radiation ERA. MNRAS, 147:279–+, 1970.
- V. Heesen, M. Krause, R. Beck, and R.-J. Dettmar. Cosmic rays and the magnetic field in the nearby starburst galaxy NGC 253. II. The magnetic field structure. A&A, 506:1123–1135, November 2009.
- L. Hernquist. An analytical model for spherical galaxies and bulges. ApJ, 356:359–364, June 1990.
- L. Hernquist. N-body realizations of compound galaxies. ApJS, 86:389–400, June 1993.
- L. Hernquist and J. E. Barnes. Dynamics of Gas in Major Mergers (Invited paper). In I. Shlosman, editor, Mass-Transfer Induced Activity in Galaxies, pages 323–+, 1994.
- J. E. Hibbard, J. M. van der Hulst, J. E. Barnes, and R. M. Rich. High-Resolution H I Mapping of NGC 4038/39 (“The Antennae”) and Its Tidal Dwarf Galaxy Candidates. AJ, 122:2969–2992, December 2001.
- W. A. Hiltner. Polarization of Radiation from Distant Stars by the Interstellar Medium. Nature, 163:283–+, February 1949a.
- W. A. Hiltner. Polarization of Light from Distant Stars by Interstellar Medium. Science, 109:165–+, February 1949b.
- W. A. Hiltner. Polarization of Stellar Radiation. III. The Polarization of 841 Stars. ApJ, 114:241–+, September 1951.
- R. W. Hockney and J. W. Eastwood. Computer simulation using particles. 1988.
- P. F. Hopkins, L. Hernquist, T. J. Cox, S. N. Dutta, and B. Rothberg. Dissipation and Extra Light in Galactic Nuclei. I. Gas-Rich Merger Remnants. ApJ, 679:156–181, May 2008.
- E. Hummel. The radio continuum-far infrared correlation and magnetic fields in SBC galaxies. A&A, 160:L4–L6, May 1986.
- E. Hummel and R. Beck. Magnetic fields in interacting galaxies: NGC 2276. A&A, 303:691, November 1995.
- R. Jesseit, M. Cappellari, T. Naab, E. Emsellem, and A. Burkert. Specific angular momentum of disc merger remnants and the  $\lambda_R$ -parameter. MNRAS, 397:1202–1214, August 2009.
- P. H. Johansson and G. Efstathiou. A model for the metallicity evolution of damped Lyman  $\alpha$  systems. MNRAS, 371:1519–1535, September 2006.
- P. H. Johansson, A. Burkert, and T. Naab. The Evolution of Black Hole Scaling Relations in Galaxy Mergers. ApJ, 707:L184–L189, December 2009a.

- P. H. Johansson, T. Naab, and A. Burkert. Equal- and Unequal-Mass Mergers of Disk and Elliptical Galaxies with Black Holes. ApJ, 690:802–821, January 2009b.
- P. H. Johansson, T. Naab, and J. P. Ostriker. Gravitational Heating Helps Make Massive Galaxies Red and Dead. ApJ, 697:L38–L43, May 2009c.
- L. V. Jones, R. J. Elston, and D. A. Hunter. The Source of Far-Infrared Radiation in Spiral Galaxies. AJ, 124:2548–2574, November 2002.
- S. J. Karl, T. Naab, P. H. Johansson, C. Theis, and C. M. Boily. Towards an accurate model for the Antennae galaxies. Astronomische Nachrichten, 329:1042–+, 2008.
- S. J. Karl, T. Naab, P. H. Johansson, H. Kotarba, C. M. Boily, F. Renaud, and C. Theis. One Moment in Time – Modeling Star Formation in the Antennae. ApJ, 715:L88–L93, June 2010.
- A. P. Kazantsev. Enhancement of a Magnetic Field by a Conducting Fluid. Soviet Journal of Experimental and Theoretical Physics, 26:1031–+, May 1968.
- K.-T. Kim, P. P. Kronberg, G. Giovannini, and T. Venturi. Discovery of intergalactic radio emission in the Coma-A1367 supercluster. Nature, 341:720–723, October 1989.
- M. G. Kivelson and C. T. Russell, editors. Introduction to Space Physics. Cambridge University Press, April 1995.
- U. Klein, R. Wielebinski, and H. W. Morsi. Radio continuum observations of M82. A&A, 190:41–46, January 1988.
- J. H. Knapen, R. S. de Jong, S. Stedman, and D. M. Bramich. Structure and star formation in disc galaxies - I. Sample selection and near-infrared imaging. MNRAS, 344:527–543, September 2003.
- J. Knapik, M. Soida, R.-J. Dettmar, R. Beck, and M. Urbanik. Detection of spiral magnetic fields in two flocculent galaxies. A&A, 362:910–920, October 2000.
- H. Kotarba, H. Lesch, K. Dolag, T. Naab, P. H. Johansson, and F. A. Stasyszyn. Magnetic field structure due to the global velocity field in spiral galaxies. MNRAS, 397:733–747, August 2009.
- H. Kotarba, S. J. Karl, T. Naab, P. H. Johansson, K. Dolag, H. Lesch, and F. A. Stasyszyn. Simulating Magnetic Fields in the Antennae Galaxies. ApJ, 716:1438–1452, June 2010a.
- H. Kotarba, H. Lesch, K. Dolag, T. Naab, P. H. Johansson, J. Donnert, and F. A. Stasyszyn. Galactic ménage à trois: Simulating magnetic fields in colliding galaxies. ArXiv e-prints, November 2010b. arXiv:1011.5735.
- F. Krause and K. H. Rädler. In Ergebnisse der Plasmaphysik und Gaselektronik, volume 2. Hrsg. Rompe, R., Steenbeck, M., Akademie Verlag, Berlin, 1971.
- F. Krause and K.-H. Raedler. Mean-field magnetohydrodynamics and dynamo theory. Oxford, Pergamon Press, Ltd., 1980.
- F. Krause and R. Wielebinski. Dynamos in Galaxies. In G. Klare, editor, Reviews in Modern Astronomy, volume 4, pages 260–286, 1991.
- M. Krause. Magnetic Fields and Star Formation in Spiral Galaxies. In Revista Mexicana de Astronomia y Astrofisica Conference Series, volume 36, pages 25–29, August 2009.

- P. P. Kronberg, H. Lesch, and U. Hopp. Magnetization of the Intergalactic Medium by Primeval Galaxies. ApJ, 511:56–64, January 1999.
- P. P. Kronberg, Q. W. Dufton, H. Li, and S. A. Colgate. Magnetic Energy of the Intergalactic Medium from Galactic Black Holes. ApJ, 560:178–186, October 2001.
- P. P. Kronberg, M. L. Bernet, F. Miniati, S. J. Lilly, M. B. Short, and D. M. Higdon. A Global Probe of Cosmic Magnetic Fields to High Redshifts. ApJ, 676:70–79, March 2008.
- B. Kulesza-Żydzik, K. Kulpa-Dybeł, K. Otmianowska-Mazur, G. Kowal, and M. Soida. Formation of gaseous arms in barred galaxies with dynamically important magnetic field: 3D MHD simulations. A&A, 498:L21–L24, May 2009.
- R. M. Kulsrud. A Critical Review of Galactic Dynamos. ARA&A, 37:37–64, 1999.
- R. M. Kulsrud and S. W. Anderson. The spectrum of random magnetic fields in the mean field dynamo theory of the Galactic magnetic field. ApJ, 396:606–630, September 1992.
- R. M. Kulsrud and E. G. Zweibel. On the origin of cosmic magnetic fields. Reports of Progress in Physics, 71(4):046901–+, April 2008.
- R. M. Kulsrud, R. Cen, J. P. Ostriker, and D. Ryu. The Protogalactic Origin for Cosmic Magnetic Fields. ApJ, 480:481–+, May 1997.
- R. A. Laing and A. H. Bridle. Rotation measure variation across M84. MNRAS, 228:557–571, October 1987.
- L. D. Landau and E. M. Lifshitz. Fluid mechanics. Pergamon Press, Oxford, 1959.
- Sir J. Larmor. How could a rotating body such as the sun become a magnet? Brit. Assn. Adv. Sci. Rep., pages 159–160, 1919a.
- Sir J. Larmor. Possible rotational origin of magnetic fields of Sun and Earth. Elect. Rev., 85:512, September 1919b.
- A. Lazarian, A. A. Goodman, and P. C. Myers. On the Efficiency of Grain Alignment in Dark Clouds. ApJ, 490:273–+, November 1997.
- H. Lesch and R. Bender. Magnetic fields in elliptical galaxies. A&A, 233:417–421, July 1990.
- H. Lesch and G. T. Birk. Can large-scale magnetic fields survive during the pre-recombination era of the universe? Physics of Plasmas, 5:2773–2776, July 1998.
- H. Lesch and M. Chiba. Protogalactic evolution and magnetic fields. A&A, 297:305–+, May 1995.
- H. Lesch and M. Chiba. On the Origin and Evolution of Galactic Magnetic Fields. Fund. Cosmic Phys., 18:273–368, 1997.
- H. Lesch and M. Hanasz. Strong magnetic fields and cosmic rays in very young galaxies. A&A, 401: 809–816, April 2003.
- Y. Li, M.-M. Mac Low, and R. S. Klessen. Control of Star Formation in Galaxies by Gravitational Instability. ApJ, 620:L19–L22, February 2005.
- C. C. Lin and F. H. Shu. On the Spiral Structure of Disk Galaxies. ApJ, 140:646–+, August 1964.

- A. Loeb and E. Waxman. Cosmic  $\gamma$ -ray background from structure formation in the intergalactic medium. Nature, 405:156–158, May 2000.
- M. S. Longair. High energy astrophysics. Cambridge University Press, Cambridge and New York, 1981.
- M. S. Longair. High energy astrophysics. Vol.2: Stars, the galaxy and the interstellar medium. Cambridge University Press, UK, 2nd ed., 1994.
- T. A. Lozinskaya. Supernovae and stellar wind in the interstellar medium. American Institute of Physics, New York, 1992.
- D. Lynden-Bell and A. J. Kalnajs. On the generating mechanism of spiral structure. MNRAS, 157: 1–+, 1972.
- V. H. Malmstrom. Knowledge of magnetism in pre-Columbian Mesoamerica. Nature, 259:390–391, February 1976.
- W. G. Mathews and F. Brighenti. Self-generated Magnetic Fields in Galactic Cooling Flows. ApJ, 488:595–+, October 1997.
- C. F. McKee and J. P. Ostriker. A theory of the interstellar medium - Three components regulated by supernova explosions in an inhomogeneous substrate. ApJ, 218:148–169, November 1977.
- A. J. Meadows. Early solar physics. Oxford: Pergamon Press, 1970.
- J. C. Mihos and L. Hernquist. Ultraluminous starbursts in major mergers. ApJ, 431:L9–L12, August 1994.
- J. C. Mihos, G. D. Bothun, and D. O. Richstone. Modeling the Spatial Distribution of Star Formation in Interacting Disk Galaxies. ApJ, 418:82–+, November 1993.
- A. C. Mitchell. Chapters in the History of Terrestrial Magnetism. J. Geophys. Res., 37:105–146, 1932.
- A. C. Mitchell. Chapters in the History of Terrestrial Magnetism. J. Geophys. Res., 42:241–280, 1937.
- H. J. Mo, S. Mao, and S. D. M. White. The formation of galactic discs. MNRAS, 295:319–336, April 1998.
- H. K. Moffatt. Magnetic field generation in electrically conducting fluids. 1978.
- J. J. Monaghan. On the problem of penetration in particle methods. Journal of Computational Physics, 82:1–15, May 1989.
- J. J. Monaghan. Smoothed particle hydrodynamics. ARA&A, 30:543–574, 1992.
- J. J. Monaghan. SPH and Riemann Solvers. Journal of Computational Physics, 136:298–307, September 1997.
- J. J. Monaghan. Smoothed Particle Hydrodynamics Code Basics. Journal of Korean Astronomical Society, 34:203–207, December 2001.
- J. J. Monaghan. Smoothed particle hydrodynamics. Reports on Progress in Physics, 68:1703–1759, August 2005.
- J. J. Monaghan and J. C. Lattanzio. A refined particle method for astrophysical problems. A&A, 149:135–143, August 1985.

- D. Moss and A. Shukurov. Turbulence and magnetic fields in elliptical galaxies. MNRAS, 279:229–239, March 1996.
- H. Mourtisen, U. Janssen-Bienhold, M. Liedvogel, G. Feenders, J. Stalleicken, P. Dirks, and R. Weiler. Cryptochromes and neuronal-activity markers colocalize in the retina of migratory birds during magnetic orientation. Proc. Natl. Acad. Sci. USA, 101:14294–14299, September 2004.
- T. Naab and A. Burkert. Statistical Properties of Collisionless Equal- and Unequal-Mass Merger Remnants of Disk Galaxies. ApJ, 597:893–906, November 2003.
- T. Naab and J. P. Ostriker. Are Disk Galaxies the Progenitors of Giant Ellipticals? ApJ, 690:1452–1462, January 2009.
- T. Naab, R. Jesseit, and A. Burkert. The influence of gas on the structure of merger remnants. MNRAS, 372:839–852, October 2006.
- T. Naab, P. H. Johansson, J. P. Ostriker, and G. Efstathiou. Formation of Early-Type Galaxies from Cosmological Initial Conditions. ApJ, 658:710–720, April 2007.
- B. B. Nath and J. Silk. Heating of the intergalactic medium as a result of structure formation. MNRAS, 327:L5–L9, October 2001.
- S. G. Neff and J. S. Ulvestad. VLA Observations of the Nearby Merger NGC 4038/4039: H II Regions and Supernova Remnants in the “Antennae”. AJ, 120:670–696, August 2000.
- A. F. Nelson, M. Wetzstein, and T. Naab. Vine – A Numerical Code for Simulating Astrophysical Systems Using Particles. II. Implementation and Performance Characteristics. ApJS, 184:326–360, October 2009.
- S. Niklas and R. Beck. A new approach to the radio-far infrared correlation for non-calorimeter galaxies. A&A, 320:54–64, April 1997.
- S. A. Orszag and C.-M. Tang. Small-scale structure of two-dimensional magnetohydrodynamic turbulence. Journal of Fluid Mechanics, 90:129–143, January 1979.
- J. P. Ostriker and P. J. E. Peebles. A Numerical Study of the Stability of Flattened Galaxies: or, can Cold Galaxies Survive? ApJ, 186:467–480, December 1973.
- T. Padmanabhan. Structure Formation in the Universe. Cambridge University Press, UK, June 1993.
- E. N. Parker. Kinematical Hydromagnetic Theory and its Application to the Low Solar Photosphere. ApJ, 138:552–+, August 1963.
- E. N. Parker. The Dynamical State of the Interstellar Gas and Field. ApJ, 145:811–+, September 1966.
- E. N. Parker. The Dynamical State of the Interstellar Gas and Field. II. Non-Linear Growth of Clouds and Forces in Three Dimensions. ApJ, 149:517–+, September 1967a.
- E. N. Parker. The Dynamical State of the Interstellar Gas and Field. III. Turbulence and Enhanced Diffusion. ApJ, 149:535–+, September 1967b.
- E. N. Parker. The Generation of Magnetic Fields in Astrophysical Bodies. II. The Galactic Field. ApJ, 163:255–+, January 1971.

- E. N. Parker. The Generation and Dissipation of Solar and Galactic Magnetic Fields. Ap&SS, 22: 279–291, June 1973.
- E. N. Parker. Cosmical magnetic fields: Their origin and their activity. Clarendon Press, Oxford and New York, 1979.
- E. N. Parker. Fast dynamos, cosmic rays, and the Galactic magnetic field. ApJ, 401:137–145, December 1992.
- J. H. Piddington. The origin and form of the galactic magnetic field. II. The primordial-field model. Cosmic Electrodyn., Vol. 3, p. 129 - 146, 3:129–146, 1972.
- F. Piontek and M. Steinmetz. The modelling of feedback processes in cosmological simulations of disc galaxy formation. MNRAS, 410:2625–2642, February 2011.
- R. W. Pogge. Ionized gas in the nuclear regions of nearby non-Seyfert spiral galaxies. ApJS, 71: 433–453, November 1989.
- K. G. Powell, P. L. Roe, T. J. Linde, T. I. Gombosi, and D. L. de Zeeuw. A Solution-Adaptive Upwind Scheme for Ideal Magnetohydrodynamics. Journal of Computational Physics, 154:284–309, September 1999.
- D. Price. Smoothed Particle Hydrodynamics. ArXiv e-prints, page arXiv:0507472, July 2005.
- D. J. Price and M. R. Bate. The impact of magnetic fields on single and binary star formation. MNRAS, 377:77–90, May 2007.
- D. J. Price and C. Federrath. A comparison between grid and particle methods on the statistics of driven, supersonic, isothermal turbulence. MNRAS, 406:1659–1674, August 2010.
- D. J. Price and J. J. Monaghan. Smoothed Particle Magnetohydrodynamics. Memorie della Societa Astronomica Italiana Supplement, 4:93–+, 2004a.
- D. J. Price and J. J. Monaghan. Smoothed Particle Magnetohydrodynamics - I. Algorithm and tests in one dimension. MNRAS, 348:123–138, February 2004b.
- D. J. Price and J. J. Monaghan. Smoothed Particle Magnetohydrodynamics - II. Variational principles and variable smoothing-length terms. MNRAS, 348:139–152, February 2004c.
- D. J. Price and J. J. Monaghan. Smoothed Particle Magnetohydrodynamics - III. Multidimensional tests and the  $\nabla \cdot B = 0$  constraint. MNRAS, 364:384–406, December 2005.
- M. Rauch, M. G. Haehnelt, and M. Steinmetz. QSO Metal Absorption Systems at High Redshift and the Signature of Hierarchical Galaxy Formation. ApJ, 481:601–+, May 1997.
- V. A. Razin. The Polarization of Cosmic Radio Radiation at Wavelengths of 1.45 and 3.3 Meters. AZh, 35:241–+, 1958.
- M. J. Rees. The origin and cosmogonic implications of seed magnetic fields. QJRAS, 28:197–206, September 1987.
- M. J. Rees. Origin of the Seed Magnetic Field for a Galactic Dynamo. In D. Lynden-Bell, editor, NATO ASIC Proc. 422: Cosmical Magnetism, pages 155–+. Dordrecht: Kluwer, 1994.
- M. J. Rees. Origin of cosmic magnetic fields. Astronomische Nachrichten, 327:395–+, June 2006.

- J. R. Reitz, F. J. Milford, and R. W. Christy. Foundations of electromagnetic theory. Addison Wesley Pub. Co., November 1992.
- F. Renaud, P. N. Appleton, and C. K. Xu. N-body Simulation of the Stephan's Quintet. ApJ, 724: 80–91, November 2010.
- T. Ritz, P. Thalau, J. B. Phillips, R. Wiltshcko, and W. Wiltshcko. Resonance effects indicate a radical-pair mechanism for avian magnetic compass. Nature, 429:177–180, May 2004.
- B. Robertson, T. J. Cox, L. Hernquist, M. Franx, P. F. Hopkins, P. Martini, and V. Springel. The Fundamental Scaling Relations of Elliptical Galaxies. ApJ, 641:21–40, April 2006.
- R. Rohde and D. Elstner. Three-dimensional dynamos in spiral galaxies. A&A, 333:27–30, May 1998.
- R. Rohde, D. Elstner, and G. Rüdiger. Dynamo induced magnetic fields in spiral galaxies. Acta Cosmologica, 23:205–208, 1997.
- S. Rosswog and D. Price. MAGMA: a three-dimensional, Lagrangian magnetohydrodynamics code for merger applications. MNRAS, 379:915–931, August 2007.
- A. A. Ruzmaikin, D. D. Sokolov, and A. M. Shukurov. Magnetic Fields of Galaxies. Kluwer Academic Publ., Dordrecht, 1988.
- G. B. Rybicki and A. P. Lightman. Radiative Processes in Astrophysics. Wiley-VCH, New York, June 1986.
- D. Ryu, H. Kang, J. Cho, and S. Das. Turbulence and Magnetic Fields in the Large-Scale Structure of the Universe. Science, 320:909–, May 2008.
- A. Sakuraba and P. H. Roberts. Generation of a strong magnetic field using uniform heat flux at the surface of the core. Nature Geoscience, 2:802–805, November 2009.
- I. Saviane, Y. Momany, G. S. da Costa, R. M. Rich, and J. E. Hibbard. A New Red Giant-based Distance Modulus of 13.3 Mpc to the Antennae Galaxies and Its Consequences. ApJ, 678:179–186, May 2008.
- T. Sawala, C. Scannapieco, U. Maio, and S. White. Formation of isolated dwarf galaxies with feedback. MNRAS, 402:1599–1613, March 2010.
- F. Schweizer, C. R. Burns, B. F. Madore, V. A. Mager, M. M. Phillips, W. L. Freedman, L. Boldt, C. Contreras, G. Folatelli, S. González, M. Hamuy, W. Krzeminski, N. I. Morrell, S. E. Persson, M. R. Roth, and M. D. Stritzinger. A New Distance to the Antennae Galaxies (ngc 4038/39) based on the Type ia Supernova 2007sr. AJ, 136:1482–1489, October 2008.
- E. Sergé. From Falling Bodies to Radio Waves. W. H. Freeman & Co. (Sd), August 1984.
- S. K. Sethi, B. B. Nath, and K. Subramanian. Primordial magnetic fields and formation of molecular hydrogen. MNRAS, 387:1589–1596, July 2008.
- M. H. Shamos. Great Experiments in Physics VIII. Henry Holt and Company, Inc., New York, 1959.
- A. Shukurov. The origin of magnetic fields in elliptical galaxies. Highlights of Astronomy, 12:731–732, 2002.
- L. Sironi and A. Socrates. The Eddington Limit in Cosmic Rays: An Explanation for the Observed Lack of Low-Mass Radio-Loud Quasars and The  $M_{\bullet}$ - $M_{\star}$  Relation. ApJ, 710:891–902, February 2010.

- A. Socrates, S. W. Davis, and E. Ramirez-Ruiz. The Eddington Limit in Cosmic Rays: An Explanation for the Observed Faintness of Starbursting Galaxies. ApJ, 687:202–215, November 2008.
- Y. Sofue and V. Rubin. Rotation Curves of Spiral Galaxies. ARA&A, 39:137–174, 2001.
- M. Soida, R. Beck, M. Urbanik, and J. Braine. Magnetic fields in the absence of spiral density waves - NGC 4414. A&A, 394:47–57, October 2002.
- L. Spitzer. Physics of Fully Ionized Gases. Interscience, New York, 1962. 2nd edition.
- L. Spitzer and R. Härm. Transport Phenomena in a Completely Ionized Gas. Physical Review, 89:977–981, March 1953.
- V. Springel. Modelling star formation and feedback in simulations of interacting galaxies. MNRAS, 312:859–879, March 2000.
- V. Springel. The cosmological simulation code GADGET-2. MNRAS, 364:1105–1134, December 2005.
- V. Springel and L. Hernquist. Cosmological smoothed particle hydrodynamics simulations: the entropy equation. MNRAS, 333:649–664, July 2002.
- V. Springel and L. Hernquist. Cosmological smoothed particle hydrodynamics simulations: a hybrid multiphase model for star formation. MNRAS, 339:289–311, February 2003.
- V. Springel, N. Yoshida, and S. D. M. White. GADGET: a code for collisionless and gasdynamical cosmological simulations. New Astronomy, 6:79–117, April 2001.
- V. Springel, T. Di Matteo, and L. Hernquist. Modelling feedback from stars and black holes in galaxy mergers. MNRAS, 361:776–794, August 2005a.
- V. Springel, T. Di Matteo, and L. Hernquist. Black Holes in Galaxy Mergers: The Formation of Red Elliptical Galaxies. ApJ, 620:L79–L82, February 2005b.
- V. Springel, S. D. M. White, A. Jenkins, C. S. Frenk, N. Yoshida, L. Gao, J. Navarro, R. Thacker, D. Croton, J. Helly, J. A. Peacock, S. Cole, P. Thomas, H. Couchman, A. Evrard, J. Colberg, and F. Pearce. Simulations of the formation, evolution and clustering of galaxies and quasars. Nature, 435:629–636, June 2005c.
- M. Steenbeck and F. Krause. On the Dynamo Theory of Stellar and Planetary Magnetic Fields. I. AC Dynamos of Solar Type. Astronomische Nachrichten, 291:49–84, January 1969.
- M. Steenbeck, F. Krause, and K.-H. Rädler. Berechnung der mittleren LORENTZ-Feldstärke  $\overline{v \times B}$  für ein elektrisch leitendes Medium in turbulenter, durch CORIOLIS-Kräfte beeinflusster Bewegung. Zeitschrift Naturforschung Teil A, 21:369–+, April 1966.
- F. Stefani, A. Gailitis, and G. Gerbeth. Magnetohydrodynamic experiments on cosmic magnetic fields. ArXiv e-prints, 807, July 2008. arXiv:0807.0299.
- D. P. Stern. Euler Potentials. American Journal of Physics, 38:494–501, April 1970.
- D. P. Stern. Representation of magnetic fields in space. Reviews of Geophysics and Space Physics, 14:199–214, May 1976.
- D. P. Stern. a Millennium of Geomagnetism. Reviews of Geophysics, 40:1007–+, November 2002.
- M. Stix. The galactic dynamo. A&A, 42:85–89, August 1975.

- J. M. Stone, T. A. Gardiner, P. Teuben, J. F. Hawley, and J. B. Simon. Athena: A New Code for Astrophysical MHD. ApJS, 178:137–177, September 2008.
- R. G. Strom and W. J. Jaegers. Extensive gaseous haloes surrounding giant elliptical galaxies - Evidence from depolarization in radio galaxies. A&A, 194:79–89, April 1988.
- K. Subramanian. Magnetizing the universe. ArXiv e-prints, February 2008. arXiv:0802.2804.
- S. Sur, A. Shukurov, and K. Subramanian. Galactic dynamos supported by magnetic helicity fluxes. MNRAS, 377:874–882, May 2007.
- Sushruta. An english translation of the Sushruta Samhita based on the original sanskrit text. Printed by J.N. Bose, College Square, Calcutta, 1907. Edited and published by K.K.L. Bhishagraatna.
- G. B. Taylor, R. A. Perley, M. Inoue, T. Kato, H. Tabara, and K. Aizu. VLA observations of the radio galaxy Hydra A (3C 218). ApJ, 360:41–54, September 1990.
- R. Teyssier. Cosmological hydrodynamics with adaptive mesh refinement. A new high resolution code called RAMSES. A&A, 385:337–364, April 2002.
- R. Teyssier, S. Fromang, and E. Dormy. Kinematic dynamos using constrained transport with high order Godunov schemes and adaptive mesh refinement. Journal of Computational Physics, 218:44–67, October 2006.
- R. Teyssier, D. Chapon, and F. Bournaud. The Driving Mechanism of Starbursts in Galaxy Mergers. ApJ, 720:L149–L154, September 2010.
- The Pierre AUGER Collaboration, J. Abraham, P. Abreu, M. Aglietta, C. Aguirre, D. Allard, I. Allekotte, J. Allen, P. Allison, J. Alvarez-Muñiz, and 438 coauthors. Correlation of the highest-energy cosmic rays with the positions of nearby active galactic nuclei. Astroparticle Physics, 29:188–204, April 2008.
- A. Toomre and J. Toomre. Galactic Bridges and Tails. ApJ, 178:623–666, December 1972.
- D. J. Tritton. Physical fluid dynamics, 2nd revised and enlarged edition. Clarendon Press, Oxford, 1988.
- B. Uyaniker and T. L. Landecker. A Highly Ordered Faraday Rotation Structure in the Interstellar Medium. ApJ, 575:225–233, August 2002.
- S. I. Vainshtein and F. Cattaneo. Nonlinear restrictions on dynamo action. ApJ, 393:165–171, July 1992.
- S. I. Vainshtein and A. A. Ruzmaikin. Generation of the Large-Scale Galactic Magnetic Field. AZh, 48:902–+, October 1971.
- J. P. Vallée. Magnetic Field versus Gas Density, in Different Physical Conditions. Ap&SS, 234:1–10, December 1995.
- J. P. Vallee. Galactic magnetic field strengths, from three different methods - a cautionary note. A&A, 296:819–+, April 1995.
- J. P. Vallee. Observations of the Magnetic Fields Inside and Outside the Milky Way, Starting with Globules ( $\sim 1$  parsec), Filaments, Clouds, Superbubbles, Spiral Arms, Galaxies, Superclusters, and Ending with the Cosmological Universe’s Background Surface (at  $\sim 8$  Teraparsecs). Fund. Cosmic Phys., 19:1–89, 1997.

- J. P. Vallee. Observations of the Magnetic Fields Inside and Outside the Solar System: From Meteorites ( $\sim 10$  attoparsecs), Asteroids, Planets, Stars, Pulsars, Masers, to Protostellar Cloudlets ( $< 1$  parsec). *Fund. Cosmic Phys.*, 19:319–422, 1998.
- T. Venturi, S. Giacintucci, D. Dallacasa, R. Cassano, G. Brunetti, S. Bardelli, and G. Setti. GMRT radio halo survey in galaxy clusters at  $z = 0.2-0.4$ . II. The eBCS clusters and analysis of the complete sample. *A&A*, 484:327–340, June 2008.
- B. Vollmer, M. Soida, A. Chung, R. Beck, M. Urbanik, K. T. Chyży, K. Otmianowska-Mazur, and J. H. van Gorkom. The influence of the cluster environment on the large-scale radio continuum emission of 8 Virgo cluster spirals. *A&A*, 512:A36+, March 2010.
- B. Vorontsov-Velyaminov. Interaction of galaxies. *Annales d’Astrophysique*, 23:379–+, February 1960.
- B. Vorontsov-Velyaminov. Interaction of Multiple Systems. In G. C. McVittie, editor, *Problems of Extra-Galactic Research*, volume 15 of *IAU Symposium*, pages 194–+, 1962.
- J. W. Wadsley, J. Stadel, and T. Quinn. Gasoline: a flexible, parallel implementation of TreeSPH. *New Astronomy*, 9:137–158, February 2004.
- P. Wang and T. Abel. Magnetohydrodynamic Simulations of Disk Galaxy Formation: The Magnetization of the Cold and Warm Medium. *ApJ*, 696:96–109, May 2009.
- Z. Wang, G. G. Fazio, M. L. N. Ashby, J.-S. Huang, M. A. Pahre, H. A. Smith, S. P. Willner, W. J. Forrest, J. L. Pipher, and J. A. Surace. The Off-Nuclear Starbursts in NGC 4038/4039 (The Antennae Galaxies). *ApJS*, 154:193–198, September 2004.
- G. Westerhout, C. L. Seeger, W. N. Brouw, and J. Tinbergen. Polarization of the galactic 75-cm radiation. *Bull. Astron. Inst. Netherlands*, 16:187–+, July 1962.
- M. Wetzstein, A. F. Nelson, T. Naab, and A. Burkert. Vine – A Numerical Code for Simulating Astrophysical Systems Using Particles. I. Description of the Physics and the Numerical Methods. *ApJS*, 184:298–325, October 2009.
- M. P. White. Numerical models of the galactic dynamo. *Astronomische Nachrichten*, 299:209–216, 1978.
- S. D. M. White and C. S. Frenk. Galaxy formation through hierarchical clustering. *ApJ*, 379:52–79, September 1991.
- S. D. M. White and M. J. Rees. Core condensation in heavy halos - A two-stage theory for galaxy formation and clustering. *MNRAS*, 183:341–358, May 1978.
- B. C. Whitmore, Q. Zhang, C. Leitherer, S. M. Fall, F. Schweizer, and B. W. Miller. The Luminosity Function of Young Star Clusters in “the Antennae” Galaxies (NGC 4038-4039). *AJ*, 118:1551–1576, October 1999.
- R. Wiatr. Konstrukcja syntetycznych map radiowych oraz trójwymiarowa wizualizacja wyników symulacji mhd z promieniowaniem kosmicznym. Master’s thesis, Univ. Toruń, Wydział Fizyki, Astronomii i Informatyki Stosowanej, Centrum Astronomii, 2006.
- L. M. Widrow. Origin of galactic and extragalactic magnetic fields. *Reviews of Modern Physics*, 74:775–823, 2002.
- H. Wiechen, G. T. Birk, and H. Lesch. Generation of magnetic seed fields in protogalactic clouds due to plasma-neutral gas friction. *A&A*, 334:388–394, June 1998.

- H. Wiechen, G. T. Birk, and H. Lesch. Self-Generation of Magnetic Fields in Weakly Ionized Astrophysical Plasmas. Ap&SS, 264:347–356, 1999.
- H. Wiechen, G. T. Birk, and H. Lesch. The origin of primeval magnetic fields: Self-consistent simulation of magnetic field generation and amplification. Physics of Plasmas, 7:701–705, February 2000.
- R. Wielebinski and F. Krause. Magnetic fields in galaxies. A&A Rev., 4:449–485, April 1993.
- R. Wielebinski and J. R. Shakeshaft. Faraday Rotation of Polarized Galactic Radio Emission. Nature, 195:982–983, September 1962.
- L. P. Williams. Michael Faraday – A Biography. Basic Books inc., New York, 1965.
- L. P. Williams. André-Marie Ampère. Scientific American, 260:72, January 1989.
- C. D. Wilson, N. Scoville, S. C. Madden, and V. Charmandaris. High-Resolution Imaging of Molecular Gas and Dust in the Antennae (NGC 4038/39): Super Giant Molecular Complexes. ApJ, 542:120–127, October 2000.
- A. M. Wolfe, K. M. Lanzetta, and A. L. Oren. Magnetic fields in damped Ly-alpha systems. ApJ, 388:17–22, March 1992.
- A. M. Wolfe, K. M. Lanzetta, C. B. Foltz, and F. H. Chaffee. The Large Bright QSO Survey for Damped LY alpha Absorption Systems. ApJ, 454:698–+, December 1995.
- A. M. Wolfe, E. Gawiser, and J. X. Prochaska. Damped Ly  $\alpha$  Systems. ARA&A, 43:861–918, September 2005.
- J. M. Wrobel and D. S. Heeschen. Current star formation as the origin of kiloparsec-scale radio sources in nearby E/S0 galaxies. ApJ, 335:677–687, December 1988.
- J. M. Wrobel and D. S. Heeschen. Radio-continuum sources in nearby and bright E/S0 galaxies - Active nuclei versus star formation. AJ, 101:148–169, January 1991.
- C. K. Xu, N. Lu, J. J. Condon, M. Dopita, and R. J. Tuffs. Physical Conditions and Star Formation Activity in the Intragroup Medium of Stephan’s Quintet. ApJ, 595:665–684, October 2003.
- A. Yahalom and D. Lynden-Bell. Simplified Variational Principles for Barotropic Magnetohydrodynamics. ArXiv Physics e-prints, March 2006. arXiv:physics/0603115.
- Y. B. Zeldovich, A. A. Ruzmaikin, and D. D. Sokoloff. The almighty chance. World Scientific Publication, Singapore, 1990.
- Ya. B. Zeldovich, A. A. Ruzmaikin, and D. D. Sokoloff. Magnetic Fields in Astrophysics, volume 3. Gordon and Breach, Science Publishers (The Fluid Mechanics of Astrophysics and Geophysics), New York, 1983.
- A. Zezas and G. Fabbiano. Chandra Observations of “The Antennae” Galaxies (NGC 4038/4039). IV. The X-Ray Source Luminosity Function and the Nature of Ultraluminous X-Ray Sources. ApJ, 577:726–737, October 2002.
- A. Zezas, G. Fabbiano, A. Baldi, F. Schweizer, A. R. King, T. J. Ponman, and A. H. Rots. Chandra Monitoring Observations of The Antennae Galaxies. I. Catalog of Source Properties. ApJS, 166: 211–248, September 2006.
- H.-X. Zhang, Y. Gao, and X. Kong. Star formation histories within the Antennae galaxies (Arp244). MNRAS, 401:1839–1849, January 2010.

## Curriculum Vitae

NAME	Kotarba Hanna Helena	
DATE OF BIRTH	October 6th 1980 in Zabrze (Poland)	
NATIONALITY	German	
EDUCATION	2008- 2011	<b>LMU Munich / MPE Garching</b> PhD student in Astrophysics
	2002-2008	<b>LMU Munich</b> Course of studies: Physics (Diplom)
	2000-2002	<b>Upper vocational school Ingolstadt</b> Degree: Advanced technical college entrance qualification General qualification for university entrance
	1997-2000	<b>Vocational school for typography Munich</b>
	1993-1997	<b>Secondary modern school Ingolstadt</b> Degree: O-level, specialization engineering
	1986-1993	<b>Primary schools Zabrze, Litzldorf, Ingolstadt</b>
TRAINING	April 2010	<b>Voluntary service as scientific editorial journalist</b> ZDF series "Abenteuer Forschung"
	2008-2009	<b>Scientific editor at Pearson publishing</b> for the german translation of "The Cosmic Perspective" by Bennett et al.
	2004-2008	<b>Student assistant at MPE and IPP Garching</b> Transcription and creation of lecture scripts, revision and creation of webpages
	2003-2005	<b>Assistant at the institute for physics at the LMU</b> Supervision of practical courses, transcription of lecture scripts
	1997-2000	<b>Apprenticeship as Media Designer (Operating)</b> at Weigert company, Neuburg a.d. Donau
LANGUAGE SKILLS	<ul style="list-style-type: none"> <li>- German (mother tongue)</li> <li>- English (fluently)</li> <li>- Polish (fluently)</li> <li>- French (elementary)</li> </ul>	



## List of scientific publications

### Refereed publications

- **Kotarba, H.**, Lesch, H., Dolag, K., Naab, T., Johansson, P.H., Donnert, J. & Stasyszyn, F.A., 2010, Galactic ménage à trois: Simulating magnetic fields in colliding galaxies, accepted for publication by *MNRAS*, *ArXiv e-prints*: 1011.5735
- **Kotarba, H.**, Karl, S.J., Naab, T., Johansson, P.H., Dolag, K., Lesch, H. & Stasyszyn, F.A., 2010, Simulating Magnetic Fields in the Antennae Galaxies, *ApJ*, 716, 1438-1452
- Karl, S.J., Naab, T., Johansson, P.H., **Kotarba, H.**, Boily, C.M., Renaud, F. & Theis, C., 2010, One Moment in Time - Modeling Star Formation in the Antennae, *ApJL*, 715, L88-L93
- **Kotarba, H.**, Lesch, H., Dolag, K., Naab, T., Johansson, P.H. & Stasyszyn, F.A., 2009, Magnetic field structure due to the global velocity field in spiral galaxies, *MNRAS*, 397, 733-747

### Conference proceedings

- Hanasz, M., Woltanski, D., Kowalik, K., & **Kotarba, H.**, 2010, Cosmic-ray driven dynamo in galaxies, *IAUS*, 274, in press
- **Kotarba, H.**, Lesch, H., Dolag, K. & Naab, T., 2010, The fate of magnetic fields in colliding galaxies, *IAUS*, 274, in press
- **Kotarba, H.**, Lesch, H., Dolag, K., Naab, T., Johansson, P.H. & Stasyszyn, F.A., 2009, Structure of magnetic fields in spiral galaxies, *IAUS*, 259, 551-552



## Danksagung

An erster Stelle möchte ich mich besonders herzlich bei meinem Doktorvater Prof. Harald Lesch bedanken, der mich nicht nur fachlich hervorragend betreut hat, sondern mir während der Doktorarbeit auch ein sehr guter Mentor und Freund gewesen ist.

Die vorliegende Arbeit entstand im Rahmen einer engen Zusammenarbeit mit der Computational Astrophysics Group (CAST) an der Universitätssternwarte der LMU in München. Deshalb möchte ich mich besonders bei dem Leiter der CAST Gruppe, Prof. Andreas Burkert, und meinen Kolleginnen und Kollegen Dr. Thorsten Naab, Dr. Peter Johansson, Dr. Matthias Gritschneider, Dr. Stephanie Walch, Herrn Simon Karl, Frau Michaela Hirschmann und Herrn Ludwig Oeser für zahlreiche Diskussionen und Anregungen und die herzliche Aufnahme in ihrer Arbeitsgruppe bedanken.

Besonderer Dank gebührt auch meinen Kollegen am Max Planck Institut für Astrophysik, Dr. Klaus Dolag, Herrn Federico Stasyszyn und Herrn Julius Donnert, deren fachliche Unterstützung zum Gelingen dieser Arbeit beigetragen hat.

Darüber hinaus danke ich meinen Kollegen in Polen, im Besonderen Prof. Michał Hanasz aus Toruń und Prof. Katarzyna Otmianowska-Mazur aus Kraków und deren Arbeitsgruppen. Sie haben mir zahlreiche Besuche an ihren Instituten ermöglicht, die zu einer inspirierenden Zusammenarbeit geführt haben.

Ich danke auch allen anderen meiner Kolleginnen und Kollegen an der Universitätssternwarte für die gute Arbeitsatmosphäre. Insbesondere danke ich dabei Dr. Rudolf Gabler, Dr. Keith Butler und Dr. Tadiusz Hoffmann, die immer zur Stelle waren, wenn das Computersystem versagte.

Für die aufmerksame Durchsicht des Manuskripts danke ich Herrn Alexander Beck.

Schließlich danke ich besonders herzlich meiner Familie und meinem Mann Marcus für ihren Glauben an mich ihre moralische Unterstützung.

Diese Arbeit wurde im Rahmen der International Max-Planck Research School on Astrophysics vom Max Planck Institut für extraterrestrische Physik finanziert.